

# Developments towards the tomographic imaging of local crystallographic structures

A

## THESIS

Submitted to the Open University, Milton Keynes  
Department of Design, Development, Environment and Materials (DDEM)  
in the Faculty for Mathematics, Computing and Technology (MCT)  
for the degree of Doctor of Philosophy

by

Dipl.-Ing. Mirko Boin  
from Berlin

Date of submission: 22 November 2010

Date of examination: 18 February 2011

Examination Panel Chair: Dr. David Sharp, The Open University

Internal Examiner: Prof. Nicholas Braithwaite, The Open University

External Examiner: Dr. Axel Steuwer, Lund University, Sweden



# Abstract

In the present work, the possibilities of a neutron imaging method are comprehensively investigated. The basic principle of the so-called Bragg edge technique is the transmission of cold and thermal neutrons through polycrystalline materials. Related to the sample's crystal structure and the atomic parameters, sudden intensity changes appear in the transmission spectrum. The position and magnitude of these Bragg edges are considered towards the analysis of the sample characteristics.

The main focus of this thesis is the feasibility of measuring crystallographic properties with this Bragg edge neutron transmission method. A theoretical neutron cross section calculation is accounted to describe the Bragg edge effect. This calculation, which is based on the crystallographic description of the sample, is implemented into the McStas Monte Carlo neutron simulation. Incorporating adjustable sample and instrument parameters, the resulting simulation tool is used to analyse individual influences on the Bragg edge spectrum. In order to allow a comparison with real experiment results, the conditions of two existing neutron instruments are simulated. The complementary time-of-flight and continuous measurement techniques are also taken into consideration in this study. In this way, the whole process of a Bragg edge transmission experiment on the ENGIN-X diffractometer and the CONRAD tomography machine is emulated.

As application examples, the crystallographic texture and residual strain information from standard specimens is analysed. Reference data from diffraction measurements is provided in order to evaluate the Bragg edge experiments. Additionally, the sample characteristics

---

are implemented to validate the experimental results. In addition, the multiple scattering phenomenon as a further influencing factor, is investigated. The simulations and the experiments show good agreements and the comparison is used to discuss the realisability and limitations of Bragg edge measurements on such instruments.

## Publications

Parts of the work included in this dissertation have been published in the following academic journals and conference proceedings:

M. Strobl, A. Hilger, M. Boin, N. Kardjilov, R. C. Wimpory, D. Clemens, M. Mühlbauer, B. Schillinger, T. Wilpert, C. Schulz, K. Rolfs, C. M. Davies, N. O'Dowd, P. Tiernan & I. Manke. *Time-of-flight neutron imaging at a continuous source: Proof of principle using a scintillator CCD imaging detector*. Nucl. Instrum. Methods Phys. Res., Sect. A. **651**(1) (2011), 149-155, doi:10.1016/j.nima.2010.12.121

M. Boin, A. Hilger, N. Kardjilov, S. Y. Zhang, E. C. Oliver, J. A. James, C. Randau & R. C. Wimpory. *Validation of Bragg edge experiments by Monte Carlo simulations towards quantitative texture analysis*. J. Appl. Cryst. **44**(5) (2011), 1040-1046, doi:10.1107/S0021889811025970

M. Boin, R. C. Wimpory, A. Hilger, N. Kardjilov, S. Y. Zhang & M. Strobl. *Monte Carlo simulations for the analysis of texture and strain measured with Bragg edge neutron transmission*. In *ECNS 2011: 5<sup>th</sup> European Conference on Neutron Scattering, Prague, Czech Republic, July 17–22*, accepted for publication in J. Phys.: Conf. Ser.



## Acknowledgements

The work presented is the account of the last three and a half years of working in the field of Bragg edge neutron transmission. It would not have been possible without the help of many people I would like to acknowledge here. Primarily, I would like to thank Prof. Lyndon Edwards from the Open University, Prof. John Bahnhart and Dr. Rainer P. Schneider from the Helmholtz Centre Berlin for Materials and Engineering (HZB, former Hahn-Meitner-Institut Berlin) who paved the way for my studies on this topic and this thesis.

I am very grateful for all sincere assistance, discussion and guidance provided by my supervisors Dr. Astrid Haibel, Dr. Jonathan A. James and Dr. Javier R. Santisteban. Furthermore, I am especially thankful for the support of Tobias Poeste and Robert C. Wimpory from the residual stress diffractometer E3. Thank you for your helpful introductions to the instrument and for the fruitful discussion about experimental methods. The close scientific teamwork and the working atmosphere over the past years is appreciated. Likewise, I would like to thank Nikolay Kardjilov and André Hilger from the CONRAD tomography machine. Their motivating ideas towards the Bragg edge transmission experiments and the detailed talks concerning the instrument and its simulation contribute to a large part towards the completion of my thesis. I would also like to give special attention to Prof. Christoph Genzel from the HZB residual stress group. His encouragements towards the finalisation of the this work and the opportunity to work in his group are also greatly acknowledged.

To Edward C. Oliver I am indebted for inviting me to ISIS. Resulting from that, we have been working in a close collaboration towards the simulation of neutron imaging experiments.

---

Moreover, I would like to reserve a special thank for the financial support realised by the student sponsorship of the Science & Technology Facilities Council (STFC, Ref: CMPC08101). Without Ed's help this would not have been possible. I thank Winfried Kockelmann for the continuation of this project and the possibility to take part in the IMAT project. In this regard, I would also like to thank all the staff from the ENGIN-X instrument. Shu Yan Zhang and Anna Paradowska, thank you very much for your support with the experimental data analysis.

I also kindly acknowledge Christian Randau from TU Clausthal. I appreciate the corporate time at the HZB at the beginning of this work and the collaboration with Munich towards the StressTexCalculator program afterwards. I am grateful for his support at the STRESS-SPEC instrument and the numerous pole figure discussions. Referring to this, Rodrigo S. Coelho from HZB is also greatly acknowledged. The exchange and discussion of experiences with texture were very useful. A further thank goes to Frederik L. Zilly for his introduction to the McStas Monte Carlo program and the conversations about neutron transmission. Equally, I am very grateful for the discussions with Prof. Axel Steuwer from ESS Scandinavia and Sven Vogel from the Los Alamos Neutron Science Center concerning Bragg edges.

Finally, I am especially thankful to my family and friends for the mental assistance and backing in the last years. My last but not least thanks go to my wife to whom I dedicate this work.

Berlin, November 2010

Mirko Boin



# Contents

<b>1. Introduction</b>	<b>1</b>
1.1. Background	1
1.2. Motivation	4
1.2.1. Experiment Planning	5
1.2.2. Applications to Instrument Development	6
1.2.3. Applications in Data Analysis	7
1.3. Structure of the Thesis	8
<b>2. Literature Review</b>	<b>11</b>
2.1. Solid States	11
2.1.1. Engineering Materials	12
2.1.2. Crystal Structures	15
2.1.3. Miller Indices	16
2.2. Neutrons for Material Science	17
2.2.1. Neutron Properties	17
2.2.2. Neutron Generation and Detection	18
2.3. Bragg Diffraction	21
2.3.1. Extinction Effects	23
2.3.2. Diffraction Techniques	25
2.4. Computed Tomography	27
2.4.1. The Tomographic Setup	28
2.4.2. Reconstruction	30

---

2.4.3.	Image Processing . . . . .	32
2.4.4.	Vector and Tensorial Tomography . . . . .	33
2.5.	Strains and Stresses . . . . .	34
2.5.1.	Residual Stress Types and Applications . . . . .	35
2.5.2.	Residual Stress Determination . . . . .	36
2.6.	Crystallographic Texture . . . . .	38
2.6.1.	Pole Figures . . . . .	40
2.6.2.	Texture Methods . . . . .	42
<b>3.</b>	<b>Bragg Edge Neutron Transmission Computation</b>	<b>45</b>
3.1.	The Transmission Intensity Spectrum . . . . .	45
3.2.	Neutron Cross Sections . . . . .	48
3.2.1.	Scattering . . . . .	49
3.2.2.	Absorption . . . . .	53
3.2.3.	Analytical Description of Measured Bragg edges . . . . .	54
3.2.4.	Discussion on Bragg Edge Amplitude Changes . . . . .	55
3.2.5.	Summary . . . . .	59
3.3.	Bragg Edge Implementation . . . . .	61
3.3.1.	The nxs Library & nxsPlotter . . . . .	61
3.3.2.	Input Parameters . . . . .	63
3.3.3.	SgInfo - Space Group Library . . . . .	64
3.3.4.	Unit Cell Initialisation . . . . .	65
3.3.5.	Neutron Cross Section Functions . . . . .	68
3.3.6.	Validation . . . . .	69
3.4.	Texture Correction . . . . .	70
3.4.1.	The March-Dollase Model . . . . .	71
3.4.2.	Implementation into nxs Library . . . . .	72
3.4.3.	Summary . . . . .	75

---

<b>4. Neutron Instruments</b>	<b>77</b>
4.1. CONRAD . . . . .	77
4.1.1. High Flux and High Resolution Positions . . . . .	78
4.1.2. Neutron Energy Selection . . . . .	78
4.1.3. Data Analysis . . . . .	80
4.2. ENGIN-X . . . . .	81
4.2.1. Instrument Setup . . . . .	81
4.2.2. Transmission Detectors . . . . .	82
4.3. Bragg Edge Measurement Alternatives . . . . .	84
4.4. E3 & STRESS-SPEC Diffractometers . . . . .	85
4.4.1. Construction . . . . .	85
4.4.2. Software . . . . .	86
<b>5. Development of a Bragg Edge Experiment Simulation</b>	<b>89</b>
5.1. McStas - Neutron Ray-Tracing Simulation . . . . .	89
5.1.1. Scientific Background . . . . .	90
5.1.2. Program Features . . . . .	90
5.1.3. Simulation Workflow . . . . .	91
5.2. Bragg Edge Simulation . . . . .	93
5.2.1. A McStas Sample Component . . . . .	94
5.2.2. Library nxs Insertion . . . . .	95
5.2.3. Input Files . . . . .	98
5.2.4. Simulation Verification . . . . .	100
5.3. Statistical Errors & Simulation Performance . . . . .	102
5.3.1. Simulation Speed . . . . .	102
5.3.2. Stratified & Importance Sampling . . . . .	105
5.4. CONRAD Instrument Simulation . . . . .	107
5.4.1. Double Crystal Monochromator . . . . .	107
5.4.2. Influence of Monochromator Properties to Bragg Edge Spectra . . . . .	113
5.5. ENGIN-X Simulation Module . . . . .	116
5.6. Summary . . . . .	118

---

<b>6. Texture Effects on the Neutron Total Cross Section</b>	<b>121</b>
6.1. Texture Determination by Neutron & X-ray Diffraction . . . . .	122
6.1.1. Pole Figure Measurements . . . . .	122
6.1.2. Data Analysis . . . . .	124
6.1.3. X-ray diffraction reference measurements . . . . .	127
6.2. Texture Mapping with Radiography on CONRAD . . . . .	129
6.2.1. Bragg Edge Determination . . . . .	130
6.2.2. Radiographic Texture Measurements . . . . .	131
6.3. Transmission Spectroscopy on ENGIN-X . . . . .	133
6.4. Evaluation of Results . . . . .	136
6.4.1. Comparison of Complementary Measurements . . . . .	136
6.4.2. Possible Sources of Error . . . . .	138
6.5. March-Dollase Simulations . . . . .	141
6.6. Conclusion . . . . .	144
<b>7. Local Strain Properties</b>	<b>147</b>
7.1. A Standard Residual Stress Sample . . . . .	147
7.1.1. VAMAS Al Ring and Plug . . . . .	147
7.1.2. Reference Strain Values . . . . .	148
7.2. Strain Implementation in McStas . . . . .	149
7.2.1. Application of Local Sample Properties . . . . .	150
7.2.2. Projected Strain in Transmission Direction . . . . .	153
7.3. Ring and Plug Simulations . . . . .	154
7.3.1. Modification for Beam Divergence . . . . .	155
7.3.2. ENGIN-X and CONRAD simulations . . . . .	156
7.3.3. Data Evaluation . . . . .	157
7.4. Validation with Experiments . . . . .	160
7.4.1. ENGIN-X . . . . .	160
7.4.2. CONRAD . . . . .	162
7.5. Discussion on Strain Reconstruction . . . . .	165
7.6. Concluding Remarks . . . . .	166

---

<b>8. Multiple scattering</b>	<b>169</b>
8.1. Motivation . . . . .	169
8.1.1. Background . . . . .	170
8.1.2. Theory . . . . .	171
8.2. Multiple scattering McStas component . . . . .	172
8.2.1. Simulation principle . . . . .	172
8.2.2. Algorithm & Implementation . . . . .	173
8.3. Simulation Testing using ENGIN-X . . . . .	176
8.3.1. Sample Thickness . . . . .	176
8.3.2. Sample-Detector Distance . . . . .	178
8.3.3. ToF vs. Wavelength Monitor . . . . .	179
8.3.4. Powder Simulation . . . . .	182
8.4. Step Wedge Investigations on CONRAD . . . . .	184
8.4.1. CONRAD Radiography Experiments . . . . .	184
8.4.2. Evaluation with Experiment Simulations . . . . .	186
8.5. Discussion . . . . .	189
<b>9. Summary</b>	<b>193</b>
9.1. Results & Conclusion . . . . .	193
9.2. Case Study: IMAT beamline . . . . .	196
9.2.1. Moderator choice . . . . .	197
9.2.2. Aluminium windows . . . . .	200
9.3. Further Work . . . . .	201
<b>References</b>	<b>207</b>
<b>A. Calculation of <math>\varphi_1</math> and <math>\varphi_3</math></b>	<b>225</b>
<b>B. Unit Cell Calculations</b>	<b>227</b>
<b>C. McStas Listings</b>	<b>229</b>
C.1. The Bragg Edge Sample Component . . . . .	229
C.2. Sample Input File “Fe.txt” . . . . .	231

---

C.3. Parameter File Reading Routine . . . . .	232
C.4. LambdaYPSD_monitor.comp . . . . .	234
<b>D. Ring and Plug Simulation</b>	<b>237</b>
D.1. Ring and Plug Sample Modification . . . . .	237
D.2. Ring and Plug Input File . . . . .	238

## **Introduction**

### **1.1. Background**

Non-destructive imaging, radiography and tomography in particular, is nowadays routinely used in quality assurance and process optimisation within the field of engineering science. Tomography is an appropriate method to investigate the internal structure of materials, composites and components and is an important technique for the investigation of scientific and engineering phenomena. Complementary, diffraction methods are used to characterise crystallographic properties of materials. Such methods are phase sensitive and allow the investigation of local lattice strain and texture distributions. Depending on the application, different radiations may be used for both diffraction and tomography. In addition to laboratory X-rays, neutron and synchrotron sources can also be utilised to provide a wide range of complementary contrast, sample size and spatial resolution. Neutron scattering, for example, is one of the most important tools used for many applications in science. In figure 1.1, the mass attenuation coefficients of selected elements are plotted for X-rays and thermal neutrons to emphasise the different strengths of interaction with matter. Compared to X-rays, neutrons are weakly attenuated by a large amount of materials, even by heavy elements. Resulting from that, the high neutron penetration depth allows the investigation of sample volumes deep inside engineering materials. For example figure 1.2, taken from Koerner et al. [2000], visualises the different absorption contrasts of neutron and X-ray radiographic images of the same object. Depending on the materials to be investigated, radiography with different sources can provide complementary results.

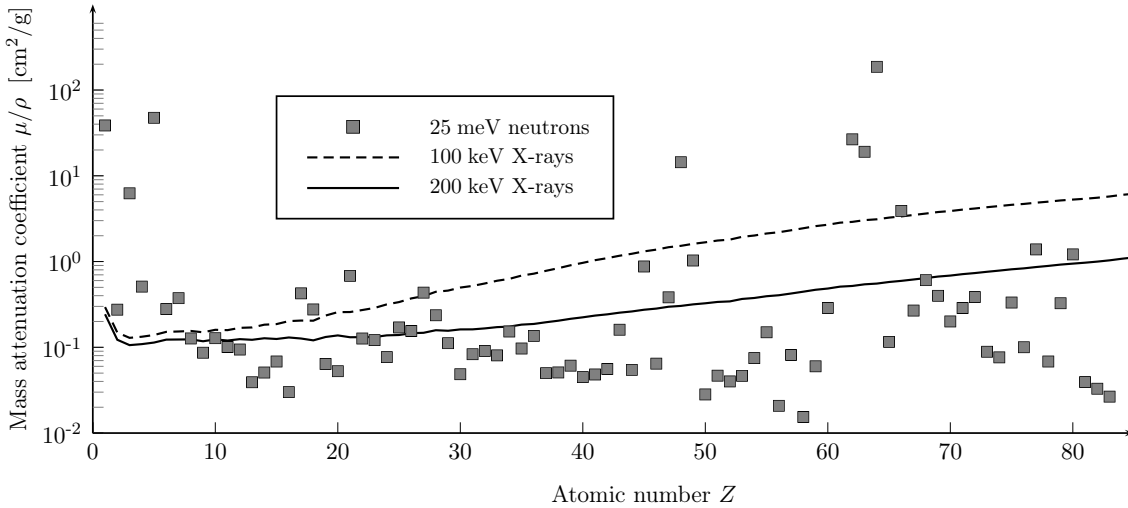


**Figure 1.1.:** *Mass attenuation coefficients of selected elements for 100 keV and 200 keV X-rays, taken from Hubbell & Seltzer [2004] and for thermal (25 meV) neutrons, calculated by means of their cross sections listed in Prince [2006]. Unlike X-rays, neutrons do not show a systematic attenuation dependence with the atomic number  $Z$ .*

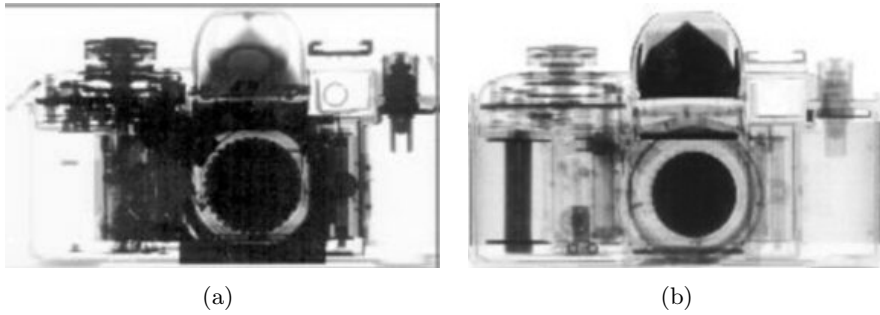


**Figure 1.2.:** *In contrast to X-ray radiography (a), the neutron radiographic image (b) of a camera, taken from Koerner et al. [2000], picks out the hydrogen containing plastic of the film spools and illustrates that the neutron attenuation is not generally mass dependent as shown in figure 1.1.*

In contrast to diffraction experiments, the geometry of a radiography/tomography setup is very simple. The neutron beam path is defined by the incident beam direction. The same direction is maintained behind an investigated specimen. The attenuated neutron signal is captured by a detector. The present state of the art of radiographic and tomographic imaging is generally confined to the evaluation of absorption to identify the type and density of material inside a specimen. However, the effect of neutron diffraction is still there. In particular, coherent elastic scattering appears if the incident wavelength is in the same order of magnitude as the crystallographic lattice distances of the investigated material. Then,



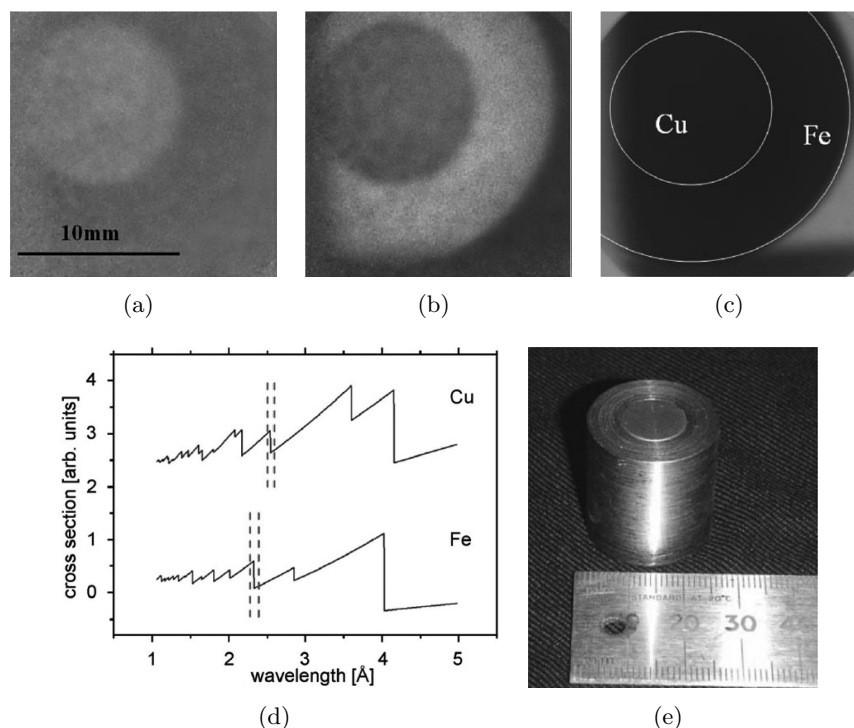


**Figure 1.3.:** Contrast enhancement between the iron and copper components of a cylinder specimen by taking radiographic images at defined neutron wavelength positions [Kockelmann et al., 2007a]. The images in (a) and (b) represent the ratio of measurements taken below and above the 220 copper Bragg edge ( $\approx 2.5 \text{ \AA}$ ) and below and above the 211 iron Bragg edge ( $\approx 2.3 \text{ \AA}$ ) respectively. Outside the Bragg edge region ( $> 4 \text{ \AA}$ ), the radiographic image (c) does not allow any deviation between the two components in the sample. The selected wavelength positions are indicated in (d) by means of the copper and iron cross section spectra. A photograph of the cylinder is shown in (e).

the neutron transmission intensity spectrum contains sudden intensity changes as a result of the crystalline properties of the sample material. Thus, it is possible to take advantage of incident monochromatic neutrons in order to analyse the wavelength-dependent neutron transmission. In radiography, for example, the contrast between different materials can be increased by this phenomenon. Figure 1.3, taken from Kockelmann et al. [2007a], shows an example of radiographic images of an iron and copper cylinder. Depending on the selection of the incident neutron wavelength, a higher radiographic contrast between both components can be achieved. The explanation of this effect is shown in figure 1.3d by means of the neutron cross section spectra of the two elements. Both graphs indicate discontinuities leading to sudden intensity changes in the transmission spectrum at defined wavelengths —

the so-called Bragg edges. The authors took advantage of the difference between both patterns by selecting different wavelengths position (indicated by the dashed lines) to measure radiographic images. As a result the transmitted intensities of the two components vary from each other (1.3a and 1.3b), while the image taken outside the Bragg edge region (1.3c), i.e. above 4 Å, disables such a deviation. The position and magnitude of these Bragg edges are related to the crystalline properties of the sample. Hence, the development of the analysis of these material characteristics using neutron Bragg edge transmission is the main core of this work.

## 1.2. Motivation

A presentation of advantageous properties of the Bragg edge neutron transmission experiment technique has been summarised by Vogel [2000] for example. One aspect is that, compared to diffraction measurements, relatively short exposure times can be applied in order to resolve structural sample parameters. In Bowman et al. [1991], this was also demonstrated based on examples of single pulse neutron time-of-flight measurements. The incident neutron flux is very high and therefore, generally, the total number of detected neutrons per second in transmission mode is also high. In contrast, most diffraction instruments detect only a small proportion of the neutrons. Even area detectors capture only a small percentage. Thus, most of the neutrons remain unused as they are scattered over  $4\pi$ , although they could be involved in the evaluation of the sample properties if they had been detected before. Another advantage is the possibility to easily improve the quality of the transmission signal. The more sample area or volume (thickness) is illuminated, the smaller the statistical error. According to that, the Bragg edge method can be applied within radiographic and tomographic instruments — the simple transmission setup is the same. Using the area captured by a radiography camera system, the Bragg edge method could be used to distinguish local changes simultaneously without changing the sample position. This would decrease the amount of measurement positions and the exposure time respectively. Related to that, high spatial resolution could be achieved.

The motivation of the present work is to enable the analysis of crystallographic sample properties with an alternative measurement method that provides shorter integration times, high spatial resolution and simple experiment setup. Measuring the sudden and sharp intensity jumps with wavelength-dependent neutron transmission enables a very quick method to determine the lattice spacing precisely [Windsor, 1981]. Therefore, the accuracy of the Bragg edge position determination is one of the key issues reviewed in this thesis. Due to the beneficial characteristics, it is useful to continue the development of this method and establish an understanding of the experimental issues. As part of this process, it is advantageous to compare measured Bragg edge patterns with theoretical calculations. In this connection simulations of different sample properties and instrument parameters have been realised. This will help to derive influences to the measured signal from the parameters tested. Therefore, the main subject presented in this thesis is the development of a Bragg edge Monte Carlo simulation together with the analysis of the transmission spectra. In the following, beneficial aspects towards this development are explained in detail.

### **1.2.1. Experiment Planning**

In order to effectively use neutron beam time, it is important to prepare the experiment carefully beforehand. Therefore, Monte Carlo simulations have already been used to compute diffraction measurements. This is especially useful when extra effects of instrument windows and sample cells to the detector signal must be estimated. Thus, it is important to determine for example how sample environment windows (e.g. beam tubes and sample holders/boxes) will overlap with the sample spectrum. Moreover, one could determine the optimum sample thickness by a calculation of a Bragg edge transmission pattern. Hence, good statistical measurements can be achieved if the sample can be prepared before. Another possible effect that might influence the transmission spectrum is the presence of preferred grain orientations within the sample (so-called texture). In the presence of texture, the Bragg edges will vary according to the crystalline orientation within the sample and a computation of this effect is helpful to determine the best orientation of the sample. In general, the determination of expected Bragg edge positions would help to discuss the feasibility of such measurements. Limitations could be defined in order to save beam time, for example. Similar to a selection

of diffraction peaks, one could focus on a smaller neutron energy/wavelength range in the Bragg edge transmission spectrum. The sudden intensity changes that occur due to the Bragg transmission edges can then be used to enable contrast enhancements in imaging experiments so that the spatial resolution of tomography experiments can be improved, for example. Therefore, it is advantageous to know the appropriate measurement positions before measurements commence. In summary, the ability to predict Bragg edge patterns and to take proper account of neutron instrument effects would be of considerable benefit to any beamline concerned with such measurements and for everybody who performs or plans such experiments.

### 1.2.2. Applications to Instrument Development

Monte Carlo simulation software has become more and more important for the development of neutron instruments. Such tools are not only useful for the preparation of experiments as reported above, but also in the design and upgrade phase of an instrument [e.g. Santisteban et al., 2006a; Šaroun et al., 2002]. Because of the instrument complexity, a large number of parameters and conditions need to be handled when changes and optimisations are under consideration. A Monte Carlo instrument simulation would help to test multiple scenarios with varying parameters. Thus, effects on the detector signal can be estimated in advance. Hence, also in Bragg edge transmission geometry it is important to know the instrumental parameters that may effect the transmission signal at the detector. For example, a new beamline at the ISIS second target station in the UK is currently being designed to enable diffraction and imaging experiments for the investigation of engineering materials [Kockelmann et al., 2007b]. The calculation, using Monte Carlo methods, of Bragg edges for different incident spectra from different moderator materials is very useful. Similarly, the count rate to achieve good quality Bragg edges can be estimated, using these methods, for different materials. Consequently, a prediction of the necessary exposure time is possible. Moreover, the above mentioned windows to terminate beamtubes and neutron guides can be included within a complete virtual instrument definition. The transmission through these components could be simulated with respect to the neutron energy state. Thus, the influence of multiple instrument parts can be taken into account. Furthermore, different sample-detector

distances can be tested easily in order to check whether different settings compromise the results. Altogether, a complete instrument setup could be mapped to a simulation tool and tested with a virtual Bragg edge experiment. The final design of a real instrument can be defined effectively by different test cases of the simulation.

### 1.2.3. Applications in Data Analysis

Taking Bragg edges into account, the transmission spectrum contains structural information about the sample. The analysis of such an experiment can be supported by computer programs and databases that predict Bragg edge positions. Moreover, the simulation of different sample characteristics can be a helpful tool for a comparison with the real measurement. Due to the transmission geometry the sample information may be convoluted and averaged over all local position along the beam path through the sample. Hence, a comparison with a simulation of known and expected parameters may help to draw conclusions from the experimental results. Thus, the investigation of strain and texture properties will become possible with this Bragg edge transmission method. In the case of texture for example, the resulting transmission pattern depends strongly on the orientation of the sample. Hence, considering Bragg edge patterns from databases and powder measurements is not always sufficient and including a texture model into the Bragg edge computation can contribute more effectively towards the final data analysis. Regarding the investigation of strain using the Bragg edge method, it is helpful to have an understanding of the signals measured in transmission mode. Therefore, the strain values of a sample that have been determined by conventional methods can be applied to a simulation module. Then, the results from the virtual experiment could give information about the feasibility of such studies and the validity of the results from real measurements. There is also a great interest to measure neutron cross sections of different materials [e.g Kockelmann & Kirfel, 2006]. Due to different instrument setups and sample orientations people have measured the same sample and got different results. A simulation tool including detailed experiment descriptions would therefore be useful to help understand the measured cross section values as a function of instrument and sample parameters.

### 1.3. Structure of the Thesis

Starting with a literature review, chapter 2 provides an overview of topics, terms and conventions relevant to this thesis. Properties of solid state materials as well as their crystalline characteristics will be introduced. The use of neutrons as a probe for the analysis of engineering materials will be described and the complementary diffraction and tomography methods, will be presented in order to provide an understanding of the Bragg edge transmission approach applied in this work. The background of strain and stress as well as crystallographic texture analysis is shown in order to provide background relevant to the possibility of the alternative measurement method investigated in this thesis.

In chapter 3, the discontinuities occurring in a neutron transmission intensity spectrum are explained by means of neutron cross sections. A detailed neutron cross section calculation is introduced based on the different types of neutron-matter interaction and the relevant individual cross sections will be described. This Bragg edge calculation will be implemented in routines into a C program library for the computation of transmission spectra depending on multiple sample/material parameters. Details of unit cell parameters and space group symmetries will be taken into account and both will be described here. The computer routines will be included in a plotting tool to predict Bragg edge patterns via the use of a graphical user interface. Finally, the resulting neutron cross sections will be validated with existing tools. Additionally, a method to model crystallographic preferred orientations towards the Bragg edge spectrum is also implemented.

Chapter 4 describes the instruments that have been used within this thesis. Two different instruments able to supply energy-selective neutron transmission measurements will be described in order to prepare for their implementation into a simulation. In addition, the neutron diffractometers used for reference measurements will also be explained.

Then, the neutron cross section calculation including the computing routing will be applied to the development of a neutron instrument simulation. Therefore, a Monte Carlo neutron simulation program will be introduced in chapter 5. By means of the available program features, the choice of the so-called McStas neutron ray-tracing environment will be justified.

A new virtual sample model including a Bragg edge simulation module will be created. The necessary material parameters to define the specimen will be applied. Utilising this, the neutron transmission instruments used within this work will be emulated with the McStas software. The energy-selective option of the CONRAD tomography instrument will be evaluated and example measurements used to verify the instrument simulation. The instrumental parameters effecting the captured Bragg edge spectrum will be discussed.

With chapter 6 the focus moves to the analysis of crystallographic properties using Bragg edge transmission. Here, texture measurements using the conventional neutron diffraction method will be presented to provide reference datasets. Based on pole figure analyses, the results will be compared with time-of-flight neutron transmission and Bragg edge radiography measurements.

Chapter 7 is concerned with the analysis of stresses and strains. By means of a residual stress sample, strain values collected with conventional neutron diffraction will be used to calculate the projected strain in the ltransmission direction. The developed Bragg edge simulation will be modified to emulate the residual stress sample. Real Bragg edge transmission measurements will be compared with the simulation.

Chapter 8 introduces the theory of multiple scattering events and their influence on the transmission detector signal. A model will be developed to simulate the effect of multiple scattering. The virtual Bragg edge sample component will be modified to include the multiple scattering model and included in the instrument definitions applied previously. By means of varying sample thicknesses and sample-detector distance the effect will be analysed. The simulation will be compared with experiments.

Chapter 9 summarises the investigations carried out in this thesis and gives suggestions for further work.





## Literature Review

The following literature review provides a summary of topics related to the presented work. Terms and definitions that will be applied in this thesis are described here. At the beginning, crystallographic structures and their denotations will be introduced. Afterwards, neutron properties will be presented in order to apply them with diffraction techniques as a probe for investigations in material science. Subsequently, basic principles of computed tomography will be shown to provide the fundamentals for the neutron transmission approach discussed in this work. Finally, strain and texture properties together with conventional investigation methods will be presented in order to allow a comparison with the Bragg edge method analysed here.

### 2.1. Solid States

The properties of solid state materials are affected by the composition and the arrangement of the components within. Here, the author refers to crystalline structures as opposed to amorphous structures. In solid state physics basically materials are investigated whose composition is characterised by periodic structures. The textbooks of Kittel [1995] and Ashcroft & Mermin [1976] for example, give a detailed overview of solid states and their characteristics. These crystalline materials can be classified by their crystallographic structure. The representative attribute of single crystals is the periodicity of their components, which can be described as a lattice structure. A perfect single crystal is therefore a material consisting of a continuous crystal lattice to the edges of the sample. In reality, the microstructure of a single crystal material can be influenced by impurity and distortion effects, defects and dis-

locations. Moreover, a real single crystal can be specified by a set of crystalline blocks each with fine differences in orientation for example. Thus, a mosaic model is used to describe an imperfect single crystal sample. The mosaicity is therefore a measure of the disorder of the crystal. The mosaic spread is a value (in angle units) representing the degree of crystal ordering. The lower the mosaic spread, the higher is the order of the crystal system. By contrast, polycrystals are based on disordered conglomerations of smaller crystals, the so-called crystallites. On the other hand, a powder sample consists of bulk crystallites, so that, the crystal orientation inside powder specimens is randomly distributed, while solid polycrystals may be influenced by a preferred orientation. The type of lattice has a strong influence on the macroscopic materials properties. For example, carbon exists with different kinds of lattices, which have totally different electrical conductivities. Graphite is a conducting material whilst diamond is an electrical insulator. Hence, it is important to have an understanding of the microstructural properties in engineering materials and how they influence their macrostructural characteristics and performance. The field of material science investigates these relations based on the study of the individual contributing chemical elements and the process they have been assembled to a final material.

### **2.1.1. Engineering Materials**

Considering the summary given in the book of Reimers et al. [2008], engineering materials can be grouped into metals, ceramics, polymers and semiconductors. More detailed introductions to the fields of materials science and engineering can be found in the books of Ashby & Jones [1998] and Callister [2007], for example. A few aspects of the presented materials will be summarised here.

Metals and their alloys have a regular crystalline microstructure, i.e. periodically repeating arrays of atom arrangements (see the following section 2.1.2). The largest portion of all are the iron (Fe) alloys — the steels. In general, the impact of the secondary elements on the alloy's properties is the main focus in the research of engineering metallic materials. For example, the amount of carbon is responsible for the hardness and tensile strength of steel, whereas the addition of chromium (Cr), nickel (Ni) and molybdenum (Mo) make steels

stainless. Furthermore, aluminium (Al), titanium (Ti) and magnesium (Mg) alloys are light metal materials. Their high strength-to-weight ratios are ideal for modern automotive and aerospace industry applications, for example. In general, the useful properties of metals can be summarised by strength, high melting points, ductility, thermal and electrical conductivity. All these properties are directly connected to the microstructure of metal, i.e. the analysis of the crystalline composition plays an important role when these characteristics shall be optimised.

Furthermore, there are materials that are neither good electrical conductors nor good insulators [Shackelford, 2004] — the semiconductors. Nowadays, they form the basis of the integrated circuits (IC) in almost every modern electronic device, such as computers, telephones, radios etc. For example, the conductivity of these materials can be changed by the application of a control voltage (e.g. transistor) in order to amplify and switch signals without mechanical movement. Moreover, the conductivity may depend on the direction (e.g. diode), which is useful when electric current shall only be allowed from one direction, the opposite direction will be blocked. Silicon (Si) is the most commercially used semiconductor material, but germanium (Ge) and gallium arsenide (GaAs) are also utilised. However, the electrical conductivity of these pure semiconductors can be changed by substituting individual atoms in the crystal lattice with other elements — a process called doping. In order to create semiconductor circuits, basically two main steps are required. At first a nearly perfect single crystals based on the semiconductor material is grown as a cylinder and then cut into thin discs (wafers). After that, the circuit components are etched or deposited on such a wafer, which can be sectioned into hundreds of small computer chips, for example, depending on the size of an IC. To increase functionality and speed of electronic devices, such as computers, smaller IC dimensions are advantageous, which is unfortunately attended by heat dissipation problems. Therefore, the research of new material designs, that use lower voltages, is required to build next generation computers, for example.

Not all engineering materials exhibit a regular structure. Polymers, for example, have a varying degree of crystallinity and can be completely non-crystalline. The final products, that are commonly known as plastics, are based on polymer raw materials — the basic

building block is a polymer molecule. Typical representatives are polyvinyl-chloride (PVC), polyethylene, polypropylene and nylons, for example. Besides the plastics, elastomers (or rubbers) exist that are elastically deformable, i.e. they can return to their original shape when the external forming forces are released [Smith, 1995]. Recent developments have led to polymeric systems exhibiting a semiconductor behaviour, for example. By connecting these materials to two electrodes, it is possible to generate light of any color, which leads to the organic light-emitting diode technology (OLED). Thus, very thin OLED flat panel displays can be produced which are flexible and less power-consuming than other existing display principles.

Ceramics and glasses are inorganic and non-metallic materials typically being composed of a combination of metallic and non-metallic elements. Traditionally, ceramics are known from clay products, silicate glass and cement. Nowadays, the ceramic materials are even more present in our everyday life. For example, many of these products are also used in electronic devices such as resistors, insulators and capacitors, i.e. the electrical properties can vary due to the material's structure. Many ceramics are crystalline but some are amorphous such as glasses. Ceramics are also famous for their high heat capacity and low heat conductance. Related to this, a well-known high-performance application is the returning space shuttle that uses many ceramic materials as heat-shielding tiles.

Altogether, these different materials are used in many situations within our modern technological society. New applications however often make new demands on materials, ensuring that the field of materials engineering remains a rapidly developing discipline in science. Lots of different methods have been developed to analyse, optimise and produce the materials presented above. Some of them are well-established and were used within this work as conventional techniques to study the properties of a material. The basic principles of these methods will be demonstrated in the following sections. However, within this thesis the author refers to an alternative method investigating crystalline materials and their properties. The fundamentals of this so-called Bragg edge method will be described later (in chapter 3).

### 2.1.2. Crystal Structures

In crystallography, a crystal structure is defined by a unique three-dimensional arrangement of atoms and a lattice, which is an array of these components repeating periodically. These arrangements can be described by so-called unit cells, which are the simplest units in the crystal. The lengths of the unit cell edges and the angles between them are called lattice parameters,  $a, b, c$  and  $\alpha, \beta, \gamma$  respectively. The positions of the atoms are given by  $(x_i, y_i, z_i)$  coordinates measured from a unit cell origin. A crystal exhibits symmetry properties, i.e. its structure passes into itself by defined translations, rotations and reflections and combinations of these. The symmetry characteristics are represented by the so-called space groups, that define the symmetry operations that leave the crystal unchanged. A total of 230 space groups exist to classify the lattice structures based on the symmetry operations. They have been enumerated by Fedorov (1891), Barlow (1894) and Schönflies [see Schönflies, 1891]. Several denotations exist to describe a space group. One is the notation by number (1-230). The Hermann-Mauguin [Hermann, 1928; Mauguin, 1931] notation usually uses four symbols describing a lattice type followed by labels for the symmetry operations applied. Moreover, there is the Schönflies notation adding a superscripted point group number to a Schönflies symbol [e.g. Patterson, 1971].

The periodicity of the crystalline structure is used to classify solid state materials. The crystal lattice is used to group the crystal structures according to their unit cell geometries. They can be divided into seven lattice systems. The most symmetric is the cubic structure. The other systems are hexagonal, tetragonal, rhombohedral (trigonal), orthorhombic, monoclinic and triclinic. An overview of their lattice parameter conventions can be obtained from appendix B. Extending the crystal systems with various possible lattice centring, one is able to describe the crystal by the so-called 14 unique Bravais lattices [e.g. Jones & March, 1973], named after the French physicist Auguste Bravais. They describe the geometric arrangement of the lattice atoms in three dimensions. In addition to the simple structure where there is no centring element, there are possibilities to find body-centred, face-centred and base-centred (also called end-centred: monoclinic and orthorhombic) crystal structures. Figure 2.1 shows the three possible Bravais lattices which form cubic crystal systems.

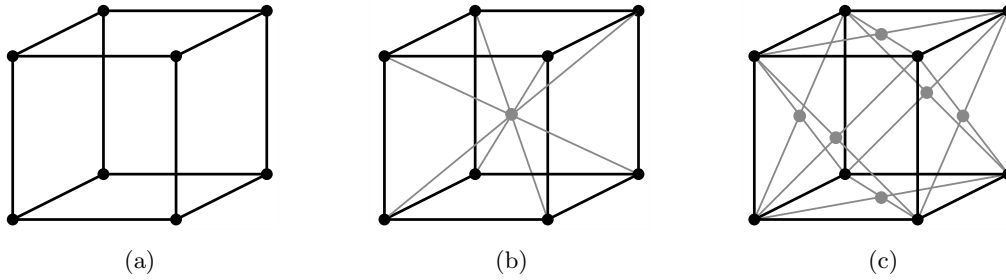


**Figure 2.1.:** Simple (a), body-centred (b) and face-centred (c) cubic crystal systems.

### 2.1.3. Miller Indices

In order to describe the orientation of a crystal, the notation of the so-called Miller indices<sup>1</sup> has been introduced. To specify the orientation of a plane of atoms within the crystal or a face, the lattice parameters will be taken into account. A lattice plane inside a crystal system can be defined by three (non-collinear) points. Here, the fractional intercepts that the plane makes on the crystallographic unit cell axes will be used [Kittel, 1995]. The next step is to take the reciprocal of the intercepts of each unit length for each axis. Then, the values will be reduced to the smallest integers having the same ratio. These numbers represent specific crystallographic lattice plane and may denote a family of planes with the same orientation since the unit cell repeats in space. The three numbers are enclosed in brackets. Negative numbers will be written with a bar. For example, the six face planes of a cubic crystal system are therefore denoted by  $(100)$ ,  $(010)$ ,  $(001)$ ,  $(\bar{1}00)$ ,  $(0\bar{1}0)$  and  $(00\bar{1})$ . Applying  $hkl$  to name the Miller indices, different definitions are known:

- $(hkl)$  - As mentioned above, parentheses are designated to a face or a family of crystal planes.
- $[hkl]$  - Square brackets are used to specify directions in the direct lattice from the origin to a point, i.e. the body diagonal of a cubic system lies in  $[111]$  direction for example.
- $\{hkl\}$  - Curly brackets identify a set of lattice plane that are symmetry-equivalent. Thus, the cubic face planes are collectively referred to as  $\{100\}$  planes. Some books also provide a similar convention used with directions [e.g. Ashcroft & Mermin, 1976].

<sup>1</sup>The denotation of crystallographic lattice planes was proposed by William Hallows Miller in 1838.

Then  $\langle hkl \rangle$  is used.

The Miller indexing system is used throughout crystallography, such as X-ray diffraction measurements, to identify lattice reflections for structural evaluations.

## 2.2. Neutrons for Material Science

Neutrons as well as synchrotron radiation, in particular photons in the X-ray domain, have a number of properties in common which make them a unique tool for materials research. Both can be used as probes for structure investigations as they are available with wavelengths in the order of atomic distances. Hence, their peak intensities diffracted by crystal planes enable the analysis of material structures on the atomic level. Thus, neutron and X-ray scattering techniques can be applied as a non-destructive tool for material investigations. However, the characteristics of both types of radiation are different. On the one hand, the neutron interaction with an atom is limited to the nucleus. On the other, X-rays interact with electron shells of the atom or electronic bandstructures. Because of that, both probes are applied to enable complementary measurements in structural research [e.g. Gurman, 1990].

As the feasibility of an alternative neutron measurement method towards the analysis of crystallographic properties is examined in this thesis, the neutron, its properties and its generation shall be considered here. For this reason, at this point the author refers to books covering similar topics, but including X-ray and synchrotron radiation introductions also [e.g. Fitzpatrick & Lodini, 2003; Reimers et al., 2008; Wiedemann, 2002].

### 2.2.1. Neutron Properties

Neutrons, discovered by Chadwick [1932], are particles of zero charge and are five to six orders of magnitude smaller than the average size of an atom [Fitzpatrick & Lodini, 2003]. According to the theory of quantum mechanics and the wave-particle duality of matter, the properties of neutrons can be described by the following relationships:

$$E = \frac{m_n v^2}{2} = \frac{h^2}{2m\lambda^2} \quad (2.1)$$

where  $E$  is the neutron energy given in  $eV$ ,  $v$  is the velocity,  $\lambda$  is the wavelength, usually given in  $\text{\AA} = 10^{-10}$  m, and  $h$  is the Planck constant. The mass of a neutron is  $m_n = 1.675 \times 10^{-27}$  kg.

As already stated, a neutron interacts with the nucleus of an atom. Considering the scattering length, a term describing the strength of the scattering potential by defining a cross-sectional area (see equation 3.6 in chapter 3), the neutron-matter interaction in general is very weak. The neutron interacts with particles inside the nucleus, i.e. protons and neutrons, via the strong nuclear force which is a short range force. This short range is illustrated taking the comparison of neutron wavelengths ( $1 \text{\AA} = 10^{-10}$  m) and the small nucleus size ( $1 \text{ fm} = 10^{-15}$  m) into account. The scattering length  $b$  depends on the number of nucleons, which is the number of protons  $Z$ , and on the mass of the atom  $A$ . In contrast to X-rays,  $b$  varies unsystematically throughout the ordering in the periodic table of elements [Bacon, 1967]. For neutrons, this enables the possibility to gain a high scattering contrast even between elements with similar  $Z$  and isotopes with different  $A$ . Moreover, the absorption of neutrons in most materials is very weak, which allows the penetration of big samples being the most significant advantage of neutrons [Reimers et al., 2008]. In contrast to conventional X-rays where only a region close to the surface ( $\mu\text{m}$  range) of the material can be analysed, the evaluations of crystallographic structures in depths up to several centimeters can be realised.

In addition to these useful properties, neutrons also have a magnetic dipole moment, which enables the possibility of using them in the analysis of magnetic structures. The topic of magnetism is an important field in neutron scattering, however, the magnetic properties will not be considered here as they are not relevant to the subject of this thesis.

### 2.2.2. Neutron Generation and Detection

Currently, there are two types of neutron producing sources — steady state fission reactors and pulsed spallation sources. In the former, neutrons are released due to controlled nuclear fission processes. In such research reactors, an assembly of  $^{235}\text{U}$  alloy plates is used to release on average 2.5 neutrons for every fissioned element. This basic principle is applied



for instance in Berlin (BER II) and Munich (FRM II). The neutrons are guided to the experiment via beam tubes pointing from the reactor to the sample position. The neutrons produced within that process have an energy in the MeV range. If they should be used in investigations of atomic arrangements in solid their velocity must be decreased such that their wavelength is in the order of inter-atomic distances [Bacon, 1967]. These fast neutrons are to be “thermalised” through impacts with so-called moderator atoms to decelerate them to the meV region. Typical moderator media are beryllium and hydrogen (actually light and heavy water) for example. The fast neutrons are slowed down by successive collision processes [Fitzpatrick & Lodini, 2003] and tend to thermal equilibrium at the temperature of the moderator. They will form a Maxwellian wavelength distribution appropriate to this temperature. A variation of the thermalisation temperature changes the centre of this distribution, such that neutrons with different energies can be provided for various types of neutron instruments. According to the energy of a neutron and its moderation, neutrons are usually classified by their “temperature” and named as “cold”, “thermal” and “epithermal” neutrons [Windsor, 1981]. Beyond that, there are more denotations that include the neutron velocity, such as fast and slow neutrons. Although there is no sharp division between the neutron categories [see L’Annunziata & Burkart, 2007; Anderson et al., 2009], a classification is available from the PSI website<sup>2</sup> and shown in table 2.1 for example.

On the other hand, in the case of spallation sources, sharp pulses of protons accelerated in a synchrotron hit a target nuclei which then releases neutrons. Targets of high atomic mass are used and are put in a highly excited state [Carpenter, 1977], such that up to 10 neutrons are evaporated from a nucleus when the energy of the accelerated protons is released. Again, the neutrons must be moderated to make them available for the instruments. Because of the pulsed character, very sharp neutron pulses are generated. The neutron brightness is then comparable to that from a fission reactor although the average flux is much lower. Both sources are complementary, i.e. they are generally optimised for different kinds of instruments. While at pulsed sources usually all available neutron wavelengths of the incident polychromatic beam are detected by measuring the neutron time-of-flight together with length of the total flight path, many instruments at steady state reactors use

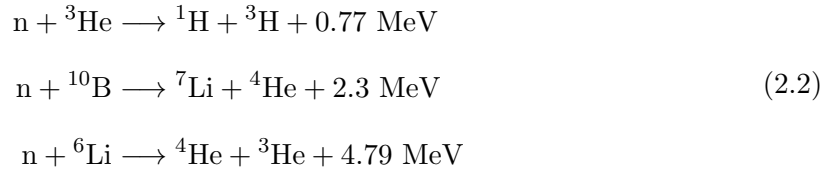
<sup>2</sup><http://neutra.web.psi.ch/What/physic.html>, Paul Scherrer Institut, Switzerland

Name	Neutron energy	Wavelength
Cold	0.5 meV - 2 meV	12.8 Å - 6.4 Å
Thermal	2 meV - 100 meV	6.4 Å - 0.9 Å
Epithermal	100 meV - 1 eV	0.9 Å - 0.28 Å
Intermediate	1 eV - 0.8 MeV	0.28 Å - 0.01 Å
Fast	> 0.8 MeV	< 0.01 Å

**Table 2.1.:** Classification of neutrons.

monochromators to select a single wavelength from the incident beam spectrum. Hence, pulsed spallation sources are very efficient when all neutrons are captured which is useful for powder diffraction experiments for example. The pulsed neutron signal is triggered with the time-of-flight detectors in order to map the captured neutrons according to their energy. But reactors are still preferred for many types of experiments such as neutron imaging as they produce continuous high neutron flux.

Neutrons have no charge, so they cannot be detected directly. They can be counted via nuclear reactions, where the neutron interacts with a nucleus to produce a charged particle. Windsor [1981] for example, presents an overview of the most important nuclear reactions for the detection of a neutron  $n$ , which are described by the following equations:



In order to detect neutrons either the charge of their ionisation of a gas ( ${}^3\text{He}$  or  ${}^{10}\text{B}$ ) or the light flash they produce in a scintillating material ( ${}^6\text{Li}$ ) can be measured [Egelstaff, 1965]. In  ${}^3\text{He}$  gas detectors for example, a thin anode wire (positively charged) collects electrons (negative charge) from the He ionisation process. Then, the detected charge is measured as a function of the anode voltage. A sketch of this approach is shown in figure 2.2a. To realise position-sensitive detectors (PSD), the anode wire is made resistive. For a linear PSD, the charge  $q$  at the two ends of the anode wire is measured independently when a neutron is captured at a position  $x$  along the detector [Windsor, 1981]. Due to the ratio  $q/x : q/(1-x)$  both the position and the charge can be determined. A two-dimensional

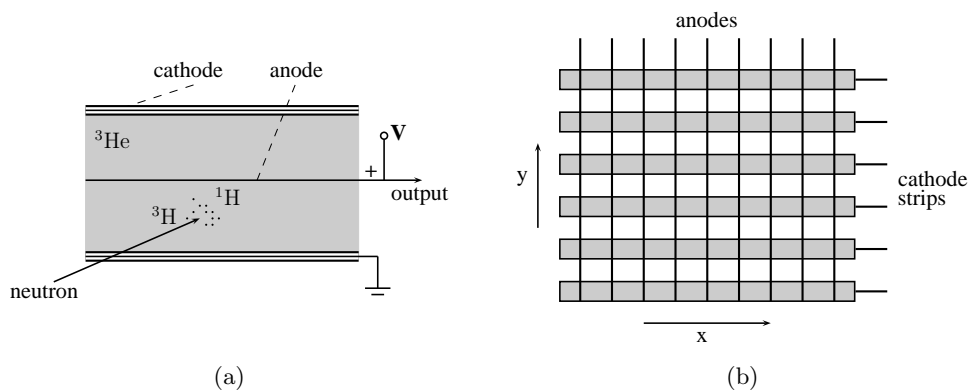


**Figure 2.2.:** Principle operation method of a  ${}^3\text{He}$  gas detector (a). An anode wire collects electrons from  ${}^3\text{He}$  ionisation processes. Thus a captured neutron can be detected. To realise a position-sensitive area detector (b), cathode strips and anodes wires are combined to measure the position  $(x,y)$  of a captured neutron.

(area/array) detector is made by dividing up the cathode into strips perpendicular to the anode wires. Figure 2.2b visualised the principle setup. Further, there is a scintillator method for detecting neutrons. Using a scintillator material, e.g. ZnS mixed with the absorber  ${}^6\text{Li}$ , then allows the visualisation of the radiation due to the conversion of neutron energy into visible light, which is applied in radiographic situations for example. Then, the emitted light can be detected by high sensitivity CCD cameras, whose electrical signals are used to capture a two-dimensional picture. The scintillation principle can also be connected to the application of photomultipliers, which can be further coupled with fibre optics for a conversion into electrical signals. Photomultipliers are then used to amplify the current that is produced by the incident light. This is particularly useful when the neutron time-of-flight needs to be resolved.

### 2.3. Bragg Diffraction

Diffraction describes the bending phenomenon of waves, such as light, sound and water waves, as they meet obstructions. In general, this also describes the process of neutron diffraction (and also X-ray diffraction), which occurs with matter because of its wave-like properties at the atomic level. However, if a regular spacing of atoms causes many diffracting waves to interfere constructively, so-called (Bragg) peaks can be measured as a coherent signal at a detector. Providing that the wavelength of an incoming beam is in the same range

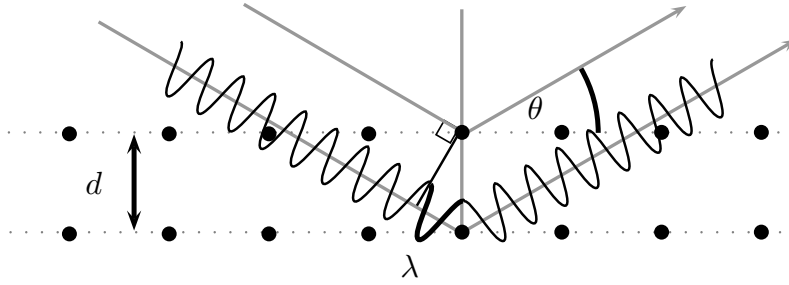


**Figure 2.3.:** Bragg's law: An incoming beam with a wavelength  $\lambda$  is scattered by a specific lattice plane having a lattice distance of  $d(hkl)$  under the angle  $\theta$ .

as the scattering and regularly repeating objects, such as the crystallographic structure of engineering materials, the phenomenon known as Bragg diffraction can occur [Cullity & Stock, 2001]. The basis of the classical diffraction theory is given by a simple equation which was derived by William Lawrence Bragg and his father William Henry Bragg [Bragg & Bragg, 1913; Bragg, 1913]:

$$n \lambda = 2d(hkl) \sin \theta \quad (2.3)$$

where  $\lambda$  is the wavelength of the incident radiation,  $\theta$  is the diffraction angle,  $n$  is an integer denoting the order of the diffraction and  $d(hkl)$  is the spacing between the  $hkl$  lattice planes. The basic principle of Bragg's law is illustrated in figure 2.3. In order to get constructive interference, the path difference of the incoming waves having the same phase must be equal to any multiple of the wavelength. For the case of a known wavelength, the equation can be applied to determine the lattice spacings from the angular dispersive scattering intensity distributions. Likewise, destructive interference is possible, i.e. the diffracting waves erases each other due to a phase difference of  $\pi$ . Consequently, the total of systematic absent and present diffraction peaks gives information about the type of lattice structure inside a specimen. Moreover, incoherent scattering occurs due the randomness of phases of a part of diffracting waves. Besides, one distinguishes between elastic and inelastic scattering. While the latter process describes a gain or loss of energy of the diffracting particle, elastic scattering defines that this energy remains constant.

The kinematical (or geometrical) theory describes the diffraction in a perfect mosaic crystal, i.e. a crystal consisting of number of small diffracting domains. It is valid for many prob-

lems investigated in materials engineering, but neglects attenuation of the primary beam, further diffraction of the secondary beam and possible interferences between primary and secondary beam [Spieß et al., 2009]. Then, the diffracted intensities differ from the kinematical description. These so-called extinction effects are considered in the dynamical theory of diffraction.

### 2.3.1. Extinction Effects

The term “extinction” is used to describe the attenuation of the measured beam intensity in comparison to the predicted one would obtain from the kinematical theory. When a neutron or X-ray beam passes through a sample, the beam intensity will be decreased due to absorption by the materials and scattering processes that will change the direction of a part of the beam, such as described previously. These two processes cannot be distinguished when looking at the primary beam after it has passed the sample. Within this context the terms attenuation and absorption, especially the “mass attenuation coefficient” and the “mass absorption coefficient”, are sometimes used synonymously. A differentiation between both can be achieved by placing a detector along the scattering directions. Thus, a correct distinction is drawn between the absorption coefficient that measures the intensity loss due to true absorption only and the attenuation coefficient that determines the total intensity loss by including the scattering.

Besides the absorption and diffraction, further phenomena can contribute to the attenuation of the beam intensity. A distinction was drawn between primary and secondary extinction by Darwin [1922], who first investigated these effects. Figure 2.4a outlines the process of primary extinction. It is shown that the beam scattered by a set of lattice planes is directed at the same diffraction angle with the following lattice planes of the same stack, such that it may be scattered again. Thus, each plane redirects a small fraction of the scattered beam back into the direction of the primary beam [Buerger, 1960]. The twice-reflected beam exhibits a phase difference of  $\pi$  relative to the primary beam. Hence, less integrated intensity will be detected due to destructive interference. With increasing depth of the crystal the intensity of the primary beam will be rapidly decreased. In the same manner, the intensity

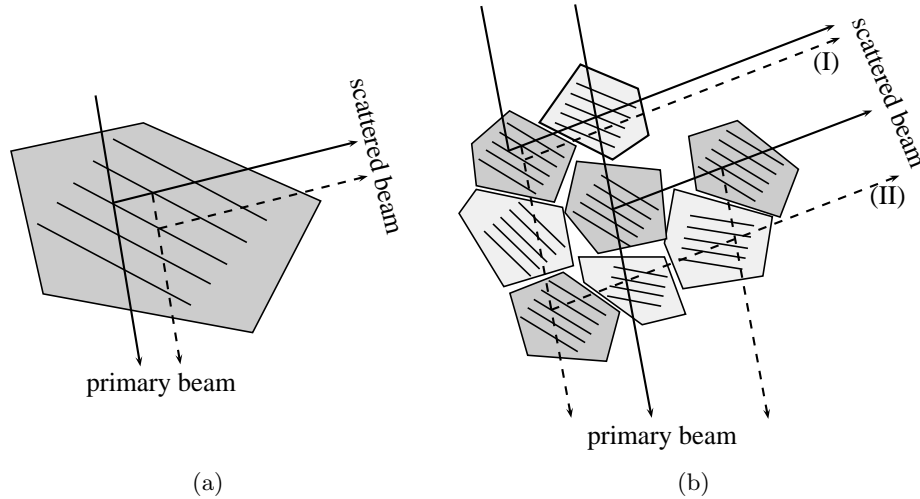


**Figure 2.4.:** Primary extinction (a) occurs due to multiple scattering at lattice planes of the same stack. Besides the normal absorption, the beam is further attenuated due to the phase difference of  $\pi$  between the two primary and between the two scattered waves. Various possible situations of extinction effects are shown in (b). While (I) visualises primary extinction, secondary extinction (II) arises because individual mosaic blocks are illuminated less due to preceding scattering centres. The scattering centres suitable for Bragg scattering are indicated in dark grey while the slightly misorientated blocks, that still contribute to the beam attenuation via normal absorption, are drawn in light grey.

of the Bragg reflection will be reduced because of waves that are scattered thrice. Then, the difference of  $\pi$  in phase is responsible for the attenuation of the reflection intensity compared to that expected from the kinematical theory. Altogether, this yields to a dynamical interaction between incident and scattered beam at every point within the crystal [Chandrasekhar, 1960]. This effect depends on the perfectness of the crystal and is therefore dedicated to ideally perfect crystals. The perfectness of a crystal is related to the misorientation (mosaicity) of the coherent scattering domains (mosaic blocks) and their size. The larger these blocks and the smaller the degree of the mosaicity the higher is the effect of primary extinction.

A real crystal is rather imperfect and exhibits less primary extinction since it has a mosaic structure. Nevertheless, the primary beam becomes weaker anyway when penetrating this crystal due to normal absorption, i.e. even when the mosaic blocks are orientated such that Bragg condition is not fulfilled the intensity is reduced. However, there is still the possibility in a mosaic crystal that multiple mosaic blocks, passed by the incident beam, are orientated

parallel to each other such that the contribution of preceding scattering event weakens the intensity. Secondary extinction denotes the effect that a primary beam is attenuated strongly by a scattering lattice plane such that the lattice planes underneath will be illuminated less. Therefore, its scattered intensity will also be reduced. This principle is sketched in figure 2.4b by various situations demonstrating both extinction effects within an imperfect crystal. With respect to secondary extinction, the drawing shows the additional attenuation due to previous scattering events along the incident beam no matter if primary extinction is allowed or not. It is obvious that this effect depends on the degree of parallelism of the mosaic blocks.

According to a quantitative phase analysis, such extinction effects must be considered especially when the attenuated scattering intensities compromise the evaluation of the results. In order to correct for the extinctions errors many approaches have already been proposed, reviewed and discussed [e.g. Darwin, 1922; Weiss, 1952b; Chandrasekhar, 1956; Zachariasen, 1963].

### **2.3.2. Diffraction Techniques**

Traditionally, X-ray diffraction has been used to determine the structure of crystallographic materials by means of a number of different techniques. Using the Laue method [Friedrich et al., 1913], polychromatic radiation (white beam) interacts with a single crystal (or a selected grain) and produces point reflections at a detector, as illustrated in figure 2.5a. This means, multiple lattice planes fulfil the Bragg equation at the same time. Using the Laue-condition, it is possible to indicate the directions and position of the diffraction reflections. Thus, the crystal structure can be analysed by means of the detected diffraction pattern. While the Laue method is used to analyse single crystals, the Debye-Scherrer method [Debye & Scherrer, 1916] is applied to investigate the crystallographic structure of powders and fine-grained polycrystals. By means of monochromatic radiation the interaction with the crystallites causes circular patterns at the detector with cone symmetry centred around the incoming beam. The principle is visualised in figure 2.5b. The intensities and positions of the detected Debye-Scherrer rings (or ring sections) are used to analyse the sample material. While the method is presented to take advantage of a single incident wavelength, another

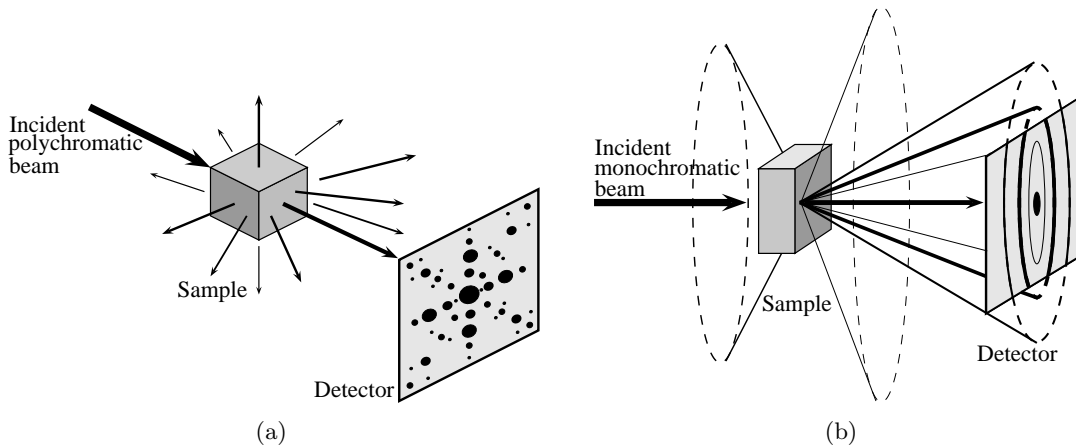


**Figure 2.5.:** Using the Laue method (a), point reflections can be utilised to analyse single crystal samples. In contrast, polycrystalline samples and powders can be investigated by means of the Debye-Scherrer rings (b).

approach is to investigate crystallographic structures by means of the beam time-of-flight (TOF). Then, a polychromatic beam is used. The analysis of the radiation particles is done on the detector side. Taking into account a fixed scattering angle as well as the source-detector distance, one is able to determine the wavelength of each particle event arising on the detector, by means of a measured particle time-of-flight. Thus, the full spectrum of the incident beam is used to characterise a specimen according to its reflection peak intensities. The crystallographic structure of the specimen is directly linked to the complete scattering intensity distribution. However, real experiments only deliver incomplete data sets, not including every possible reflection. Hence, fitting algorithms together with structure estimates have to be used to identify the atomic positions within the unit cell. An example, taken from Young [1995], showing a powder diffraction pattern is given in figure 2.6. The peak positions and amplitudes are evaluated to analyse the sample properties. Moreover, the measured curve is superimposed on a predicted spectrum which has been calculated using the so-called Rietveld refinement<sup>3</sup> [Rietveld, 1969], to estimate the crystallographic structure. The lower curve shows the difference between measurement and computation to evaluate the results. The vertical lines in between indicate the positions of the Bragg reflections.

<sup>3</sup>By means of a Rietveld refinement, the crystal structure is then specified due to iterative adjustments of the structure estimate by fitting a theoretical line profile to the measured one. It was devised by Hugo Rietveld in 1969 to characterise crystalline materials with their diffraction pattern.



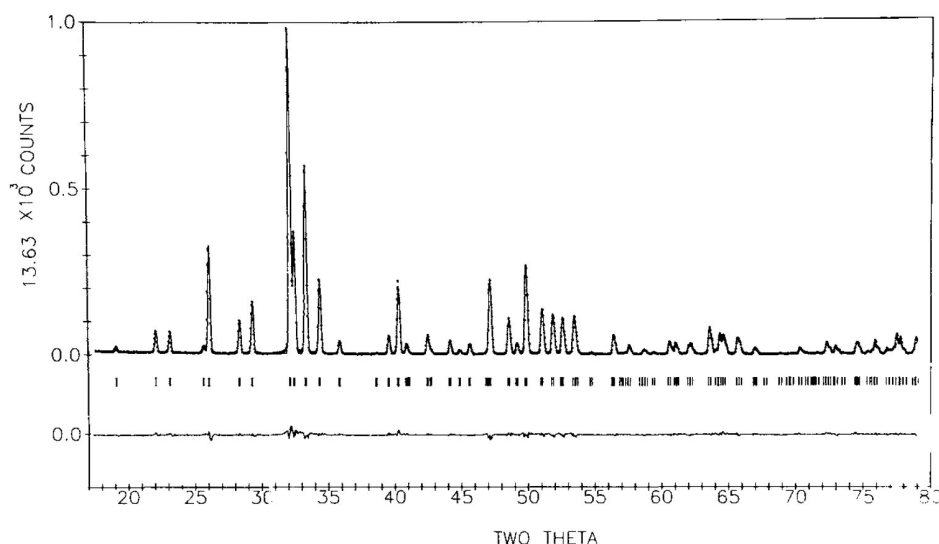


**Figure 2.6.:** *The diagram, taken from Young [1995], shows a measured powder diffraction pattern superimposed by a Rietveld plot. The lower curve represents the difference between the calculated and the measured spectrum. The vertical lines in between indicate the reflection positions determined by Bragg's law.*

The work presented in this thesis applies these conventional and well-established diffraction methods to provide reference datasets of crystallographic sample properties. These results will be compared with measurements and simulations of the Bragg edge transmission method (chapter 3) in order to evaluate its results and to bring forward the development of this alternative measurement technique. However, a detailed description of the analysis of a neutron diffraction pattern towards the determination of crystallographic preferred orientations, i.e. texture (see section 2.6), is given in chapter 6.1.

Since the wavelengths of synchrotron radiation and neutrons are available in the same order of magnitude as the atomic spacing of crystalline materials, both probes (also laboratory X-rays) are used as complementary techniques [Withers & Webster, 2001] to analyse crystallographic structures. The different penetration depths and the diversity of the scattering contrast stated above, strengthens these complementarities even further.

## 2.4. Computed Tomography

Tomography images the interior structure of real objects three-dimensionally. Originally developed for medical reasons [Kalender, 2000], computed tomography (CT) is nowadays

used for example in archaeology, biology and material science. There are many textbooks [e.g. Banhart, 2008; Buzug, 2005; Hsieh, 2003; Maire et al., 2000; Kak & Slaney, 1988], that present a complete and detailed outline of the principles and problems of computed tomography. The term tomography is derived from the Greek words “tómos” and “gráphein” which mean “cut” or “slice” and “writing” respectively. It describes the process of evaluating a number of radiographic images to obtain three-dimensional pictures or at least slices of the interior of real objects.

### 2.4.1. The Tomographic Setup

The application of the tomographic principle in general is probably best known from medical science. There, the object of interest is the human body, but also in other fields tomography is the appropriate measurement method. In material science for example, there is a wide range of applications which also include many recently developed methodical variations, such as the Bragg edge imaging examined within this work. Strobl et al. [2009], for example, gives a summary of recent activities in the field of neutron radiography and tomography covering the investigations of the water flow and agglomerations in fuel cells, hydrogen storage capabilities of new materials, internal structure changes of batteries during discharge and oil sedimentations in engine components. A tomographic image of the latter is shown in figure 2.7b as a 3D reconstruction as well as selected cross sections in 2D.

The starting point of a tomography image is a radiography measurement, where the attenuated beam intensity behind a specimen is detected. In figure 2.7a, the schematic principle of such a measurement is visualised. The beam intensity transmitted through a sample is measured as a radiographic image. Traditionally, films have been used for the detection but today detector systems based on CCD cameras are well established to capture two-dimensional radiographic images. In material science, this is usually performed by a setup of a CCD camera and a scintillator screen converting the radiation to visible light behind an absorbing object [e.g. Banhart, 2008]. An example of this detection principle is shown in section 4.1 by means of the CONRAD tomography beamline utilised within this thesis. The absorption radiography and tomography take advantage of the radiation attenuation caused

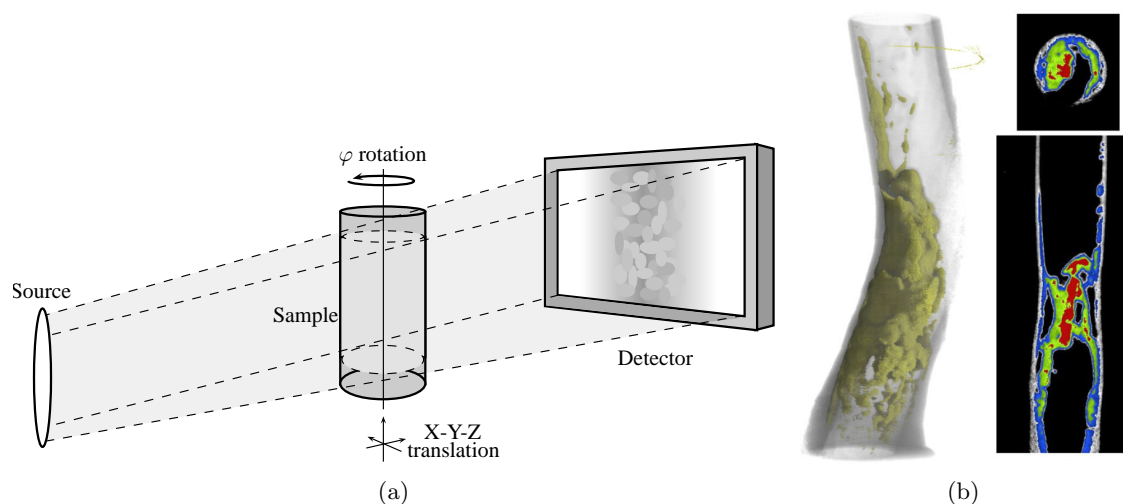


**Figure 2.7.:** *CT measurement principle (a): A specimen is irradiated to uncover its interior by means of radiographic images taken behind the object. The attenuated beam intensity at the detector will be measured from a number of perspectives by rotating the sample. As a result, a tomographic image, either in 3D or in 2D cross sections, can be reconstructed from the radiographic pictures. The example (b) shows fuel and oil sediments in an aircraft engine vent pipe [Strobl et al., 2009].*

by different thicknesses and densities of materials inside the investigated object. The information contained in a single row of a radiographic image equals a projection of the dedicated slice of the specimen. In order to be able to visualise the interior as a 2D image of that slice or as a 3D volume from multiple slices, a number of projections from different perspectives is required. Extending the radiography, the tomography method takes many radiographic pictures to obtain the necessary projections. The specimen is therefore rotated, as indicated in figure 2.7, about  $180^\circ$  (for a parallel beam) or about  $360^\circ$  (if the beam geometry is a fan or cone) in small increments. Detailed principles of re-formatting the captured projections with regard to the beam geometry and towards a tomographic reconstruction are shown in Hsieh [2003] and Li [2006] as applied examples. However, the detector system is always placed in transmission direction behind the sample, i.e. compared to diffraction methods, the scattering angle is  $0^\circ$ . If the complete measurement is finished, the radiographic images recorded are used to reconstruct a three-dimensional tomographic image with the aid of a computer which applies the techniques described in section 2.4.2.

In many cases, it is advantageous to take additional flatfield images to provide a correction for the initial radiography image  $I_{radio}$ . Therefore, a second image  $I_{flat}$  is taken under the same conditions but without the sample. Hence, this type of measurement is also called openbeam measurement. By this means, an inhomogeneous illumination of the image, dust and dirt particles on the camera lens or the scintillator screen as well as the possibility that the CCD detector pixels have different sensitivities can be corrected to avoid a distortion of measurement results. For this reason (and for an initial alignment), the sample is mounted on a  $xyz$ -translation table in order to move the sample into and out of the beam window. Furthermore, a darkfield image  $I_{dark}$  can be applied to adjust for the detector noise. Then, a picture without the radiation (a closed shutter for instance) is taken with the same exposure time to correct for possible charge carriers in the CCD chip that have been produced by thermal energies but not by visible light. Both methods belong to the class of raw picture corrections and can be applied as follows:

$$Tr = \frac{I_{radio} - I_{dark}}{I_{flat} - I_{dark}} \quad (2.4)$$

Finally, this correction provides the determination of the ratio between incident and attenuated beam which is equal to the transmission image  $Tr$ .

### 2.4.2. Reconstruction

A tomography image, either a 2D slice or a 3D volume, cannot be measured directly, but can be reconstructed from the radiographic images taken. The grey values in the captured images represent the beam intensities attenuated by the specimen. Each image pixel is therefore considered being an integral attenuation function of position. Using the total of all radiographic images, i.e. considering all rotation steps, one is able to estimate the coefficients of this function and therefore the interior of the sample.

Supposing a linear relation between the attenuation coefficient and the density of a material, the integral attenuation captured by a single line of a radiographic image represents the projection  $p$  of a sample slice  $f(x, y)$  under a certain angle  $\varphi$ . All possible line integrals of  $f$  as visualised in figure 2.8 are defined as the Radon transform [Radon, 1917], which was

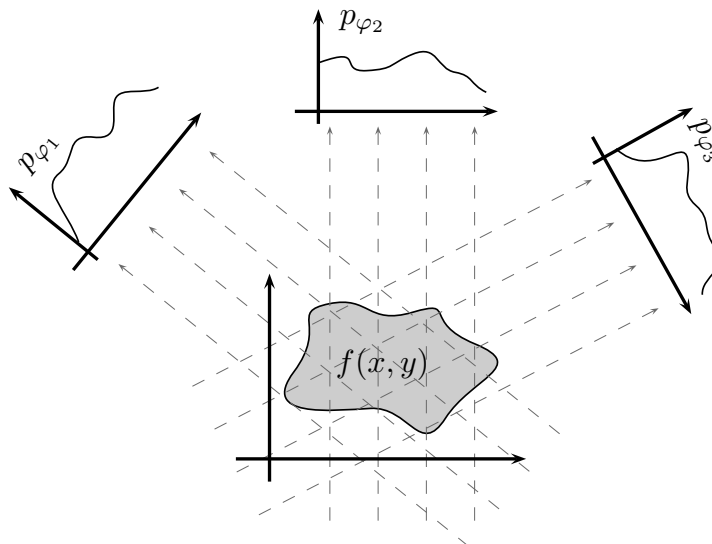


**Figure 2.8.:** Schematic principle of projections of a sectional sample plane under selected angles.

developed by the mathematician Johann Radon. It describes the integral transform of a two-dimensional function over the set of all lines. Hence, the tomography is concerned with the problem of the inversion of the Radon transform to reconstruct the attenuation coefficient as a function of position.

There are several techniques to compute the reconstruction [Herman, 1980]. A well-established method is the filtered backprojection, which implements the idea to backproject the radiographic images over an area or in space taking the point of view into account. Using a transformation into the Fourier space, the reconstruction can be realised by the Fourier slice theorem, which is described as follows:

1. Let  $f(x, y)$  be the object function to be reconstructed and  $F(u, v)$  its two-dimensional Fourier transform:

$$f(x, y) \xrightarrow{\text{2D-FFT}} F(u, v) \quad (2.5)$$

2. Further, the projection  $p_\varphi(x)$  of  $f$  under a certain angle  $\varphi$  and its one-dimensional Fourier transform  $P$  are known:

$$p_\varphi(x) \xrightarrow{\text{1D-FFT}} P_\varphi(u) \quad (2.6)$$

Then,  $P_\varphi(u)$  equals a line through the origin in the two-dimensional Fourier function  $F(u, v)$  taken at the angle  $\varphi$ . Thus, it is possible to get the object function  $f(x, y)$  from the Radon transform, that means all projections  $p$ , by applying the inverse Fourier transform of  $F(u, v)$ . Once enough projections to fill the entire Fourier space have been collected, the reconstruction can be implemented using the fast version of the Fourier transform (FFT) and the inversion in two-dimensional space. Additionally, the problem of overlapping projections in the Fourier space origin is handled by high-frequency filtering [e.g. Boin, 2005].

Moreover, there are other methods to reconstruct tomographic images. The discrete nature of the projection data is not considered by the analytical model of the backprojection, but by iterative reconstruction methods for example. Algebraic reconstruction techniques (ART), presented in the books of Hsieh [2003] and Herman [1980] for example, usually design an algorithm according to a discrete numerical model [Haimerl, 2003]. At first, an assumption of the distribution of objects in a tomographic slice is made with the help of the captured projections. From this, new radiographic projections are calculated and compared with the measured images. Then, an adjustment coefficient is determined and the grey value distribution of the objects to be in demand is assumed again. This iteration is done until a stop criterion is satisfied. In Hentschel et al. [2005] for example, all projections of a slice, stored as a so-called sinogram image, are used to selected predominant sine-shaped traces to reconstruct single elements of the image, from which new projections are calculated to be subtracted from the sinogram.

### 2.4.3. Image Processing

The reconstruction presented above produces tomographic images only, but does not evaluate anything within the image. The analysis of tomography experiments is performed by image processing which obtains useful information from the interior of the investigated object. In material science there are a lot of applied questions that can be answered by absorption tomography. For example, one can investigate cracks and micro-cracks in engineering materials or pore size distributions in ceramic or metallic foams. In Jähne [2005] for instance, general principles of digital image processing are presented. The thesis of Rack [2006] shows

a lot of applied examples of how imaging can be performed according to different questions. By means of the binarisation of a tomography image, for instance, the pores inside metal foams could be evaluated (size, shape and distribution). Therefore, the grey value image was converted to a binary image using thresholds. A common problem in tomography is to automatically separate components within a sample. Therefore, an analysis of the so-called histogram, which is a graphical representation showing the distribution of the grey values, could be applied to binarise objects of interest in the tomographic image [Kirste, 2005]. The binary information of whether a pixel is part of the object or not can help to do succeeding calculations. Linear filtering can be used to sharpen the complete image and enhance edge-detection algorithms. The Euclidean distance transform can be implemented to detect particles, which possibly grow during in-situ experiments [Nöthe et al., 2003]. Additionally, segmentation of different objects is done by a watershed transform of the tomographic image and is improved by erosion and dilatation processes [Beucher & Lantuejoul, 1979; Jähne, 2005].

Another large part of image processing in tomography is the handling of image defects: the so-called artefacts [e.g. Boin, 2005; Hsieh, 2003]. Artefacts can arise from a number of causes, for example, motion and even small metallic artefacts can result in streaks and stripes drawn over the whole image. The so-called ring artefacts are well-known images errors in computed tomography. They appear as concentric rings within the image and complicate the post-processing of the data. In Boin & Haibel [2006] for instance, filtering methods have been implemented to compensate for such artefacts.

#### **2.4.4. Vector and Tensorial Tomography**

The procedure of the traditional absorption tomography described above is to reconstruct a scalar quantity (the attenuation coefficient) within a slice representing the interior of a sample. However, applications exist where a reconstruction of a vector field from its integral form is required. Some example are imaging of fluid flow velocities [e.g Norton, 1989], visualisation of electric fields with the aim to resolve the “state” of the human brain [Petrou & Giannakidis, 2008] by means of electroencephalography (EEG), for example, non-destructive stress imaging

of transparent samples in photoelasticity [e.g. Sharafutdinov, 1992] and the reconstruction of magnetic domains from neutron tomography measurements [Hochhold et al., 1996].

A good introduction to the problem of vector tomography is given by Giannakidis et al. [2010], for example, who describe the reconstruction of a vector field from its line integrals as an underdetermined problem. In contrast to the recovery of a scalar function, the vector field requires two (2D) or three components (3D) to be reconstructed. A reconstruction method was developed which solves a system of linear equations, each describing the tomographic projection of the vector field along a line segment under a certain angle. This procedure was applied to the reconstruction of a simulated electric field created by a static charge and calculated by Coulomb's law. However, many of the applications are concerned with constraints that must be considered when a vector field should be reconstructed successfully. For the case of resolving the magnetic structure of a sample from neutron spin rotations for example, the specific sequence of traversed pixels must be considered because the spin rotation operator describing the effect on the neutron wave function depends on this path-ordering feature [Jericha et al., 2007].

While scalar values describe quantities without any directional part, vectors, as utilised for the different applications, represent quantities with a single direction, such as the velocity of fluid flow. In addition, tensors are link more than one directional part to a physical quantity. Stress, as introduces in the following section, is one example for that. Hence, the application of stress reconstruction, as mentioned above, can be termed as tensorial tomography.

## 2.5. Strains and Stresses

An important factor in a component's design is the analysis of stresses. While load induced stresses are caused by external by forces, there are also stresses inside closed systems occurring without any applied loads and momenta [Mura, 1987]. The term residual stresses refers to the mechanical stresses within the interior of a material or component when no external forces or stresses are present on the component (at constant temperature conditions). These kinds of stresses are caused by a wide range of influences. For instance, heat treatment and



quenching or welding, drilling and shot peening are typical processes that create phase change or structural deformation. Residual stresses appear subsequently as a result of inhomogeneity in deformation, crystal defects, grain boundaries, etc.

### 2.5.1. Residual Stress Types and Applications

Residual stresses are classified [e.g. Macherauch et al., 1973; Wolfstieg & Macherauch, 1976; Kloos, 1979] by their range of coverage inside the material. Therefore, residual stresses  $\sigma$  are classified as first, second and third order stresses (also known as type I, II, III residual stresses). First order stresses are homogeneous over broad material domains, i.e. a large number of grains, they are also called macrostresses. Type II stresses are homogeneous within small domains of a single grain or a phase, the residual stresses of type III are homogeneous over a few interatomic distances, the smallest crystal domain of a material. Both types II and III are known as microstresses [Noyan & Cohen, 1987]. The residual stresses  $\sigma(\vec{r})$  at a certain position  $\vec{r} = (x, y, z)$  results from the sum of the individual values. According to the phase selectivity of X-ray stress determination methods, the denotation of the residual stresses was extended by the average value of several crystallites [Hauk & Nikolin, 1988] to define the phase-homogeneous residual stresses  $\langle\sigma\rangle^\alpha$  [Fitzpatrick & Lodini, 2003]:

$$\langle\sigma\rangle^\alpha = \sigma^I + \langle\sigma^{II}\rangle^\alpha + \langle\sigma^{III}\rangle^\alpha \quad (2.7)$$

Residual stresses are auto-balancing, i.e. their resulting forces inside a closed system must disappear externally.

Residual stress determination in engineering components is important for multiple applications. The investigation of the stress states at the surface of a material is essential because the surface of is usually exposed to the highest applied stresses. The initiation of cracks at the surface can then lead to failure of the complete component. Therefore, one of the tasks in the field of strain and stress analysis is the stress optimisation in near-surface layers towards the prolongation of the component life. A way to improve the life and performance of a materials is to introduce compressive residual stresses by shot peening, a mechanical surface treatment [Fitzpatrick & Lodini, 2003]. The evaluation of the surface layers after this

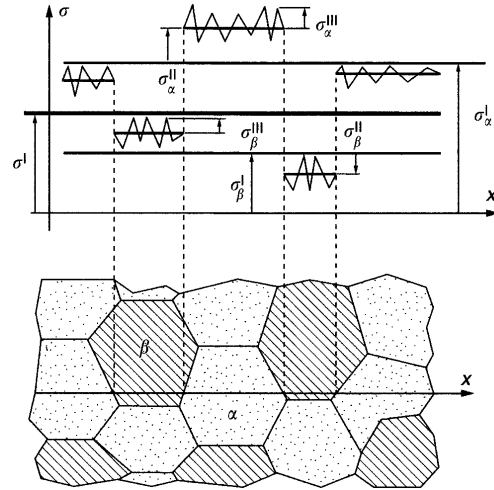


**Figure 2.9.:** Classification of residual stresses ( $\sigma^I, \sigma^{II}, \sigma^{III}$ ) after Fitzpatrick & Lodini [2003] by means of a two-phase material indicated by  $\alpha$ - and  $\beta$ -phase.

treatment is dedicated to X-ray and synchrotron measurements, but can also be performed with neutrons. However, the high penetration depth of neutrons are ideal to study residual stressess in welds, for example. The region of this type of joints can be full of high levels of stress gradients, which can cause unexpected component failure, either by sudden fracture or by fatigue, stress corrosion cracking and creep cavitation [Hutchings et al., 2005]. The welding process introduces tensile stresses, whose development depends on many thermal and mechanical parameters (e.g. parent plate size, heating, metal flow). Hence, a current topic in the materials engineering discipline is to limit the extent of the residual stresses by modifying the welding parameters and performing additional treatments. Again, residual stress measurements are used to evaluated the developed strategies.

### 2.5.2. Residual Stress Determination

The stress state at a point is described by a symmetric second-order tensor whose components  $\sigma_{ij}$  ( $i, j = 1, 2, 3$ ) represent the forces  $F_i$  in different directions  $x_i$  characterised by the surface  $S_j$ .

$$\sigma_{ij} = \sigma_{ji} = \frac{\partial F_i}{\partial S_j} = \begin{pmatrix} \sigma_{11} & \sigma_{12} & \sigma_{13} \\ \sigma_{21} & \sigma_{22} & \sigma_{23} \\ \sigma_{31} & \sigma_{32} & \sigma_{33} \end{pmatrix} \quad (2.8)$$

Residual stresses cannot be measured directly, they can only be determined by their effects on a material [Pyzalla, 2001]. By means of diffraction methods, elastic stresses are evaluated

based on the induced lattice strains  $\varepsilon$ . Using Bragg's law (equation 2.3), the strain along the reciprocal lattice vector  $hkl$ , with knowledge of a stress-free lattice parameter  $d_0$ , is given by the following equation:

$$\varepsilon_{\phi\psi}(hkl) = \frac{d_{\phi\psi}(hkl) - d_0(hkl)}{d_0(hkl)} \quad (2.9)$$

where  $d(hkl)$  is the lattice spacing determined by the Bragg angle  $\theta$  and the wavelength  $\lambda$  in case of an angle and energy dispersive mode respectively. With reference to a sample coordinate system, the measurement direction of the strain value  $\varepsilon_{\phi\psi}$  is defined by the azimuth angle  $\phi$  and the tilt angle  $\psi$ . Figure 2.10a demonstrates this principle. The correlation between the measured lattice strains and the appropriate stresses follows from Hooke's law.

$$\sigma = E \varepsilon \quad (2.10)$$

where  $E$  is the Young's Modulus (the modulus of elasticity), which describes the stiffness of a material. It is given in units of pressure (for example: MPa) and can be determined experimentally from the slope of a stress-strain curve measured under external tensile loads.

Residual stresses can be investigated for example by mechanical or destructive methods [Lu, 1996] which destroy the equilibrium of the residual stress state. Moreover, non-destructive methods can be applied, that are advantageous because they leave the sample intact for further measurements. Here, as stated above, the diffraction method is considered as multiple radiation sources are available that are phase-sensitive and complement one another according to their properties. The basic principle is to detect the exact position of the diffraction peak. With monochromatic radiation, the diffraction angle is measured. By means of Bragg's law, the  $hkl$  lattice spacing  $d(hkl)$  is derived. Related to that, time-of-flight and energy-dispersive diffraction measurements are considered likewise under evaluation of the detected time-of-flight or energy signal. This procedure is applied for residual stress samples as well as for reference samples to determine the strain value  $\varepsilon(hkl)$ . A measurement is conducted for different local positions to analyse the strain and stress state depending on the sample position. Traditionally, the  $\sin^2\psi$  method is used to measure stresses. The linear relation of the lattice spacing between two principal directions and the sine of the angle between

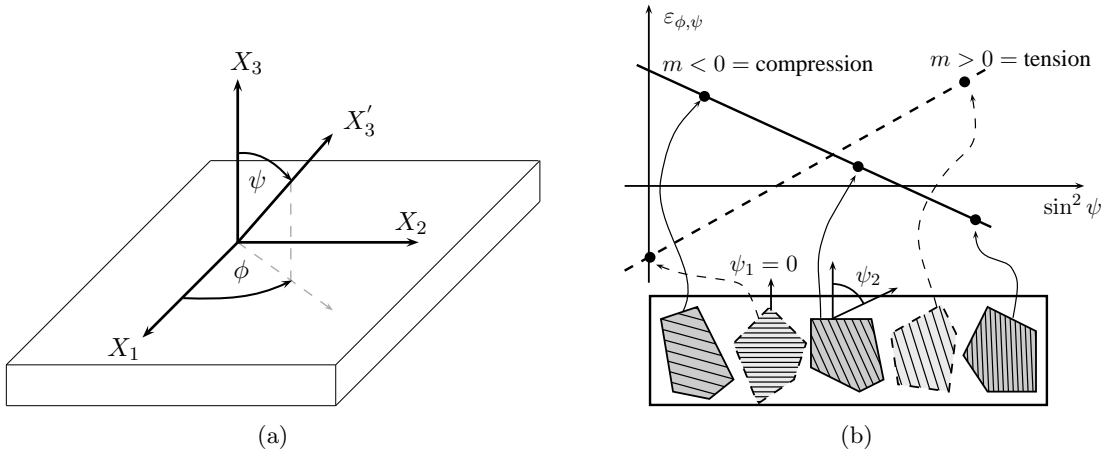


**Figure 2.10.:** Coordinate system (a) to measure strain with diffraction after [Fitzpatrick & Lodini, 2003]. The laboratory coordinate system with the axis  $X'_3$  is related to the sample coordinates  $X_1$ ,  $X_2$  and  $X_3$  by the orientation angles  $\phi$  and  $\psi$ . In (b), the principle of the  $\sin^2 \psi$  method is visualised: By measuring the strain from different directions the stress state at a sample position can be obtained from the slope  $m$ .

them is applied. The slope  $m$  of this relationship is then proportional to the stress. The basic principle of this technique is shown in figure 2.10b. This application is useful for near surface measurements with low penetrating radiations such as X-rays. However, if the principal directions of a specimen are known and neutrons, with higher penetration depth, are available, one saves time by measuring the lattice spacing for the three different orientations  $(\phi, \psi) = (0^\circ, 90^\circ), (90^\circ, 90^\circ)$  and  $(0^\circ, 0^\circ)$ .

## 2.6. Crystallographic Texture

Compared to single crystals and powder samples, which ideally provide only one and random crystallite orientations respectively, the majority of engineering materials exist with a non-random distribution of crystallites in which one or more orientations are preferred [Brokmeier, 2006]. The existence of a preferred crystallographic orientation is known as texture. The term crystallographic texture refers to the total amount of orientations of crystallites of a polycrystalline sample. General aspects of texture are introduced in the textbooks of Bunge [1993] and Kocks et al. [2000] for example. As texture analysis is a statistical method, a sufficient number of grains and their orientation  $g$  have to be obtained in order to give the orientation distribution function (ODF)  $f(g)$ , which is a three dimensional representation of

the texture:

$$f(g) dg = \frac{dV}{V} \quad (2.11)$$

where  $dV/V$  is the volume fraction of crystallites lying within an orientation increment  $dg$ . For an experimental analysis of texture, it is important to always relate the orientation to the sample coordinate system  $K_A$ . Therefore, the sample orientation is usually chosen with respect to the shape of the sample or to its deformation mode. For instance, the rolling direction (RD) is given by a rolling process. Applying other methods, such as welding and extrusion, RD is also sometimes generalised as reference direction. Figure 2.11 outlines this geometry. The transformation of the sample orientation  $K_A$  to the grain orientation  $K_B$  can be performed by the Euler angles  $(\varphi_1, \Phi, \varphi_2)$  with the Bunge convention [Bunge, 1993]. Moreover, texture may vary depending on the local sample position, such that a gradient of preferred orientations is obtained. Taking the local sample point  $(x, y, z)$  into account the ODF is extended to a six-dimensional texture, which is also called orientation stereology [Bunge & Schwarzer, 2001].

Similar to single crystals, texture in polycrystalline samples describes the anisotropy of material properties and is therefore an influencing factor in materials development and property optimisation. Hence, it is important to evaluate preferred crystallographic orientations in order to predict anisotropic behaviour and optimise the texture for industrial applications [Reimers et al., 2008]. Selected applications, where texture analysis methods are required to modify material characteristics, are presented in the book of Engler & Randle [2009], for example. By means of Young's modulus  $E$  (equation 2.10), figure 2.12a shows how the elastic properties of single-crystalline iron differ from a polycrystalline texture-free bulk sample. The example shows, that parameters such as strength, ductility and toughness, also depend on crystallographic preferred orientations. A further example is the minimisation of the material waste by balancing the texture when steel and aluminium alloy sheets are shaped for car body pieces or beverage cans by deep-drawing. Figure 2.12b shows the so-called earing effect, that should be avoided, of a textured Al sheet after deep-drawing.

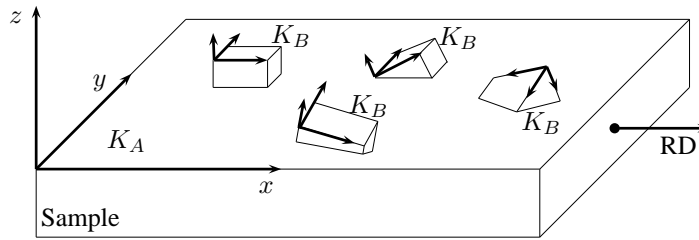


**Figure 2.11.:** Relation of the sample coordinate systems  $K_A$  and the crystal coordinate systems  $K_B$  after [Bunge, 1993]. RD is the rolling or reference direction.

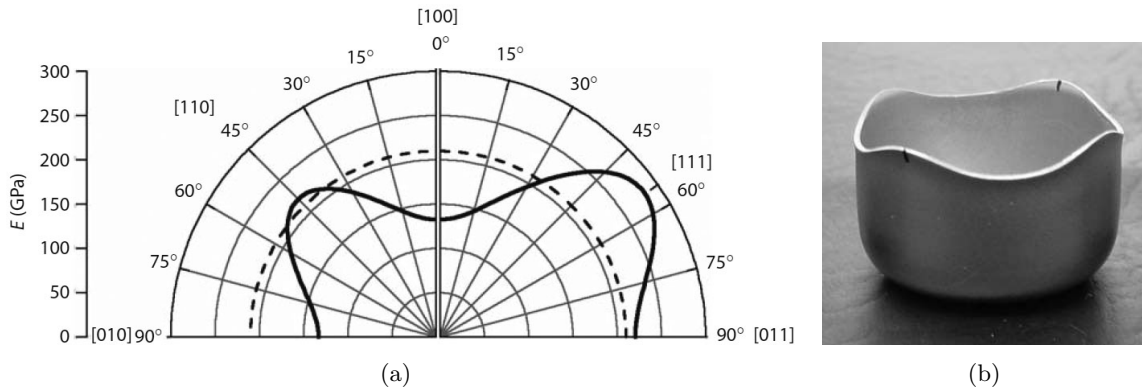


**Figure 2.12.:** Two examples of texture influence on material properties from Engler & Randle [2009]: Young's modulus (a) of elasticity of single-crystalline iron as a function of the crystal direction and compared with the texture-free polycrystalline material and the appearance of "ears" at a deep-drawn cup (b) made from a textured Al alloy sheet.

### 2.6.1. Pole Figures

A typical method of representing the texture of a sample is the application of pole figures that provides graphical interpretation of preferred crystal orientations. Compared to the definitions stated above, a pole figure is a two-dimensional model — a projection of the ODF. Moreover, it is directly connected to the parameters obtained from a texture experiment. For example, the detected intensities of one selected  $hkl$  reflection, i.e. under a fixed  $2\theta$ -Bragg position, of any sample orientation are normalised and assigned to a  $hkl$  pole figure. Then, a representative number of crystallites of the selected crystallographic  $hkl$  axis (pole) is plotted in a stereographic projection against the sample orientation, which is usually denoted by directions that refer to the material's manufacturing process. As a result, a pole figure shows the statistical distribution of a  $hkl$  lattice plane given by its normal. The sample direction is variable. Taking the orientation angles for the sample rotation and tilting

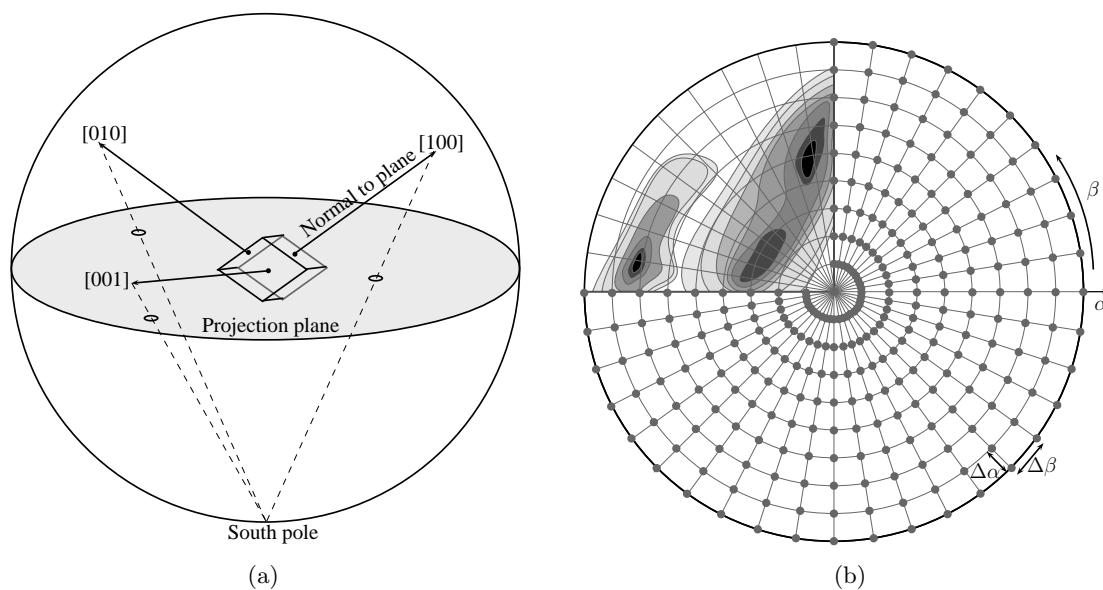


**Figure 2.13.:** Stereographic projections (a) of the lattice reflections from a fixed sample orientation. In a pole figure (b) the projected intensity of a single  $hkl$  reflection is plotted against every possible sample orientation.  $\Delta\alpha$  and  $\Delta\beta$  denote the measurement grid. As an example, a section of the pole figure is used to demonstrate the intensity distribution by means of filled contour lines.

into account, the pole figure intensities are then assigned to the polar grid with  $\alpha$  and  $\beta$  angles. The basic principle of the stereographic projection and a sketch of a pole figure are visualised in figure 2.13. Traditionally, a pole figure measurement is based on a scan using an equiangular grid, say  $5^\circ \times 5^\circ$ . In figure 2.13b, this is referred to as  $\Delta\alpha$  and  $\Delta\beta$  respectively. In principle, any other grid resolution is possible, but with respect to the strength and sharpness of the texture, the number of points to be scanned should be adjusted carefully. The final presentation of a pole figure usually uses contour lines to deviate between the detected intensity levels. Therefore, an interpolation between the measured points of the pole figure grid is applied. In the sketch, this is visualised by means of a simulated texture denoted by the filled contour lines in a section of the pole figure. Chapter 6 provides examples and a detailed description of pole figure measurements made using X-ray and neutron diffraction in order to allow a comparison between these conventional techniques and the Bragg edge transmission method investigated in this thesis. A further possibility to visualise crystallographic preferred orientations is to plot the sample direction relative to the crystal direction by means of so-called inverse pole figures. Then, the sample direction is constant

while the scattering vector, i.e. the  $hkl$  lattice plane, is variable.

In some cases it is not possible to scan over the whole pole figure, in particular, when a sample is measured in the reflection mode, i.e. the incident beam is reflected by the sample surface but not by a gauge volume deep inside the sample volume. During a pole figure measurement the specimen will be tilted, which, for example at  $\alpha = 90^\circ$ , could lead to a point where the incident and the reflected beam is parallel to the sample surface depending on the experimental setup. Then, the measured signal would be corrupted and as a result the pole figure would show inconsistent texture data. Instead, incomplete pole figures can be used for the texture evaluation. In the demonstration of figure 2.13b the positions close to  $\alpha = 90^\circ$ , i.e. the outer rings, will be left empty. However, a complete pole figure can be reconstruct from the ODF. Then, a number of pole figures from independent  $hkl$  reflection is needed for the ODF information. Towards the definition of the three-dimensional ODF, three angles are required to describe the orientation of crystals with respect to the sample axes. Since the pole figure provides a two dimensional representation of the texture, two or more pole figure are required to calculate the ODF. The number of pole figures and choice of  $hkl$  reflections depends on the crystal system and sample symmetry. As the pole figure could be seen as a projection of the ODF, its the calculation from measured pole figures is related to algorithms used in tomography. Today, many software packages are available to compute this [Hielscher & Schaeben, 2008].

### 2.6.2. Texture Methods

Many procedures are used to determine preferred crystallographic orientations. They can be divided into two different methods. On the one hand, there are optical methods to characterise the microstructure of a material. Traditionally, microscopes have been used in geology and metallurgy to obtain preferred morphological orientation, i.e. the shape of grains for example. On the other hand, diffraction techniques are nowadays applied to determine crystallographic orientations. With X-ray diffraction, the orientation of  $hkl$  lattice plane is measured by setting a detector according to the Bragg angle. Then, the diffracted intensity at a certain sample orientation is proportional to the fraction of crystallite orientated to



fulfil Bragg's law. Due to the small penetration depth, only thin samples can be analysed. Otherwise, a reflection mode on a flat sample surface is used. In this particular case, only incomplete pole figures can be measured. Additionally, synchrotron X-rays are used in the same manner, but with fine focusing, very small beam sizes and high intensities. Hence, synchrotron X-rays can also be applied to investigate local texture changes. In both cases, Debye-Scherrer rings are captured that express the texture by systematic intensity variations on each ring. Neutron diffraction is used similarly, but it provides high penetration and low absorption and therefore it is suitable to measurements of large samples. An application of neutron diffraction texture determination is shown in chapter 6.

The previous diffraction methods take advantage of a large gauge volume. Thus, the resulting intensity and orientation information is averaged over a large number of crystallites. Another way is to measure single crystallites. Although the statistics are limited, it is possible to determine the orientation and location of a grain in comparison to its neighbours. By this means, a transmission electron microscope (TEM) allows studies on very fine-grained materials and provides high spatial resolution of below 10 nm. Moreover, the scanning electron microscope (SEM) is available with electron back-scatter diffraction (EBSD) as kind of an add-on package. In contrast to the TEM, the EBSD method is not restricted to very thin samples. Although, the investigated sample surface must be polished as well, the specimen preparation is not that critical. The sample inside the SEM is tilted around  $70^\circ$  towards a diffraction camera, that detects the so-called Kikuchi patterns [Kikuchi, 1928], which are indexed automatically [Wright & Adams, 1992] to determine the grain orientation. The sample is further scanned with increments smaller than  $1\ \mu\text{m}$  by stage translations and beam deflections to measure a grain map of the sample surface. Thus, grain statistics provide morphology, orientation, size and boundary information for example. A detailed comparison of the methods presented here is given by Wenk & Houtte [2004] for example.



## Bragg Edge Neutron Transmission Computation

This chapter provides a detailed summary of the Bragg edge theory. Based on a collection of neutron scattering and absorption cross sections the occurrence of the Bragg edge phenomenon inside the transmission intensity spectra of crystalline materials will be introduced. The cross section calculation will be implemented within a computer program. To achieve this, a general sample description including its crystallographic structure will be developed. The computation will operate with the unit cell description of the sample material to include its atomic composition. Finally, the resulting program will be validated with existing tools.

### 3.1. The Transmission Intensity Spectrum

In neutron transmission experiments, a detector system, placed behind a specimen, detects the transmitted intensity attenuated by neutron-matter interactions inside the sample. The intensity decrease  $dI$  along a transmission path  $dx$  is proportional to that path and to the incident intensity  $I$ :

$$dI = -\mu I dx \quad (3.1)$$

where  $\mu$  is a proportionality factor. The negative sign refers to the decrease of the intensity, i.e.  $dI$  is always negative. In order to allow the calculation for long transmission paths, a summation of  $dI$  for very small  $dx$  is necessary. The integration then delivers the Beer-Lambert law which is used to express the transmission  $Tr$ , where  $I_1$  and  $I_0$  are the detected and the incident neutron intensity respectively,  $l$  is the transmission path length through the

sample and  $\mu$  refers to as the attenuation coefficient usually given in  $\text{cm}^{-1}$ :

$$\int_{I_0}^{I_1} \frac{dI}{I} = \int_0^l -\mu dx$$

$$\ln\left(\frac{I_1}{I_0}\right) = -\mu l \tag{3.2}$$

$$Tr = \frac{I_1}{I_0} = \exp(-\mu l)$$

Thus, depending on the sample thickness, the incident intensity is affected by an exponential decrease. The parameter  $\mu$  depends on the selected material (and its density) and is the variable of interest in tomography experiments [Banhart, 2008]. Reconstructing the transmitted intensities, one is able to visualise in 3D the interior structure of a specimen by means of different attenuation coefficients. Up to this point the neutron energy- or wavelength-dependence of the attenuation term has been neglected, but this dependence is derived here.

Neutron wavelength-dependent transmission intensity spectra captured by experiments investigating different materials and information from the nuclear engineering side are stored in several databases and programs, such as the NIST database search form [Chantler, 1995], XOP [del Río & J., 1997] and JANIS<sup>1</sup> for example. These databases can manage many different standardised formats in order to display and transform experimental and theoretical data. Many of these calculations and look-up tables do not take into account the crystallographic influence and microstructural effects of the investigated sample on the attenuation process in a transmission experiment. The transmission intensity spectrum from polycrystalline material for thermal neutron wavelengths shows sudden intensity changes. In figure 3.1 the neutron transmission through an iron powder sample is plotted. Here, the intensity increases steeply at special wavelength positions. This effect occurs because of the crystallographic properties of the material. Figure 3.2 visualises how the material's lattice structure affects the incident neutron beam. In all three presentations the same set of lattice planes is selected. While there is Bragg diffraction in 3.2a depending on the lattice spacing  $d_{hkl}$ , the Bragg angle  $\theta$  is increased with the neutron wavelength  $\lambda$ . Applying  $\theta = 90^\circ$  to Bragg's law in 3.2b results in backscattering. The set of lattice planes is still the same, but orientated

---

<sup>1</sup><http://www.nea.fr/janis/>, Java-based Nuclear Data Display Program

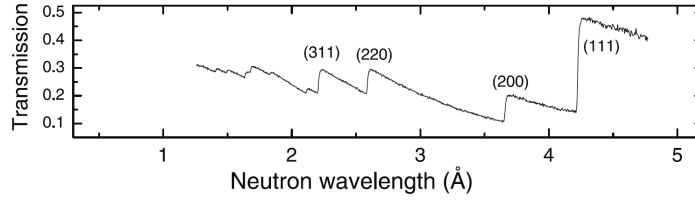


**Figure 3.1.:** The transmission intensity spectrum (taken from Santisteban et al. [2002a]) from an (fcc) iron sample shows steep increases at certain wavelength positions. These positions are indicated with the (hkl) lattice plane.

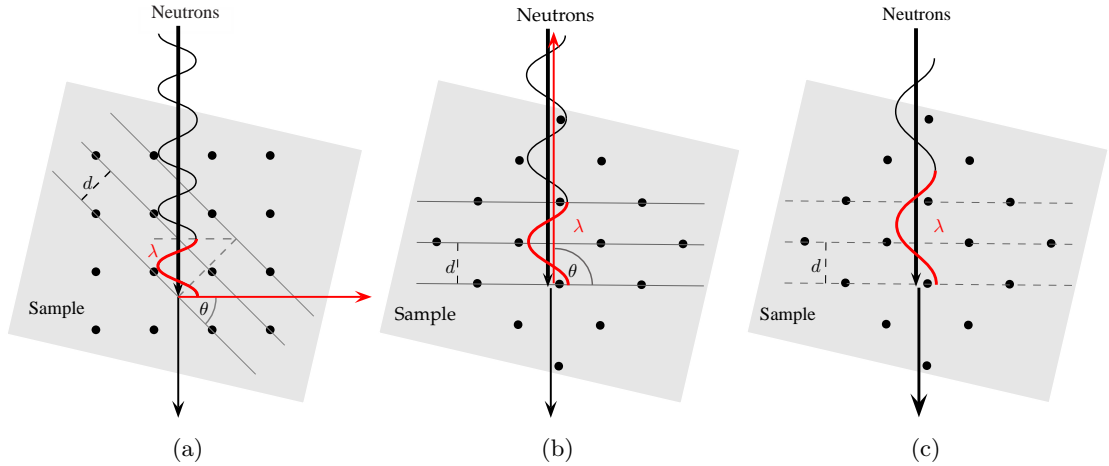


**Figure 3.2.:** Bragg edge transmission principle: In (a), the incoming neutron wavelength  $\lambda$  is scattered under  $2\theta$  depending on the lattice spacing  $d_{hkl}$  ( $\lambda < 2d_{hkl}$ ). Backscattering (b) follows from increasing  $\lambda$  such that  $\lambda = 2d_{hkl}$ .  $\theta = 90^\circ$  is applied to Bragg's law. If  $\lambda > 2d_{hkl}$  no scattering by this particular lattice plane can occur.

such that diffraction with  $\lambda = 2d_{hkl}$  is possible. With  $\theta > 90^\circ$  there will be no Bragg diffraction possible for this particular lattice plane. At wavelengths  $\lambda > 2d_{hkl}$ , the Bragg equation is not fulfilled anymore. Therefore, the lattice planes in figure 3.2c are indicated by dashed lines. The transmitted intensity will rise because the fraction of neutrons to be scattered by this lattice plane disappears — more neutrons can be transmitted. That is why, the sudden transmission changes inside the wavelength spectrum have been called Bragg edges. The position of  $\lambda = 2d_{max}$ , with  $d_{max}$  being the biggest possible lattice spacing of the material, is also called as the Bragg cut-off position. Properties of solids have been investigated using multiple neutron measurement techniques. In Fermi et al. [1947] for example, the scattering amplitudes have been determined with Bragg edge neutron transmission. Also measuring at the Chicago reactor source, Bragg edges have been utilised by Winsberg et al. [1949] in order to determine the scattering lengths of Ca, Ti, and Tl. In the 1990's, the transmission

method was applied at the spallation sources LANSCE, Los Alamos [e.g Priesmeyer, 1992] and at ISIS, Didcot UK [e.g. Wang & Edwards, 1997]. A more comprehensive review of the Bragg edge history was already given by [e.g. Vogel, 2000; Steuwer, 2009]. Nowadays, there is an emphasis on investigations towards the development of Bragg edge imaging experiments. The IMAT beamline proposed in Kockelmann et al. [2007b] should therefore be able to combine radiography and tomography with neutron diffraction measurements. Energy-resolved radiography will then be applied exploiting the Bragg edge transmission signal.

The quantification of the neutron fractions being scattered and absorbed — especially for the critical case around  $\lambda = 2d_{hkl}$ , that results in Bragg edge transmission spectra — is described by so-called neutron cross section calculations in the following sections. By this means, a Bragg edge computation will be possible. Hence, the simplified presentation of the transmission in equation 3.2 will be extended by the wavelength dependence of neutron cross sections. The basic quantity of the attenuation coefficient  $\mu$ , that has been used before to describe the beam penetration of materials, is therefore determined by:

$$\mu = N \sigma_{total}(\lambda) = \frac{\rho}{A} N_A \sigma_{total}(\lambda) \quad (3.3)$$

where  $\sigma_{total}$ , which is depending on the neutron wavelength  $\lambda$ , is the microscopic total neutron cross section to be calculated in the following and  $N$  is the number of scattering centres. Thus, the expression  $\mu$  is also described as the macroscopic cross section taking the number of nuclides interacting with a neutron into account. Furthermore,  $N_A$  is the Avogadro constant ( $\approx 6.022 \times 10^{23} \text{mol}^{-1}$ ),  $\rho$  is the density and  $A$  the atomic weight.

## 3.2. Neutron Cross Sections

The interaction between neutrons and matter is described quantitatively by neutron cross sections which depend on the material properties as well as on the neutron energy [Jevremovic, 2008]. The model for calculating Bragg transmission edges will be explained in this section.

The fraction of neutrons performing different neutron-matter interactions can be quantified by means of cross sections. Neutron cross sections are given in barns (1 barn= $10^{-24}$  cm<sup>2</sup>) and represent the cross-sectional area of a chemical element towards an incoming neutron to perform scattering or absorption. In the thesis of Vogel [2000] neutron cross section calculations have been reviewed and applied to a program that is able to perform Rietveld refinements using Bragg transmission edges. This so-called BETMAN program was developed in that thesis to take advantage of Bragg edge transmission experiments for the determination of structural details of a polycrystalline sample. Here, the neutron cross section calculation shall be summarised in order to provide an understanding for the simulations implemented and applied in the following chapters.

The total microscopic neutron cross section  $\sigma_{total}$  of an isotope is the cross sectional area “presented” to an incoming neutron to interact with the material. It is given by its incoherent and coherent scattering as well as its absorption contributions:

$$\sigma_{total}(\lambda) = \sigma_{coherent}(\lambda) + \sigma_{incoherent}(\lambda) + \sigma_{absorption}(\lambda) \quad (3.4)$$

It should be mentioned that this calculation does not include magnetic interaction as it is not considered in this work. Nevertheless, the term “total” cross section  $\sigma_{total}$  will be used throughout this thesis for the description of neutron absorption and scattering effects. The calculation of the individual scattering and absorption cross sections will be presented in the following. The sum of these contributions is used to compute the transmission probability including the attenuation coefficient  $\mu$ .

### 3.2.1. Scattering

The probability for a neutron to be scattered is determined by the coherent, incoherent, elastic and inelastic neutron scattering cross section contributions. The total scattering cross section  $\sigma_s$  is given by [e.g. Granada, 1984]:

$$\sigma_s(\lambda) = \bar{\sigma}_{coh} \left( S_{coh}^{el}(\lambda) + S_{coh}^{inel}(\lambda) \right) + \bar{\sigma}_{inc} \left( S_{inc}^{el}(\lambda) + S_{inc}^{inel}(\lambda) \right) \quad (3.5)$$

The average cross sections  $\bar{\sigma}$  are calculated by the scattering length  $b_n$  of the contributing nuclei, whereas the functions  $S$  describe the neutron energy influence as well as the effect of the spatial nuclei arrangement to the cross sections. Extending the example of a binary compound presented in Granada [1984, equation 19] to a general case with different contributing isotopes  $n$ , the average cross sections are calculated by each atom concentration  $c_n$  and its nuclear constant  $\sigma_{inc,n}$ .

$$\begin{aligned}\bar{\sigma}_{coh} &= 4\pi \left( \sum_n c_n b_n \right)^2 \\ \bar{\sigma}_{inc} &= 4\pi \left( \left( \sum_n c_n b_n^2 \right) - \left( \sum_n c_n b_n \right)^2 \right) + \sum_n c_n \sigma_{inc,n}\end{aligned}\tag{3.6}$$

The evaluation of the average cross sections are necessary as they are included in onward calculations. The neutron wavelength-dependent elastic and inelastic scattering parts will be described by the functions  $S$  in the following. However, the structural parameters, which are included in the elastic coherent scattering cross section shall be specified first. By means of a structure factor  $F_{hkl}$ , the crystallographic arrangement will be applied to the neutron cross section calculation by:

$$F_{hkl} = w_{hkl} \sum_n o_n b_n \exp(2\pi i (hx_n + ky_n + lz_n)) \exp\left(-\frac{B_{iso,n}}{4d_{hkl}^2}\right)\tag{3.7}$$

where  $w_{hkl}$  is the multiplicity of a lattice plane and  $o_n$  is the site occupation factor, which relates to the atom concentration  $c_n$ . Furthermore, the placement  $(x, y, z)$  of the  $n$ -th atom is used to calculate the structure factor with respect to the  $hkl$  lattice plane.  $B_{iso}$  is the so-called isotropic displacement factor, which was introduced to the calculation by Vogel [2000] to fit a refinable parameter that describes the deviation of an atom from its average position due to thermal motion. On the basis of the so-called Debye-Waller<sup>2</sup> factor, Vogel applies the attenuation correction to the coherent elastic scattering process. With regard to an implementation (see section 3.3) of the neutron cross sections, the factor  $B_{iso}$  will be

---

<sup>2</sup>The Debye-Waller factor is named after Peter Debye and Ivar Waller and describes the temperature dependence of the scattered intensity [Debye, 1913; Waller, 1923]. In general, the factor decreases with an increasing temperature and increasing Miller indices [Kittel, 1995].



calculated by:

$$B_{iso} = \frac{3h^2\varphi_1(\theta)}{Mk_B\theta_D} \quad (3.8)$$

$M$  is the mass of the scattering nucleus and  $\theta_D$  is the Debye temperature of the scattering element. For the purpose of its implementation, the function  $\varphi_1(\theta)$  with its argument  $\theta = T/\theta_D$  is described in the appendix A.

Taking the structural parameters of the material into account, a description for the coherent elastic part  $S_{coh}^{el}$  is given by Granada [1984, equation 3]. Combining the definition of the structure factor  $F_{hkl}$  the following expression, also given in Lovesey [1986], can be used to characterise the coherent elastic scattering cross section  $\sigma_{coh}^{el}$  for any type of crystal structure. The thesis of Vogel [2000] derives this relation.

$$\bar{\sigma}_{coh} S_{coh}^{el}(\lambda) = \sigma_{coh}^{el}(\lambda) = \frac{\lambda^2}{2V_0} \sum_{d_{hkl}=0}^{2d_{hkl}<\lambda} |F_{hkl}|^2 d_{hkl} \quad (3.9)$$

The summation runs over all sets of lattice planes, indicated by the  $hkl$  Miller indices, with a lattice spacing  $d_{hkl}$  smaller than half the size of the selected wavelength  $\lambda$ .  $V_0$  is the unit cell volume. Thus, the discontinuities inside the thermal transmission range, i.e. the attenuation coefficient variation and the outlined behaviour in figure 3.2 can be quantified. According to that, a transmission edge will occur at  $\lambda = 2d_{hkl}$ . Concluding, the lattice spacing defines the Bragg edge position while the structure factor determines whether a crystallographic lattice plane and therefore the individual Bragg edge in the transmission spectrum is systematically absent or not.

The fraction of neutrons that scatter elastically is also influenced by incoherent scattering. The definition of the incoherent elastic component is based on the assumption of thermal motion of the nuclei. The energy dependent expression from Granada [1984, equation 4] has been transformed by Vogel [2000] using the isotropic atomic displacement factor  $B_{iso}$  described above. Applying the neutron wavelength, the expression for a single nucleus becomes:

$$S_{inc}^{el}(\lambda) = \frac{\lambda^2}{2B_{iso,n}} \left( 1 - \exp\left(-\frac{2B_{iso,n}}{\lambda^2}\right) \right) \quad (3.10)$$

For the purpose of a unit cell calculation, the contributions are simply added for each atom  $n$  inside the unit cell as they do not depend on the crystal structure:

$$\sigma_{inc}^{el}(\lambda) = \bar{\sigma}_{inc} \sum_n S_{inc}^{el}(\lambda) \quad (3.11)$$

The inelastic contributions to the neutron cross section calculation describe the probabilities for a neutron to lose or gain energy when interacting with the crystal lattice, i.e. it involves the creation and annihilation of phonons. It was shown in Binder [1970] that the incoherent part of the inelastic scattering cross section is a good approximation for the coherent part in the thermal neutron range. Hence, the total inelastic scattering cross section is described by:

$$\sigma_{total}^{inel}(\lambda) = \sigma_{coh}^{inel}(\lambda) + \sigma_{inc}^{inel}(\lambda) = (\bar{\sigma}_{coh} + \bar{\sigma}_{inc}) S_{inc}^{inel}(\lambda) \quad (3.12)$$

For the calculation of the incoherent inelastic contribution Granada [1984] proposed the following procedure. At first the incoherent elastic scattering contribution  $S_{inc}^{el}$  (see equation 3.10) is evaluated. Then, the total incoherent part, which is given by a rapidly converging mass expansion [Placzek, 1954; Granada, 1984] is calculated:

$$S_{inc}^{total}(\lambda) = \sum_{n=0}^{\infty} \left(\frac{m}{M}\right)^n A_n(\lambda, \theta) \quad (3.13)$$

with  $m$  being the neutron mass.  $A_n$  and its parameters are also given in Granada [1984]. As stated by Vogel [2000] the whole integration process will slow down the calculation, especially when the neutron cross section computation is performed multiple times for different wavelengths. Therefore, an approximation for the epithermal range given in Granada [1984] is used here. Again, the isotropic displacement factor is applied to the calculation, such that the total incoherent scattering cross section for a monoatomic structure is determined by:

$$S_{inc}^{total}(\lambda) = \left(\frac{M/m}{M/m + 1}\right)^2 \left(1 + \frac{9m^2 \varphi_3(\theta) \varphi_1(\theta) \lambda^2}{2M^2 B_{iso,n}}\right) \quad (3.14)$$

where  $\varphi_3$  is given by [Granada, 1984; Vogel, 2000] and will be evaluated in appendix A for the purpose of its implementation in section 3.3. Finally, the incoherent inelastic part is

obtained by the difference of both the total and the elastic part:

$$S_{inc}^{inel}(\lambda) = S_{inc}^{total}(\lambda) - S_{inc}^{el}(\lambda) \quad (3.15)$$

The inelastic part is calculated for each contributing nucleus to obtain the total inelastic scattering cross section for a unit cell. Additionally, one is now able to apply the approximation given in equation 3.12 to compute the coherent inelastic part individually.

### 3.2.2. Absorption

The absorption cross section is determined by the neutron velocity  $v$ . For the thermal and cold neutrons the absorption cross section  $\sigma_{abs}$  decreases with the neutron energy. In this low energy region  $\sigma_{abs}$  is inversely proportional to  $v$  and hence it is often referred to as the  $1/v$ -region. This dependency results from the fact that the longer a neutron stays in the environment of a target nucleus the greater is the chance to be absorbed [Windsor, 1981]. Most reference absorption cross section datasets have been measured and stored in terms of a standard neutron velocity of  $v = 2200$  m/s. Using these existing values to calculate the absorption cross section for a different value, the proportionality of  $1/v$  can be used. Transforming this into a wavelength dependence results in:

$$\sigma_{abs}(\lambda) = B \frac{1}{v} = B \frac{m\lambda}{h} \quad (3.16)$$

With  $\sigma_{abs}^{2200}$  being the measured absorption cross section related to the neutron velocity of 2200 m/s or equivalent wavelength of  $1.798 \text{ \AA}$ , another constant available from databases will be applied. Finding the solution of the proportionality factor  $B$ , a general term for the determination of  $\sigma_{abs}(\lambda)$  can be used:

$$B = \frac{h}{1.798 \text{ \AA} \cdot m} \times \sigma_{abs}^{2200} \quad (3.17)$$

$$\sigma_{abs}(\lambda) = \frac{\sigma_{abs}^{2200}}{1.798 \text{ \AA}} \lambda$$

The absorption does not depend on the spatial arrangement of the atoms inside a unit cell. Therefore, the absorption for a complete unit cell is determined by the sum of absorption

cross sections calculated for each individual atom.

### 3.2.3. Analytical Description of Measured Bragg edges

In the previous sections it was shown, that the Bragg edges are displayed as sharp discontinuities of the coherent elastic neutron cross section. Nevertheless, due to the finite instrument resolution a broadening of the measured Bragg edges occurs. But, in order to determine the edge positions and the corresponding lattice spacing precisely, a model including the instrument influences is required. For the case of time-of-flight transmission experiments at spallation sources Santisteban et al. [2001] presented a theoretical three-parameter expression to fit a measured Bragg edge, whose origin is briefly summarised as follows. Neutrons created by spallation are moderated by collision processes within the moderator. Due to the uncertainty in time and position at which a neutron leaves the moderator, the neutron flight path and time-of-flight cannot be measured precisely. In order to account for this effect, the fitting model applies a resolution function  $R(\lambda', t)$  describing the neutrons of wavelength  $\lambda'$  and time  $t$  arriving at the detector. In total, the authors describe the Bragg edge by means of the ratio between incident ( $I_0$ ) and transmitted neutrons ( $I$ ):

$$I(t)/I_0(t) = \exp[-nw\sigma_0(\lambda_t)] \left( \exp[-nw\sigma_{hkl}(\lambda_t)] + \{1 - \exp[-nw\sigma_{hkl}(\lambda_t)]\} \int_{2d_{hkl}}^{\infty} R(\lambda', t) d\lambda' \right) \quad (3.18)$$

where  $n$  is the number of atoms per unit cell,  $w$  is the sample thickness,  $\sigma_{hkl}$  is the coherent elastic scattering cross section of a selected  $hkl$  lattice plane and  $\sigma_0$  describes other than the coherent elastic contributions. Consequently, equation 3.18 introduces a sharp step function by including the sudden changes of  $\sigma_{hkl}$  at the edge position. In order to describe the shape of a Bragg edge, a resolution function proposed by Kropff et al. [1982], modelling the diffraction peaks at the ISIS pulsed spallation source, is used — namely a Gaussian convoluted with a decaying exponential. Figure 3.3a visualises a least-squares fit of such a peak. However, in Santisteban et al. [2001] the function was integrated analytically to provide the expression

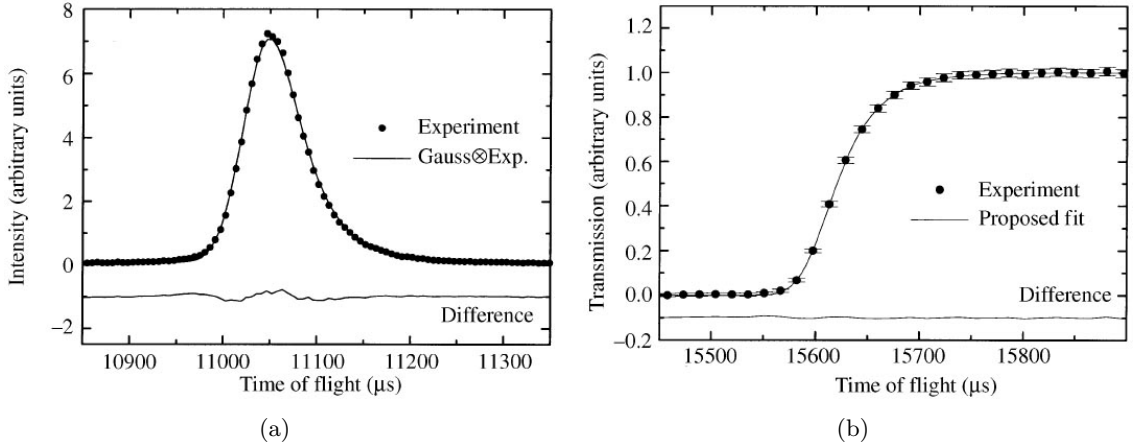


**Figure 3.3.:** Experimental 110 diffraction peak (a) and Bragg edge (b) fitted with the proposed model. Both plots have been taken from Santisteban et al. [2001].

for the broadening of a Bragg edge:

$$\int_{2d_{hkl}}^{\infty} R(\lambda', t) d\lambda' = \frac{1}{2} \left[ \operatorname{erfc} \left( -\frac{t - t_{hkl}}{\sqrt{2}\sigma} \right) - \exp \left( -\frac{t - t_{hkl}}{\tau} + \frac{\sigma^2}{2\tau^2} \right) \operatorname{erfc} \left( -\frac{t - t_{hkl}}{\sqrt{2}\sigma} + \frac{\sigma}{\tau} \right) \right] \quad (3.19)$$

where  $\sigma$  is the deviation of the Gaussian. The exponential decaying with the time constant  $\tau$  starts at a time  $t_{hkl}$ , which equally describes the Bragg edge position. As an example, figure 3.3b shows the experimental 110 iron edge fitted by the proposed function.

The expression will be applied in chapter 7 (equation 7.7) to determine the lattice parameters of a residual stress sample by Bragg edge neutron transmission. Moreover, the investigation of the same sample at a constant reactor source will be presented. Therefore, the fit function will be modified according to the descriptions made by Strunz et al. [1997]. A Gaussian will be used to model the resolution function and describe the edge broadening at a steady-state reactor (see equation 7.9).

#### 3.2.4. Discussion on Bragg Edge Amplitude Changes

It follows from equation 3.2 that the transmission signal is always  $0 \leq Tr \leq 1$ , while 1 represents the case that the incident intensity equals the measured intensity. The other case describes that no intensity transmitted through a sample could be measured. In gen-

eral, the amplitude of the measured transmission depends on the neutron transmission path through the sample, which is equated with the thickness of a sample, and on the attenuation coefficient  $\mu$ . Consequently,  $Tr$  tends to 1 for very thin samples and materials exhibiting low attenuation. For such a case, the sample is almost “invisible” to neutrons. As reviewed above,  $\mu$  depends on many structural parameters and atomic properties which influence the transmission signal. For example, the larger the density of the sample (the packing density of the material) the higher is the attenuation. However, the impact of the individual parameters on the Bragg transmission edges should be discussed here.

Although, the Bragg edges are displayed as sudden intensity changes, their occurrence might be diminished by the overall transmission. Related to the influence of the sample thickness and the attenuation coefficient mentioned above, the Bragg edge information might get lost in the statistical uncertainty of a transmission measurement, when  $Tr$  tends to 0 or 1. In order to demonstrate this effect, the transmission spectra of an iron sample with different thicknesses are shown in figure 3.4. As a consequence, one has to take both properties into account, the scattering and the absorption strength of a material. With regard to a transmission measurement, it may be required to optimise the experimental configuration. This includes an estimation of the ideal sample thickness in order to resolve the desired quantity, i.e. to find an optimum between a sample that is either too thick or too thin for the impact of the coherent elastic scattering cross section to be resolved. In Santisteban et al. [2001] for example, a function was derived to map the resolution of an instrument measuring the interplanar lattice distances (by means of Bragg edges) for different materials to the sample thickness. Besides these general considerations, the Bragg edge signal relates to the coherent elastic interaction between the neutron and the sample’s crystal structure. The shape, position and magnitude of a Bragg edge is directly connected to the crystalline characteristics covering the following information:

- crystalline phase,
- lattice spacing (stress and strain),
- crystallographic orientations (texture).

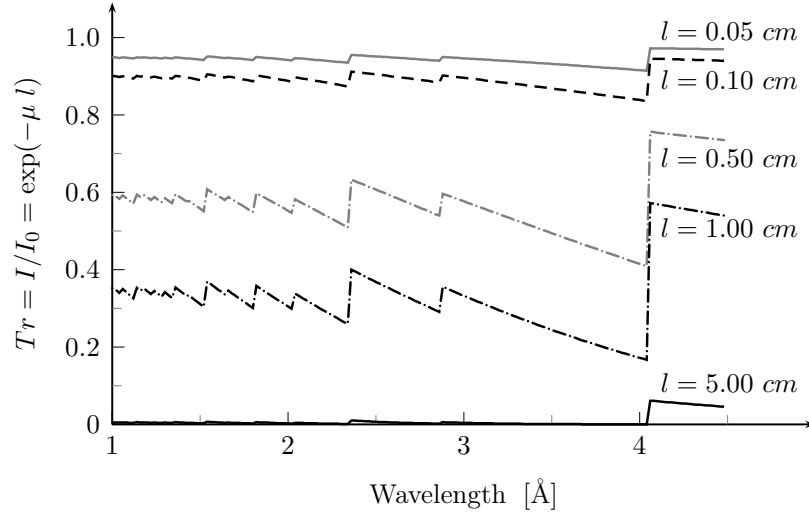


**Figure 3.4.:** Ideal transmission spectra (b) through an iron (bcc) sample with a number of thicknesses  $l$  of iron calculated by means of the neutron cross section presented above.

As presented above, the coherent elastic scattering cross section (equation 3.9) corresponds to the unit cell structure, such that a Bragg edge will occur (or be absent) depending on the structure factor  $F$  at a wavelength position being equivalent to two times the lattice spacing  $d$ . Thus, it is possible to distinguish between different materials and its phases, i.e. between various crystalline forms of these elements. Santisteban et al. [2002a], for example, showed the possibility to measure in situ phase transformations with Bragg edge neutron transmission. After austenisation, i.e.  $\gamma$ -Fe (fcc), a EN24 steel sample was put in a 380 °C furnace to detect the phase transformation to  $\alpha$ -Fe (bcc). In figure 3.5a, the measured Bragg edge spectra at four different times are plotted. From these transmission spectra, the phase fractions (see inset) have been determined with respect to the transformation time. In the diagram, the (111) and (200) Bragg edges identify the  $\gamma$ -Fe at the beginning of this process. With increasing time, the Bragg edge shape changes. The two edges become smaller while they are superimposed by the  $\alpha$ -phase, which only includes the (110) edge within this wavelength range. Although, the  $\alpha$ -phase material dominates the Bragg edge spectrum, the fcc structure of the  $\gamma$ -phase can still be detected by means of the (111) and (200) edges. The example shows how the amplitudes of Bragg edges can be affected because of different phases and materials. Furthermore, the position of a Bragg edge (of a single phase material) can be shifted due to lattice strains and stresses and thermal expansion. Figure 3.5b, taken

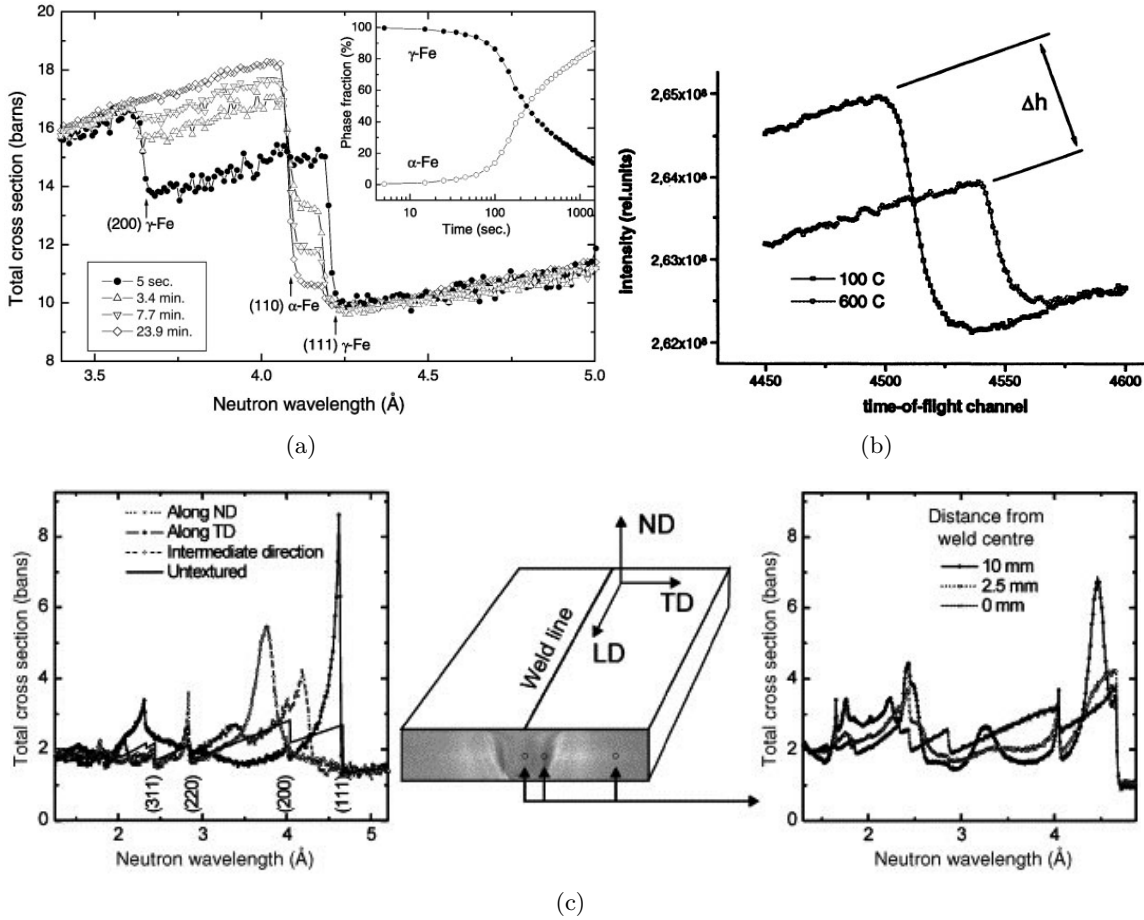


**Figure 3.5.:** Influences on the Bragg edge spectrum: In (a), the Bragg edges spectra, taken from Santisteban et al. [2002a], demonstrate the phase transformation from  $\gamma$ -Fe (fcc) to  $\alpha$ -Fe (bcc). The inset shows the phase fractions at individual time steps derived from the measured transmission spectra measured in Priesmeyer et al. [1999]. The effect of thermal expansion on the Bragg edge is shown in (b), by means of a steel sample. Due to the change of the lattice distance, the edge position is shifted. Furthermore, the increasing temperature (600 °C) affects the Debye-Waller factor, which reduces the Bragg edge amplitude by  $\Delta h$ . The influence of crystallographic preferred orientations is visualised in (c) by means of a welded Al plate [Santisteban et al., 2006b].

from Priesmeyer et al. [1999], demonstrates such a shift by means of the (321) Bragg edge of  $\alpha$  iron (bcc). The graph compares the edge positions of a steel measured at 100 °C and 600 °C using the time-of-flight signal. The edge shift due to thermal expansion of the lattice spacing  $d$  is clearly visible. Moreover, a reduction of the measured edge height, indicated by  $\Delta h$ , is apparent and is explained by the application of the Debye-Waller factor. It follows from equation 3.8, that the higher the temperature the smaller is  $B_{iso}$ , which is included in the structure factor calculation (equation 3.7). Thus, the diffracted intensity for each



reflection, and therefore the Bragg edge amplitude, is reduced. Within this work, the Bragg edge shift due to residual stresses will be investigated (see chapter 7). A further influence on the Bragg edge amplitude is the crystallographic texture. The presented neutron cross section calculations are valid for powders and ideal polycrystalline samples, i.e. samples consisting of random grain orientations. However, preferred crystal orientations will affect the measured intensities within the Bragg edge spectrum. In particular, a Bragg edge might be enhanced or reduced, similar to the measurement of a diffraction peak, depending on the number of crystallites being orientated to perform Bragg scattering. As an example, figure 3.5c, which has been taken from Santisteban et al. [2006b], shows the Bragg edge spectra of a welded Al plate, measured from different orientations (left) and at different local sample positions (right). It is apparent, that the shape of a Bragg edge can be deformed due to the existence of texture. The ability to resolve texture information from Bragg edge transmission measurements is examined in chapter 6. Furthermore, the background and a model to correct the neutron cross section calculation for the texture influence is presented in section 3.4.

### 3.2.5. Summary

The neutron cross section calculations presented in this section can be applied to single atoms as well as to material compositions. The definition of a sample material is handled by its unit cell description. The initialisation of a unit cell (see section 3.3.4) includes the spatial arrangement as well as the properties of all contributing atoms. Then, the cross section calculations presented above will be applied to each individual unit cell atom. In parallel, the crystal structure is included in the Bragg edge calculation, i.e. the number of atoms inside a unit cell and their spatial arrangement is considered. For a bcc iron for example, the unit cell is composed of two iron atoms placed at  $(0,0,0)$  and  $(\frac{1}{2},\frac{1}{2},\frac{1}{2})$  in the unit cell coordinate system. To calculate the total cross section for this unit cell, the cross sections for a single iron atom will be multiplied with number of unit cell atoms. Visualising the atoms as spheres, the  $(0,0,0)$  atom is placed with only  $\frac{1}{8}$  of its volume inside the unit cell. Although not needed for the unit cell description, the other corners of the cubic lattice are also filled with iron atom, as shown in figure 2.1b, each contributing with  $\frac{1}{8}$ . Furthermore, the  $(\frac{1}{2},\frac{1}{2},\frac{1}{2})$

atom contributes with its whole volume = 1. As a result, the arrangement of all atoms in the Bravais lattice delivers the number of unit cell atoms  $N_0$  for a bcc structure:

$$\underbrace{1 \cdot 1}_{\text{centre atom}} + \underbrace{8 \cdot 1/8}_{\text{corner atoms}} = 2 = N_0 \quad (3.20)$$

Here, one has to differentiate between the representation of the Bravais lattice and the unit cell. The same principle must be considered for any other crystal structure, if  $\sigma_{total}$  is calculated.

Lacking better descriptions the algorithms presented above contain approximations. It was already shown, for example, that the inelastic incoherent scattering cross section is approximated by the inelastic coherent one (see equation 3.15). However, further approximations and restrictions within the Bragg edge calculations shall be summarised here. According to that, [Vogel, 2000, equation 3.30] already stated that the evaluation of  $\sigma_{inc}^{inel}$  is valid for epithermal neutrons only. Furthermore, multiple Debye temperatures are known for some materials. [Binder, 1970, section 4] for example, mentioned different values for aluminium depending on the method of their determination. On the other hand, there are elements with unknown Debye temperature values and default values must be applied. Consequently, a refinement depending on the Debye temperature of each contributing atom was proposed. Moreover, the quality of the mass expansion (equation 3.13) for other than monoatomic systems is not known [Vogel, 2000]. Additionally, the one-phonon approach used for the inelastic part, was reported to be inadequate in special circumstances [Binder, 1970]. However, the incoherent approximation is applied here. The model of the Debye-Waller factor implemented through  $B_{iso}$  is valid for isotropic atomic displacements. Anisotropic cases are not considered here. Nevertheless, the restriction to the isotropic case is a good approximation for metals and alloys [Vogel, 2000]. In addition, the Debye temperature model is valid for materials with big atomic masses such as solids, but not for light material such as hydrogen and deuterium. As a consequence, the neutron cross section calculation described here is not reliable for samples with a large fraction of hydrogen for example. Though, for the field of materials engineering the current Bragg edge calculation is considered as a powerful tool for the studies presented in this thesis. The materials investigated here exhibit predominant coherent elastic scattering

cross sections. Hence, the errors introduced by the inaccuracy of the presented calculations (e.g. incoherent approximation) are expected to be small.

### 3.3. Bragg Edge Implementation

In the following the implementation of the neutron cross section calculation into a computer program will be described. Based on the creation of library routines, a computation of Bragg edge transmission spectra will be enabled. Thus, depending on materials definition a prediction of Bragg edge positions and amplitudes will be possible. Furthermore, a program is presented to visualise this calculation. Finally, an algorithm to account for crystallographic preferred grain orientations is implemented. Thus, a mechanism for the correction of transmission intensities through textured samples can be applied within the Bragg edge calculation. Altogether, the program routines created are prepared for a Bragg edge neutron transmission simulation applied within the next chapters.

#### 3.3.1. The `nxs` Library & `nxsPlotter`

The neutron cross section calculation which was described above (section 3.2) has been adapted to create a computer software that allows the computation of Bragg edge neutron transmission. On the one hand, it was the aim to provide a simulation tool for Bragg edge transmission experiments with adjustable instrument parameters. One should be able to compare experimental Bragg edge results from a real neutron instrument with the theoretical calculations presented here. Therefore, a neutron instrument simulation using the Bragg edge approach will be developed in chapter 5. On the other hand, the same routines applied for a simulation of an instrument should be available for further applications also. For example, the visualisation of ideal Bragg transmission edges depending on different materials parameters can be realised likewise. Once implemented, the collection of neutron cross sections can be used for multiple applications. Thus, a stand-alone software tool to predict Bragg edges at certain wavelength positions will be realised. Therefore, the necessary neutron cross section calculation routines have been implemented and compiled into a new library to realise this availability. These library routines could then be shared to be used by multiple programs.

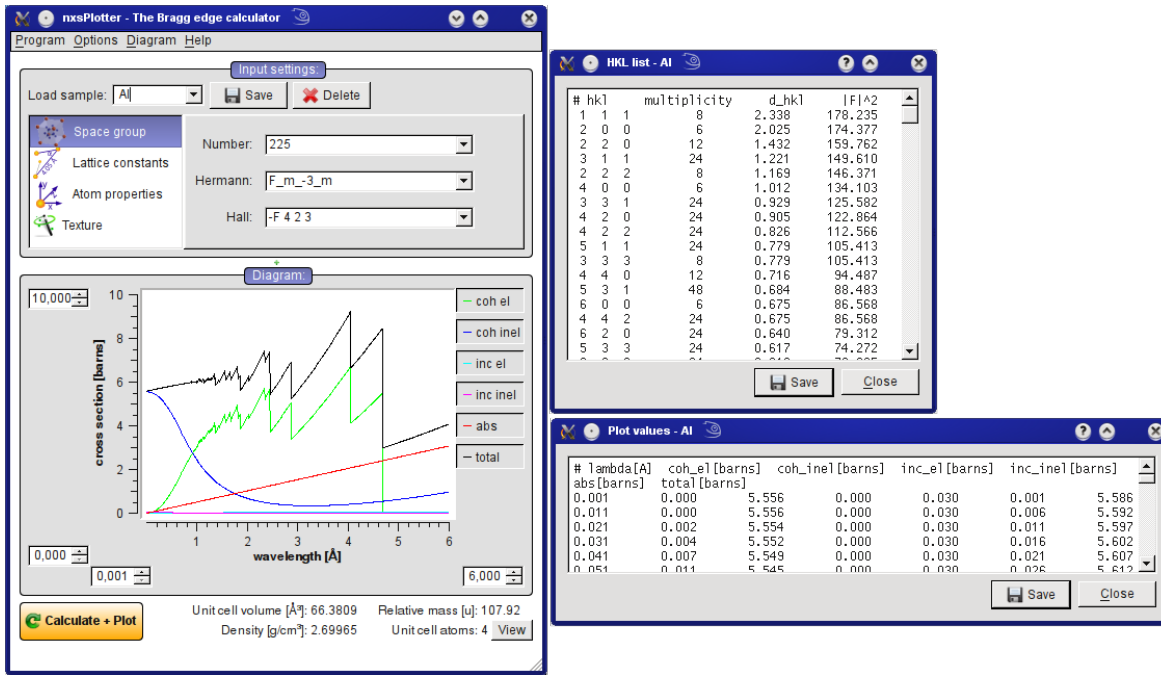


Figure 3.6.: Screenshots of the *nxsPlotter* program.

The following procedures have been created within this work. They have been written in the C programming language and compiled into the new so-called **nxs** library, which is an abbreviation for neutron cross sections. Using this term, the important cross section calculation routines are called **nxsAbsorption** and **nxsCoherentElastic** for example. In order to utilise the implemented **nxs** routines within applications, an overview of the available functions is given in figure 3.7, which is shown at the end of the implementation description to summarise the program workflow. The decision for the C programming language is based on the possibility to easily use these sources for the neutron simulation software package *McStas* [Willendrup, 2004]. This software will be extended in chapter 5 with the **nxs** library routines in order to provide virtual Bragg edge transmission experiments. Furthermore, this library could also be included to build a standalone application written in C or C++, but also other interfaces and programming languages are conceivable which allow native C code calls. Moreover, the C program code can be compiled and executed on multiple platforms. Thus, the availability is extended even more.

Using the **nxs** library implementation, a new program called **nxsPlotter** was created to apply Bragg edge calculation and plot wavelength-dependent neutron cross sections. Addi-

tionally, the nxsPlotter program is based on the Qt4 C++ class libraries<sup>3</sup> for programming graphical user interfaces (GUI). Thus, intuitive forms for the assignment of input parameters as well as Bragg edge plots have been realised. As an example, the nxsPlotter user interface is shown in figure 3.6. The two windows on the right-hand side also belong to the nxsPlotter program and show the ability to print out results from the internal calculation, such as the individual lattice spacings and structure factors as well as single neutron cross section values forming the Bragg edge spectrum. Consequently, a quick prediction of Bragg edges within a given wavelength range based on a unit cell description of the sample material is possible. In the following, the necessary input parameters to control nxsPlotter and the nxs library routines will be discussed.

### 3.3.2. Input Parameters

In order to describe the implementation details and the usage of the nxs library as well as the nxsPlotter tool, it is necessary to have an understanding of the parameters that are needed to calculate the Bragg edge spectrum. The neutron cross sections have already been presented in section 3.2. Here, the input parameters that are used in the Bragg edge implementation are derived. The necessary information could be abstracted as follows:

- the incoming neutron wavelength,
- the sample's crystal structure,
- the lattice parameters,
- the material composition (atomic properties).

As wavelength-dependent cross section calculations are realised here, the neutron wavelength  $\lambda$  is needed. This scalar value is assigned in Ångström ( $1 \text{ \AA} = 0.1 \text{ nm}$ ). A conversion from neutron energies or velocities is not handled by the nxs library routines itself.

The material's crystal structure and its lattice parameters, i.e. the arrangement of atoms, is described in terms of its unit cell. The unit cell definition will be obtained from the space

---

<sup>3</sup>Qt is a cross-platform framework widely used for the development of applications with graphical user interfaces. Version 4 is presented in the book of [Blanchette & Summerfield, 2008] for example and freely available from <http://qt.nokia.com/>.

group number that is given as an input parameter. For this purpose the existing **SgInfo** library routines, described in section 3.3.3, have been included in the computation. Taking advantage of this library, a unit cell is initialised and the crystal structure (for example cubic, hexagonal or orthorhombic) can be obtained. Related to the crystal structure definition the lattice parameters  $a, b, c$  (Å) and  $\alpha, \beta, \gamma$  (°) will be assigned to the unit cell description. The sample composition is defined by each individual atom and its properties, such as the atomic mass  $M$  (given in  $u \approx 1.66 \times 10^{-27}$  kg), the Debye temperature  $\Theta_D$  (K) and the placement  $(x, y, z)$  inside the unit cell (see Wyckoff position in section 3.3.4). The average (thermal) scattering lengths and absorption cross sections, that are applied here, are constants depending on the selected element. They are given in fm and barns =  $10^{-24}$  cm<sup>2</sup> respectively and can be obtained from databases such as the NIST<sup>4</sup> website. By way of example, the absorption, incoherent and coherent scattering cross sections ( $\sigma_{abs}^{2200}$ ,  $\sigma_{inc}$ ,  $\bar{\sigma}_{coh}$ ) and scattering lengths ( $b_{coh}$ ) are shown in table 3.1 for a few elements.

Isotope	$b_{coh}$	$\bar{\sigma}_{coh}$	$\sigma_{inc}$	$\sigma_{abs}^{2200}$	Debye temp.	mass
Al	3.449	1.495	0.0082	0.231	429	26.98
Fe	9.45	11.22	0.4	2.56	464	55.85
Mg	5.375	3.631	0.08	0.063	400	24.31

*Table 3.1.: Atomic properties of selected elements.*

### 3.3.3. SgInfo - Space Group Library

The existing ANSI C calculation routines provided by the SgInfo library [Grosse-Kunstleve, 1998], written by Ralf W. Grosse-Kunstleve and freely available from the project website<sup>5</sup>, have been used to compute unit cells as well as their lattice reflections. Additionally, the SgInfo library was superseded by a part of the open source package “Computational Crystallography Toolbox” (cctbx) which is written in C++ programming language [see Grosse-Kunstleve et al., 2002]. Because of the compatibility to the simulation tool McStas (see chapter 5), which is based on C programming, the original C routines from the SgInfo package have been applied here to provide the necessary variables and procedures for the neutron

<sup>4</sup><http://www.ncnr.nist.gov/resources/n-lengths/>, NIST Center for Neutron Research

<sup>5</sup><http://cci.lbl.gov/sginfo/>, SgInfo - Space group Info

cross section calculation. Furthermore, the website provides a comprehensive reference section with detailed descriptions about the usage and internal calculations of the library. The SgInfo source files have been included in the nxs library as proposed in the SgInfo documentation.

The Bragg edge calculation makes use of the space group initialisation functions to create a unit cell. Moreover, the routines to find lattice reflections and symmetry equivalent lattice planes have been applied. Although, the SgInfo library provides many more features to perform single crystal data analysis for example, only the unit cell initialisation is used in the Bragg edge implementation.

### 3.3.4. Unit Cell Initialisation

Prior to the wavelength-dependent Bragg edge calculation, a few crystal properties and variables must be initialised first.

- type of unit cell (notation),
- arrangement of atoms,
- unit cell volume, density and mass.

By including the SgInfo routines, as described above, a unit cell is computed at first. Therefore, three different notations are allowed — the space group number, Schönflies symbols and Hermann-Mauguin symbols — to define a unit cell and its crystal system. All three options are provided by the GUI of the nxsPlotter program as well. The input values will be compared with an internal look-up table to generate symmetry matrices for further calculations. A C struct called **UnitCell** was created to define and hold the crystal data. Then, the actual unit cell initialisation is handled by the `initUnitCell` function.

Once a unit cell is generated, atoms and their properties can be added to the crystal via the **AtomInfo** struct, that was created to store the properties for one atom. Choosing an element, the following properties are assigned for the computation: the coherent scattering length  $b_{coh}$ , the incoherent scattering and absorption cross section  $\sigma_{inc}$ ,  $\sigma_{abs}^{2200}$ , the atomic mass  $M$ , the

Debye temperature  $\Theta_D$  and the Wyckoff<sup>6</sup> position  $(x, y, z)$ . This Wyckoff position belongs to a set of points that describe the placements and the number (multiplicity) of equivalent atoms inside the unit cell. Depending on the symmetry of the generated unit cell up to 27 Wyckoff positions are possible, which can also be labelled by the so-called Wyckoff letter in combination with the multiplicity. These notations are used by a lot of programs, such as the applications available from the Bilbao Crystallographic Server<sup>7</sup>. A list for all possible Wyckoff positions and letters with respect to a selected space group is also provided by the International Tables for Crystallography, Vol. A [Hahn, 2006]. Instead of the Wyckoff letters, the `nx` library uses the  $xyz$ -coordinates to determine the occupancy of a given atom inside the unit cell. From the generated `SgInfo` symmetry matrices the available coordinates are calculated and stored to the `AtomInfo` struct also. To complete the unit cell definition and finalise the sample material, more atoms can be added to the initial crystal and placed at defined Wyckoff positions. Therefore, an interface function called `addAtomInfo` has been implemented to assign the atomic properties to the `UnitCell` struct.

For the unit cell volume calculation of the general case of a triclinic crystal system the description of the volume of a parallelepiped can be used, such that it can be determined by its edges. Depending on the given lattice spacing values  $a, b, c$  and angles  $\alpha, \beta, \gamma$ , the unit cell volume  $V_0$  is calculated by the general expression:

$$V_0 = abc \sqrt{1 - \cos^2\alpha - \cos^2\beta - \cos^2\gamma + 2 \cos\alpha \cos\beta \cos\gamma} \quad (3.21)$$

Faster procedures are also provided for convenience and performance issues. In case of a cubic crystal system for instance, where  $a = b = c$  and  $\alpha = \beta = \gamma = 90^\circ$ , the expression  $V_0 = a^3$  will be used. An overview of the unit cell volume calculation with respect to the crystal system is provided in the appendix B. Now, the unit cell mass  $M_0$  is calculated in terms of all individual atoms, i.e. the sum of their atomic weights. The unit cell density  $\rho_0$ , which is

---

<sup>6</sup>The term Wyckoff position is named after the collection of equivalent positions in space groups in the book of [Wyckoff, 1922].

<sup>7</sup><http://www.cryst.ehu.es/>, Bilbao Crystallographic Server



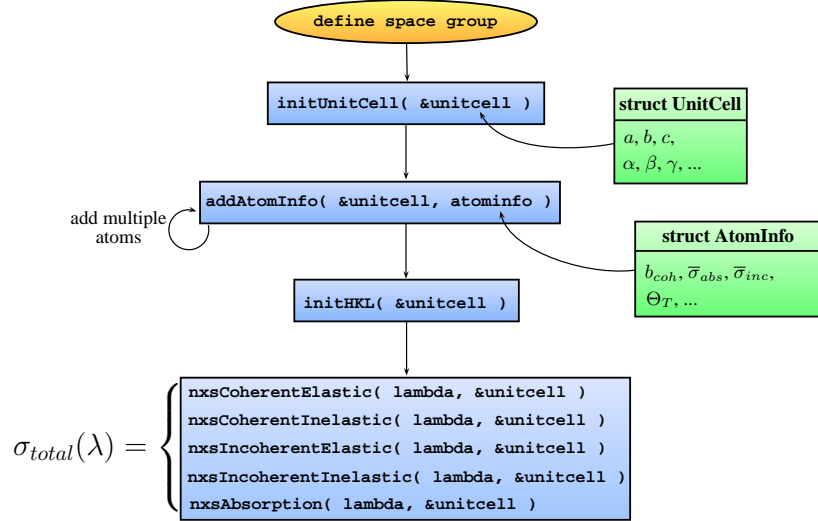


**Figure 3.7.:** Workflow of the neutron cross sections calculation using the routines implemented into the *nxs* library. The upper part consist of the unit cell initialisation routines, that have to be called only once. Below, the individual neutron cross section routines are listed.

considered to calculate the attenuation coefficient, is determined equally equivalently, i.e.:

$$M_0 = M_1 + M_2 + \dots + M_n \quad ; \quad \rho_0 = \frac{M_0}{V_0} \quad (3.22)$$

Finally, the  $hkl$  lattice reflections can be initialised. Using the *SgInfo* routines, a list of crystal lattice reflections up to a given maximum index<sup>8</sup> number  $hkl_{max}$  is generated according to the above defined space group and unit cell parameters. Symmetry equivalent lattice planes as well as the  $hkl$  multiplicity will also be stored at this stage. As a last step during this initialisation process, the individual lattice spacings  $d_{hkl}$  (see appendix B) and the structure factors  $F_{hkl}$  will be computed by means of the  $hkl$  index numbers and the given unit cell parameters. The initialisation of the lattice reflections is integrated within an interface function called **initHKL**.

The complete unit cell initialisation process described here has been implemented and compiled into the *nxs* C library. Towards a Bragg edge calculation, the workflow of the implemented routines to be applied is shown in figure 3.7.

<sup>8</sup>With decreasing the maximum  $hkl$  index, the calculation speed is increased. According the wavelength spectrum of interest, one is able to limit  $hkl_{max}$  by a minimum Bragg edge visible.

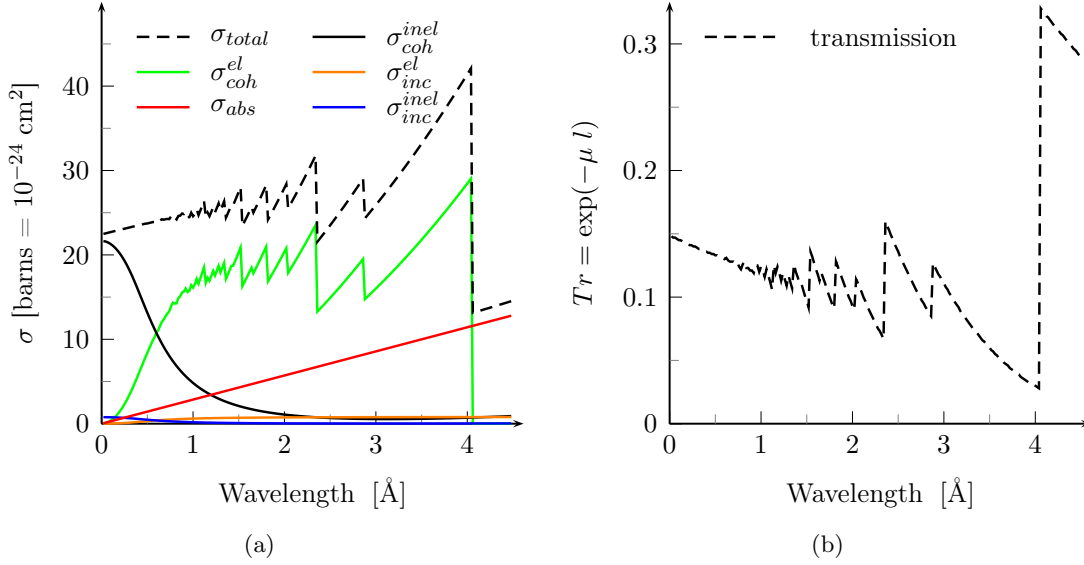


**Figure 3.8.:** Theoretical neutron cross sections (a) for a bcc iron unit cell and ideal transmission spectrum (b) through 2-cm thick iron calculated by the `nxsPlotter` software.

### 3.3.5. Neutron Cross Section Functions

After initialising the unit cell parameters and its  $hkl$  lattice reflections, the user is now able to apply the `nxs` base functions that represent the C implementation of the neutron cross sections calculations. Calling the `nxs` routines, each individual cross section can be calculated as a function of the neutron wavelength “lambda” and by means of the `UnitCell` struct which contains the necessary parameters from the unit cell initialisation. The return value will be a double term specifying the current cross section value. In `nxsPlotter`, this is done by a single click on the “Calculate + Plot” button. Then, unit cell and cross section calculation within a given wavelength spectrum is computed. The input parameters will be assigned from the input mask. The program workflow (figure 3.7) is the same. As plotted in figure 3.8a, the result from continuous calculations is a Bragg edge spectrum. The resulting diagram shows the individual neutron cross sections of iron (body-centred cubic) indicated by separate colours. As state in section 3.2.5, the neutron cross sections are calculated in terms of a complete unit cell. This is convenient for the calculation of the attenuation coefficient. Using the equations 3.2 and 3.3, an ideal transmission spectrum for a given sample thickness  $l$  can be plotted as well. Consequently, figure 3.8b shows the transmission through 2-cm thick iron. In order to compare the total cross section calculated here, one is

also able to normalise  $\sigma_{total}$  by the number of contributing unit cell atoms. In case of the iron example, the cross section values are twice as big as the values of resulting from programs and databases considering monoatomic structures only. Hence, the two unit cell atoms at  $(0,0,0)$  and  $(\frac{1}{2},\frac{1}{2},\frac{1}{2})$  must be considered within a comparison.

### 3.3.6. Validation

The implementation of the neutron cross section calculation has been validated with existing tools. The output of nxsPlotter was compared with the values computed by the BETMAN program from [Vogel, 2000] and the CRIPO code by [Kropff & Granada, 1977]. CRIPO is a command line program written in Fortran and calculates neutron cross sections for monoatomic systems. The program is able to differentiate between cubic (bcc and fcc) and hexagonal structure, but unit cell arrangements are not considered. Thus, the Bragg edges can be compared for systems such as the iron example presented before (figure 3.8). However, the nxsPlotter values must be normalised by the number of unit cell atoms since CRIPO calculates neutron cross sections per atom. Taking these conditions into account, both results are identical. Additionally, the Bragg edge results for complex unit cell definition (multiple atoms) have been compared with the output of BETMAN. BETMAN is provided with example files to be loaded with the program. These files contain the necessary information to initialise a unit cell as described in section 3.3.4. Although a theoretical total neutron cross section calculation is then used to perform a Rietveld refinement on measured transmission spectra, the values for the individual cross sections can be exported to text files. Thus, a NaCl unit cell definition, for example, was available towards a validation of the nxs calculation results. The neutron cross section spectrum of NaCl computed by BETMAN is shown in figure 3.9. Using the nxsPlotter GUI, a new sample was defined by the application of the NaCl structure. Therefore, a space group and the appropriate lattice spacing have been defined — a fcc crystal lattice with  $a = b = c = 5.64 \text{ \AA}$ . Furthermore, the Na and Cl atoms including their properties (section 3.3.2) have been added to the structure in order to compose the unit cell. The atom properties as well as their Wyckoff positions are listed in figure 3.9. As a result, the individual neutron cross sections have been calculated. For overview reasons, only the total cross section (red dotted line), which is the sum of all in-

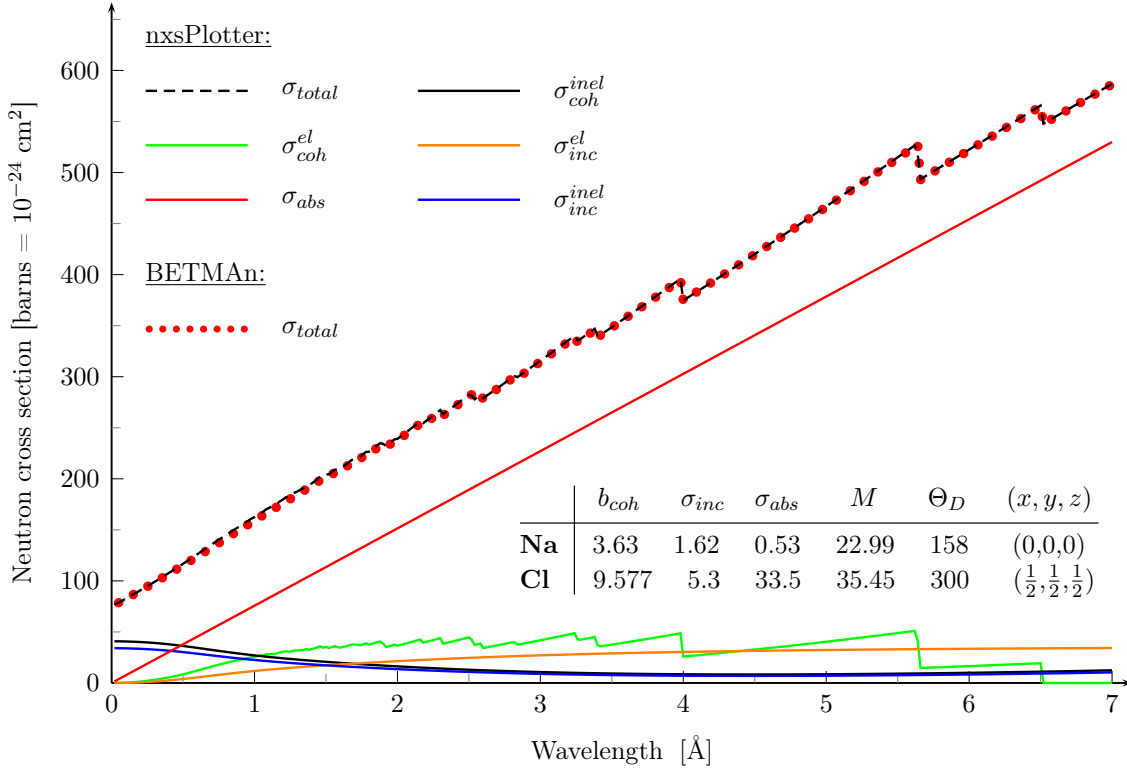


**Figure 3.9.:** Comparison of the neutron cross section calculation in *nxsPlotter* and *BETMAN* by means of a *NaCl* crystal structure.

dividual cross sections, is compared in the diagram. It is evident that both the *nxsPlotter* and the *BETMAN* results agree. Only very small differences occur due an unknown Debye temperature value for Cl. In the present *nxsPlotter* calculation  $\Theta_D = 300$  K was used.

Altogether, this verifies the *nxs* implementation as part of an application of the neutron cross sections. The plotting program can be applied in order to predict the Bragg edge positions and amplitudes within a given wavelength window and for known material parameters. Moreover, the routines implemented in the *nxs* library can be included in further applications. Hence, the code will be used for neutron experiment and instrument simulations, which are described in the following chapters.

### 3.4. Texture Correction

So far, the presented Bragg edge implementation assumes that the sample material consists of a random distribution of crystallographic grain orientations, such as a powder specimen.

The presented algorithms do not consider the relation of the crystallite orientation direction and the sample and instrumentation geometry, i.e. the Bragg edge transmission direction. The influence of preferred crystallographic orientations inside a sample towards the incoming neutron beam direction has been neglected up to now. According to [Brokmeier, 2006], the fraction of engineering materials being single crystals or randomly orientated polycrystalline is very small compared to the materials exhibiting preferred orientations. Hence, it is important to consider the so-called texture influence on Bragg edge transmission experiments. A correction method for the neutron cross section algorithm will be implemented also.

### 3.4.1. The March-Dollase Model

Following the description from [Vogel, 2000], a texture correction may be implemented within the Bragg edge calculation provided by the nxs library. Here, the so-called March-Dollase model [March, 1932; Dollase, 1986] is used to apply changes to the diffracted intensities and therefore to the Bragg edge transmission spectrum as well.

In the case of neutron diffraction, the intensity captured with a detector system varies with the amount of orientated grains inside a polycrystalline sample material. If the grains are not randomly orientated, but have a preferred crystallographic orientation, the probability of detecting them via selected lattice planes differs with respect to their arrangement and therefore to the sample orientation. The March-Dollase equation 3.23 is applied to describe this probability:

$$P(\alpha_{\vec{H}}) = \left( r^2 \cos \alpha_{\vec{H}} + \frac{1}{r} \sin^2 \alpha_{\vec{H}} \right)^{-\frac{3}{2}} \quad (3.23)$$

where  $\alpha_{\vec{H}}$  is the angle between the preferred orientation direction  $\vec{H}$  and the reciprocal lattice vector of the selected reflection [Dinnebier & Billinge, 2008]. In figure 3.10 this relation is drafted. The refinable parameter  $r$  indicates the degree of the texture. For the case of a random orientation, like a powder sample,  $r = 1$ . A convenient method of correcting diffraction intensities for the structure determination is to use the March-Dollase function within a Rietveld refinement of different materials, which is available in many software packages, such as GSAS [Larson & Von Dreele, 2004], Fox [Favre-Nicolin & Černý, 2002], FullProf [Rodríguez-Carvajal, 2001] and MAUD [Lutterotti, 2000]. In principle, the reflected inten-

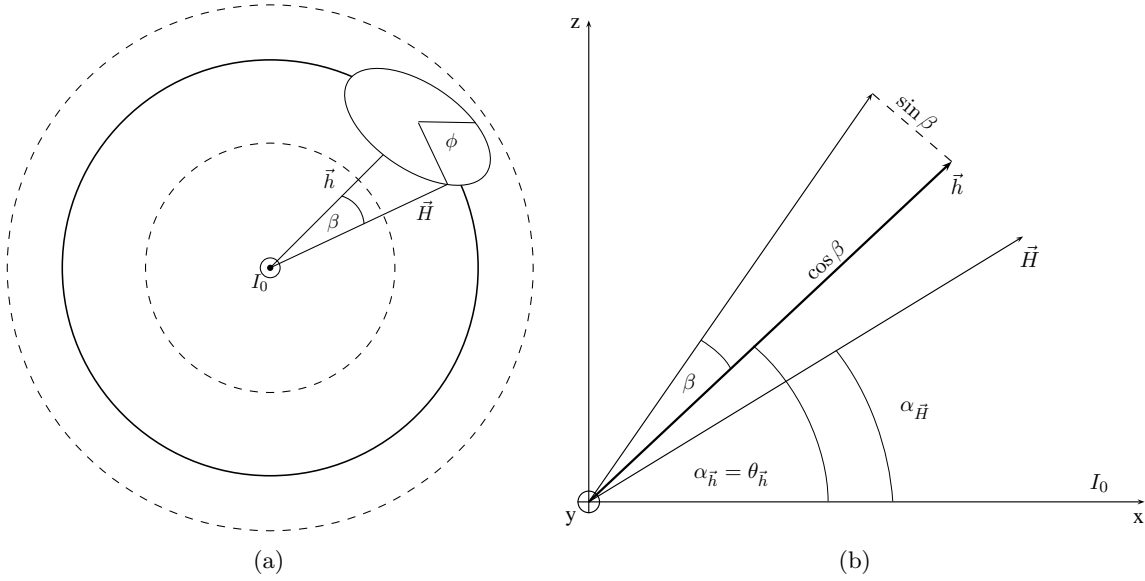


**Figure 3.10.:** The March-Dollase integration path (a) of the preferred orientation  $\vec{H}$  around the diffracting lattice plane normal  $\vec{h}$  as presented by [Vogel, 2000]. In (b), the view is changed to demonstrate the correlation between the utilised vectors and angles. The  $x$ -axis is parallel to the incident beam  $I_0$ .

sities are normalised by the appropriate structure factor and the multiplicity in order to fit them against the March-Dollase equation as a function of scattering angles. According to the Bragg edge transmission geometry, this approach is modified here.

### 3.4.2. Implementation into nxs Library

The March-Dollase model is applied to the transmission geometry to provide a correction for Bragg edge experiments. As the material structure influence on the transmitted intensity is represented by the coherent elastic scattering cross section, a correction factor to equation 3.9 using this probability must be applied. In figure 3.10a, the normal vector  $\vec{H}$  of a preferred crystallographic lattice plane is used to describe the orientation distribution around the sample direction  $\vec{S}$ . Thus, a correction function  $P_{\vec{H}}(\alpha_{\vec{H}})$  with  $\alpha_{\vec{H}}$  being the angle between  $\vec{H}$  and  $\vec{S}$  is used to determine the corrections  $P_{\vec{h}}(\alpha_{\vec{h}}(\lambda))$  for every other lattice reflection  $\vec{h}$ , which are multiplied with  $\sigma_{coh}^{el}$ :

$$\sigma_{coh}^{el}(\lambda) = \sum_{\vec{h}} \sigma_{coh,\vec{h}}^{el}(\lambda) P_{\vec{h}}(\alpha_{\vec{h}}(\lambda)) \quad (3.24)$$

The individual grain orientation angles  $\alpha_{\vec{h}}$  between the preferred orientation axis and  $\vec{h}$  are determined by the application of Bragg's law, as they are perpendicular to the Bragg angle:

$$\alpha_{\vec{h}}(\lambda) = \frac{\pi}{2} - \arcsin\left(\frac{\lambda}{2d_{\vec{h}}}\right) \quad (3.25)$$

Furthermore, a grain with the preferred orientation  $\vec{H}$  can be arranged additionally in any direction with angle  $\beta$  between  $\vec{H}$  and  $\vec{h}$ . Hence, the probability for that grain to be found by the lattice vector  $\vec{h}$  is given by all possible directions of  $\vec{H}$  around  $\vec{h}$  (as visualised by figure 3.10). The variable  $\phi$  parametrises this integration path to provide a description for the probability.

$$P_{\vec{h}}(\alpha_{\vec{h}}(\lambda)) = \frac{1}{2\pi M_{\vec{h}}} \sum_{hkl} \int_0^{2\pi} P_{\vec{H}}(\alpha_{\vec{H}}(\alpha_{\vec{h}}(\lambda), \beta, \phi)) d\phi \quad (3.26)$$

The integration runs over all symmetry-equivalent lattice planes as they have a different angle to  $\vec{H}$ . The multiplicity  $M_{\vec{h}}$  of the reflection  $\vec{h}$  is used to normalise the probability function. For the implementation of this correction, the multiplicity as well as the symmetry-equivalent lattice planes and their  $hkl$  indices are determined during the unit cell initialisation process described in section 3.3.4. The SgInfo library, that is used in this initial stage, already provides functions to calculate these parameters. The March-Dollase model from equation 3.23 can now be applied to reflection-specific probabilities  $P_{\vec{h}}$ , such that the integral becomes:

$$\begin{aligned} P_{\vec{h}}(\alpha_{\vec{h}}(\lambda)) &= \frac{1}{2\pi M_{\vec{h}}} \sum_{hkl} \int_0^{2\pi} \left( r^2 \cos^2 \alpha_{\vec{H}}(\alpha_{\vec{h}}(\lambda), \beta, \phi) + \frac{1}{r} \sin^2 \alpha_{\vec{H}}(\alpha_{\vec{h}}(\lambda), \beta, \phi) \right)^{-\frac{3}{2}} d\phi \\ &= \frac{1}{\pi M_{\vec{h}}} \sum_{hkl} \int_{-\frac{\pi}{2}}^{\frac{\pi}{2}} \left( \left( r^2 - \frac{1}{r} \right) \cos^2 \alpha_{\vec{H}}(\alpha_{\vec{h}}(\lambda), \beta, \phi) + \frac{1}{r} \right)^{-\frac{3}{2}} d\phi \end{aligned} \quad (3.27)$$

which is now depending on  $\cos \alpha_{\vec{H}}$ . Applying the case of a preferred orientation around the incident beam direction, the term  $\cos \alpha_{\vec{H}}$  is calculated by:

$$\cos \alpha_{\vec{H}} = \begin{pmatrix} 1 \\ 0 \\ 0 \end{pmatrix} \cdot \vec{H}(\phi) = \cos \beta_{\vec{h}} \cos \alpha_{\vec{h}} - \sin \beta_{\vec{h}} \sin \alpha_{\vec{h}} \sin \phi \quad (3.28)$$

A detailed derivation of the complete integration path  $\vec{H}(\phi)$  for the March-Dollase model is presented in [Vogel, 2000]. As visualised in figure 3.10, the basic principle for a description of the integration path is given by a circle of radius  $\sin \beta_{\vec{h}}$ , which is rotated and shifted from the direction around the incident beam onto the unit sphere along the normal  $\vec{h}$  of the diffracting lattice plane. The calculation of the matrices describing this transformation is shown in [Vogel, 2000, appendix D]. With a preferred orientation axis parallel to the incident beam, the calculation of the correction factors becomes:

$$P_{\vec{h}}(\alpha_{\vec{h}}(\lambda)) = \frac{1}{\pi M_{\vec{h}}} \sum_{hkl} \int_{-\frac{\pi}{2}}^{\frac{\pi}{2}} \left( \left( r^2 - \frac{1}{r} \right) (\cos \alpha_{\vec{h}}(\lambda) \cos \beta - \sin \alpha_{\vec{h}}(\lambda) \sin \beta \sin \phi)^2 + \frac{1}{r} \right)^{-\frac{3}{2}} d\phi \quad (3.29)$$

According to its implementation, it is useful to describe the numerical way of the integration as there is no analytical solution [Vogel, 2000]. At first  $\sin \beta$  and  $\cos \beta$  are calculated and stored for each lattice reflection including their symmetry-equivalent  $hkl$ , which is achieved by the dot product:

$$\begin{aligned} \vec{H} \cdot \vec{h} &= |\vec{H}| |\vec{h}| \cos \beta \\ \cos \beta &= \frac{a h + b k + c l}{\sqrt{a^2 + b^2 + c^2} \sqrt{h^2 + k^2 + l^2}} \end{aligned} \quad (3.30)$$

where  $a$ ,  $b$  and  $c$  describe the preferred orientation direction  $\vec{H}$ . The integral limits  $[-\frac{\pi}{2}; \frac{\pi}{2}]$  are used to calculate  $N$  discrete points and their values of  $\sin \beta \sin \phi$  and store them into a look-up table. Another pre-calculation is performed using  $M$  values of  $P_{\vec{H}}(\alpha_{\vec{H}})$  with  $\cos \alpha_{\vec{H}}$  inside  $[-1; 1]$  in order to store them within another look-up table.

As  $\alpha_{\vec{h}}$  depends on the neutron wavelength  $\lambda$  (see equation 3.25), the rest of the correction calculation is done in parallel with the neutron cross section determination. Therefore,  $\sin \alpha_{\vec{h}}$  and  $\cos \alpha_{\vec{h}}$  are calculated for each  $\vec{h}$  contributing to the coherent elastic scattering cross section. As a next step,  $\cos \alpha_{\vec{H}}$  is computed using equation 3.28 for each symmetry-equivalent lattice plane. This takes into account the pre-calculated values for  $\cos \beta$ ,  $\sin \beta$  and  $\sin \phi$  which relate to the set of equivalent planes. Using the value of  $\cos \alpha_{\vec{H}}$  as kind of an index for the look-up table of  $P_{\vec{H}}(\alpha_{\vec{H}})$ , the final correction factor — to be applied to the coherent elastic



part (equation 3.24) — can be expressed by the following summation:

$$P_{\vec{h}}(\alpha_{\vec{h}}(\lambda)) \approx \frac{1}{\pi M_{\vec{h}}} \sum_{\beta} m_{\beta} \sum_{i=0}^N \left( \frac{1}{N+1} P(\cos \alpha_{\vec{H},\beta,i}) \right) \quad (3.31)$$

where  $m_{\beta}$  is a multiplicity factor giving the opportunity to speed up the calculation, if symmetry-equivalent planes with the same  $\beta$  have been found before.

### 3.4.3. Summary

The March-Dollase texture correction presented above has been implemented to the nxs library and can be applied to the neutron cross section calculations. By adjusting the March-Dollase factor  $r$ , one is able to describe the degree of the texture [Zolotoyabko, 2009]. Therefore, the nxs library is extended by the `initMarchDollase` and `addTexture` functions. Both provide an interface towards the internal March-Dollase calculation described before. A C struct `MarchDollase` is defined to determine the calculation accuracy (e.g. given by  $M$  and  $N$ ) as well as to store the number of preferred orientations. Furthermore, a C struct called `Texture` is applied to define the orientation parameters. This provides the possibility to setup a preferred orientation direction  $\vec{H} = (a, b, c)$  and its strength. In order to allow the adding of more than one preferred orientation direction to the sample and the `UnitCell` struct respectively, another parameter  $f$  was implemented, which describes the fraction of grains exhibiting one of the given preferred orientations. Uniting these input parameters within in the `Texture` struct, the `addTexture` function can be called to assign the texture parameters to the internal March-Dollase calculation. Finally, the correction factor  $P_{\vec{h}}(\alpha_{\vec{h}}(\lambda))$  is applied to the coherent elastic scattering cross section by calling the `nxsCoherentElasticTexture` function. The total workflow of this application is shown in figure 3.11. As the `nxsPlotter` program is based on the nxs library routines, the texture correction is available in the graphical user interface also. Depending on the correction factor  $P_{\vec{h}}(\alpha_{\vec{h}}(\lambda))$ , the slope on the short wavelength side and the magnitude of a Bragg edge decreases or increases and therefore the texture parameters deform the Bragg edge spectrum. The texture influence on Bragg edge transmission experiments and an application of the March-Dollase correction will be described in chapter 6. There, the differences to the theoretical texture-free neutron cross

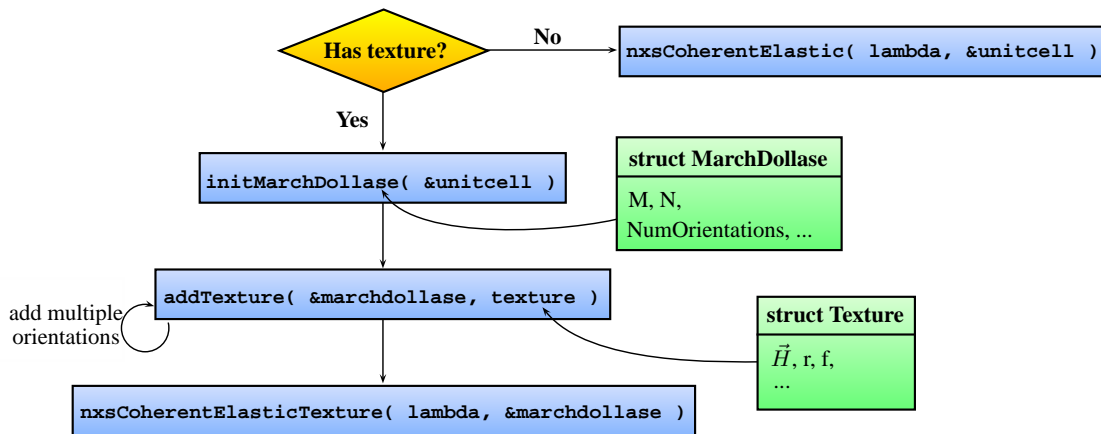


*Figure 3.11.: Workflow of the March-Dollase texture correction using implemented *nxs* library functions.*

section will be visualised. Based on experiments, the simulation of Bragg edges including crystallographic preferred orientations will be validated.

## Neutron Instruments

This chapter describes the principle setups of the neutron instruments used within this work. Foremost, the transmission geometry will be explained. Two instruments, the CONRAD instrument at Helmholtz Centre Berlin (HZB) and ENGIN-X at ISIS, have been used to measure Bragg transmission edges. In addition, the E3 (HZB) and STRESS-SPEC (FRM-II, Munich) diffractometers are also illustrated as both have been used to conduct conventional neutron diffraction measurements. Their experimental results have been applied as reference datasets for a comparison with the Bragg edge method later in this work. The basic principle of these instruments will be shown at this stage.

### 4.1. CONRAD

The CONRAD instrument is designed for tomography, hence, in contrast to diffraction measurements, the transmitted intensities behind the specimen are captured. The attenuation of the primary neutron beam due to the interaction with the sample is the measured variable. Therefore, the basic principle is to place a detector system along the incident beam direction behind the sample. The CONRAD instrument at the BER-II steady-state research reactor in Berlin was built to perform cold neutron radiographic and tomographic experiments. The instrument is located at the end of the curved neutron guide NL1b facing the cold source of the research reactor [Hilger et al., 2006].

#### 4.1.1. High Flux and High Resolution Positions

The flux at the end of the neutron guide is approximately  $2 \times 10^8$  neutrons/cm<sup>2</sup>/s. This so-called high-flux position is used to perform fast (real-time) experiments and high-speed tomography. In [Kardjilov et al., 2005] for instance, an exposure time of 1 ms was achieved to capture radiographic images of a small model aircraft engine with a rotation speed of 6000 rpm. The beam size at this position is approximately  $(3 \times 5)$  cm<sup>2</sup>. The spatial resolution is limited to 300  $\mu$ m while the beam collimation that has been measured in L/D is around 70, where L is the distance between aperture and measurement position and D is the diameter of the aperture. Figure 4.1 shows the simulated wavelength spectrum, that is available at the high-flux position, ranging from 2  $\text{\AA}$  to 12  $\text{\AA}$ .

The instrument is extended by a 5 m collimation flight tube behind the high-flux position. In this way, a second measurement position behind that evacuated tube is used to gain higher spatial resolution by an optimum L/D ratio of 500. Measurements with a resolution up to 100  $\mu$ m and a beam cross section of around  $(10 \times 10)$  cm<sup>2</sup> are possible but with less neutron flux density of  $2 \times 10^7$  neutrons/cm<sup>2</sup>/s [Kardjilov et al., 2009a]. The two measurement positions have been sketched in figure 4.2.

#### 4.1.2. Neutron Energy Selection

In order to enable a neutron energy-selective option, the first high-flux position is replaced by a wavelength-tunable device [Treimer et al., 2006]. The position behind the neutron guide is used to install a double monochromator device for the wavelength selection. As shown in figure 4.3 two highly orientated pyrolytic graphite (HOPG) single crystals are placed always parallel to each other such that first crystal reflects the incident neutron from the upper beam part down to the second graphite crystal. Both monochromator pieces can be rotated according to the Bragg angle  $\theta$  to select a neutron wavelength. The second monochromator crystal is additionally mounted on a linear translation stage which is used to adjust the reflection geometry depending on the opening angle of both crystals. By this means, the neutrons will be reflected back to the original forward beam direction. A shutter is installed to block the lower beam part which is normally used to perform “white” beam imaging

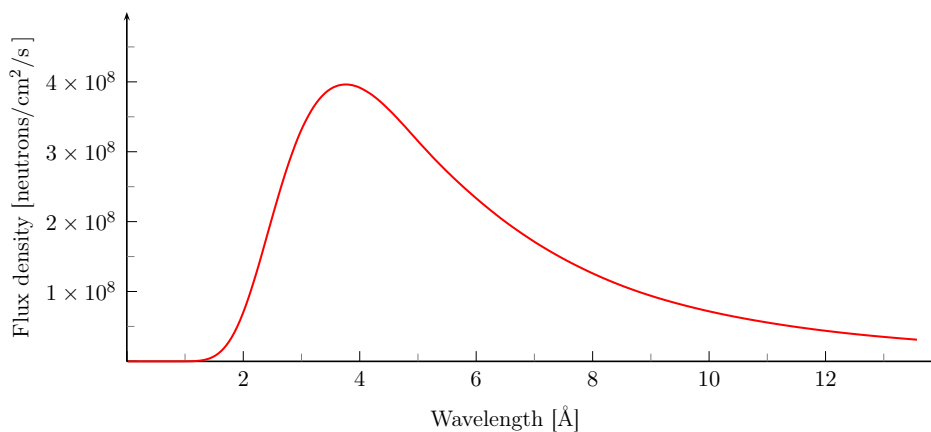


**Figure 4.1.:** The CONRAD beam spectrum at the high flux position behind the neutron guide simulated with McStas.

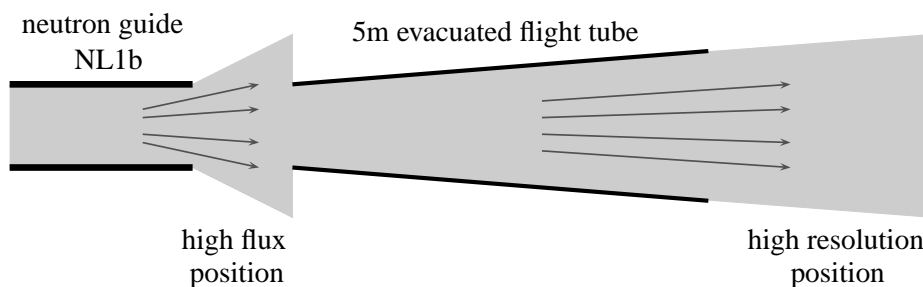


**Figure 4.2.:** Schematic setup of the CONRAD tomography instrument after Kardjilov et al. [2005].

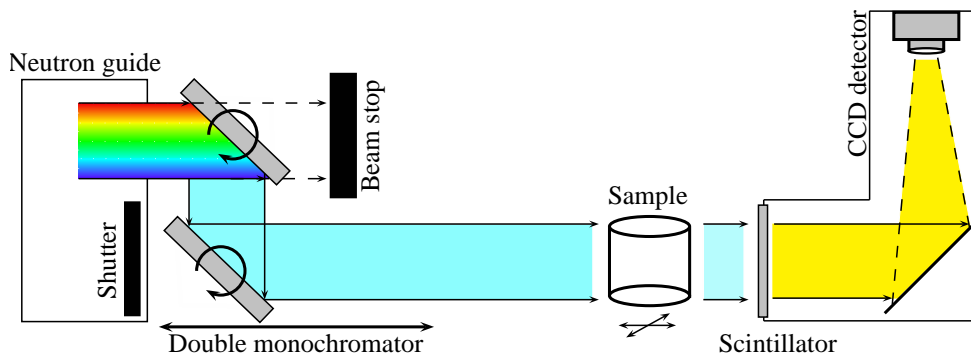


**Figure 4.3.:** The wavelength-selective option on CONRAD: The upper beam part from the neutron guide is used to select neutron energies. The double monochromator setup can be aligned to fulfill the Bragg equation for a selected wavelength by rotating and shifting the monochromator crystals. The chosen wavelength is further used for transmission experiments. The lower beam part as well as transmitted neutrons from the first monochromator will be blocked by a shutter and a beam stop respectively.

measurements, i.e. the full energy spectrum. Consequently, a monochromatic neutron beam selection with a wavelength resolution of  $0.01 < \Delta\lambda/\lambda < 0.1$  between  $2 \text{ \AA}$  to  $6.5 \text{ \AA}$  is realised. This setup changes the beam size at the detector stage to approximately  $(6 \times 18) \text{ cm}^2$  and the flux between  $2 \times 10^4$  and  $10^5$  neutrons/cm<sup>2</sup>/s depending on the selected wavelength. The beam position is not affected significantly by this setup, i.e. the detector system can be mounted at the same place as before. Only, the horizontal beam spread and therefore the intensity distribution on the detector screen will vary according to the selected opening angle of the monochromator system.

Using this double monochromator setup, one is able to perform neutron wavelength-dependent transmission experiments. By aligning the monochromator positions for each step of a measurement, wavelength scans can be performed to capture the Bragg edge spectrum of a crystalline sample material. The energy-dependent neutron flux, i.e. the incident intensity variation, is then corrected for each wavelength step by normalisation with flatfield images taken at the same wavelength position but without the sample. Additionally, there is the option to perform polarised neutron imaging experiments, which makes the instrument even more a multi-purpose instrument. In Kardjilov et al. [2008] for example, a neutron spin polariser and analyser have been used to filter the spin components in the neutron beam. Thus, the magnetic field inside a sample has been analysed by taking radiographic images. The thesis of Hilger [2009] covers this topic.

#### 4.1.3. Data Analysis

The intensity of the transmitted neutrons is captured by an Andor DW436N-BV CCD camera with  $2048 \times 2048$  pixels of  $(13.5 \times 13.5) \mu\text{m}^2$  size each. But before, optical elements and a converter screen have been installed to capture the transmitted neutron intensity. A ZnS/<sup>6</sup>Li scintillator screen is used to re-emit the absorbed energy from the incoming neutrons in the form of visible light [Baechler et al., 2002]. To shield the CCD camera and its electronics from transmitted neutrons the converted light is additionally reflected upwards by a mirror into a 50-mm-focus Nikon camera lens. The right part in figure 4.3 visualises this principle. This setup is about to be improved to gain even better resolution, which is

realised mainly by another neutron converter screen. In Kardjilov et al. [2009b], a 10  $\mu\text{m}$  Gadolinium Oxide Scintillator (Gd<sub>2</sub>O<sub>2</sub>S(Tb)) scintillator screen in combination with a 200-mm Nikon macro camera lens was tested to provide a 1:1 projection of the neutron signal to the CCD camera. Thus, a resolution of around 25  $\mu\text{m}$  will be achieved. Due to the camera images taken, the evaluation of radiographic and tomographic experiments is related to image processing. For example, the first analysis step is usually to perform dark- and flatfield correction as introduced by equation 2.4. Thus, the wavelength-dependent intensity variations as well as the inhomogeneous illumination of the camera picture can be normalised. Afterwards, the transmission signal can be visualised by means of each image pixel and evaluated with further signal processing routines. Within this thesis, the free Java-based image processing and analysis program ImageJ [e.g. Collins, 2007] has been used. This software is available from its project website<sup>1</sup> and provides a broad spectrum of features. It reads many image formats and is able to handle even raw image camera data. Further, the program applies filters and standard image processing algorithms. Another useful aspect is the ability to create own plugins and run macros over multiple images.

## 4.2. ENGIN-X

In addition to the tomography machine presented above, there is also the possibility to take advantage of a neutron time-of-flight signal to analyse Bragg transmission edges. Following this approach the materials engineering neutron diffractometer ENGIN-X at ISIS in Didcot, UK, will be presented here.

### 4.2.1. Instrument Setup

The ENGIN-X instrument is concerned with research into residual stress [Dann et al., 2003, 2004] and studies of thermodynamical properties of engineering materials (see ENGIN-X website<sup>2</sup>). In contrast to a fission reactor the ISIS spallation source provides a pulsed neutron beam via accelerated protons hitting a target material of high atomic mass. Using a 100 K liquid methane moderator, the neutrons on ENGIN-X are thermalised to provide a wavelength

---

<sup>1</sup><http://rsbweb.nih.gov/ij/>, ImageJ

<sup>2</sup> <http://www.isis.stfc.ac.uk/instruments/engin-x/engin-x2900.html>, ENGIN-X, ISIS

spectrum of approximately  $0.5 - 6 \text{ \AA}$  with a high-flux range over  $1 - 3 \text{ \AA}$  [Santisteban et al., 2006a] and a total integrated flux density of about  $1.4 \times 10^6 \text{ neutrons/cm}^2/\text{s}$  [Kockelmann et al., 2007a]. The incident neutron beam spectrum at the sample table position is shown by figure 4.4. The diffractometer takes advantage of the neutron time-of-flight signal to analyse the detected neutron intensity. For neutron diffraction measurements the instrument has been equipped with two detector banks located 1.5 m away from the instrument focus and perpendicular to the incident beam direction, both fixed at  $\pm 90^\circ$ . These so-called north and south detector banks consist of 1200 ZnS/ $^6\text{Li}$  scintillator detector elements each, arranged in order to cover an angular span of  $76^\circ \leq 2\theta \leq 104^\circ$  horizontally and  $\pm 21^\circ$  vertically. The scintillators are monitored via fibre optics using photo-multiplier tubes. Triggered with the neutron pulse frequency, the detector elements measure the neutron intensity against the time-of-flight signal, which is combined with the incident path length of 50 m moderator-sample distance to resolve the neutron energies and wavelengths respectively. Figure 4.5 illustrates the instrumental setup. The diffractometer control as well as the experimental data analysis is based on the OpenGenie software [e.g. James et al., 2004]. By means of this program, one is able to perform measurements using a command line as well as script-based data evaluation and visualisation of the experiment results. According to this, peak fitting and structure refinement routines have already been implemented to be applied to the measured diffractogram data. In this work, the OpenGenie routines have been used to extract individual intensity spectra from the transmission detectors.

#### 4.2.2. Transmission Detectors

In addition to the two detectors described above the ENGIN-X diffractometer is equipped with a third detector system along the beam direction behind the sample position, i.e. in transmission geometry at a Bragg angle of  $\theta = 0^\circ$ . This pixelated transmission detector is composed of a  $10 \times 10$  array of  $(2 \times 2) \text{ mm}^2$  time-of-flight detector elements, on a vertical and horizontal pitch of 2.5 mm [Santisteban et al., 2002b]. Again, fibre optics light guides transmit scintillated light to Hamamatsu H6568 photo-multiplier tubes [Santisteban et al., 2003]. Analysing the time-of-flight signal similarly to the diffraction banks via the scintillation detector elements, the transmitted signal can be used for Bragg edge studies, as the full



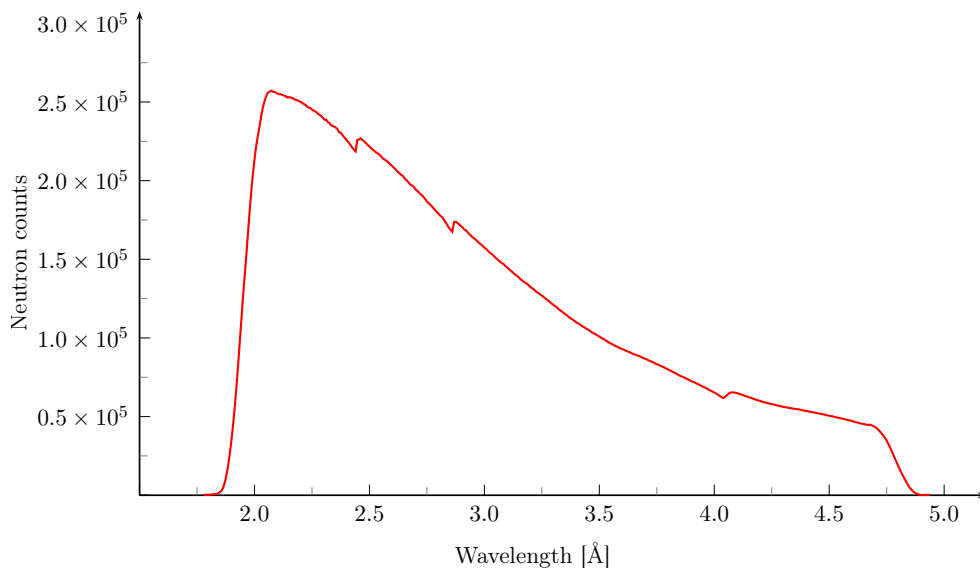


**Figure 4.4.:** *The ENGIN-X neutron beam spectrum measured by the transmission detector. The discontinuities in the spectrum occur due to the transmission through aluminium windows of the evacuated beam guide.*

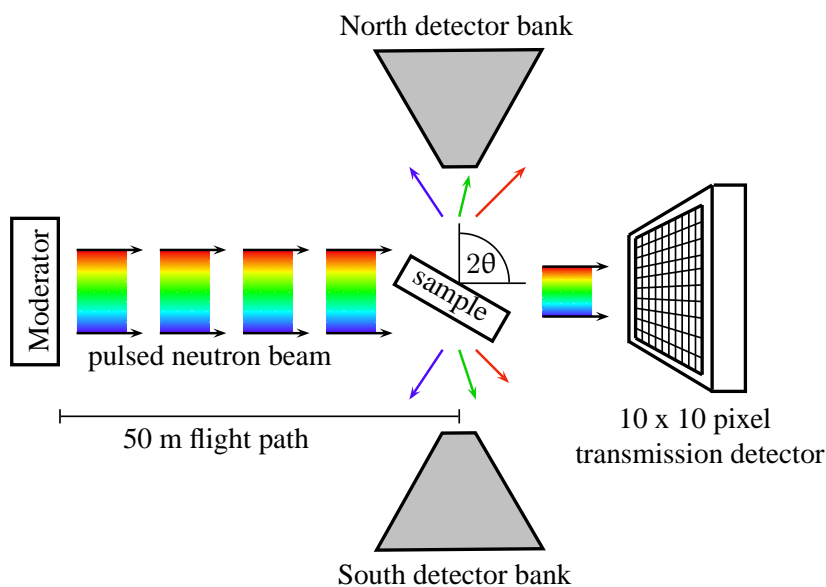


**Figure 4.5.:** *The ENGIN-X setup: Thermal neutrons are provided by the liquid methane moderator. Two time-of-flight detector banks and a pixelated time-of-flight detector array capture the diffracted and transmitted neutron intensity respectively.*

spectrum will be monitored. Although the detector array consists of 100 pixel elements only and the spatial resolution is very low compared to the CONRAD tomography machine — considering the pixel size and the gaps between, the resolutions differ in two orders of magnitude — this system equally enables the detection of local differences in the transmitted

beam spectrum depending on the sample properties. Moreover, the time-of-flight technique provides a better wavelength resolution given in terms of lattice spacing precision of  $\Delta d/d = 10^{-4}$  [Steuwer et al., 2003] which makes it more accurate for determining Bragg edge positions than the CONRAD instrument. In Steuwer et al. [2003] for example, this setup has been used for in-situ uniaxial tensile loading experiments. The interplanar lattice distances have been determined by measuring the Bragg edge transmission spectrum of textured and untextured specimens subjected to different loading conditions. Furthermore, the feasibility of using this transmission method for quantitative phase analysis was shown by Steuwer et al. [2004] and Santisteban et al. [2003].

A second instrument following the same approach of measuring time-of-flight neutron transmission signal is available at LANSCE, Los Alamos USA. A review of the instrument including a comparison with the ENGIN machine, the predecessor of ENGIN-X, is available in Santisteban et al. [2002c].

### 4.3. Bragg Edge Measurement Alternatives

The transmission geometry enables further possibilities to perform Bragg edge measurements. In the presentation of Strobl [2009] for example, the transmission geometry of a new VSANS instrument at HZB was used to capture Bragg edges. A chopper-based time-of-flight system was applied to cut the neutron spectrum from the continuous cold source at selected wavelength positions. The time window between the chopper discs is aligned to the neutron velocity and therefore to the neutron wavelength of interest. The chopper disc rotation velocity is adjusted step by step to enable a wavelength scan for Bragg edge transmission experiments. Another conceptual method was proposed by Tamaki [2005]. A series of single crystals with different orientations and mosaicities as well as super-mirrors and Bragg cut-off polycrystals shall be positioned in the primary beam to filter selected energies (and energy bands). By means of this setup and similar to the filtering of digital signals [Smith, 1999], a wavelength selection from the incident beam spectrum can be reached. Both applications have not been used in this thesis as they are still under development and not available compared to the presented instruments.

## 4.4. E3 & STRESS-SPEC Diffractometers

In contrast to the instruments presented above, the E3 and STRESS-SPEC diffractometers are designed to perform neutron diffraction experiments only. Both instruments are almost identical in construction. They are dedicated to measurements of residual stress in engineering materials [Wimpory et al., 2008; Hofmann et al., 2007]. Due to the similar setup, the instrumentation principles are presented by means of the E3 diffractometer. Relevant differences between both instruments will be stated.

### 4.4.1. Construction

Figure 4.6 shows a schematic drawing of the E3 diffractometer at the BER-II research reactor, Berlin. The instrument is placed at the neutron tube T3 [Poeste et al., 2006]. A monochromator is used to select a single wavelength from the incident polychromatic neutron beam. Here, a vertically focusing and horizontally bent perfect Si monochromator [Mikula et al., 1992; Kulda et al., 1992] is applied. The monochromator device consists of 5 vertically arranged Si(100) crystal rows providing neutrons with  $1.48 \text{ \AA}$  wavelength [Wimpory et al., 2008]. Additionally, the STRESS-SPEC diffractometer is equipped with a monochromator changer. Thus, Ge(311), Si(400) and PG(002) crystals can be applied to provide wavelengths from  $1 - 2.4 \text{ \AA}$ . This is useful to cover a broad spectrum of materials to be analysed. Moreover, the different monochromator crystal properties enable possibilities to measure multiple sample characteristics. For example in section 6.1, the higher beam divergence of the Ge(311) monochromator has been applied to investigated texture, for which it is not important to have low divergence and a precise monochromatic beam but to maximise the neutron flux at the sample. Both instruments provide the opportunity to obtain better resolution using collimators behind the monochromator. The diffractometers are provided with omega circles to rotate the sample stage. Upon linear horizontal (x and y) and vertical (z) translation tables are installed to move samples with a maximum load of 300 kg. Additional goniometers and Eulerian cradles can be installed on the translation table to measure all kinds of orientation without dismounting the sample [Poeste et al., 2006]. Towards the definition of the gauge volume, primary and secondary slit systems are applied before and behind the sample respectively. Available slit dimensions are of  $0.5 - 5 \text{ mm}$  in vertical and horizontal

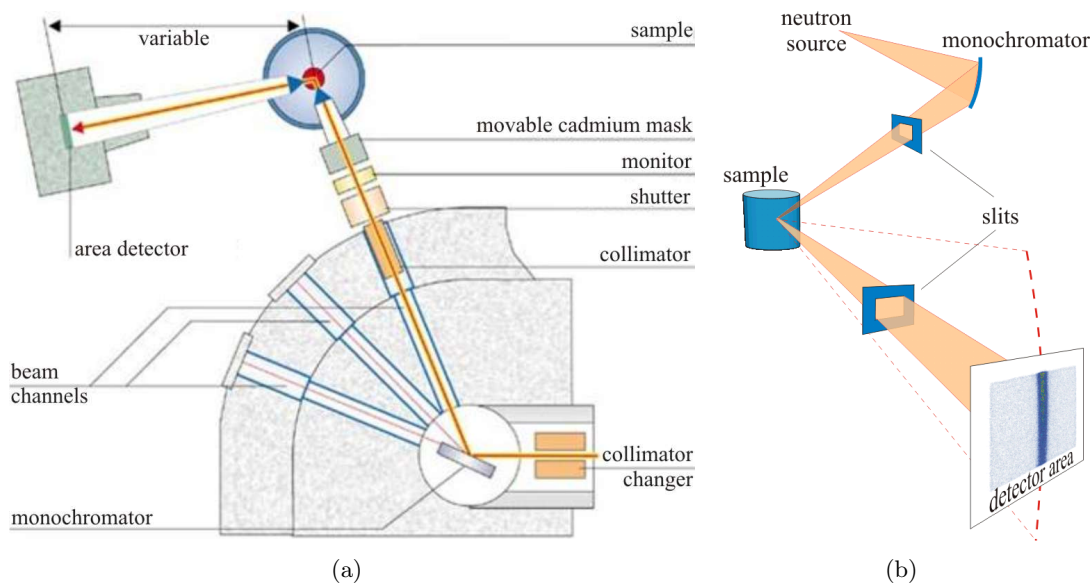


**Figure 4.6.:** Schematic drawing (a) and detection principle (b) of the E3 diffractometer.

direction. Matchstick slits with a maximum dimension of 20 mm also exist. Thus, local and global sample characteristics can be measured. Finally, the scattered neutrons will be measured by a  $^3\text{He}$  position-sensitive area detector, connected to a  $2\theta$  motor in order to drive the detector to a selected sample reflection. On E3,  $256 \times 256$  channels within an area of  $(300 \times 300) \text{ mm}^2$  distinguish the detected neutron positions. A variable sample-detector distance of up to 1500 mm defines the angular range captured on one  $2\theta$  position. Thus, it is possible to measure reflections within a maximum range of  $35^\circ$  to  $110^\circ$ . The STRESS-SPEC detector is smaller ( $200 \text{ mm} \times 200 \text{ mm}$ ). Nevertheless, it is equipped with the same number of channels. Hence, slightly different parameters must be considered within the analysis of the experiment data. Another monitor before the sample exists to detect the incident intensity. Thus, measurements that take account of the neutron count rate can be conducted. A third monitor is available behind the sample to measure transmitted neutrons.

#### 4.4.2. Software

Both machines, E3 and STRESS-SPEC, are controlled by the CARESS<sup>3</sup> software to drive monochromator, slit, sample and detector motors. Furthermore, the CARESS data file for-

<sup>3</sup>[http://www.helmholtz-berlin.de/intern/betrieb/experimentsysteme/aufbau-eines-systems/caress\\_de.html](http://www.helmholtz-berlin.de/intern/betrieb/experimentsysteme/aufbau-eines-systems/caress_de.html), CARESS project website

mat is used to store the detector images and the appropriate instrument parameters as well as the sample orientation. Due to the diffraction geometry Debye-Scherrer ring sections (in the case of polycrystalline samples) will be captured in the detector image, such as shown in figure 4.6b. Usually, the intensity of these rings is summarised to obtain a reflection peak from the current measurement position. For example, the strength of the peak intensity as well as its position can be interpreted to reveal individual sample properties. For this purpose, two programs are available to evaluate the images of the detector signal. The TVtueb [Hoffmann et al., 2003] and StressTexCalculator [Randau et al., 2011] software enable the possibility to fit the diffracted neutron intensities using the stored raw data. Both are able to read the CARESS data format. The latter is to be advanced permanently and has been applied within this thesis. Using the conventional and well established neutron diffraction method, the instruments have been used to provide reference datasets for samples investigated in this work. Thus, the following Bragg edge transmission investigations will be compared with reliable results.



## **Development of a Bragg Edge Experiment Simulation**

In the previous chapters, the implementation of Bragg edge calculation algorithms within a C library has been realised. By means of the stand-alone plotting program `nxsPlotter`, the specific material properties have been applied as input parameters. Thus, the ability to plot theoretical Bragg edge spectra by the application of the neutron cross section calculation routines has been shown. Furthermore, different instruments being able to measure Bragg edge transmission spectra have been presented. In this chapter, the `nxs` program library will be used to extend an existing neutron ray-tracing software package to simulate Bragg edge transmission experiments. Towards the application of Monte Carlo simulations, the `McStas` program package will be described. Simulations based on the development of a new virtual Bragg edge sample component will be realised. The Bragg edge sample component will be created and applied within virtual implementations of real neutron instruments. By means of substantial testings, the individual influences of instrumental parameters to the Bragg edge transmission pattern will be investigated.

### **5.1. McStas - Neutron Ray-Tracing Simulation**

The `McStas` neutron ray-tracing package is a code for the simulation of neutron scattering experiments and instruments [Lefmann & Nielsen, 1999]. It is an ongoing project which is conducted at Risø National Laboratory, Denmark and the Institute Laue-Langevin in Grenoble, France. This section introduces the basic principles of a `McStas` neutron simulation.

### 5.1.1. Scientific Background

McStas is the abbreviation for “Monte Carlo Simulation of Triple Axis Spectrometer” [Nielsen, 1998] and the code was initially developed to create executable Monte Carlo ray-tracing algorithms for triple-axis spectrometers and similar neutron instruments. Monte Carlo methods refer to a class of algorithms that rely on repeated random sampling to determine a final result. The name “Monte Carlo” is a reference to the Monte Carlo Casino, Monaco [Metropolis & Ulam, 1949] and refers to the randomness and repetitive nature of gambling processes inside a casino. The Monte Carlo technique is an application of the law of large numbers [James, 1980]. In order to determine a discrete statistical mean value depending on a number of parameters, all parameters are sampled randomly within an interval. By means of a series of computations, the discrete value converges to the mathematical mean value of the same interval, described by a continuous integrable function. However, Monte Carlo methods are applied when analytical descriptions are not known, not valid or too complex. Using (pseudo-) random generators these algorithms are most conveniently applied on a computer. Monte Carlo simulations are very useful for problems with a large degree of freedom. Thus, for example the implementation of neutron instrument simulations is suited to the application of Monte Carlo methods.

McStas enables the possibility of analysing experimental data from existing instruments as well as designing, optimising and upgrading instruments and their components [e.g Farhi et al., 2002; Lieutenant et al., 2005]. Moreover, instrumental parameters and setup configurations can be simulated in advance of real experiment runs. The software package has been steadily customised to the users’ demands. For example even polarised neutron experiments can be simulated using McStas. More of its features will be described in the following.

### 5.1.2. Program Features

Although there are other neutron simulation packages available such as, e.g. VITESS [Lieutenant et al., 2004], NISP [Seeger & Daemen, 2004] and RESTRAX [Šaroun & Kulda, 1997], it was decided to use the McStas framework for the implementation of a Bragg edge experiment. Here, a few program features will be mentioned to justify this decision.



- Open-source project, platform-independent
- Large component library
- Multiple output formats
- Parallel computing
- User support

The McStas program can be obtained from its project website<sup>1</sup> and is distributed under the GNU General Public License (GPL), i.e. its source code is available also. In particular, this is very useful in order to develop new components, such as the Bragg edge simulation, and extend the McStas library. Another useful feature is, that McStas has been found to run on all existing computer systems, such as Unix/Linux, Windows, MacOS [Willendrup, 2004]. The existing library contains a lot of components, such as neutron sources, samples and detection monitors, that are ready to use for a virtual experiment. Furthermore, the simulated data can be stored in various output formats to analyse and visualise the experimental results. The Matlab, Scilab and PGPLOT formats are only a few possibilities to handle the data. In addition to that, it is also possible to self-define own output formats for other programs. The McStas software package also allows parallel computing, i.e. each simulated neutron can be processed by a different cpu. Nowadays, even desktop computers have multiple processors (or cpu cores), that can be used to decrease the simulation time. The McStas manual [Willendrup et al., 2008] provides detailed information about the different possibilities of parallel computing. The McStas command line and GUI tools have these options included already. Finally, there is a mailing list available to contact the developer team and other users also for any kind of support concerning the McStas simulation. Users can also contribute their ideas and modules to the neutron diffraction community.

### 5.1.3. Simulation Workflow

In the following the McStas workflow will be described to provide an understanding of the simulation principle. As presented above, multiple components are available to define a neutron experiment or instrument simulation. These modules have to be arranged inside

---

<sup>1</sup><http://www.mcstas.org/>, McStas - A neutron ray-trace simulation package

a so-called instrument definition file, which is used to run a simulation. As McStas is a ray-tracing tool, a single neutron will be generated at the beginning and sent through all following components to the end of the instrument definition. This will be processed until the maximum number of neutrons to be simulated (given as an input parameter) has been reached. As a result, one is able to trace each single neutron through the virtual experiment. The neutron generation is usually handled by a source component, that is placed normally at the origin of the coordinate system. Within this component, a single neutron will be created with a state vector  $(x, y, z)$ , a velocity vector  $(v_x, v_y, v_z)$ , a time  $t$ , three spin parameters  $(s_x, s_y, s_z)$  and a so-called neutron weight factor  $p$ , which is applied and described in detail in section 5.2.2 (equation 5.3). Depending on the simulated source nature and its input parameters neutrons with different so-called state parameters are generated to be used with further components. Thus, a Maxwellian wavelength distribution can be simulated by inserting the `Source_Maxwell_3` component for example. Afterwards, each created neutron is sent to the next component. In the simple setup of figure 5.1 a sample component is placed after the source component to handle scattering events for all incoming neutrons. As for most of the McStas library components, at first it will be checked whether the neutron really hits the sample, depending on its geometry, or if it is passed. Here (see figure 5.1), the sample's intended purpose is to simulate neutron scattering. Therefore, the neutron state parameters will be changed by the calculation of physical laws inside the sample. In particular, the state vector and the velocity vector will be changed according an individual scattering event inside the sample. By this means, the direction and position of the current neutron is changed. Moreover, the neutron velocity and spin parameters can be changed here. Subsequently, the neutron will be sent to the next component module within the instrument definition file. This happens for each simulated neutron regardless of scattering or passing. Due to the check at the beginning of each component, the correct neutron beam path is guaranteed. As long as a neutron is not absorbed by a component, it will be sent to the end of the instrument definition. Finally, the neutron will be captured by a detector component, that collects the neutron properties of interest for further evaluation. Thus, wavelengths, spatial distributions, time-of-flight signal or polarisations can be analysed using the appropriate monitor component.

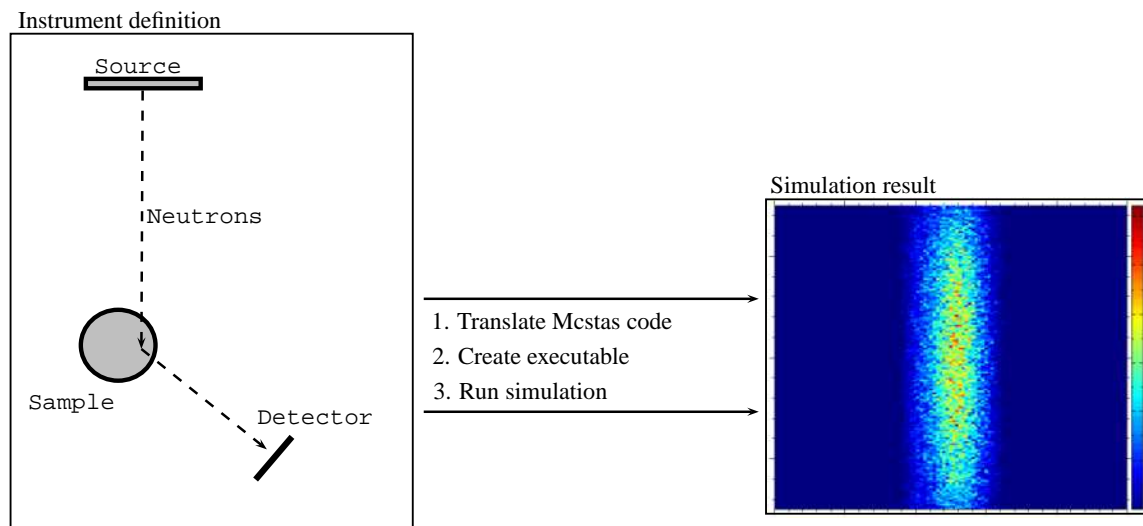


**Figure 5.1.:** Workflow and design steps of McStas (from left to right): Inside an instrument definition file the experimental components are arranged. The instrument file is used to create a simulation program. With the help of the McStas plotting tools the simulation results can be visualised.

Completing the instrument definition, one is able to translate the instrument file from its McStas code into a C program. Then, the C code is compiled to an executable simulation program. These steps are handled by the McStas tools, which are available as part of the McStas GUI as well as from the command line. The simulation can now be started with chosen input parameters, such as the number of neutrons to be simulated or the output format of the resulting files. Thus, the compiled executable can be used for multiple simulations with different parameters. Only, once the instrument definition is changed the simulation program needs to be re-compiled. The simulation results, for example the neutron intensity distribution captured by a position-sensitive area detector can also be visualised by the McStas tools, such as shown in figure 5.1.

## 5.2. Bragg Edge Simulation

The McStas neutron ray-tracing package was chosen to provide a simulation tool being executable on common computer platforms and applicable on different (virtual) instruments and neutron sources. Based on the neutron cross section calculations described in section 3.2, it was decided to create a new McStas sample component. Within Monte Carlo algorithms,

probabilities are commonly used to describe microscopic physical processes [Willendrup et al., 2008]. Hence, the implementation of neutron cross sections in McStas towards the individual neutron event propagations is a suitable method. In order to simulate Bragg edge neutron transmission, the dependence on sample properties and materials parameters must be realised. Therefore, the change of the neutron transmission signal will be handled by the implementation of the neutron cross calculation routines into a sample module. Instrumental parameters effecting the transmission spectrum will be applied and tested afterwards.

### 5.2.1. A McStas Sample Component

Although there are a lot of components for different purposes available, there was no Bragg edge transmission module in the McStas library. As mentioned above McStas is an open source project. The instrument definition and library component files are written in a C-like meta language allowing C commands to be used for calculations. Thus, a new Bragg edge component has been created to implement the transmission behaviour for the range of cold and thermal neutrons. In order to give an understanding of the workflow inside a sample component and to prepare the implementation of the Bragg edge simulation, an introduction to a McStas module will be provided in the following. Afterwards, the structure of a sample component is used to embed the neutron cross section calculation routines (nxs library) in the simulation. Consequently, the main program parts described here are provided with listings.

In principle, a McStas component definition is divided into four parts. At first, a header information marks the beginning of a component using reserved keywords. For example, the component name for a new Bragg edge component can be given by

```
DEFINE COMPONENT BraggEdge_Powder
```

This component is accessed from within an instrument definition file by calling the name `BraggEdge_Powder`. The McStas translation process then looks for the component file named `BraggEdge_Powder.comp`. Hence, the component file should have the same name. Associated with the header are the input and output parameters as well as their predefined default values and the neutron state parameters (section 5.1.3), that will be accessible from all following sections inside the component definition.

```
DEFINITION PARAMETERS ( string space_group="229" )  
SETTING PARAMETERS ( double xwidth=0.05, double yheight=0.05, double  
zthick=0.05 )  
STATE PARAMETERS ( x,y,z,vx,vy,vz,t,s1,s2,p )
```

Moreover, the component is defined by different sections. Summarising the **DECLARE**, **SHARE** and **INITIALIZE** section, one is able to declare global variables, define functions that will be shared by the whole simulation code (particularly important if more than one instance of the component will be used) and initialise parameters. **INITIALIZE** is executed only once at the beginning of the simulation [Willendrup et al., 2008]. As a third part, there is a **TRACE** section to compute the interaction between each neutron and the component. Using appropriate calculations, the neutron state parameters will be changed inside this program part. This section is executed for each incoming neutron. Concerning a Bragg edge transmission sample component, the wavelength-dependent neutron cross section calculation routines (see implementation in section 3.3) will be called within this program section. Section 5.2.2 gives more details about the Bragg edge implementation in McStas. As stated before, the C syntax and calls will be used for these calculations as the complete code will be translated to ANSIC anyway. Finally, McStas provides the closing **SAVE**, **FINALLY** and **MCDISPLAY** component sections to complete the simulation process. Thus, it is possible to monitor the simulated neutron intensity for example and save it to a file. Furthermore, results can be printed and the component itself can be visualised by a drawing which is helpful in order to debug the simulation and trace the neutron trajectory.

### 5.2.2. Library nxs Insertion

The Bragg edge transmission calculations from chapter 3, which have been implemented and compiled into a C library (chapter 3.3) will be used here to perform McStas neutron simulations. Following the scheme of a standard McStas sample component, the implementation steps for a new sample module shall be described here. As the calculation routines have already been implemented, the nxs library is included within the final simulation program. Hence, the library header file **nxs.h** is embedded using the **include** command inside the **SHARE** section.

**SHARE**

```
%{  
  %include "nxs.h"  
  ...  
%}
```

The header file<sup>2</sup> as well as the library file called `libnxs.a` must be located in the same directory as the component. The final instrument definition file that includes the Bragg edge sample component is then translated and compiled by embedding the library file and extending the include and library search paths. This is handled by the command line tool `mcrun`, for instance.

```
mcrun -c -I. -L. -lnxs InstrumentDefinition.instr
```

The **DECLARE** section provides global variables that will be used for the simulation process. By this means, a variable to describe the neutron wavelength for example is declared here, but calculated later. Similarly, the declaration of the unit cell variable is done within this program part. It was stated in section 3.3.4 that a few parameters must be initialised prior to the actual neutron cross section calculation, e.g. lattice spacing parameters, structure factors and the unit cell volume. As this has to be performed only once, the unit cell initialisation, including the parameters describing the crystal lattice and atom properties, is called by the **INITIALIZE** part of the sample component. Here, the `nxs` initialisation functions will be applied.

**INITIALIZE**

```
%{  
  ...  
  initUnitCell( &unitcell );  
  addAtomInfo( &unitcell, atominfo );  
  initHKL( &unitcell );  
  ...  
%}
```

This program section is used to determine the sample geometry based on the input parameters. For example, by means of predefined McStas library functions, the sample size is calculated in order to prepare the neutron-matter interaction within the appropriate sample dimensions. Also, neutron-independent values can be pre-calculated here, which saves

---

<sup>2</sup>The `sginfo.h` header from the SgInfo library (see section 3.3.3) must also be located in a directory known to the compiler as it is included by the `nxs.h` header file.

computing time, because the subsequent program part will be executed for each simulated neutron individually.

Finally, the **TRACE** section calculates the actual interaction between neutron and component. This computation is repeated for each generated neutron. Before interacting, each neutron is tested whether it penetrates the sample volume or not. At the same time the sample entrance and exit points in terms of intersection times are determined on the basis of the neutron state and velocity vectors and the sample geometry parameters. Here, the internal McStas **box\_intersect** or **cylinder\_intersect** routines, depending on the sample geometry determined before, have been applied. If an incoming neutron hits the sample further calculations are applied. Otherwise, it passes the current component and skips the following procedures. At first, the neutron velocity  $v$  is calculated by means of its velocity vector and transformed to the wavelength  $\lambda$ .

$$v = |\vec{v}| = \sqrt{v_x^2 + v_y^2 + v_z^2}; \lambda = \frac{h}{m_n v} \quad (5.1)$$

The neutron velocity is used to calculate the full transmission path  $l$  through the sample with the intersection times  $t_1$  and  $t_2$ , which is related to the sample thickness.

$$l = v (t_2 - t_1) \quad (5.2)$$

In order to calculate the attenuation coefficient and the transmission probability, the individual nxs cross section functions implemented in section 3.3.5 can now be applied to the simulation.

```
TRACE
%{
...
double xssect_total = nxsCoherentElastic( lambda, &uc ) +
                      nxsIncoherentElastic( lambda, &uc ) +
                      nxsCoherentInelastic( lambda, &uc ) +
                      nxsIncoherentInelastic( lambda, &uc ) +
                      nxsAbsorption( lambda, &uc );
%}
```

The total neutron cross section value is applied to the attenuation coefficient calculation (equation 3.3) in order to determine the transmission probability expressed by equation 3.2.

To simulate the transmission intensity, McStas supports two different ways to handle the neutron interaction. It is obvious to remove a neutron from the simulation trajectory if it should be absorbed by the sample component. Therefore, one could compare the calculated transmission probability with a randomly generated value between 0 and 1. Then, a neutron is absorbed if the generated value is bigger than the calculated probability and transmitted otherwise. McStas provides the macro function **ABSORB** to remove the current neutron and continue the simulation with the next neutron from the beginning of the instrument definition. The final neutron intensity is then determined by the non-absorbed neutrons only. A second way to calculate the transmission intensity is to take advantage of the neutron weight parameter  $p$  introduced in McStas [Willendrup et al., 2008, section 4.2]. The transmission probability  $p_{tr}$  can simply be used to change the initial neutron weight  $p_0$ :

$$p = p_0 p_{tr} = p_0 \exp(-\mu l) \quad (5.3)$$

Thus, every neutron is allowed to transmit through the sample. The final intensity, captured by a McStas monitor component for example, will then be evaluated taking the neutron weight parameter into account. This method speeds up the simulation as it improves the statistics with the same amount of neutrons.

### 5.2.3. Input Files

The Bragg edge simulation requires the knowledge of sample parameters. On the one hand, the sample geometry is given as for most McStas components by its width, height and thickness to define a cuboid object. Alternatively, a cylinder shape can be chosen by setting a radius and height variable. The geometry definition is done in the instrument file at the stage of its instantiation.

```
COMPONENT sample = BraggEdge_Powder(  
  xwidth = 0.02, yheight = 0.02, zthick = 0.01,  
  filename = "Fe.txt"  
) AT (0, 0, 1) ABSOLUTE
```

On the other hand, material parameters are needed to calculate the Bragg edge effect. As described before, unit cell parameters and atomic properties will be used to compute neutron



cross sections. One possibility would be to extend the number of input parameters for the Bragg edge sample component by each variable listed in section 3.3.2. For the case of multi-atomic material compositions, this would lead to an immense number of input variables. Therefore, it was decided to encapsulate the input values to an input file. In the example above, the file `Fe.txt` is used to provide the necessary parameters. A complete listing of such a file demonstrating an iron structure is given in the appendix C.2.

The parameter file is stored as a text file with a format to be read using the McStas data file reading routines, which are also supported by the McStas library. Applying the file reading functions, one has to include the appropriate library header declaration file inside the `SHARE` of the sample component.

```
%include "read_table-lib"
```

Thus, several functions are available to read tabulated data and header information from files during the simulation. Using the existing McStas table reading and parsing functions, a routine was written to apply the input file mechanism to the Bragg edge sample component. The complete listing of this routine is shown separately in appendix C.3. The function is attached to the sample's `SHARE` section. The basic principle is at first to access the input file by its name. The next step is to parse the header information available from the file contents. Each line starting by a `#` character is treated as a header line and can be evaluated by parsing a keyword. From the parsing results one is able to assign the value to a variable within the simulation component. In the example below, the space group number can be accessed by parsing the `space_group` keyword, which enables the possibility to initialise a unit cell. This way, the lattice spacing and angle values will also be determined and assigned to the nxs library functions as input parameters. Furthermore, the individual properties of each atom inside the unit cell are stored to the input file. The nxs cross section calculation also supports other than monoatomic unit cell definitions. As the number and type of unit cell atoms are variable for each material, the atom properties are listed in a tabulated format. By means of the header information, the read-out routine determines the column position of each variable for a correct assignment.

```
# space_group    229
# ...
# column_x       7
# column_y       8
# column_z       9
#
26  9.45  0.4  2.56  55.85  464.0  0  0  0
```

The example shows the assignment of an iron atom. It demonstrates, that the atom position (x,y,z), which is the Wyckoff position, is listed in columns number 7, 8 and 9. The last lines (without #) contain the actual table data<sup>3</sup>, i.e. the Wyckoff position of the first atom listed here is (0,0,0). Additionally, the coherent scattering length (9.45 fm), the average incoherent scattering (0.4 barns) and absorption cross sections (2.56 barns), the atomic mass (55.85 u) and the Debye temperature (464 K) are accessible this way. On the basis of this mechanism, more atoms and its properties can be added, stored to and read from the input file without changing the reading routine inside the McStas component.

As kind of a fallback solution the input file reading routine also provides default parameters towards the cross section calculation. This is useful for test purposes, if the input file is missing or if it is incomplete. Then, the parameters describe the alpha iron unit cell (bcc crystal structure), as described above, which will be used for the simulation. Thus, it is possible to simulate Bragg edges even without a parameter file.

#### 5.2.4. Simulation Verification

The above developed Bragg edge sample module has been integrated inside a simple virtual instrument. This includes simulation components, such as a neutron source and a detector, that already exist within the McStas library. In detail, the **Source\_simple** component providing neutrons with a flat wavelength distribution, a  $(1 \times 1) \text{ cm}^2$  primary **Slit**, the new **BraggEdge\_Powder** sample with a thickness of 2 cm and a wavelength-dispersive monitor **L\_monitor** capturing the transmitted neutron intensity inside wavelength channels. All components are aligned towards the transmission geometry. A sketch of this setup is shown

---

<sup>3</sup>The first value is intended to be a label for the atom type. Unfortunately, it is not possible to set character or string values such as “Fe” or “Si4+” if the McStas table reading routines are used. Hence, the atomic number is simply used here for the identification for the atom. This is considered in the source code listed in appendix C.3.

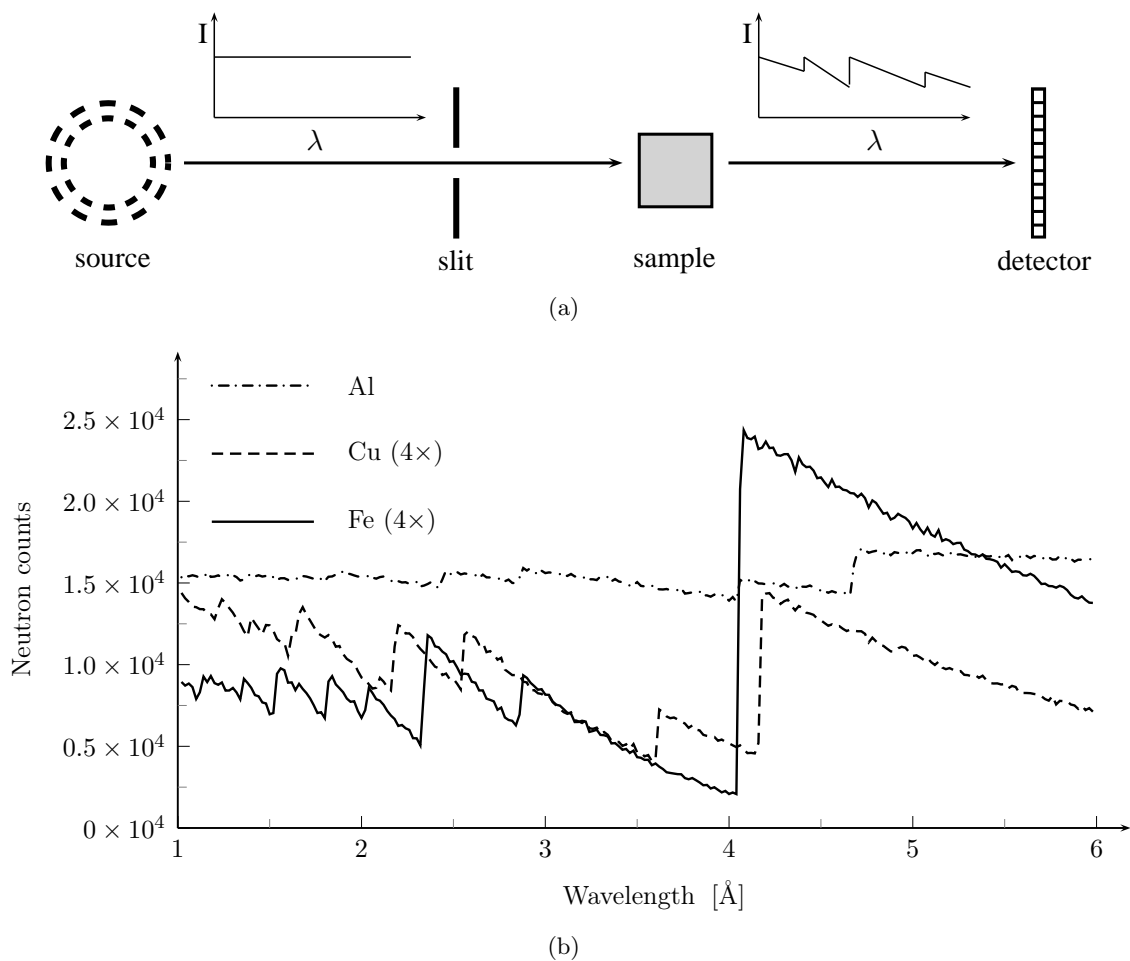


**Figure 5.2.:** Schematic drawing (a) of a very simple McStas Bragg edge simulation. Simulation details: Flat wavelength distribution (1 - 6  $\text{\AA}$ ), ( $10 \times 10$ )  $\text{cm}^2$  source window, ( $1 \times 1$ )  $\text{cm}^2$  slit size, 500 detector channels. The resulting transmission spectrum (b) shows the simulated Bragg edges. The Fe and Cu results have been scaled by a factor of 4.

in figure 5.2a. The simulation has been executed with different material definitions (Al, Cu, Fe) utilising the input file mechanism. As a result, the numbers of transmitted neutrons detected by the wavelength monitor are shown in figure 5.2b. For all three tests the same initial number of neutrons was applied to the virtual instrument. Due to the weak attenuation of Al, the values of transmitted neutrons for Cu and Fe have been scaled by a factor of 4. The diagram shows, that the Bragg edge sample component within a McStas instrument definition works properly. Moreover, the application of a simple instrument definition shows already the contrast of different materials.

### 5.3. Statistical Errors & Simulation Performance

In McStas, individual neutron event propagation is computed for each instrument component. The simulation result represents the integration of all neutron events over the propagation path [Willendrup et al., 2008]. Therefore, it estimates measurable quantities at the instrument. Thus, the sum of all neutrons histories, hitting a monitor component for example, accounts for the detected neutron intensity  $I$ :

$$I = \sum_i p_i = N\bar{p} \quad (5.4)$$

The neutron weight factor  $p$  has already been introduced (see section 5.2.2). The number of neutrons is denoted by  $N$  and  $\bar{p}$  is the averaged neutron weight. Moreover, the statistical variance of  $p_i$  is approximated by [e.g. Willendrup et al., 2008, equation 4.8]:

$$\sigma^2 \approx \sum_i p_i^2 \quad (5.5)$$

Assuming that the neutron weights  $p_i$  follow a Gaussian distribution, the accuracy of a simulation will be improved by larger values of  $N$ . Finally, the neutron intensities and their uncertainties computed in McStas will be stored by the monitor or detector components. Therefore, values of  $N$ ,  $I$  and  $\sigma^2$  will be considered for each measured dimension.

#### 5.3.1. Simulation Speed

The performance of the simulation and the quality of the results depends on many variables. The number and the complexity of components included in a simulation program vary with the type of investigation. Hence, it is very difficult to establish a general prediction of the computation time. Last but not least the simulation speed is always related to the performance of the computer system used. In order to get an idea of the necessary simulation time to calculate a Bragg edge spectrum within a virtual experiment, a simple instrument setup is sketched. In the example of figure 5.2, a neutron source with a flat wavelength distribution, a small slit, the Bragg edge sample component and a wavelength monitor was tested. This instrumental setup is considered for the following examination. The simulation

has been executed with  $10^8$  neutrons. The resulting Fe transmission spectrum has been compared with the neutron cross section calculation in order to present a value for the signal quality of this simulation. Thus, a standard deviation about the theoretical curve of about 2 % could be determined, which shows a reasonable signal-to-noise ratio in the simulated Bragg edge transmission spectrum at the detector. As a result, the diagram in figure 5.2b clearly shows the different Bragg edges and the statistical noise on the transmission curve is small, especially when the height of a Bragg edge is considered. Thus, the edge positions can clearly be distinguished. On a single computer (2200 MHz) the run duration of this example was 150 s. However, a more realistic instrument simulation will slow down the simulation speed. A complex instrument definition with a Maxwellian neutron source, neutron guides, slit systems and monochromators before the sample for example, would result in a much higher ratio of simulated neutrons not being detected at the end of the instrument. Hence, more neutrons would need to be simulated to achieve good quality results. The CONRAD instrument simulation that will be presented in section 5.4 was tested with  $10^{10}$  neutrons. Because of the higher complexity and the number of neutrons, the execution time would therefore last several hours for just one wavelength position. Thus, a complete Bragg edge spectrum would need a number of days to be computed. Here, the difference between a real experiment and the simulation becomes apparent. While neutrons propagate from the source to the detector almost instantly, the computation of a single neutron describing the same process needs hundreds and thousands of calculation steps. According to that, it is useful to consider approximations within components that will not affect the final results. Moreover, one should restrict the parameter range of the simulation to the main focus of interest. Sometimes, both can only be realised by a modification of existing McStas components. Additionally, one could take multiple computers into account to calculate parts of a complete simulation in parallel and merge the results afterwards. In order to improve the simulation speed, the proposed options will be discussed and applied in the following.

McStas provides the opportunity to split a simulation into several parts. Thus, the individual parts can be executed on multiple computers separately and in parallel. As a result, a simulation will be completed much faster or more neutron events can be computed within

the same time. Therefore, the McStas tools support different methods. For all possibilities, the program takes advantage of the ideal situation that each neutron ray is simulated independently. None of the neutrons interferes with other simulated neutron rays. On the one hand, the user is able to split a virtual experiment into different tasks. For example, multiple sample orientations can be simulated on different computers simultaneously. In addition to the manual program execution, an automatic method distributing simulation steps on computer grids exists as well [Willendrup et al., 2008]. Afterwards, the final simulation results can be merged using the `mcformat` tool. On the other hand, another approach is recommended for computer clusters. McStas supports the usage of the Message Passing Interface (MPI) — a specification to enable communication between many computers. Thus, a comfortable method exists to simulate each neutron within a virtual instrument separately on another computer. Another possibility would be to divide the total number of neutrons to be simulated and to execute the program individually with fewer neutrons on many computers. Then, the simulation results must be collected and merged manually. By means of the MPI implementation MPICH2 [e.g. Gropp, 2002], the following Bragg edge simulations have been executed on a cluster of homogeneous computer systems. In order to activate parallel computing with MPI, the `mcrun` tool must be called with appropriate switches. The instrument definition will be translated by the MPI compiler and a file specifying the computer names to be used is applied to execute the simulation. However, additional configurations on all involved computers are required. More details about this preparation and the basic MPI usage are given in the McStas manual [Willendrup et al., 2008, section 5.6.2]. Within this work, 5 dual-processor computers ( $4 \times 2$  AMD Opteron processors,  $1 \times$  AMD Athlon 64 X2 dual core processor) with 2200 MHz each, using a 64-Bit operating system (Linux openSUSE 11.1), have been operated for McStas simulations. Usually, 9 processors/cores were involved in the simulation. As predicted in the McStas manual, the duration time was reduced to one ninth of the original simulation by this procedure.

Similar to neutron beam time, processor speed, even in modern computer systems and program execution time on high-performance clusters is limited. Optimisations can be realised when simulating Bragg edge neutron transmission. A first modification to the

BraggEdge\_Powder sample component was applied in section 5.2.2. There, the usage of the neutron weight enables all neutrons to contribute to the transmission signal at the detector. In contrast to an individual neutron absorption within the sample, the same amount of simulated neutrons will then account for better statistical results. Therefore, the weight of each neutron is adjusted by a factor representing the probability to transmit through the sample. However, in some cases it is necessary to remain with the original neutron absorption. If there is no solution for the weight factor transformation or if its description is too complex as it depends on many variables, the virtual neutron is better to be `ABSORBED`. The multiple scattering simulation implemented in chapter 8 is an example for that.

### 5.3.2. Stratified & Importance Sampling

In order to accelerate the simulation and improve statistics respectively, additional Monte Carlo features can be applied. One modification applied within this work is known as stratified sampling [Willendrup et al., 2008]. By means of the McStas keyword `SPLIT` in front of a component within the `TRACE` section of an instrument definition, the simulation workflow will be split into two parts. The first part is normally computed. Then, for each neutron reaching the component with the `SPLIT` keyword, the second part is repeated  $n$  times. The number of repetition  $n$  is defined directly after `SPLIT`. Thus, a representative amount of neutrons can be applied multiple times with the “interesting” part of the simulation, e.g. the Bragg edge sample. Consequently, the fraction of neutrons lost in propagation before is decreased — the bigger part of the computation time is used for the Bragg edge phenomenon.

Another modification can be applied within the `BraggEdge_Powder` module by adjusting the neutron cross section calculation. As the total neutron cross section depends on the neutron wavelength, the calculation is repeated for each individual neutron (within the component’s `TRACE` section). However, the neutron cross section calculation can be executed once at the beginning of the simulation (within the `INITIALIZE` section). Therefore, all cross sections will be calculated within a wavelength range of interest. Then, a minimum  $\lambda_{min}$  and maximum wavelength  $\lambda_{max}$ , as well as the number  $B$  of values to be calculated within this range, will be applied in order to store the cross section values in a look-up table. Inside the

component's TRACE section, only the index value addressing the appropriate cross section in the look-up table has to be determined by means of the actual neutron wavelength.

$$index = B \frac{\lambda - \lambda_{min}}{\lambda_{max} - \lambda_{min}} \quad (5.6)$$

With  $B$ , the wavelength step size and therefore the precision of the Bragg edge simulation is defined. Thus, the simulation speed is enhanced without influencing the statical results. Towards the simulation of a simple Bragg edge experiment as visualised by figure 5.2 an improvement of approx. 23 % was achieved relative to a simulation without look-up tables. Unfortunately, this value will be decreased with the growing complexity of an instrument definition, i.e. the speed improvement will get lost with number of calculation performed outside the BraggEdge\_Powder sample component. Moreover, this modification is not applicable if the material properties vary with their local position inside the sample. Hence, a lattice spacing gradient, for example, requires the neutron cross sections to be calculated depending on the sample position. A simulation of this is type applied in chapter 7, where the principle of the look-up table cannot be used.

A more general method is to limit the simulated neutron wavelength range also at the beginning of the instrument definition. Hence, the source component can be instantiated with variable input parameters defining neutron wavelengths that will be detected at the end. By this means, the same number of neutrons is simulated within a smaller range. Again, the statistical variance will be decreased. With regard to neutron scattering, the McStas manual refers to direct focusing where, in order to avoid wasting time in computing neutrons that scatter into irrelevant directions, a weight transformation is applied for all neutrons such that scattering in a particular direction is forced [Farhi et al., 2009]. In some cases existing components have to be modified to achieve this. As an example for the Bragg edge simulation, a modification of the neutron producing source component is used in section 5.4.1 to avoid computing neutrons that will never reach the detector. Thus, only neutron wavelengths being important for a selected instrument setting will be simulated. All these techniques are related to the Monte Carlo term "importance sampling".



In summary, the McStas software provides many possibilities to limit the range and extent of a simulation. Although, the costs of computer power and execution time is much lower compared to the production and measurement of neutrons for example, the access to high performance computers and to computing time on cluster systems can sometimes be restricted, especially when a simulation cannot be executed exclusively. In such case, the application of the presented sampling techniques can be useful.

## 5.4. CONRAD Instrument Simulation

To gain a better understanding and a validation for Bragg edge transmission experiments conducted on the CONRAD tomography machine, the double monochromator option introduced in section 4.1 is simulated with McStas. By means of a virtual instrument, the influence of the instrumental setup on the Bragg edge spectra is now analysed.

### 5.4.1. Double Crystal Monochromator

As stated in section 4.1.2, a double monochromator setup is placed at the high-flux position of the instrument directly behind the neutron guide. Taking the BER-II neutron source and the guide into account, the simulation of the source and the neutron guide is included in the following simulation<sup>4</sup>. Therefore, the existing `Source_Maxwell_3` component has been applied to parametrise a continuous neutron source with Maxwellian distributions. Likewise, the NL1B neutron guide is inserted in the virtual CONRAD instrument. Later, the source component was modified to realise importance sampling and speed up the complete instrument simulation. In the following, it is highlighted that the double monochromator option not only selects one neutron wavelength  $\lambda$  but also other wavelength  $\lambda_i$ . This occurs due to higher order crystal reflections such that  $\lambda$  is always a multiple of  $\lambda_i$ . Therefore, a wavelength range limitation inside the source component must take the higher order reflections of the monochromator crystals into account. Towards this importance sampling application, the `Source_Maxwell_3` component has been modified within its TRACE section. An additional input parameter specifying the wanted neutron wavelength  $\lambda$  was added to the component.

---

<sup>4</sup>The work presented in this section has been realised in cooperation with André Hilger from the Helmholtz Centre Berlin.

Then, the neutrons are generated by a random choice between three orders  $\lambda_i$ , where  $\lambda_1 = \lambda$ ,  $\lambda_2 = \lambda/2$  and  $\lambda_3 = \lambda/3$ . Higher orders are neglected here. Moreover, a random deviation of  $\pm 10\%$  around each  $\lambda_i$  has been implemented in the source component. Thus, the complete neutron range shall be covered for the following simulation. Simultaneously, a speed improvement is achieved. However, the main focus of this section is the implementation of the double crystal monochromator.

The double monochromator system consists of two HOPG(002) single crystals aligned parallel to each other and one upon the other with a fixed distance of  $D = 7$  cm. The crystal lattice spacing is given by  $d_{002} = 3.348 \text{ \AA}$ . The length of a monochromator plate is  $L = 6$  cm and the width is 6 cm. As shown in figure 5.3, the single crystal will be rotated according to a Bragg angle  $\theta$ , which is used to select a single neutron wavelength. To provide a comfortable control of the instrument simulation, the positioning of the monochromator crystals is done by specifying a wanted neutron wavelength  $\lambda$ . Similar to the real instrument control, the user is able to apply the wavelength as an input parameter for the instrument definition.

$$\theta = \arcsin\left(\frac{\lambda}{2 d_{002}}\right) \quad (5.7)$$

Additionally, the lower crystal plate is mounted on a linear translation stage which moves in the direction of the initial neutron flight path. This is necessary to meet the reflected neutrons from the upper crystal with respect to the scattering angle  $\theta$ . Therefore, the translation  $Z$  is determined by:

$$Z = D \tan(90^\circ - 2\theta) \quad (5.8)$$

According to the given parameters, two instances of the **Monochromator\_flat** component from the McStas library were chosen to simulate the wavelength selection. So far, no assumptions on different penetration depths into the single crystal have been made. Hence, there is no monochromator thickness needed. A reflectivity  $r = 91\%$  was chosen to be the input parameter for the **Monochromator\_flat** component. This value was determined after a few trial simulations and comparisons with test measurements performed on CONRAD. Good intensity agreements have been found using this value. Moreover, this means that a

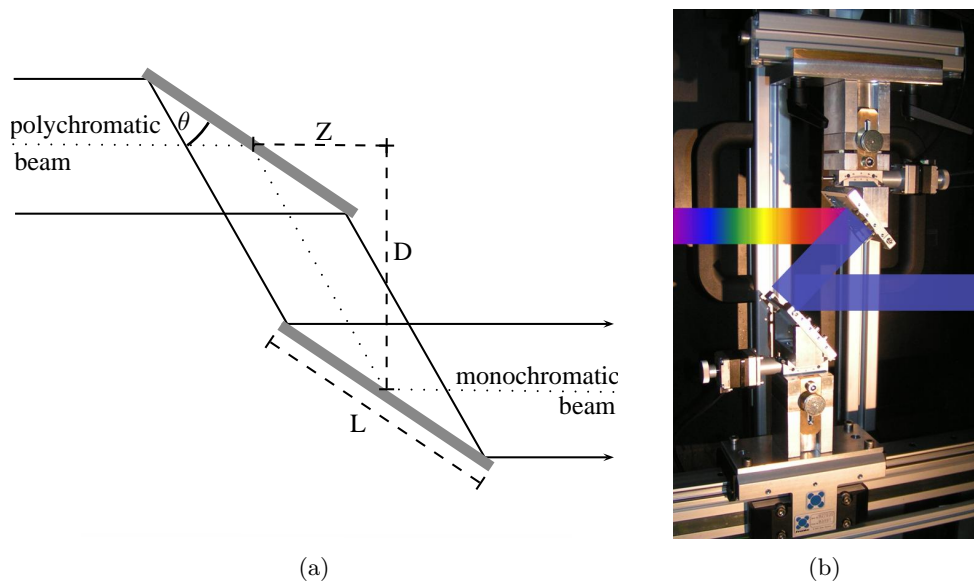


**Figure 5.3.:** Schematic drawing (a) and photo (b) of the double monochromator option on the CONRAD tomography machine.

wavelength-dependent reflectivity is neglected up to now. Furthermore, the monochromator component expects a mosaicity value, which has its most influence on the peak width of the selected wavelength. Here, a single value  $m$  will be used for the description of both, the vertical and a horizontal mosaicity.

McStas provides the opportunity to trace every single neutron. Thus, the state parameters and the neutron properties can be analysed and visualised in any possible way. Hence, the wavelength selection on CONRAD was examined carefully using the simulation. Both the influence of higher order monochromator reflections and the peak width of a selected wavelength were investigated. Due to the instrument setup it was expected to have a space-dependent wavelength distribution on the detector screen. As shown in figure 5.4a, a band of different wavelengths is reflected by the monochromator due to its mosaicity. Consulting Bragg's law, longer neutron wavelengths  $\lambda_i$  are reflected under higher Bragg angles  $\theta_i$ . Because of the double monochromator geometry (parallel alignment), the wavelength distribution should correlate with the detector height. For the purpose of the signal analysis, a monitoring component `LambdaYPSD_monitor` was created to count neutrons and store their wavelength and their height position at the detector area. The component was adapted from the existing energy-dispersive position-sensitive monitor `EPSD_monitor`. Similar to any other

McStas monitor component, the `LambdaYPSD_monitor` captures every neutron arriving at the component. The monitor geometry is simplified to a plane area. Therefore, the neutron position parameters  $x, y$  will be compared with a defined monitor size (width and height). Related to that, the neutron velocity is converted to a wavelength (equation 5.1), then the neutron wavelength must fit within the range specified for the monitor area. Finally, the neutron intensity in terms of  $N$ ,  $I$  and  $\sigma^2$  (see section 5.3) will be stored relative to the neutron wavelength and its local position on the monitor. Thus, a map depending on the monitor height and the neutron wavelength is created. At the end of the simulation, this map is stored to a data file using a pre-defined macro function within the `SAVE` section of the component. As a result, the detector image can be visualised by the McStas plotting tools. A full listing of the new component is provided in the appendix C.4. The component size and the wavelength range as well as the filename to store the monitor image can be defined as input parameters.

The simulation performed here is equivalent to an open beam measurement and its evaluation, i.e. there is no sample in the beam to be transmitted. The resulting monitor picture of the `LambdaYPSD_monitor` component for a simulation of a wavelength selection of  $4 \text{ \AA}$  is shown in figure 5.4b. The diagram shows the intensity distribution related to the neutron wavelength and the detector height. A significant fraction of wavelengths around  $2 \text{ \AA}$  resulting from the second order monochromator reflection are also visible. Moreover, it is shown that neutron wavelength distribution on the detector area correlates with the detector height — both intensity lines are inclined. Thus, the wavelength distribution is visualised. The slope that is visible in figure 5.4b was evaluated to predict a wavelength change relative to the detector height. Therefore, the detected neutron intensities  $I$  are used to calculate the centre of mass  $M$  related to the neutron wavelength  $\lambda$  for each  $y$  detector position.

$$M(y) = \frac{1}{\sum_{\lambda} I(\lambda, y)} \sum_{\lambda} \lambda I(\lambda, y) \quad (5.9)$$

The resulting wavelengths  $\lambda = M(y)$  are fitted to a linear function  $f(y) = m y + n$  to determine the slope  $m$  of the wavelength change. According to the simulation presented in figure 5.4b, the wavelength selected to be  $4.0 \text{ \AA}$  changes by approx.  $10^{-2} \text{ \AA/cm}$ . The simula-

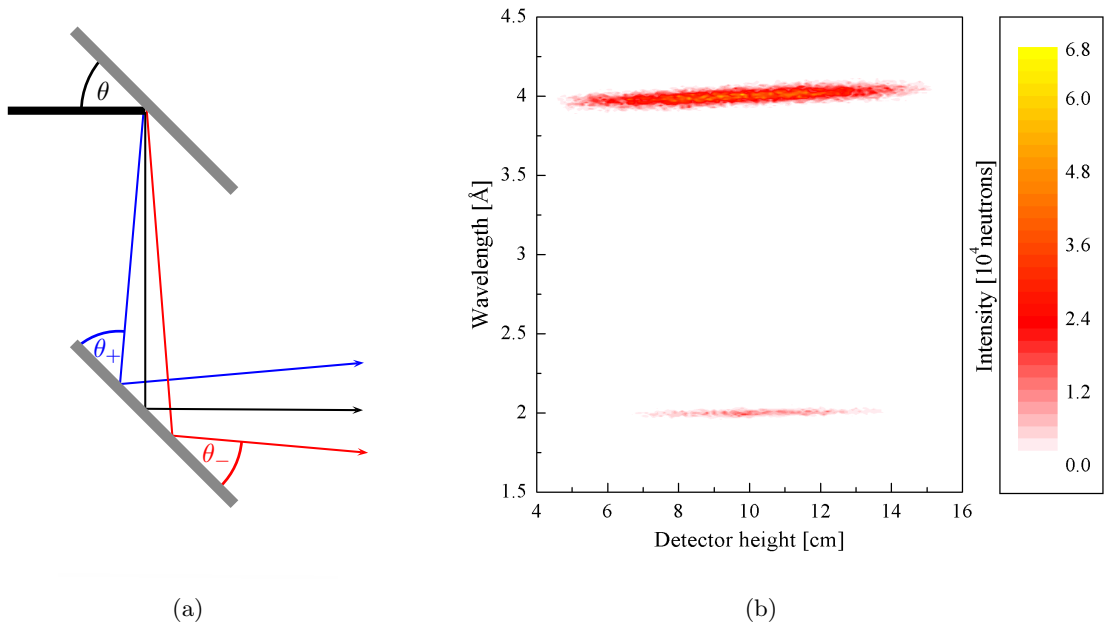


**Figure 5.4.:** Schematic drawing (a) of the wavelength distribution behind the double monochromator. Due to the crystal mosaicity the setup selects wavelengths, that are scattered unequally back in the forward transmission direction (denoted by  $\theta_+$  and  $\theta_-$ ). As a result, the wavelength distribution at the detector position (b) correlates with the height. The `LambdaYPSD_monitor` component was created to detect and visualise this wavelength slope. For an example monochromator setting the detected first ( $4 \text{ \AA}$ ) and second order ( $2 \text{ \AA}$ ) wavelengths show an inclined distribution at the detector.

tion module provides the opportunity to test the wavelength change with different instrument settings. Consequently, the same simulation was started with different monochromator mosaicities and wavelength selections. Afterwards, the centre of mass  $M$  was evaluated for each setting in order to find the wavelength slope  $m$  as described above. An excerpt of the input parameters tested and results evaluated is shown in table 5.1. Although, the listed wavelength increase per cm is around the value stated above, the results vary according to the mosaicity and the input wavelength, i.e. the monochromator orientation. There is a significant change of the wavelength increase depending on the monochromator. As a result, the slope decreases with the selected wavelength. Moreover, a small gradient is shown relative to the selected mosaicity. In order to test this theory, real measurements at the CONRAD instrument have been conducted. The current detector system (CCD camera) only allows evaluation of the transmitted neutron intensities based on the grey values assigned to each pixel of a captured radiographic image. Therefore, a Bragg edge spectrum is always obtained from a series of

radiographies with different input wavelength. The wavelength slope relative to the detector position can only be analysed by means of strong differences in the transmission spectrum. An evaluation of the wavelength distribution at the detector, such as presented above in the simulation of the instrument is not possible. Hence, the Bragg edges of an aluminium sample, as strong intensity changes, have been used. Consequently, the analysis of the wavelength slope refers to the Bragg edge positions of the transmitted sample material. The aluminium is a good choice as it exhibits two Bragg edges clearly visible in the transmission spectrum of the CONRAD instrument. Consequently, the (111) and (200) Bragg edges at around 4.7 Å and 4.1 Å respectively have been evaluated as any further Bragg edge would be either too small or located within a low neutron statistics area. Hence, further edge position cannot be analysed on CONRAD within reasonable exposure times. The two given Bragg edge positions have been evaluated for 5 different local sample positions. In figure 5.5, the positions have been plotted and fitted to a linear function. The resulting wavelength slope  $m$  is shown as well. Although, the absolute value does not match exactly with the theoretical results from table 5.1, the dependence on the selected input wavelength (monochromator orientation) is also visible. The differences to the simulation can be explained by the uncertainties related to the exact monochromator behaviour as well as by the averaging over a region of interest within the radiographic images taken at CONRAD, which is necessary in order to evaluate the Bragg edge signal.

neutron wavelength [Å]	wavelength increase [ $10^{-3}$ Å/cm]		
	monochromator mosaicity		
	0.5°	0.8°	1.0°
2.0	12.95	12.87	12.82
3.0	12.09	12.07	12.01
4.0	10.85	10.82	10.79
4.7	9.58	9.50	9.56
5.0	8.91	8.95	8.93

**Table 5.1.:** Analysis of the simulated wavelength increase relative to the detector position due to the double crystal monochromator setup.

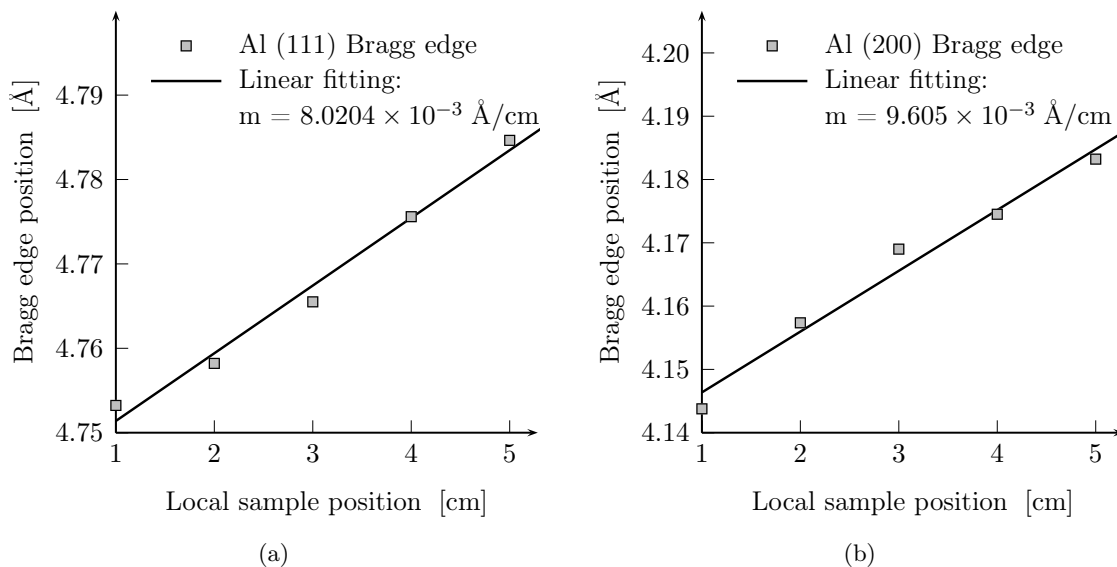


**Figure 5.5.:** Analysis of the measured (111) and (200) Bragg edge position depending on the sample position relative to the detector height.

Altogether, the simulation showed that the CONRAD wavelength-selective option is sensitive according to a selected (local) detector position as well as to the selected wavelength itself. The theoretical results have been compared and confirmed with measurements of an aluminium sample. Ideally, the Bragg edge analysis on CONRAD must be related to the local sample/detector position.

#### 5.4.2. Influence of Monochromator Properties to Bragg Edge Spectra

So far, the virtual CONRAD instrument has been implemented and the double crystal monochromator and position-sensitive wavelength detection has been reviewed. Now, the Bragg edge transmission sample component, created in section 5.2, will be applied to the instrument simulation.

The CONRAD instrument was simulated with different input parameters. On the one hand, different materials and also different thicknesses have been tested. Here, it was decided to simulate an iron and an aluminium powder sample as both materials scatter differently due to the difference of the coherent elastic scattering cross section. The mosaic spread of the monochromator crystals was also varied. Originally, the mosaicity of the current monochro-

mator setup is  $0.8^\circ$  (as given by the manufacturer<sup>5</sup>), but there is a systematic uncertainty as this value has not been verified by neutron measurements. Hence, different mosaicity values have been tested as well. Moreover, because a wavelength-dependent reflectivity profile is not known, the reflectivity is assumed to be constant for any neutron. Thus, the dependency on the neutron wavelength is neglected for the following simulations. For each named input parameter, a wavelength scan from  $3 \text{ \AA}$  to  $5 \text{ \AA}$  in steps of  $0.01 \text{ \AA}$  was performed using the Bragg edge component described above (section 5.2), i.e. the simulation program was executed for each single wavelength step. The same conditions as on the real CONRAD instrument are used for a Bragg edge transmission experiment. Additionally, flatfield images have been computed in the same wavelength range to provide a normalisation of the varying neutron flux density.

The diagrams shown in figure 5.6 result from the simulation of an iron (bcc, lattice constant  $a = 2.866 \text{ \AA}$ , sample thickness  $l = 1 \text{ cm}$ ) and an aluminium sample (fcc,  $a = 4.05 \text{ \AA}$ ,  $l = 3 \text{ cm}$ ). The detector results from the transmission simulations (including flatfields) have been recalculated to the total neutron cross section  $\sigma_{total}$ , which is the parameter originally computed within the simulation. In order to visualise the effect of the monochromator influence all values are compared with the theoretical neutron cross section (dashed lines). Therefore, the transmitted intensities have been normalised by the appropriate flatfield intensities, the sample thickness and the unit cell volume. The calculation of the attenuation coefficient (equations 3.2 and 3.3) has been applied. The dashed reference cross sections were calculated using the nxsPlotter program. Although the weak scattering cross section of aluminium turns into a noisy Bragg edge transmission signal (figure 5.6b), the difference of the evaluated and the ideal reference cross sections can be seen for both presented materials. The influence of the monochromator mosaicity is most visible in the iron diagram, figure 5.6a. Depending on the degree of mosaicity, the selected wavelength is reflected with a growing peak width. Due to the amount of contributing wavelengths, the Bragg edge is smoothed around its initial position and the step function changes to a slope. Furthermore, the effect of the higher order reflections is shown in the iron Bragg edge spectrum. Generally, the total neutron cross section values outside the Bragg edge area ( $\lambda > 4.1 \text{ \AA}$ ) are higher than the the-

---

<sup>5</sup>Optigraph, manufacturer of HOPG monochromators, <http://www.optigraph.fta-berlin.de/>



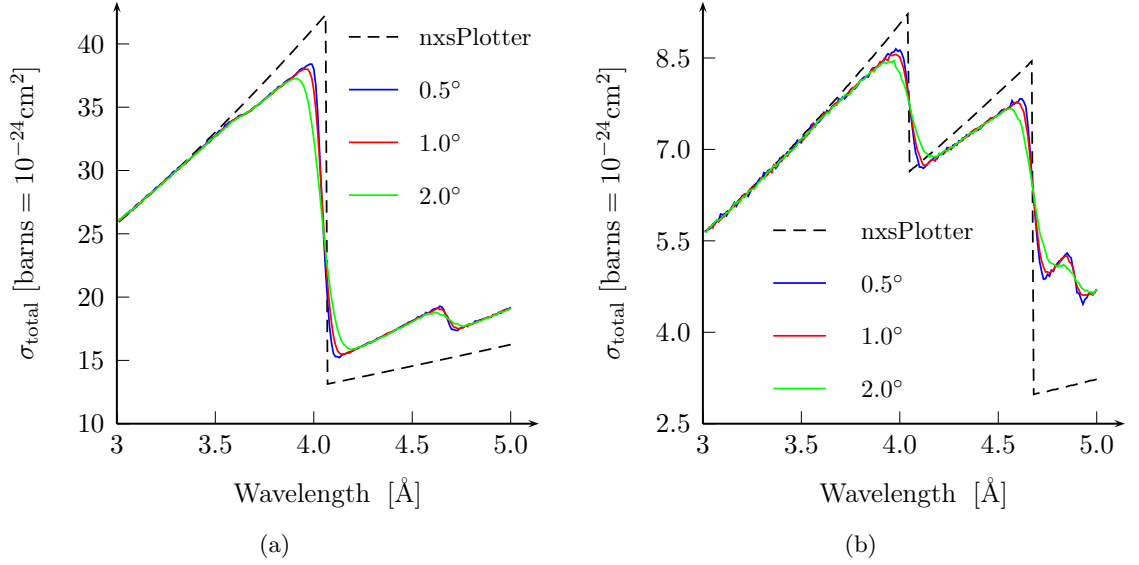


**Figure 5.6.:** Bragg edge experiment simulations with different monochromator mosaicities ( $0.5^\circ$ ,  $1.0^\circ$ ,  $2.0^\circ$ ). The simulation results have been normalised to the total neutron cross section for a comparison with the input cross sections (dashed lines) calculated with the *nxs* routines. The diagrams show the simulation results from an iron bcc sample (a) and an aluminium fcc sample (b).

oretical values (dashed line). Because of the second and third order reflections, that are also present in the selected neutron beam, further contributions to the total cross section appear. In particular, the incident intensity is attenuated even more due to the interaction of the smaller wavelengths. The flatfield measurements capturing the incident neutron intensity do not resolve these multiple monochromator reflections. Hence, the total neutron cross section is increased at this point. This can also be seen in the aluminium simulation. Moreover in figure 5.6a, there is a small peak at about  $4.7 \text{ \AA}$ , that results from the original (211) iron Bragg edge. This is because there is a significant fraction of second order wavelengths around  $2.34 \text{ \AA}$  showing a Bragg edge due to the lattice reflection at  $d_{211} = 1.17 \text{ \AA}$ .

The Bragg edge application on CONRAD using the double monochromator device has been emulated successfully. The simulations have shown that the wavelength-selective option influences the Bragg edge spectrum as kind of a systematic error. Nevertheless, the CONRAD simulation module allows the instrumental characteristics to be emulated and therefore to be used in comparison with real experiments investigating material's properties.

## 5.5. ENGIN-X Simulation Module

In order to compare measurements on ENGIN-X with the Bragg edge simulation developed here, a description of the real instrument has been applied to the McStas definitions. Therefore, the ENGIN-X model, introduced in [Santisteban et al., 2006a] for strain scanning performance analyses, has been extended towards the simulation of Bragg edge transmission experiments. The ISIS neutron source in terms of a McStas moderator component (see project website<sup>6</sup>) as well as neutron guides and slit systems have already been implemented. Here an additional monitoring component designed to capture transmitted neutrons was added to the virtual instrument towards the analysis of transmitted neutrons. The implementation of the real  $10 \times 10$  pixels ENGIN-X time-of-flight transmission detector has been represented by a simplified single time-of-flight monitor component `TOF_monitor`. This component already existed within the McStas component library. As a result, an instrument simulation has been created taking the ENGIN-X parameters into account. In the following chapters, the ENGIN-X simulation will be applied to investigate multiple problems related to the analysis of Bragg edges. In these simulations the detector size will be chosen to be as big as the simulated Bragg edge sample or defined manually, so that neutrons passing the sample will be ignored. As an applied example, figure 5.7 shows the transmission spectrum for a 2 cm thick iron sample. The intensity is plotted against the neutron time-of-flight. The diagram includes both, the openbeam and the transmission simulation (scaled by a factor of 3). From both curves, the attenuation coefficient has been calculated and compared with the theoretical plot (dashed line) computed with `nxsPlotter`. The plot shows a reasonable agreement with the theoretical calculation, which verifies the ENGIN-X simulation with McStas relating to the Bragg edge neutron transmission experiments.

Just like the real instrument, the simulation also measures the neutron time-of-flight instead of the actual neutron wavelength or energy. Due to the collision processes in the moderator there is an uncertainty in time and position at which the neutrons leave the moderator [Santisteban et al., 2001], which affects the shape of the Bragg edges. In order to demonstrate that this effect is included in the developed simulation, figure 5.8 shows a de-

---

<sup>6</sup> <http://www.isis.rl.ac.uk/Computing/Software/MC/index.htm>, ISIS Computing Group

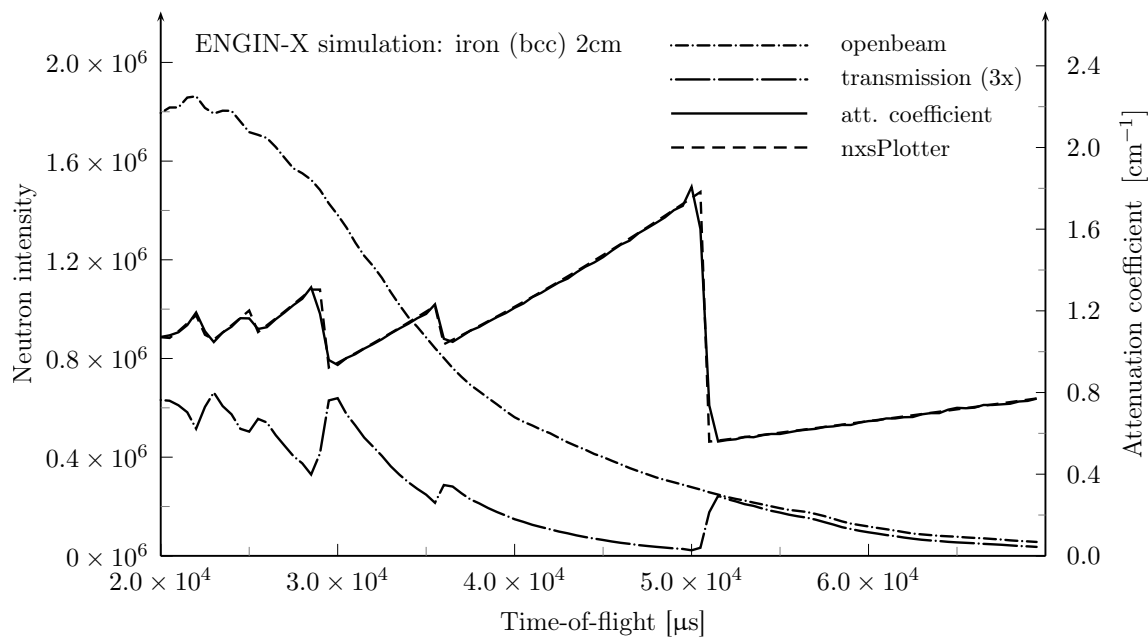


**Figure 5.7.:** *McStas simulation of the ENGIN-X instrument in transmission mode: openbeam and transmitted beam (multiplied by a factor of 3) have been detected. From that the attenuation coefficient is calculated and compared with the nxsPlotter curve.*

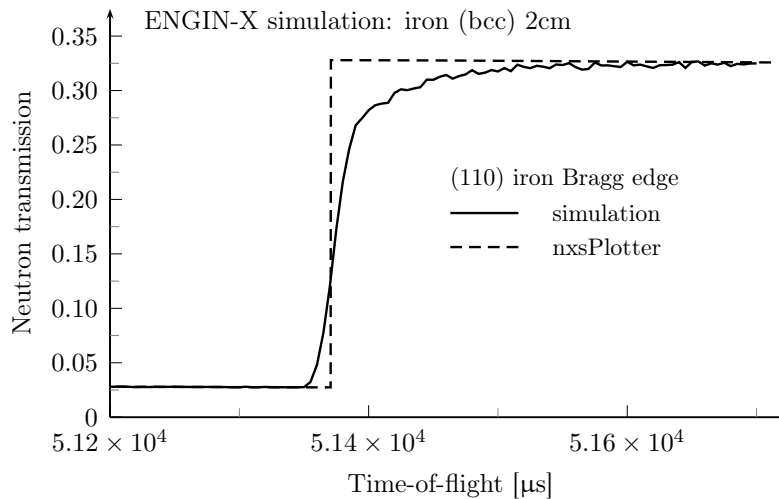


**Figure 5.8.:** *Bragg edge broadening due to uncertainties in the determination of the neutron time-of-flight.*

tailed view of the (110) iron Bragg edge. The comparison with the theoretical plot reveals the broadening of the edge.

## 5.6. Summary

In this chapter a Bragg edge simulation program was developed. The previously developed neutron cross section calculation routines have been applied within a new sample component for McStas. The resulting program was verified by simple simulation tests that provided the same transmission results as expected by the `nxsPlotter` tool. Furthermore, the instrumental parameters of the CONRAD and ENGIN-X machine have been applied to extend the simulation. Thus, the emulation of both instruments was realised. The growing complexity of the instrument computation was discussed. Likewise, different strategies have been presented in order to improve the performance of the simulation. The mentioned features, falling in the categories of stratified and importance sampling, have been applied within this work to speed up the computing time. According to that, a computer cluster was built to run the McStas simulations exclusively and in parallel.

The CONRAD instrument simulation was prepared towards applications presented in the following chapters. The validation of the CONRAD simulation was focused on the wavelength selection option. Therefore, the wavelength signal resulting from the double crystal monochromator was evaluated. The analysis of real CONRAD measurements showed, that the wavelength increase along the detector height is comparable to that obtained in the simulation. Moreover, a dependency of the monochromator mosaicity and the Bragg edge slope was established. Additionally, the contribution of higher order reflections was shown. In parallel, the simulation of the ENGIN-X machine was modified. The instrument description was extended with a transmission monitor and the Bragg edge sample module. As a result, the emulation of transmission measurements is available.

The results presented in this chapter covered the influence of the instrumental parameters and limitations to the Bragg edge transmission. Here, only constant material properties have been taken into account, such as the lattice spacing that is connected to the Bragg edge position. Towards the analysis of varying and local sample characteristics, which is the original intention of a Bragg edge transmission experiment, the next chapters are concerned with the sample geometry, crystallographic preferred orientations, i.e. texture, and lattice

spacing determination against the background of stress and strain analysis. With both the ENGIN-X and CONRAD implementations, a simulation tool was developed to test and validate experiments investigating such properties with Bragg edge neutron transmission.

Throughout the following chapters, the resulting detector signal of the developed simulation will be compared with the theoretical neutron cross sections (or attenuation coefficients) calculated with the nxs routines as it has been done within this chapter. It should be noted that for these comparisons the term “theoretical” is used to name the computed neutron cross sections from the nxsPlotter program, that are applied to the Bragg edge experiment simulations using McStas. Although the following simulations are no less theoretical, a distinction between both, the input (nxs values) and the output of the simulations, is drawn in order to clarify the influence of instrumental parameters and effects of investigated sample properties on the data analysis.



## **Texture Effects on the Neutron Total Cross Section**

In this chapter, different types of experiments investigating a textured aluminium cylinder specimen will be presented. The main motivation for these studies is to investigate the utilisation and valuation of the Bragg edge transmission method as a means of analysing preferred crystallographic orientations. Reference measurements using conventional neutron and X-ray diffraction have been conducted and so-called pole figure experiments have been performed in order to provide values for comparison with the Bragg edge transmission results presented later in this chapter.

A qualitative texture analysis following the same approach was already presented in the work of Santisteban et al. [2006b]. Moreover, the effects of preferred crystal orientations in various forms of aluminium on the total cross neutron section have been measured by Arnold & Weber [1948]. Here, the investigations are extended towards a quantitative analysis. Using the CONRAD tomography machine, Bragg edge radiography measurements have been conducted to visualise texture effects. The ENGIN-X instrument was also used to measure the same sample with time-of-flight neutron transmission. Finally, a comparison of all results will be shown and possibilities and restrictions discussed. The computer simulation presented previously (chapter 5) has been utilised in the evaluation of the Bragg edge results. Thus, the theoretical model of the March-Dollase texture correction (section 3.4), implemented with respect to the Bragg edge transmission geometry, has been applied and compared with the experiment.



*Figure 6.1.: A textured Al cylinder sample.*

## 6.1. Texture Determination by Neutron & X-ray Diffraction

The crystallographic orientation distribution of a drawn aluminium wire sample (figure 6.1) was measured by a conventional texture measurement method using neutron diffraction on the E3 and STRESS-SPEC diffractometers as well as on the ETA X-ray diffractometer at HZB. This section describes the basic principle of so-called pole figure measurements for the quantification of the sample texture. The results from the experimental data will be shown. In section 6.4.1, these values will be used as a reference for a comparison with Bragg edge transmission measurements.

### 6.1.1. Pole Figure Measurements

The diffractometers E3 and STRESS-SPEC (see section 4.4) have been applied to measure the preferred crystallographic orientation using neutron diffraction. Both instruments are designed to perform residual stress measurements. However, here the instrument geometry was used to conduct texture analysis experiments.

The instruments are equipped with a two-dimensional position-sensitive detector system. The captured diffracted neutron intensity is mapped on the  $256 \times 256$  pixel array. The detector is attached to a  $2\theta$ -motor to be driven according to a Bragg reflection of the sample material. In case of a polycrystalline sample or a powder, Debye-Scherrer ring parts are detected such as visualised in figure 6.2. Bunge & Klein [1996] already stated the advantages of area detectors in pole figure experiments. For instance, in contrast to single detectors, the high angular resolution in  $2\theta$  enables peak broadening effects due to different crystallite sizes to be visualised. Depending on the detector span and the distance to the sample multiple reflections can be captured simultaneously. Hence, overlapping peaks can also be separated



according to  $2\theta$ . Furthermore, the detector height as a kind of an additional dimension allows the analysis of very sharp textures as the interruptions and intensity changes in the Debye-Scherrer cones can be localised very precisely [Bunge & Klein, 1996]. On a linear or single detector system, the location of these sharp intensity changes may get lost in the selected measuring grid if the sampling rate of Debye-Scherrer ring is too small. With the help of this setup, the neutron intensity variations will be detected under every possible sample orientation. Therefrom, the crystallographic texture information will be derived.

The instruments allow the sample to be rotated and tilted in order to measure well-defined orientations. Therefore, an Eulerian cradle can be placed on top of the original sample table and adjusted to the centre of the neutron beam. Here, the setup was aligned such that the tilting was along the direction of the scattering vector, i.e. the Eulerian cradle was orientated with  $\theta$  relative to the primary beam. Figure 6.2 shows the sample alignment inside the Eulerian cradle and the mapping of the diffractometer coordinate system into the Cartesian coordinates of the detector plane. The rotation angle is indicated by  $\phi$  and  $\chi$  is the tilting angle. In order to make a pole figure measurement, the detector position was driven to a reflection of the sample material. Then, the sample was rotated in steps of  $5^\circ$  from  $0^\circ$  to  $360^\circ$  and tilted in  $10^\circ$  steps from  $0^\circ$  to  $90^\circ$  respectively. For each sample orientation step the scattered neutron intensities have been captured by the detector and stored to separate images. Altogether, the detector was driven to 3 different  $2\theta$  positions to map up to 5 reflections. This was possible due to the horizontal detector span that covered around  $10^\circ$  of  $2\theta$  depending on the sample-detector distance. Thus, two or more reflections could be detected by one detector position. Because of the different E3 and STRESS-SPEC parameters and neutron wavelengths defined by the instrument monochromator settings, the measurement positions differ. Table 6.1 summarises the measurement positions and the monochromator setups used for the texture analysis on both instruments. The sample cylinder has a diameter of 11.8 mm and a height of 8 mm. Hence, the primary and secondary windows were selected to be big enough such that the neutron beam covered the whole sample. Therefore, the variable matchstick slits have been adjusted. Thus, the gauge volume was defined by the whole sample and the global orientation distribution was measured.

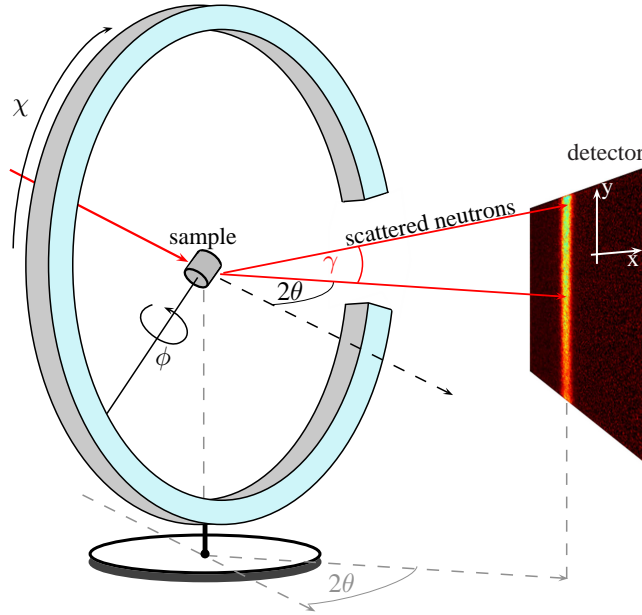


**Figure 6.2.:** Schematic drawing of the Eulerian cradle and the sample orientation used for the experimental setup of a texture diffraction measurement. The picture also shows the mapping of the diffraction angles onto the detector plane.

Instrument	$2\theta$ detector position	Covered (hkl) reflections
<b>STRESS-SPEC</b>	$41^\circ$	(111), (200)
monochromator: Ge(311)	$64^\circ$	(220)
wavelength: $1.511 \text{ \AA}$	$79^\circ$	(311), (222)
<b>E3</b>	$46^\circ$	(200)
monochromator: Si(100)	$62^\circ$	(220)
wavelength: $1.486 \text{ \AA}$	$77^\circ$	(311), (222)

**Table 6.1.:** Experimental parameters for different pole figure measurements performed on E3 and STRESS-SPEC.

### 6.1.2. Data Analysis

The collected experiment data has been analysed using the **StressTexCalculator** software developed by Randau et al. [2011] (see figure 6.3). The program reads the detector images to enable a selection of reflection intensities to be analysed. Therefore, a diffraction intensity spectrum is prepared. The detected intensities are summed up towards to their correct  $2\theta$  position, i.e. along a Debye-Scherrer cone. According to the calculations in Bunge & Klein [1996], a correlation image is computed to map the Bragg angles  $2\theta$  and the angles  $\gamma$  of the diffraction plane into the pixels  $(x, y)$  of the detector reference plane. This principle

is shown in figure 6.2. In order to map each image pixel to a  $2\theta$  value, the instrument orientation must be considered. Similar to the developments described in Garbe [2009], the StressTexCalculator program takes the detector and pixel size, the sample-detector distance and the  $2\theta$  detector position into account. Thus, the appropriate intensity summation along the Debye-Scherrer cones is realised. The resulting spectrum is used to identify the position and the area of a selected peak. Moreover, the possibility exists to determine and cut out the background signal of the intensity spectrum. In this regard, a range covering the background signal has to be selected. On the basis of these selected sampling points, a background function can be found by fitting a polynomial function of  $n$  degrees [Press et al., 2007], where  $n$  is a variable parameter. Hence, the background is subtracted from the intensity signal for each  $2\theta$  position.

For the evaluation of the peak intensities, the amplitude of the Gaussian function used to fit the shape of a selected peak is considered. Equation 6.1 shows that the position  $x_0$ , which relates to the reflection at  $2\theta$ , the amplitude  $A_0$  and the width  $w$  of the selected peak parametrise the intensity characteristics.

$$g(x) = A_0 \exp\left(-\frac{(x - x_0)^2}{2w^2}\right) \quad (6.1)$$

An offset  $y_0$  is not used here, as it is expected to be erased by the previous background correction. The principle of the background correction and the fitting routine is visualised in figure 6.3b. At first, the position and the width of the peak are set manually to provide initial values for the fitting procedure. Starting the evaluation process, the software computes the fitting for every detector image loaded to the program. Based on the initial parameters and the background correction, the area of the resulting Gaussian is calculated by equation 6.2. This is applied for each sample position which relates to one pole figure measurement.

$$\int_{-\infty}^{\infty} A_0 \exp\left(-\frac{(x - x_0)^2}{2w^2}\right) dx = A_0 w \sqrt{2\pi} \quad (6.2)$$

According to Garbe [2009], the information about the diffraction angles  $2\theta, \gamma$  and the sample orientation  $\phi, \chi$  is used to map the calculated intensities onto the polar coordinates  $\alpha$  and

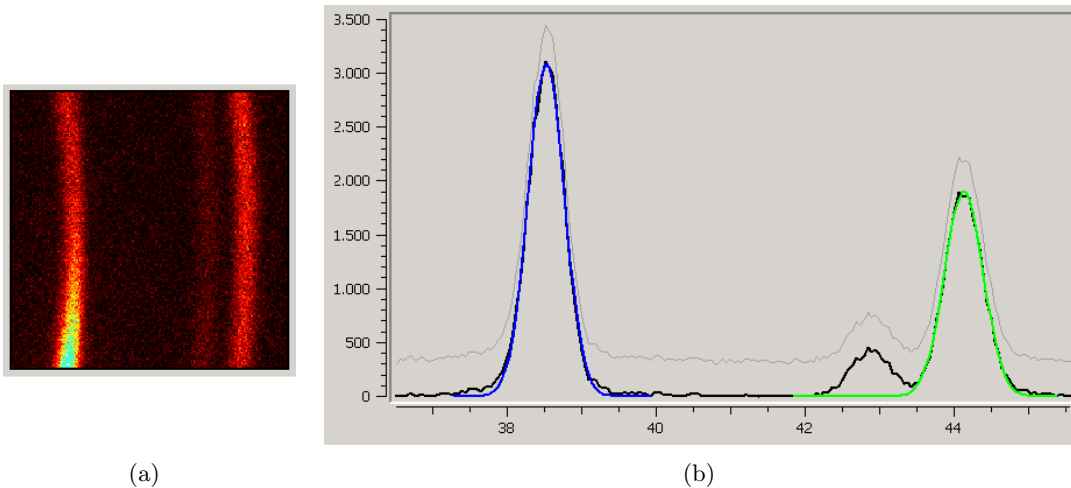


**Figure 6.3.:** Extracts of the *StressTexCalculator* software: Detector image (a) and peak fitting using the diffractogram data (b).

$\beta$ . A detailed derivation of the relation between the pole figure coordinate system and the sample orientation is given by Bunge & Klein [1996]. Consequently, the measured data is interpolated to represent the data on a regular grid with the distance  $\alpha$  and the angle  $\beta$  from the origin. The integral intensities will be stored to a pole figure file to represent the fraction of crystallites fulfilling the scattering condition according to the sample orientation. Here, the PFPlot file format<sup>1</sup> is used to export the calculated data.

As the diffracted intensities are directly connected to the amount of orientated crystallites the degree of preferred crystallographic orientation, i.e. texture, can be expressed by the pole figure intensities. The fitted intensities have been normalised to values representing multiples of a random distribution (m.r.d.) in order to compare the results subsequently (see section 6.4.1). The normalisation was done by dividing the individual intensity values by their arithmetic mean value. Hence, for a texture-free sample, such as a powder, m.r.d. = 1 ideally. Consequently, for values of m.r.d. < 1 fewer crystallites were orientated such that they fulfil the Bragg condition, while for values of m.r.d. > 1 more crystallites contribute to the detected reflection intensity. As an example, the resulting pole figures of the (111), (200) and (311) reflections are shown in figure 6.4. The circular symmetry around the sample axis is apparent. The crystallographic (111) plane is parallel to that axis with a rotational degree

<sup>1</sup>PFPlot: A program written by C. Umlauf and K. Ullemeyer (2006) to represent pole figures, Institute for Earth Sciences, University of Freiburg, Germany.

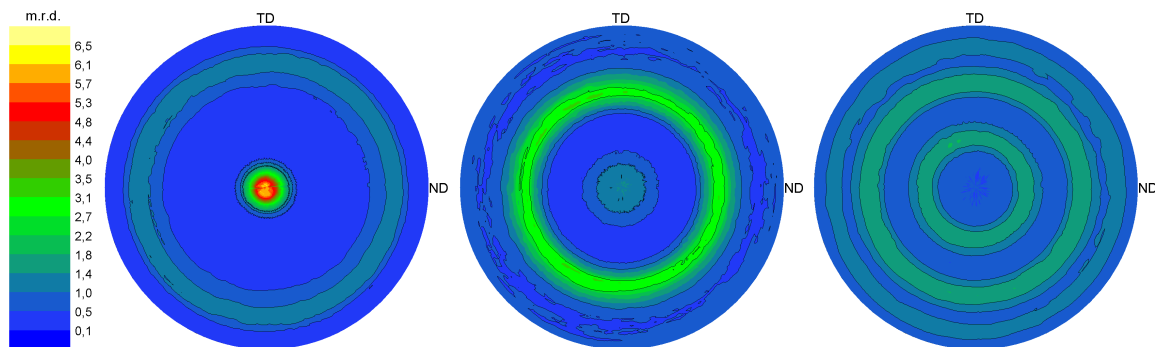


**Figure 6.4.:** From left to right: Pole figures of  $(111)$ ,  $(200)$  and  $(311)$  reflection showing the intensity distribution — each normalised to multiples of a random distribution (m.r.d.).

of freedom of about  $10^\circ$ . This type of texture is known as fibre texture [e.g. Deniz et al., 2007]. In the following the pole figure intensities determined here will be used as a reference dataset for a comparison with experiments based on Bragg edge neutron transmission.

### 6.1.3. X-ray diffraction reference measurements

In order to verify the neutron diffraction result, the texture sample has been investigated using a conventional X-ray diffractometer — the ETA instrument at HZB. A photograph and the schematical view of ETA is shown in figure 6.5 [Haase et al., 2001]. The instrument is based on a SEIFERT  $\theta$ - $\theta$ -diffractometer, i.e. both the X-ray tube and the detector can be rotated in the vertical plane according to Bragg's law. The sample was placed on the  $\Phi_2$ -rotation table and tilted by  $\Psi$  using the Eulerian cradle segment. For a single pole figure, the orientations of the sample were scanned using a  $5^\circ \times 5^\circ$  grid with  $0^\circ \leq \Phi_2 \leq 360^\circ$  and a limitation of  $0^\circ \leq \Psi \leq 85^\circ$  because of the reflection geometry. The  $\Phi_1$ -rotation was not used in this experiment. The sample alignment was conducted by means of an  $xyz$ -translation table and a laser and CCD camera system focussing to the centre of the diffractometer.

The specimen's texture information was obtained from a number of pole figure measurements, namely from the selected (hkl) reflections listed in table 6.2. The positions of the (hkl) reflections have been determined by means of a  $2\theta$ -scan. A copper anode and a setting of 40 kV and 45 mA have been used to generate X-rays. The reflected intensities have been detected by means of secondary (001) LiF monochromator which reflects X-rays of one

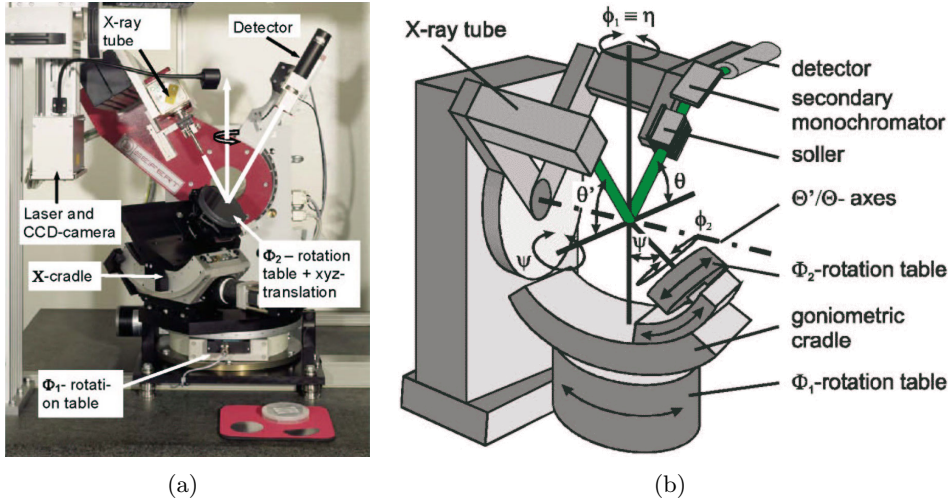


**Figure 6.5.:** Photograph (a) and schematical setup (b) of the ETA X-ray diffractometer after [Haase et al., 2001].

wavelength to the direction of the scintillation monitor. For each of the pole figure steps, the exposure time was 15 s. In contrast to the neutron measurements presented above, where Debye-Scherrer ring sections have been detected, the X-ray diffractometer is only capable to measure single intensity values with its detector. The table also shows, that the X-ray penetration depth in the sample material deviates strongly (between 1  $\mu\text{m}$  and 25  $\mu\text{m}$ ) depending on the selected Bragg angle and on the sample orientation, i.e. the tilting angle. The values listed here have been calculated according to the descriptions presented in [Noyan et al., 1995] for example.

Instrument setting	selected reflection	$2\theta$ setting	Penetration depth
<b>ETA</b>	(111)	$38.18^\circ$	1.08 – 12.48 $\mu\text{m}$
anode: Cu	(200)	$44.43^\circ$	1.25 – 14.43 $\mu\text{m}$
voltage: 40 kV	(220)	$64.81^\circ$	1.78 – 20.46 $\mu\text{m}$
current: 45 mA	(311)	$77.97^\circ$	2.09 – 24.01 $\mu\text{m}$
exposure time: 15 s	(222)	$82.17^\circ$	2.18 – 25.08 $\mu\text{m}$

**Table 6.2.:** Experimental parameters for the texture measurement on the ETA X-ray diffractometer. The X-ray penetration depth deviates depending on the selected Bragg angle and on the sample orientation.

According to a comparison with the Bragg edge measurements presented in the next sections, the obtained pole figures have to be normalised to m.r.d. such as shown above (section 6.1.2). However, due to the reflection geometry incomplete pole figures with the

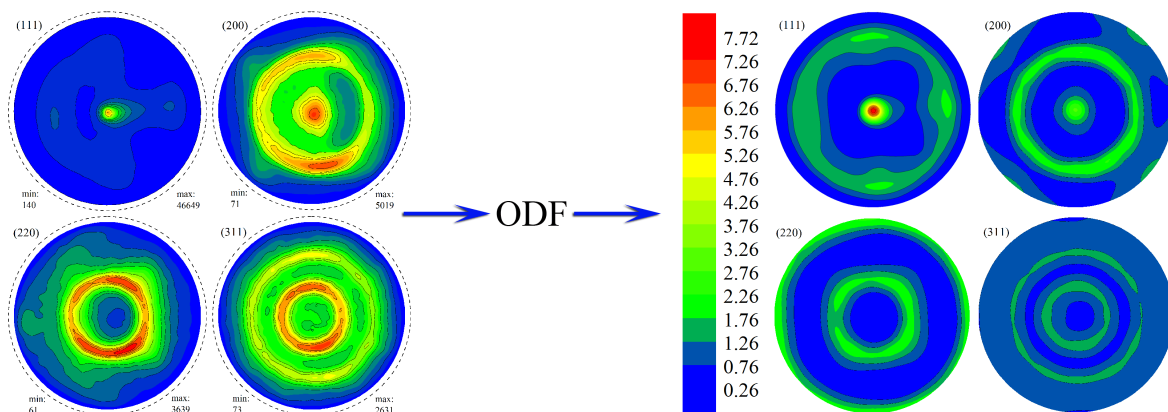


**Figure 6.6.:** The measured pole figures (left) with an upper limit of  $\Psi = 85^\circ$ , indicated by the outer dashed circles, have been used to calculate the ODF. From that, the full pole figures (right) have been reconstructed to achieve a consistent normalisation to m.r.d.

upper limit of  $\Psi = 85^\circ$  have been measured. Hence, an ODF calculation was required to reconstruct the information necessary for a consistent normalisation. For this purpose, the MTEX toolbox for quantitative texture analysis [Bachmann et al., 2010] has been applied. The measured pole figure files were imported to the software, which then calculated the ODF. The resulting pole figures exhibit the same circular symmetry as stated above and will be used in section 6.4.1 as a reference for the transmission studies. Figure 6.6 visualises this process. The intensities of the measured pole figures are shown as X-ray detector counts (min/max), whereas the reconstructed pole figures are normalised to m.r.d.

## 6.2. Texture Mapping with Radiography on CONRAD

The cylindrical aluminium sample presented above (figure 6.1) was further investigated on the neutron tomography machine CONRAD. Here, the neutron beam attenuation has been measured in transmission geometry (detector position at  $2\theta = 0^\circ$ ). Using the monochromatic instrument option, a series of measurements has been performed to analyse the texture influence on the transmitted neutron beam. As the following experiments capture the beam attenuation with the CCD camera system (see instrument description in section 4.1), all data has been determined from radiographic images.

### 6.2.1. Bragg Edge Determination

As a first step towards the analysis of the preferred crystallographic orientation using Bragg edge information, a wavelength scan was performed. Here, the double monochromator was applied to select well-defined wavelengths, i.e. the monochromator crystals were orientated according to a Bragg angle in order to choose a wavelength as presented in section 4.1. Scanning the crystal orientations, radiographic images have been captured for a series of wavelength positions. For a rough determination of the sample's Bragg edge position, the wavelength was shifted from 3 Å to 5 Å in steps of 0.02 Å. For each of these steps, flatfield images (open beam measurements) have been measured additionally. Thus, the incident intensity variation as well as the inhomogeneous screen illumination in front of the CCD camera could be corrected. The exposure time for each image was 200 s. The sample orientation for this initial experiment was set to the reference (rolling) direction determined by the diffraction analysis. Hence, the circular base area of the sample cylinder was transmitted as visualised by the radiographic images in figure 6.8.

The collected radiographic images have been normalised by their appropriate flatfields. Then, a region of interest was selected to cover the sample area inside the resulting images. Here, an area of around 15000 pixels was selected to calculate the mean value of their grey values [Jähne, 2005]. This is equivalent to the area of approx.  $(8 \times 8)$  mm<sup>2</sup> around the circle centre. The mean values are plotted in figure 6.7 according to their wavelength positions to represent the Bragg edge transmission spectrum of the aluminium sample. Here, the (111) Bragg edge can clearly be identified by means of the strong intensity changes around 4.6 Å. Moreover, a small variation around 4.0 Å can be seen as the (200) Bragg edge. This becomes even more clear if the lattice constant of aluminium [Witt, 1967],  $a = 4.0495$  Å, and Bragg's law (equation 2.3) are considered. The error bars in the diagram represent the standard deviation of the mean intensities. They are shown here to indicate, that the statistical measurement errors do not influence the Bragg edge spectrum that much. The two dashed vertical lines mark the wavelength positions and monochromator orientation respectively for the experiments presented next.



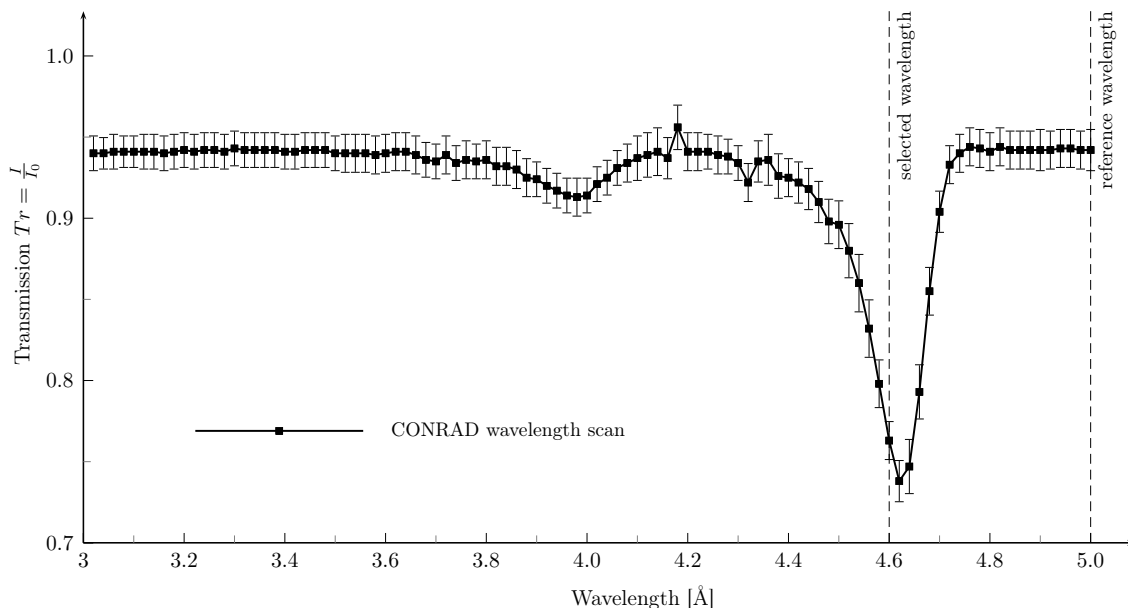


**Figure 6.7.:** Wavelength scan using the double monochromator setup on CONRAD. The transmission spectrum shows the (111) and Bragg edge of the aluminium cylinder sample. On the basis of this spectrum, two wavelengths were selected in order to perform additional measurements. The error bars indicate the standard deviation of the mean intensity values of a selected region of interest for each wavelength step.

### 6.2.2. Radiographic Texture Measurements

The initial wavelength scan presented above was used to identify a selection of wavelengths for the actual texture investigations with Bragg edge neutron transmission. The neutron wavelength was set close to the top of the Bragg edge. Here, the wavelength position  $\lambda_s = 4.6 \text{ \AA}$  was used to perform radiographic measurements with different sample orientations. Therefore, the sample was rotated around its diameter from  $0^\circ$  to  $90^\circ$  and measured in steps of  $5^\circ$ . The exposure time for each step was 200 s. Again, flatfield images have been taken to correct the incident intensity. A second run with the same settings, i.e. the sample rotation, but with a different wavelength of  $\lambda_r = 5.0 \text{ \AA}$  was conducted to provide reference images outside the Bragg edge area.

For each sample orientation step, the following image processing routines have been applied to the experimental dataset. After a flatfield correction for each individual sample orientation, the transmission images of  $\lambda_r$  have been used to normalise the transmission of

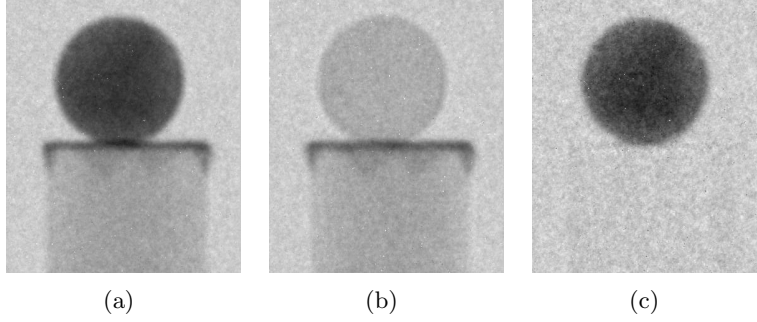


**Figure 6.8.:** *Thickness correction: The sample thickness influence on the attenuation signal was corrected for each step of sample rotation. (a) is the measurement at the Bragg edge position (4.6 Å). A reference measurement (b) with a wavelength outside the Bragg edge area (5.0 Å) was used to perform the correction. Finally, the resulting image (c) contains the information about the total neutron cross section without a thickness influence. The sample table is not visible anymore.*

$\lambda_s$  by equation 6.3:

$$\begin{aligned}
 Tr(\lambda_s) &= \frac{I_s}{I_{0,s}} = \exp(-\mu l) \\
 \frac{\ln(Tr(\lambda_s))}{\ln(Tr(\lambda_r))} &= \frac{-\mu_s l}{-\mu_r l} = \frac{\mu_s}{\mu_r}
 \end{aligned} \tag{6.3}$$

With respect to the same sample orientation, the neutron transmission path  $l$  through the sample is eliminated by means of this method. Thus, the different sample thicknesses corresponding to the orientations are no longer influencing the transmitted intensity. If both measurements,  $\lambda_s$  and  $\lambda_r$ , were conducted with the same instrument setup (sample table alignment), it is a convenient method to correct precisely the exponential attenuation relative to the sample dimensions for every image pixel. Hence, arbitrary sample geometries in any orientation can be corrected. The application of this method is shown by figure 6.8. As a secondary effect, the sample table in the resulting picture 6.8c has disappeared, i.e. the attenuation of this material is similar for both wavelengths. Although, the thickness correction results depend on the reference attenuation coefficient  $\mu_r$ , the (111) orientation can be analysed. This is possible, because  $\mu_r$  is expected to be constant for all sample rotation steps since it is measured outside the Bragg edge area. That means there is no coherent scattering contribution that could be affected by the preferred crystallographic orientation. Moreover, due to the normalisation to m.r.d.,  $\mu_r$  will disappear. Hence,  $\mu_r$  is not influencing

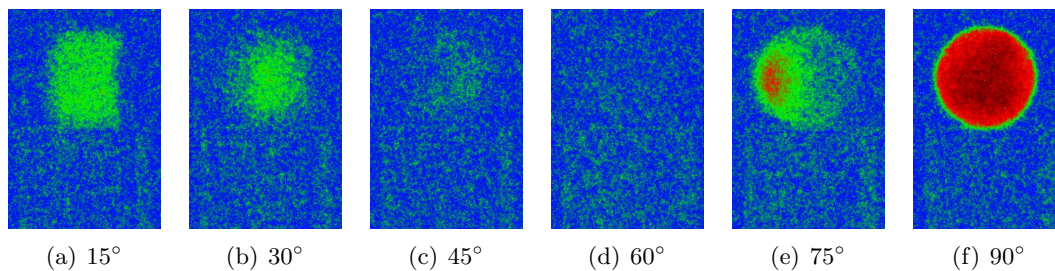


**Figure 6.9.:** Radiographic images after sample thickness correction. According to the sample orientation the transmitted intensity changes. The pictures are coloured to emphasise this effect.

the degree of texture that is determined here.

As an example, the resulting images are shown in figure 6.9 for selected sample orientations. The pictures have been coloured to emphasise the intensity changes according to the sample orientation after the thickness correction. In the figures, blue indicates a very small coherent elastic scattering contribution to the attenuation coefficient  $\mu_s$ , i.e.  $\frac{\mu_s}{\mu_r} \approx 1$ , while red and black denote high values for  $\mu_s$ . It is apparent, that the transmitted intensity varies depending on the angle between the incident beam and the rolling direction of the sample. Thus, the influence of coherent elastic scattering could be demonstrated even in transmission geometry. The experiment showed that the tomographic setup on CONRAD can be applied to visualise texture effects. Moreover, a quantitative evaluation of the radiographic images, taking the calculation in 6.3 into account, has been performed as well. The results will be presented within a comparison (section 6.4.1) with all measurements presented in this chapter.

### 6.3. Transmission Spectroscopy on ENGIN-X

The textured aluminium sample was also investigated on ENGIN-X, at the ISIS spallation source. In combination with its transmission detector system (see section 4.2.2) the diffractometer was used for time-of-flight transmission measurements. Similar to the experiments on CONRAD presented above, the sample was rotated from  $0^\circ$  to  $90^\circ$  in  $5^\circ$  steps. In contrast to the CCD camera system on CONRAD the pixel resolution of the transmission detector on ENGIN-X is not comparable. However, the measured signal provides a full time-of-flight transmission spectrum with a better wavelength resolution. Hence, it was expected to resolve

more details inside the Bragg edge spectrum.

The aluminium sample was aligned such, that its centre and the rotation axis have been mapped onto the pixel at the 5th column and the 7th row of the detector array. Using a 25 Hz chopper setting, for each step the total count for beam current was 80  $\mu\text{A}$ , which is equivalent to an exposure time of 1 h. An open beam measurement without the sample has been conducted also. Therefore, the exposure time was approx. 1.5 h at 120.7  $\mu\text{A}$ . For the analysis of the experiment, the angular steps have been normalised by the open beam measurement taking the different total beam current into account. The resulting detector signal was converted from a time-of-flight signal  $t$  to a wavelength spectrum using the neutron path lengths  $L = L_1 + L_2$  with the de Broglie relation:

$$\lambda = \frac{h}{p} = \frac{ht}{m(L_1 + L_2)} \quad (6.4)$$

where  $p$  is the momentum and  $m$  is the mass of the neutron. The primary beam path  $L_1$  on ENGIN-X is 50 m. The pixelated detector system was placed closely behind the sample, in this case the secondary beam path  $L_2 = 6$  cm away from the rotation axis. The attenuation coefficient was resolved from the wavelength spectrum taking the different transmission paths of the individual angular steps into account. As the transmission of the centre pixel was considered, the path lengths relative to this pixel have been calculated. Here, the assumption was made that the cross section of the cylinder sample in the same plane of the detector pixel is equivalent to a rectangle with edge lengths  $a = 11.8$  mm (diameter of the cylinder) and  $b = 8$  mm (height of the cylinder). Hence, the orientation-dependent transmission paths  $l(\alpha)$  are determined by:

$$l(\alpha) = \begin{cases} \frac{a}{\cos \alpha} , & \alpha < \arctan\left(\frac{b}{a}\right) \\ \frac{b}{\sin \alpha} , & \text{otherwise} \end{cases} \quad (6.5)$$

where  $\alpha$  is the sample rotation angle. The basic principle of this calculation is shown in figure 6.10. Thus, the attenuation coefficients can be normalised according to the sample geometry and its orientations  $\alpha$  during the experiment. As an example, the resulting spectra for selected orientations have been plotted in figure 6.11. The diagram shows, that the

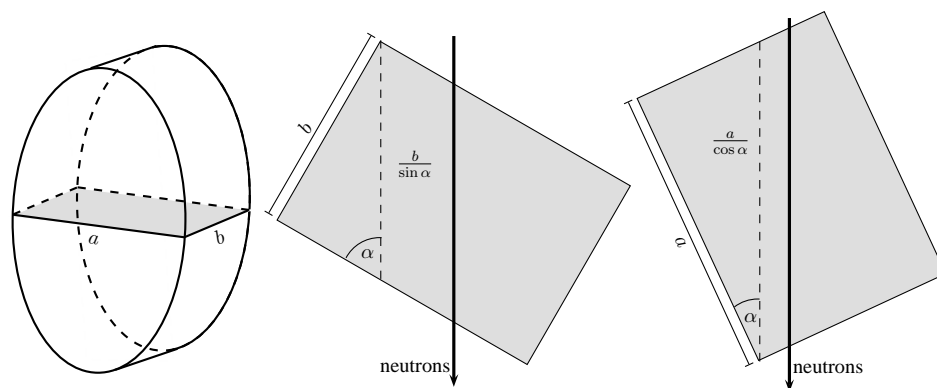


**Figure 6.10.:** Principle calculation of the neutron transmission path through the sample cross section depending on the cylinder rotation angle  $\alpha$ .

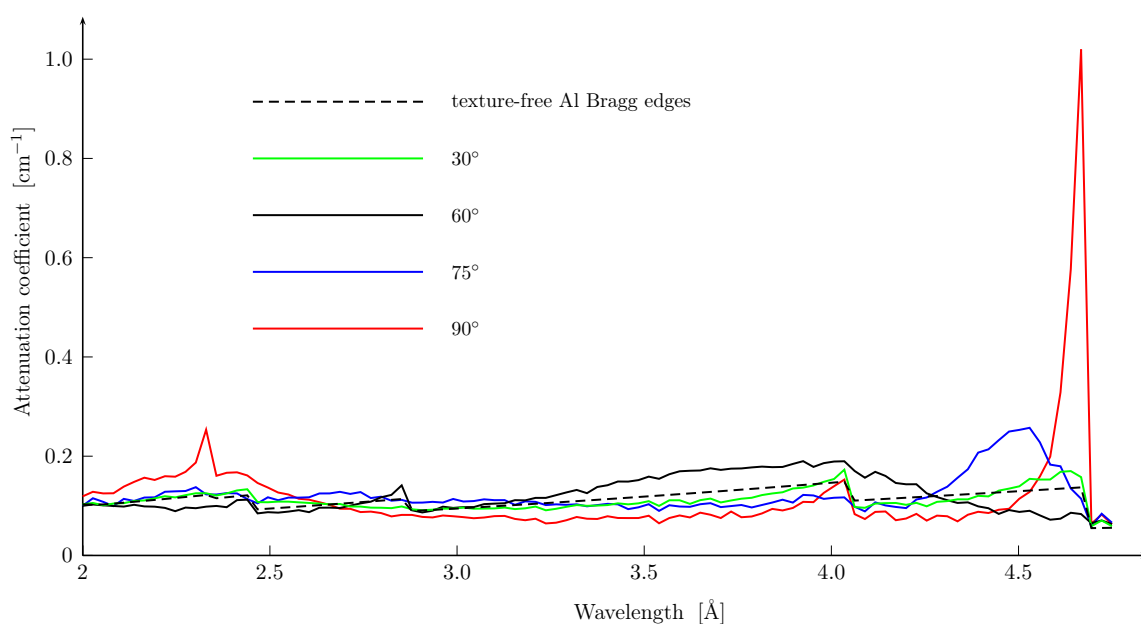


**Figure 6.11.:** Overview of Bragg edge spectra of selected sample orientations. The influence of preferred crystallographic orientations on the Bragg edge shape can clearly be seen as the shape of the Bragg edges changes enormously. The dashed line shows the texture-free Al curve calculated with *nxsPlotter*.

different sample orientations have a tremendous effect on the Bragg transmission edges. The transmission spectra differ strongly depending on the orientation angle. Under  $90^\circ$ , for example, the (111) edge has a very high amplitude, while it is deformed at  $75^\circ$  and disappears under  $60^\circ$ . In contrast, at  $30^\circ$  there is almost no effect to the Bragg edges compared to the theoretical aluminium spectrum (dashed line). Consequently, the influence of the sample texture has been demonstrated with the Bragg edge mode on ENGIN-X. Moreover, the transmission spectra provide a high wavelength resolution. For a quantitative

analysis, a wavelength position was chosen similar to the radiography approach described in section 6.2.1. The evaluation will be discussed in the following.

## 6.4. Evaluation of Results

In order to compare the results from the diffraction and transmission measurements, presented before, the datasets have been re-arranged using the same notation and normalisation. The pole figure diagrams from the conventional texture measurement method have been used as a reference dataset for the validation of the Bragg edge transmission experiments. As the sample was aligned differently, the sample rotation conducted in the transmission measurement is seen to be equivalent to the tilting process during the pole figure measurements (section 6.1). Hence, the tilting direction in diffraction mode and the rotation in transmission have been compared here.

### 6.4.1. Comparison of Complementary Measurements

The pole figure intensities from the (111) reflection have been integrated along each circle to represent a single intensity value for each tilting position. The intensities were normalised to multiples of a random distribution (m.r.d.). Additionally, the equivalent (222) lattice reflection, measured on STRESS-SPEC, has been evaluated. Thus, the conventional diffraction experiments could be checked to be consistent. As reported in Santisteban et al. [2006b], the integration around the rings of a pole figure  $P_{hkl}$  corresponds exactly to the number of crystallites that will also affect the value of the coherent elastic scattering cross section  $\sigma_{coh}^{el}$ . Further, the texture influence was described as follows [Santisteban et al., 2006b]:

$$R(\lambda, d_{hkl}) = \int_0^{2\pi} P_{hkl}(\alpha, \beta) \quad (6.6)$$

$$\sigma_{coh}^{el}(\lambda) \Leftarrow \sigma_{coh}^{el}(\lambda) R(\lambda, d_{hkl})$$

Taking the normalisation to m.r.d into account,  $R(\lambda, d_{hkl})$  equals a weighting of  $\sigma_{coh}^{el}$  based on the number of crystallites with orientations  $\alpha$  and  $\beta$ . This is similar to the March-Dollase treatment, which becomes even more clear if the radius  $\beta$  of the pole figure  $P_{hkl}$  is

considered to be the individual grain orientation angle defined by equation 3.25. Hence, the implementation of the March-Dollase model in transmission geometry has been tested as well. The application of the texture model and the comparison with the conducted experiments will be presented in section 6.5. Now the main interest is in the comparison of the experimental results. According to the equations 6.6, the Bragg edge transmission results must fit to the integrated pole figure intensities. Consequently, the integration values are obtained at first. The gradients representing the tilting direction of the neutron diffraction experiments are plotted as dashed graphs in the diagram 6.12.

The Bragg edge results have been treated. From the scaled radiographic images measured on CONRAD, i.e. normalised with the 5.0 Å measurements, a region of interest was selected to collect the grey values from the sample area for each angular step. The mean values and their standard deviations were calculated and stored relative to the sample position. By means of the nxs routines, the theoretical neutron cross sections for Al (figure 6.13) can be calculated. Thus, it is further possible to correct for the influence of other than the coherent elastic scattering part  $\sigma_{coh}^{el}(\lambda)$  of the total cross section, such that their impact on the texture result disappears. Using the values from figure 6.12, the difference  $\sigma_{total}(\lambda) - \sigma_{coh}^{el}(\lambda)$  for the measured 4.6 Å position and a value for the attenuation coefficient at 5.0 Å can be determined in order to eliminate the other scattering and absorption cross sections from the evaluated radiographic images (figure 6.9). Accordingly, the coherent elastic scattering cross section is available for each step of the sample rotation to represent the texture. Again, a normalisation of  $\sigma_{coh}^{el}(\lambda)$  to m.r.d. has been applied. Similar to the wavelength position selection in section 6.2.1, the wavelength spectra, captured on ENGIN-X, were used to define a Bragg edge position and to record the attenuation coefficient over the sample rotation. Here, the wavelength position of 4.6 Å was used, which is very close to the edge. The treatment to correct for the other cross section contributions has been performed as well. For both Bragg edge transmission experiments, the variation with the sample rotation is plotted with dotted solid lines. The diagram (figure 6.12) shows the integrated pole figure intensities from the neutron diffraction measurements and the Bragg edge transmission results respectively. Compared to the reference data, taken from the conventional diffraction texture experiments

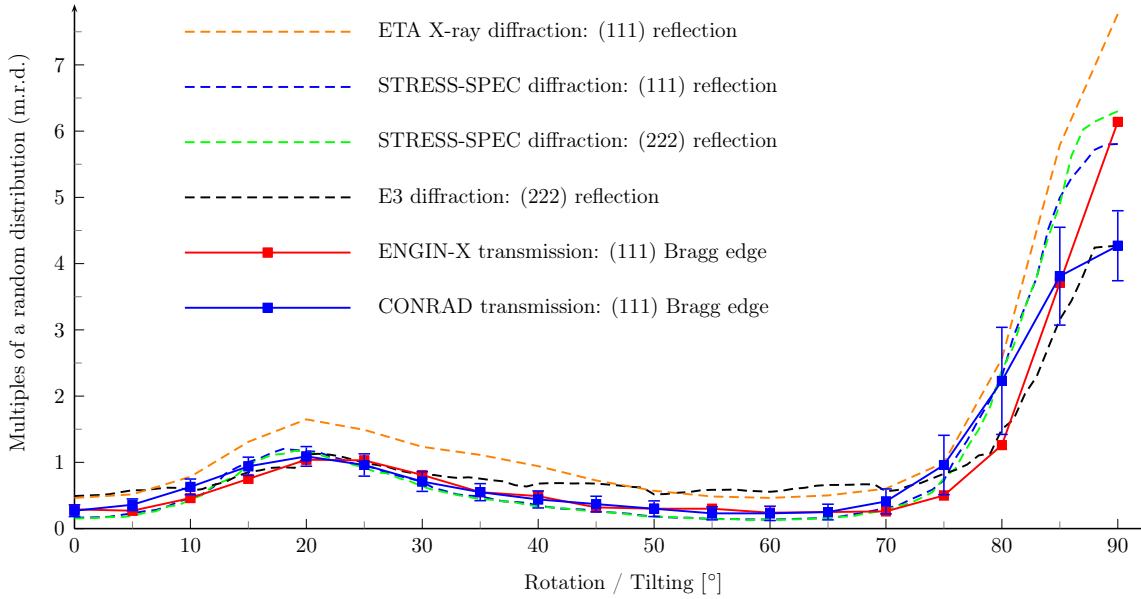


**Figure 6.12.:** The diagram shows the comparison of texture analysis using Bragg edge transmission and the conventional diffraction method. The dashed curves represent the diffraction measurements and the analysis over the tilting direction, while the dotted solid lines result from the transmission experiments with sample rotation. All results have been normalised to multiples of a random distribution.

on ETA, STRESS-SPEC and E3, the transmission experiments show a reasonable agreement. The intensity variations with the sample rotation position are clearly visible for all measurements. But differences in magnitude, especially for the preferred orientation direction at  $90^\circ$ , are visible also.

#### 6.4.2. Possible Sources of Error

Referring to the diffraction measurements, there is already a noteworthy difference between the results of E3 and STRESS-SPEC, although both have been used as a reference. Consequently, they should be equal. The variations occur due to different instrument settings. The work of Randau & Brokmeier [2009] for example, presents the influence of different pole figure windows to the results of quantitative texture analysis. A pole figure window is defined by the instruments aperture taking the beam divergence, the slit system, the monochromator system and the Bragg angle into account. It denotes the maximum pole figure accuracy and is given in values of an angular span  $\alpha \times \beta$ , i.e. a measurement using a pole figure grid smaller than the  $\alpha$  and  $\beta$  would not be useful. Here, the Si monochromator on E3, for



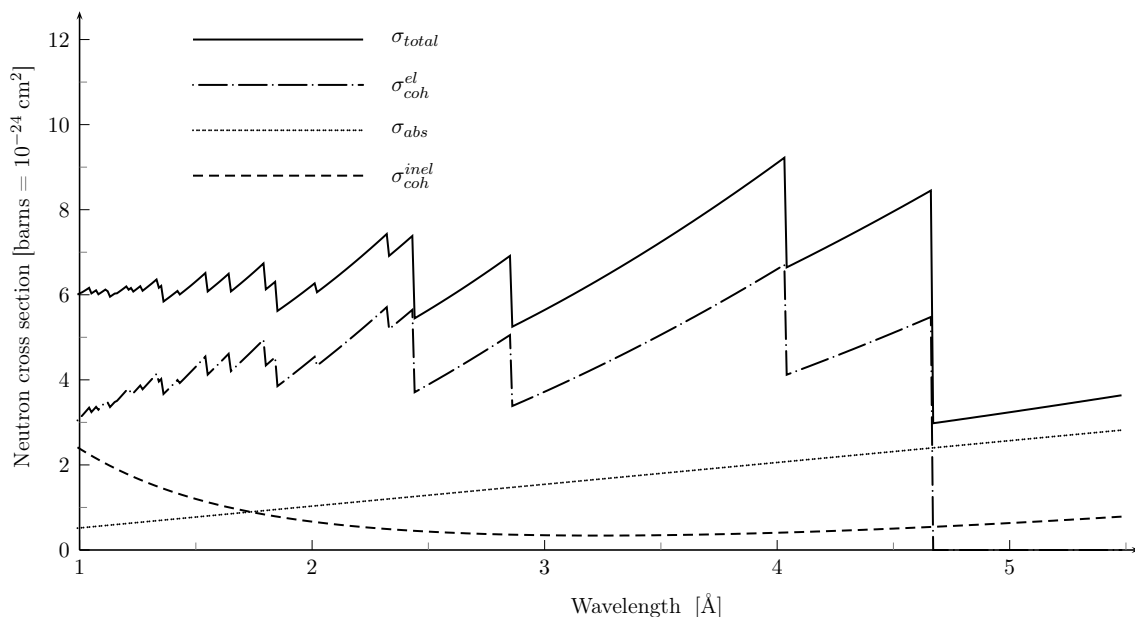


**Figure 6.13.:** Theoretical neutron cross sections for an Al unit cell (fcc) calculated by the *nxsPlotter* software.

instance, provides less beam divergence than the Ge monochromator on STRESS-SPEC and therefore a higher precision in detecting a grain orientation. But in contrast, the probability for a grain to be detected using the same pole figure grid is lower. Hence, fewer neutrons will be scattered and the sharpness of a texture due to little misalignments may get lost. A continuous pole figure measurement would ensure a rather comprehensive coverage of the crystallites in the specimen [Randle & Engler, 2000]. However, using the same technique on different machines may cause different results with respect to a quantitative comparison. Details about the error values are not specified in the diagram as the relative errors from the Gaussian fitting in StressTexCalculator for each pole figure point are very small. The maximum error is 7 % while the mean error is 3 %, which means that the statistical inaccuracy is not much effecting the results. Moreover, the X-ray results (ETA) deviate from the neutron diffraction measurements, which occurs basically due to the low penetration depth. In the neutron experiments the whole sample volume was illuminated, i.e. the evaluated texture information represents the average properties of the sample. This is comparable to the Bragg edge studies as the radiographic projections also average the information. In contrast to that, the ETA results only contain information from the sample surface (1  $\mu\text{m}$  - 25  $\mu\text{m}$ ). Nevertheless, the resulting pole figures coincide with the neutron measurements

which shows that the preferred crystallographic orientation is homogeneous over the whole sample, i.e. global texture. Consequently, the plotted gradients in figure 6.12 show the same trends with insignificant differences.

Towards the Bragg edge studies, the best fit to the reference measurements results from the ENGIN-X transmission experiments. Here, the red curve in figure 6.12 lies between the results of both diffraction instruments and even the maximum at  $90^\circ$ , i.e. the rolling direction, is comparable. A statistical error is given by the detector electronics. As the error values in the Bragg edge region are in the range of 1.3 % and 2.1 % the error bars are not shown explicitly in the diagram. Altogether, the evaluation of ENGIN-X transmission spectra provide a very good agreement. The deviation to the diffraction method is as small as the difference between both diffractometers using the same method. The CONRAD results vary more from the reference. In the rolling direction, the intensity differs with a factor of around 1.4, which is similar to the deviation between E3 and STRESS-SPEC. Altogether, the amplitude of the blue dotted solid curve seems to be reduced compared to the others. The error bars indicate the standard deviations determined for each sample orientation when the grey value averaging has been performed inside the selected region of interest (see section 6.2.1). Hence, the error range shown here is related to the statistical errors. However, a larger error occurs from the double monochromator device on CONRAD. On the one hand, there is the large peak width that follows from the mosaicity of the monochromator crystals. This means the wavelength resolution at CONRAD, compared to ENGIN-X, is very weak. The given ratio of  $\frac{\Delta\lambda}{\lambda} = 3\%$  covers a broad region next to the selected wavelength. Thus, the captured intensity close to the Bragg edge position ( $4.6 \text{ \AA}$ ) is smoothed by its environment, i.e. the region after the Bragg cut-off is also included in the signal. Necessarily, the evaluated attenuation coefficient is lower and therefore the texture is never as sharp as measured on ENGIN-X. Likewise, the wavelength spread and the beam divergence enlarge the angular detection range of the reflected neutron intensities, which is equivalent to an increase of the instrument's pole figure window. Thus, the influence of the preferred orientation direction on the transmitted beam is visible from a wide angle of view. For example in figure 6.9 at  $75^\circ$ , the evaluated attenuation coefficients vary depending on the local position within the

beam window due to this effect. As a result, the error bars in figure 6.12, that represent the standard deviation of the measured grey values, are increased in that region (from  $75^\circ$  to  $90^\circ$ ) because of this instrument influence. On the other hand, the higher order reflections reduce the detected attenuation as well. Especially in the region of  $4 \text{ \AA}$  to  $5 \text{ \AA}$  the second order reflections between  $2 \text{ \AA}$  and  $2.5 \text{ \AA}$  have an increasing effect due to the increasing flux density (see figure 4.1). There, the total neutron cross section for aluminium is lower, which decreases the measured attenuation a bit more. Consequently, the analysed texture degree is smaller. Both monochromator properties and their influence on the Bragg edge transmission spectrum have been discussed before in section 5.4.1. However, the tendency of the intensity change due to the sample texture is apparent as well.

## 6.5. March-Dollase Simulations

In chapter 3, the theoretical texture influence on the Bragg edge shape has already been taken into account. Here, the implementation of the March-Dollase texture correction in section 3.4 has been applied within the McStas neutron simulation. Therefore, the Bragg edge sample module and the interface functions to utilise texture parameters have been tested. Thus, the March-Dollase implementation has been validated with the experimental results presented above.

Consulting the ENGIN-X transmission spectrum (figure 6.11) at the sample orientation of  $90^\circ$ , the `nxsPlotter` program was used to find an agreement between the measured and a calculated Bragg edge spectrum. Therefore, the March-Dollase implementation has been tested with the software. The graphical user interface provides a quick opportunity to test different input parameters and visualise the resulting neutron cross sections. Thus, the texture influence could be tested easily. Taking the ENGIN-X results analysed above into account, the (111) lattice reflection shows a strong preference in the direction of the cylinder axis. Hence, this preferred crystallographic orientation has been applied to the weight function of the March-Dollase model. In figure 6.14, the tests have been extended to the McStas simulation of the ENGIN-X instrument. The Bragg edge sample module has been modified to use the `addTexture` function (see section 3.4.2) to a virtual aluminium sample.

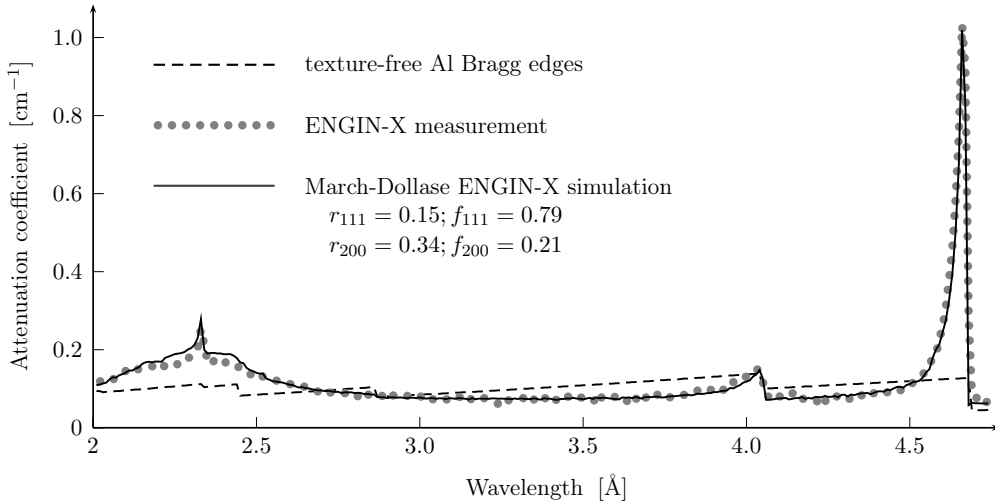


**Figure 6.14.:** *The texture influence on Bragg edges: Compared to the texture-free Bragg edge spectrum (dashed line), the simulated and measured ENGIN-X spectrum exhibit huge differences according to the attenuation coefficient.*

The March-Dollase correction will then be applied to the coherent elastic scattering cross section calculation and therefore to every neutron hitting the sample. As a result, a further simulation module has been created in order to test the March-Dollase parameters within an emulation of existing neutron instruments. The diagram 6.14 shows the comparison of the measured and simulated ENGIN-X machine applying the textured aluminium specimen. The results of the simulation and real experiment as well as the texture-free Bragg edges are plotted in terms of the attenuation coefficient for this textured aluminium sample. Using a March factor of  $r_{111} = 0.15$ , the Bragg edge shape changes intensely. The diagram exhibits a good agreement especially for the (111) Bragg edge. Moreover, the (222) edge at  $2.34 \text{ \AA}$  is effected by this influence. Due to the equivalency of lattice symmetry, the attenuation coefficients in front of the edge positions increase strongly. For both reflections, the (111) and (222), the same type of slope is clearly visible for the ENGIN-X measurement as well as for the McStas simulation. However, the spectrum is compared with the texture-free Bragg edges in order to emphasise the texture effect on Bragg edges once more. Although the (111) edge already provides a good fit, the spectrum would still have misfits at  $4.05 \text{ \AA}$ . Hence, a second preferred orientation at (200) has been applied to the March-Dollase simulation in this McStas run. Consequently, the diagram plot of the simulation agrees to the measured ENGIN-X spectrum. Therefore, a value of  $r_{200} = 0.34$  was used. Finally, the fractions of

grains provided with one of the two selected preferred orientations have been selected. For the complete ENGIN-X transmission simulation, they have been chosen to be  $f_{111} = 0.79$  and  $f_{200} = 0.21$  respectively. The only deviation between measured and simulated curves can be obtained around the area of the (222) Bragg edge. Although both plots follow the same gradient in principle, differences around  $2.34 \text{ \AA}$  are revealed. A possible explanation can be found by the contributions of the reflections not mentioned previously. Thus, the (220) and (311) Bragg edges at  $2.86 \text{ \AA}$  and  $2.44 \text{ \AA}$  respectively, could be recognised as contributing towards a March-Dollase correction as well. However, including their correction calculation would increase the McStas computation time.

In order to validate the radiography measurements, the same March-Dollase correction parameters have been applied to a McStas simulation of the CONRAD instrument. In particular, the double monochromator option, which was presented in section 5.4.1, has been used in combination with the new textured Bragg edge sample component. Similar to the real experiments, the simulation has been performed from  $3 \text{ \AA}$  to  $5 \text{ \AA}$  in  $0.02 \text{ \AA}$  steps. Including the flatfield measurements for each wavelength step, the simulation was executed 200 times. Again, the final results have been converted to attenuation coefficients. The diagram in figure 6.15, shows a comparison of the CONRAD texture measurements and its McStas simulation. In the first instance, the comparison exhibits a significant difference for all wavelength positions, which appears as a shift along the y-axis. A reason for this can be found by the peak width of the wavelength selection (mosaicity) and the higher order reflections of the double monochromator. As stated in section 5.4.2 a wavelength-dependent reflectivity profile is not known for the monochromator crystals. Hence, it is possible that the contribution of the simulated higher order reflections is higher than for the real one. In this case, the Bragg edge curve would be shifted such as shown by the simulation. However, it is also apparent that the (111) and (200) Bragg edges appear in the same way. For both, the simulation and the measurement, the Bragg edges are broadened likewise. Moreover, the Bragg edge amplitudes are comparable. The extinction of the (111) Bragg edge, for instance, has a strong impact on the textured sample. There is a distinct difference between the maximum attenuation measured on CONRAD and ENGIN-X, which

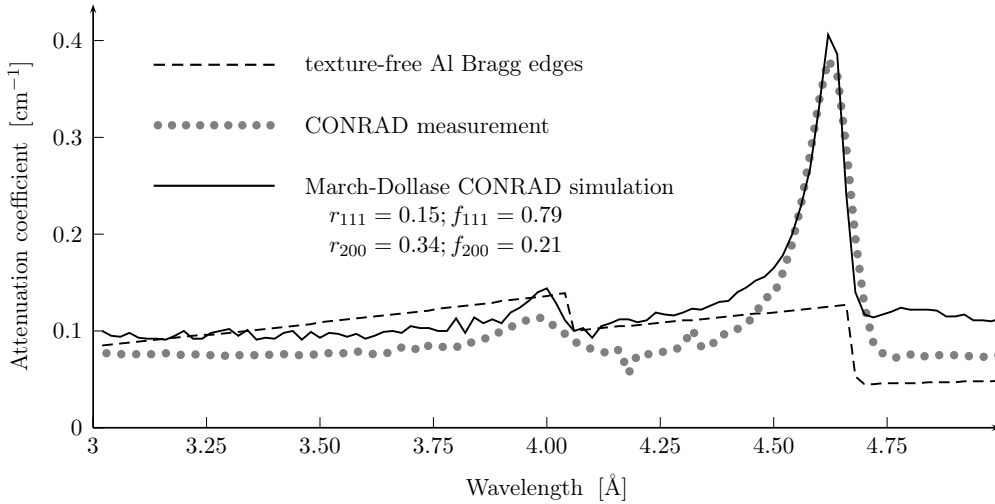


**Figure 6.15.:** *The texture influence on Bragg edges: Compared to the texture-free Bragg edge spectrum the simulated and measured spectrum exhibit huge differences according to the attenuation coefficient.*

is confirmed by the McStas instrument simulation. The systematic error on CONRAD due to the monochromator setup has been emulated and showed similar results. Likewise, the validation of the simulation model using the March-Dollase approach was demonstrated. As a result, the texture degree of a sample obtained from measurements on CONRAD is always smaller than of those measured on ENGIN-X for example. Nevertheless, a possible way of reconstructing the texture degree was shown with McStas.

## 6.6. Conclusion

In this chapter, the preferred crystallographic orientation of an Al cylinder sample has been evaluated by means of different neutron measurement techniques. The pole figure diffraction measurements have been conducted to provide a reference dataset from a traditional texture method. The results exhibited a symmetric fibre texture. In order to investigate the aluminium sample cylinder with Bragg edge neutron transmission, the CONRAD tomography machine and the ENGIN-X diffractometer in combination with the transmission detector were used. Thus, a time-of-flight signal and radiographic images respectively have been analysed with regard to the characterisation of the same sample. For the analysis of the Bragg edge transmission experiments the reference pole figure data has been taken into account. With regard to the presented aluminium sample, the comparison showed that the

Bragg edge method is reliable with respect to a quantitative data analysis. Taking the difference between the two diffraction measurements on E3 and STRESS-SPEC into account, the Bragg edge transmission method equally enables conclusions to be drawn regarding preferred orientations within a specimen. The best fit to the diffraction results is obtained from the ENGIN-X measurements. The differences to the CONRAD results were investigated using the McStas neutron instrument simulation. Consequently, the March-Dollase texture correction of the coherent elastic scattering cross section was applied in combination with the appropriate McStas instrument model. For both, the ENGIN-X and CONRAD simulation, the same March-Dollase parameters have been applied. The McStas simulation showed a good agreement with the measured results. The deviations of the CONRAD results compared to the other experiments have been reconstructed.

As stated in Vogel [2000], so far an experimental validation of the texture model was still missing. In the present work the March-Dollase model was implemented and included in McStas instrument simulations. For the case of the fibre texture of the aluminium cylinder, the results of the measurements conform to the simulation of both, the time-of-flight and the radiography instruments. Hence, the March-Dollase model is evaluated to be a reasonable tool for the analysis of Bragg edge texture experiments. Although, the radiography measurements provide a smaller texture degree than the ENGIN-X data, if the normalised intensities (m.r.d) are considered, the results have been reconstructed with the help of the texture simulation. Related to that, the wavelength-selective option on CONRAD becomes even more a beneficial tool for the investigation of engineering materials. With the texture properties a further instrument feature has been demonstrated. For the first time, the crystallographic texture was visualised by means of radiographic images. The intention to quantitatively determine the sample texture with Bragg edge transmission has been reached. Combined with the high spatial resolution, the radiography images further allow the investigation of local changes in the Bragg edge spectrum. Thus, local texture variations could also be visualised with the transmission method.

The March-Dollase approach was reported to be successful according to the evaluation of transmission experiments. Nevertheless, more complex texture corrections may be needed to

allow the analysis of Bragg transmission edges from arbitrary samples. Here, a very simple axial symmetric fibre texture has been investigated and agreed with a simulation model for the orientation at  $90^\circ$ . However, for any other sample orientation it was difficult to achieve good agreement with the March-Dollase model. There were no further March factors found to match exactly with the remaining transmission spectra measured on ENGIN-X (figure 6.11), which reveals the weaknesses of the model. With regard to the analysis of diffractogram data, more powerful models exist in programs such as MAUD [Lutterotti, 2000] for example. In particular, another correction may be needed if the sample has other than cylindrical symmetry [Larson & Von Dreele, 2004]. Hence, an implementation of spherical harmonics [Schaeben & Boogaart, 2003] or the WIMV model [Matthies & Vinel, 1982] with respect to the Bragg edge transmission geometry could improve the data analysis for more general cases.



## Local Strain Properties

The Bragg edges occurring in the transmission intensity spectrum are related to the crystallographic structure and the lattice parameters of a sample material. Similar to a Bragg peak measured with neutron diffraction, the position of a Bragg edge is connected with the lattice spacing of a specific reflection by the relation  $2d_{hkl} = \lambda$ . Thus, one could measure lattice parameters by Bragg edge neutron transmission. Investigating the variation of a Bragg edge position, the different lattice spacings could be applied to strain and stress analyses, which is a common method on residual stress and strain diffractometers. This chapter describes the approach of measuring strain with Bragg edge neutron transmission. Based on a standard residual stress sample a simulation is created to perform Bragg edge studies. Moreover, experiments on CONRAD and ENGIN-X are performed to test the feasibility of this method.

### 7.1. A Standard Residual Stress Sample

#### 7.1.1. VAMAS Al Ring and Plug

For the analysis of residual stress and strain measurements with neutron transmission, a comparison to the conventional diffraction method is useful. Therefore, a reference sample already measured with neutron diffraction has been investigated. Here, the results of a VAMAS TWA20<sup>1</sup> round-robin exercise have been used for the evaluation of the Bragg edge transmission measurements. Initially, an aluminium shrink-fit ring and plug sample [Webster, 2000] was prepared to present a situation of practical importance. Residual stresses have

---

<sup>1</sup>Versailles Project on Advanced Materials and Standards (VAMAS): The TWA20 program is concerned with residual stress measurements by neutron diffraction.



**Figure 7.1.:** Photograph of the aluminium (Al 7050) shrink-fit ring and plug taken from the VAMAS report [Webster, 2000]. Left: the joined ring and plug provided with residual stresses. Right: a reference plug for  $d_0$  measurements.

been introduced elastically by the adoption of an interference fit. Therefore, an oversize plug was cooled down to fit into the ring and afterwards the assembly was returned to room temperature. The sample height and diameter are 50 mm each (ring and plug). A photograph of both is shown in figure 7.1. Furthermore, a reference plug of 25 mm diameter is provided to measure the reference lattice parameter. It was fabricated from an Al 7050 rolled plate.

### 7.1.2. Reference Strain Values

The ring and plug sample was analysed within the VAMAS round-robin exercise by neutron diffraction at 18 different neutron sources. Thus, a reliable set of reference data can be used for a comparison with studies being concerned with this specimen. With neutron diffraction the residual stresses have been obtained by measuring lattice strains. By means of measuring the diffraction angle (in case of constant wavelength measurements) or the neutron time-of-flight (in case time-of-flight measurements), the strain is calculated by the signal change relative to a reference value (see equation 2.9). Due to the cylindrical sample symmetry the three principle directions to determine the stress state coincide with the radial, hoop and axial directions. The neutron diffraction measurements have been conducted along the sample diameter to map the strain gradient. The reference values, i.e. the stress-free lattice spacing  $d_0$ , are obtained from the reference plug for all three principle directions. Then, the obtained lattice strains are used to calculate the radial, hoop and axial stresses with respect to the elastic modulus and Poisson's ratio. The VAMAS report [Webster, 2000] provides a detailed

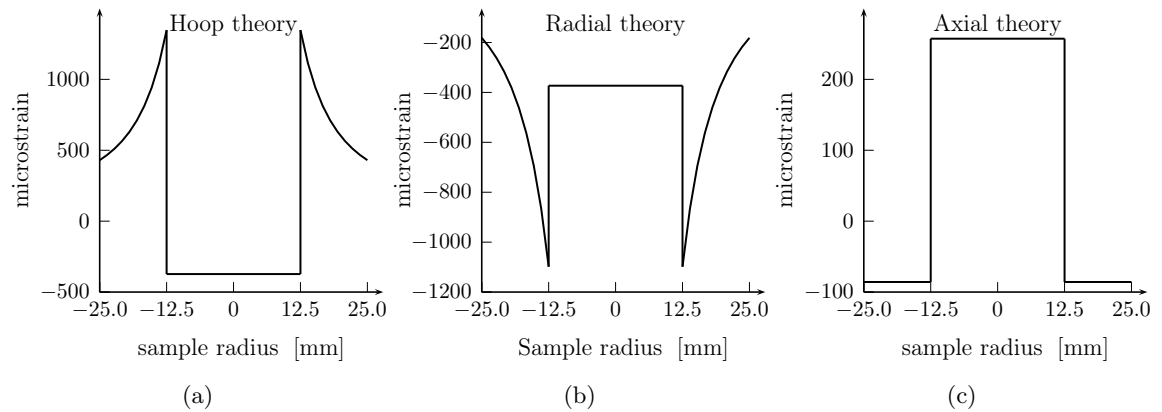


**Figure 7.2.:** Theoretical ring and plug strain values for the hoop (a), radial (b) and axial (c) directions after [Webster, 2000] plotted against the sample radius.

explanation of this calculation. Moreover, an analytical solution, based on the elasticity theory [Southwell, 1941], for the residual stresses in the ring and plug sample is presented. This takes into account the manufacturing parameters (the sample radius and the pressure exerted at the ring-plug interface) and gives the opportunity to compare the measured results. Using this calculation, the theoretical strain values for the three principle directions are as plotted in figure 7.2. All three principle directions point out the discontinuities in the ring-plug interface at  $\pm 12.5$  mm sample radius.

The strain values presented in the diagrams have been used in the following sections to enable a comparison with the Bragg edge transmission measurements. Moreover, the data obtained here has been applied within a simulation of the ring and plug measurement. In order to support the descriptions presented next, it should be noted that any of the following Bragg edge simulations and measurements has been conducted with the ring and plug sample standing on the instrument table with its orientation as is shown in the photograph 7.1. Terms such as effective lattice spacing and projected strain will be derived and investigated.

## 7.2. Strain Implementation in McStas

In the following, the ring and plug data discussed above will be applied to a comparison with results obtained by the Bragg edge neutron transmission method. Therefore, the parameters from the diffraction analysis and the theoretical strain values from figure 7.2 respectively will

be used. This section introduces the fundamental difference between the transmission and diffraction results. By means of Bragg edge measurements, the so-called projected strain will be evaluated and compared with theoretical examinations. In order to provide an understanding of the projected strain, its calculation towards the neutron transmission geometry will be explained. Then, the ring and plug strain values will be implemented into the simulation of the CONRAD and ENGIN-X instrument.

### 7.2.1. Application of Local Sample Properties

The parameters of the ring and plug sample have been applied to the Bragg edge sample simulation prepared in chapter 5. The simulation takes advantage of specific crystallographic information given by an input file, such as presented in section 5.2.3 and in appendix C.2. Thus, the unit cell parameters and the lattice spacings could be initialised. Here, the influence of strains and stresses shall be simulated additionally. Hence, the initial lattice spacing defined globally within the unit cell initialisation is not valid anymore. Even more, it varies depending on the local position inside the sample. Moreover, it is defined by the local stress state simplified by the three principle strain directions. Therefore, the presented results from the neutron diffraction and the theoretical strain values for the hoop, radial and axial direction have been utilised here.

In order to enable a Bragg edge transmission strain simulation within McStas the initially created `BraggEdge_Powder` component was extended. Here, the simulation will be restricted to lattice spacing calculations according to a local position inside the ring and plug sample. However, any other local property changes could also be implemented. For example, the previously discussed texture information could vary depending on the local position inside the sample. Towards the strain, the hoop, radial and axial lattice spacing values relative to their sample radius position have been used as input parameters for the simulation. These values have been calculated before by means of the theoretical strain (figure 7.2), i.e. the reference lattice spacings  $d_0$  were applied. Further, the calculated lattice spacing values have been tabulated and stored to a file that will be used within the following simulations. The procedure of reading an input file during the McStas computation is similar to the routine

described in section 5.2.3. Again, the `read_table-lib` routines available in McStas have been included here. Similar to the input files used before, the unit cell parameters are stored as kind of a header information. In contrast, the individual atomic information has been moved to the header part as well. Details of the file structure can be obtained from the example listing given in appendix D.2. Here, the focus is on the tabulated lattice spacing values calculated before. Hence, the table read-out routines have been applied to assign the values to the principle sample directions for further computation within the simulation.

For the neutron cross section calculation, the lattice spacing parameters have been considered in the coherent elastic part (equation 3.9). Here, the hoop, radial and axial lattice distances have been applied to determine the lattice spacing in neutron transmission direction. At first, a random event point along the neutron transmission path inside the sample component is selected. According to the neutron position parameters, the position inside the sample is located by means of the cylinder radius  $r$ . Taking the notational convention in McStas into account that  $z$  is the forward neutron direction and  $x$  is perpendicular to the beam in the horizontal plane, the local radius position is calculated by:

$$r = \sqrt{x^2 + z^2} \quad (7.1)$$

Further, the radius position is used to determine the three principle lattice spacings from the input file table. Here, the  $d$ -values are stored with respect to discrete radius positions (see appendix D.2). Therefore, it is useful to interpolate between the listed values. The actual radius  $r$  is applied to look for the two neighbouring values  $r_a$  and  $r_b$  given in the input table. From these two positions the hoop, radial and axial lattice spacings  $d$  are determined for the current radius position by linear interpolation:

$$d = \frac{d_a - d_b}{r_a - r_b} (r - r_b) + d_b \quad (7.2)$$

Now, the effective lattice spacings can be calculated taking the neutron flight direction into account. In the neutron transmission direction of the given ring and plug setup the lattice spacing  $d_{tr}$  depends on the hoop  $d_{hoop}$  and radial  $d_{rad}$  components. The axial part is neglected

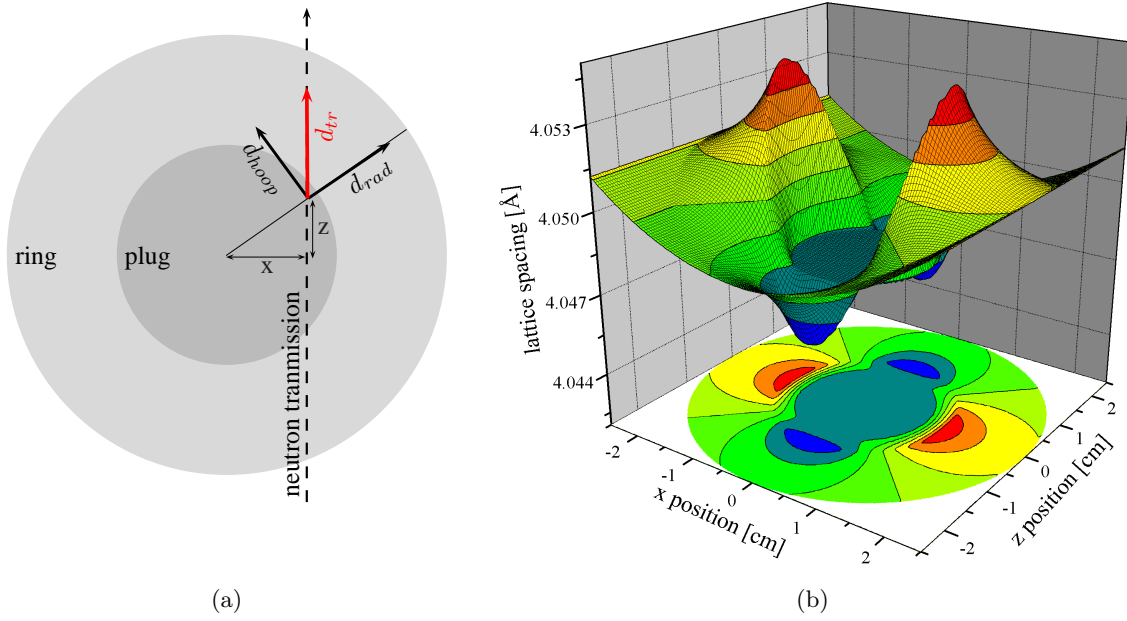


**Figure 7.3.:** Determination of the effective lattice spacing  $d_{tr}$  towards the neutron transmission direction  $z$  by means of the hoop and radial components (a). The diagram (b) shows a map of the resulting  $d$ -values, that will be used in the Bragg edge computation.

so far — a parallel neutron beam is assumed. The geometry of this calculation is visualised in figure 7.3a. Using a  $\sin^2 \psi$  approach, the lattice spacing is linear with the square of sine of the angle between two principle directions [e.g. Fitzpatrick & Lodini, 2003]. Hence,  $d_{tr}$  is determined by:

$$\sin^2 \psi = \frac{x^2}{r^2} \quad (7.3)$$

$$d_{tr} = (d_{hoop} - d_{rad}) \sin^2 \psi + d_{rad}$$

where  $\psi$  is the angle between  $d_{tr}$  and  $d_{rad}$ . In McStas, the lattice spacings in transmission direction  $z$  will be calculated for each neutron intersecting the sample component with respect to its local position. Hence, the values for  $d_{tr}$  vary with the local sample position. If a complete horizontal plane of the sample is penetrated by neutrons the circular plane can be used to visualise the effective lattice spacings relative to the specimen. Therefore, figure 7.3b shows a map<sup>2</sup> of effective  $d$ -values  $d_{tr}$  calculated by means of the theoretical hoop and radial strain for each local position inside the sample. The  $d$ -spacings were used for the neutron

<sup>2</sup>Due to limitations of the 3D representation the  $d$ -values have been extrapolated to the diagram boundaries. The contour plot at the bottom shows the correct sample geometry.

cross section calculation to enable the Bragg edge transmission simulation. According to the application of the nxs library routines, the individual  $hkl$  lattice distances are calculated for each neutron separately as the d-spacing differs at each position. Consequently, in McStas the  $hkl$  initialisation procedures have been moved from the INITIALIZE section to the TRACE section. Depending on the selected position along the neutron transmission path through the sample, the effective d-value is applied to the coherent elastic cross section calculation.

### 7.2.2. Projected Strain in Transmission Direction

The introduction of strain by means of the lattice spacing variation is a reasonable method as the d-values measured before with conventional diffraction can simply be applied to this simulation as an input file. Using the input file reading mechanism described above, the experimental results can be easily compared with the simulation. Another possibility would be to use the strain values  $\varepsilon$  as applied in [Abbey et al., 2009]. Then, the calculation of the effective strain  $\varepsilon(r)$  depending on the cylinder radius  $r$  is given by:

$$\varepsilon(r) = \varepsilon_{rad} \sin^2 \psi + \varepsilon_{hoop} \cos^2 \psi \quad (7.4)$$

For this case, the reference lattice distance  $d_0$  must be known in order to calculate the effective d-spacings and apply the neutron cross section calculation. The input file structure and the reading routines in McStas could be the same. However, the current simulation program is restricted to the case of cubic crystal systems. For the  $hkl$  lattice spacing calculation, the unit cell parameter  $a$  is assessed by the input d-spacing or strain values. This is possible, because in the cubic case this relation depends on one variable only. For any other case more parameters would be needed and the program routines must be changed. In [Daymond et al., 1999] for example, the same problem for the hexagonal case is discussed within a Rietveld refinement to fit stresses from diffraction patterns and resolve the unit cell parameters.

Altogether, the calculation of the effective lattice spacings in the neutron transmission direction for every single local sample position allows a theoretical consideration of signal detected behind the sample. Due to the interaction with a multitude of neutrons, a transmission detector represents an averaged signal containing all values of  $d_{tr}$  and  $\varepsilon_{tr}$  respectively

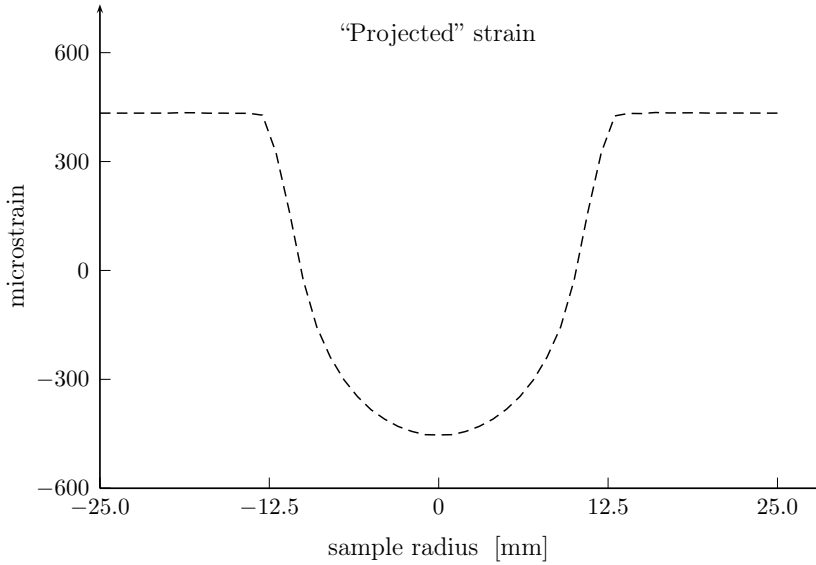


**Figure 7.4.:** Theoretical projected strains determined by averaging over all effective strain values along the neutron transmission path  $z$ .

along a single transmission path  $z$ . Considering the terms used in radiography and tomography, a “projected” strain signal should be detected. Since a parallel beam geometry has been assumed, the average over all local strain values at the same sample position  $x$  can be calculated. This can be applied to all values of  $x$  representing the sample width. As a result, the ideal projected strain can be visualised such as shown in figure 7.4.

### 7.3. Ring and Plug Simulations

So far, the calculated lattice spacings  $d_{tr}$  (diagram 7.3b) have been applied to the computed projected strain in the neutron transmission direction  $z$ . Up to now, an ideal case without any instrument influence was considered. Thus, the third strain component, the axial strain, was neglected. Although, its influence on a measurement with the sample orientation presented above is supposed to be very small it should be considered inside the simulation of a real instrument. Hence, the calculation of the effective  $d$ -values in the neutron transmission direction has been extended here. However, the projected strains obtained in figure 7.4 will be used as reference for comparisons with the simulation results determined in the following.



### 7.3.1. Modification for Beam Divergence

According to a realistic ring and plug simulation inside a virtual instrument, the beam divergence, i.e. the widening of the neutron beam due to the instrument aperture, must be taken into account. Consequently, the lattice spacing calculation inside the ring and plug simulation component has been modified to include the incoming beam direction. The effective d-value does not depend on the local neutron position only but on its flight direction also. Hence, the d-value  $d_{xz}$  in the horizontal plane is determined using the dot product of the neutron velocity vector  $\vec{v}$  and the radial vector  $\vec{r}$ . At first, the neutron event position  $(x, z)$  inside the sample and the velocity components  $v_x$  and  $v_z$  are considered to calculate  $\psi$ , the angle between two principle directions (see equation 7.3).

$$\begin{aligned}\vec{r} &= \begin{pmatrix} x \\ z \end{pmatrix} ; \vec{v} = \begin{pmatrix} v_x \\ v_z \end{pmatrix} \\ \psi &= \arccos \left( \frac{\vec{r} \cdot \vec{v}}{|\vec{r}| |\vec{v}|} \right) \\ d_{xz} &= (d_{hoop} - d_{rad}) \sin^2 \psi + d_{rad}\end{aligned}\tag{7.5}$$

This calculation is similar to the determination of  $d_{tr}$  in equation 7.3 except that neutron flight direction is considered. As a next step, the axial strain component is accounted here. Therefore, the vertical velocity component  $v_z$  is included to calculate a second angle  $\phi$  between the neutron flight direction and the y-axis (the height of the sample). The evaluation follows the same principle as shown by equation 7.5 except that  $\vec{r}$  and  $\vec{v}$  are modified.

$$\begin{aligned}\vec{r} &= \begin{pmatrix} 0 \\ 1 \\ 0 \end{pmatrix} ; \vec{v} = \begin{pmatrix} v_x \\ v_y \\ v_z \end{pmatrix} \\ \phi &= \arccos \left( \frac{\vec{r} \cdot \vec{v}}{|\vec{r}| |\vec{v}|} \right) \\ d_{tr} &= (d_{xz} - d_{axial}) \sin^2 \phi + d_{axial}\end{aligned}\tag{7.6}$$

Now, the effective d-value  $d_{tr}$  in the transmission direction is influenced by the axial strain component also — but depending on the incoming neutron flight direction. From equation 7.6, for  $\phi = 0^\circ$ , if the neutron direction is parallel to the y-axis (sample height), then, the axial strain is equal to the effective strain in the neutron direction. If  $\phi = 90^\circ$  there is no axial influence in the neutron signal. This is the case of an absolute parallel beam geometry

as assumed before. Everything in between considers all three principle strain directions. In the current setup, the influence of the axial strain increases with the beam divergence. This mechanism has been applied to extend the BraggEdge\_Powder component in McStas. The calculation of  $d_{tr}$  is repeated for every single neutron entering the virtual sample. Thus, the instrumental influence has been included to the simulation of the CONRAD and ENGIN-X machines.

In the following, the virtual ring and plug sample has been applied in order to simulate neutron transmission experiments on CONRAD and ENGIN-X. Equivalent to the simulations presented in the previous chapters, the neutron transmission signal is captured by different monitor components. Therefore, position-sensitive intensity detectors and time-of-flight monitors have been established respectively. For both cases, Bragg edge spectra should be simulated and evaluated with respect to different local sample positions.

### 7.3.2. ENGIN-X and CONRAD simulations

On the virtual ENGIN-X instrument the sample is therefore shifted perpendicular to the neutron beam in the horizontal plane. Contrary to this, on CONRAD repeated transmission intensity detectors have been installed behind the sample next to each other. The size of the detector and monitor elements was  $(2 \times 2) \text{ mm}^2$ . Thus, different local sample areas have been covered within both simulations. On ENGIN-X, the full time-of-flight spectrum has been captured for every single sample position. On CONRAD, a wavelength scan from  $4.4 \text{ \AA}$  to  $4.8 \text{ \AA}$  with  $0.01 \text{ \AA}$  steps was performed. The local sample information was captured by the detector arrangement. In both cases, the neutron transmission signal was analysed and additional flatfield/openbeam simulations were performed.

The local lattice spacing variations simulated here are expected to change the Bragg edge position in the neutron transmission spectrum. This is equivalent to the Bragg peak shift in diffraction measurements. Since, the effective lattice spacing calculation (diagram 7.3b) has been included in the simulation, the Bragg edge position should be affected by the total of d-values along the neutron beam path. According to the evaluation of the simulations, two different algorithms have been tested in order to analyse the Bragg edge position in the

transmission spectrum.

### 7.3.3. Data Evaluation

For both virtual experiments the transmission signal was calculated for each measurement step. Therefore, the flatfield and openbeam simulations have been considered. Then, the resulting Bragg edge spectrum was interpreted. For the analysis of the ENGIN-X transmission spectra a fit function  $Tr$  was used by Santisteban et al. [2001]. It has been applied to the transmission values of both instrument simulations:

$$Tr(t) = \exp(-nw\sigma_0) \left\{ \exp(-nw\sigma_{hkl}) + (1 - \exp(-nw\sigma_{hkl})) \right. \\ \left. \times \frac{1}{2} \left[ \operatorname{erfc} \left( -\frac{t - t_{hkl}}{\sqrt{2}\sigma} \right) - \exp \left( -\frac{t - t_{hkl}}{\tau} + \frac{\sigma^2}{2\tau^2} \right) \operatorname{erfc} \left( -\frac{t - t_{hkl}}{\sqrt{2}\sigma} + \frac{\sigma}{\tau} \right) \right] \right\} \quad (7.7)$$

Here,  $t_{hkl}$  is the Bragg edge position,  $\tau$  and  $\sigma$  are parameters describing asymmetric and symmetric instrumental broadenings to be fitted. The atomic density  $n$ , the local sample thickness  $w$  and the total neutron cross section  $\sigma_{hkl}$  can be defined before the fitting. Here, the cross section  $\sigma_0$  at the long wavelength side of the edge, which is accounting for contributions other than the coherent elastic part of the current  $hkl$  reflection, is also isolated. The fit function considers the uncertainties of time and position at which neutrons leave the moderator [Santisteban et al., 2001] and is therefore especially useful for the description of the Bragg edge signal measured on neutron time-of-flight machines, such as ENGIN-X. The basic principle is to include a function that describes the shape of a diffraction peak measured on such instruments — here, a Gaussian convoluted with a decaying exponential [Kropff et al., 1982]. For the Bragg edge description, the integral of this functions is taken, which is the term in square brackets in equation 7.7. Thus, the equation takes the resolution function of the instrument into account. In OpenGenie, the ENGIN-X instrument control and data analysis software, an implementation of the fitting routine is available for instance. This routine has been applied to the evaluation of the Bragg edge position and the resulting fit is visualised in figure 7.5. In this figure, a fit function for a single Bragg edge was found. Here, the (111) edge of the aluminium sample was chosen. The fitting procedure has been repeated for every single sample position investigated with the simulation. Further, the fitted Bragg

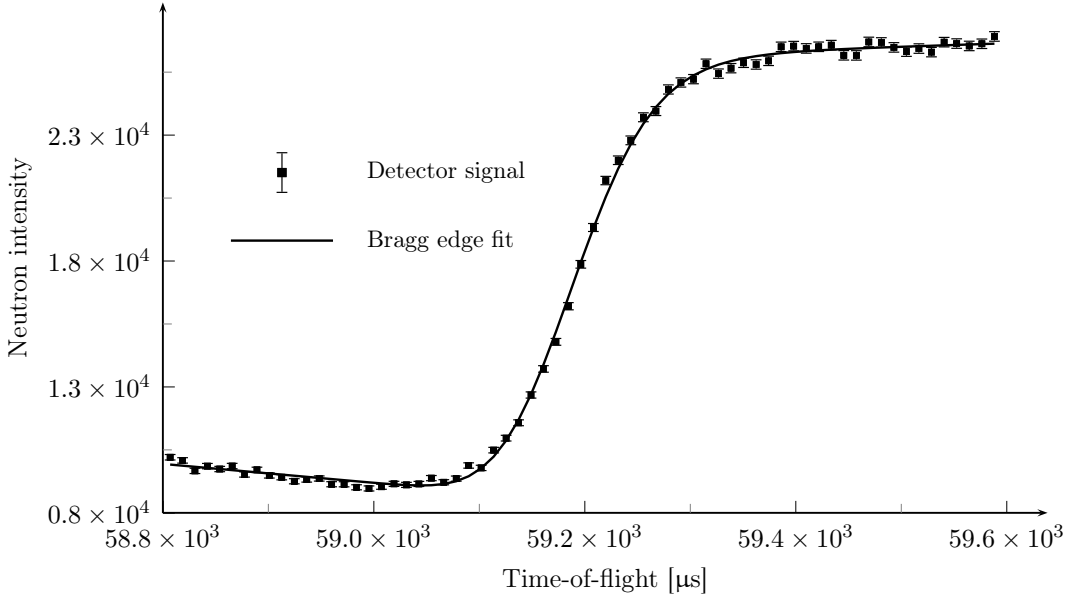


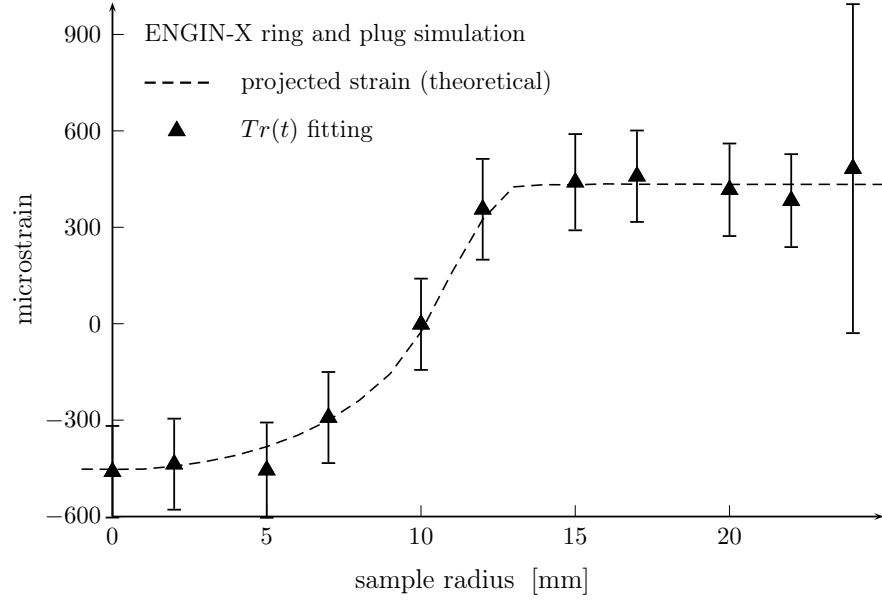
**Figure 7.5.:** Bragg edge fitting on ENGIN-X using the  $Tr$  function proposed in Santisteban et al. [2001].

edge positions have been converted to strains using the reference plug values. In case of the ENGIN-X results, the neutron time-of-flight position  $t$  in microseconds was used:

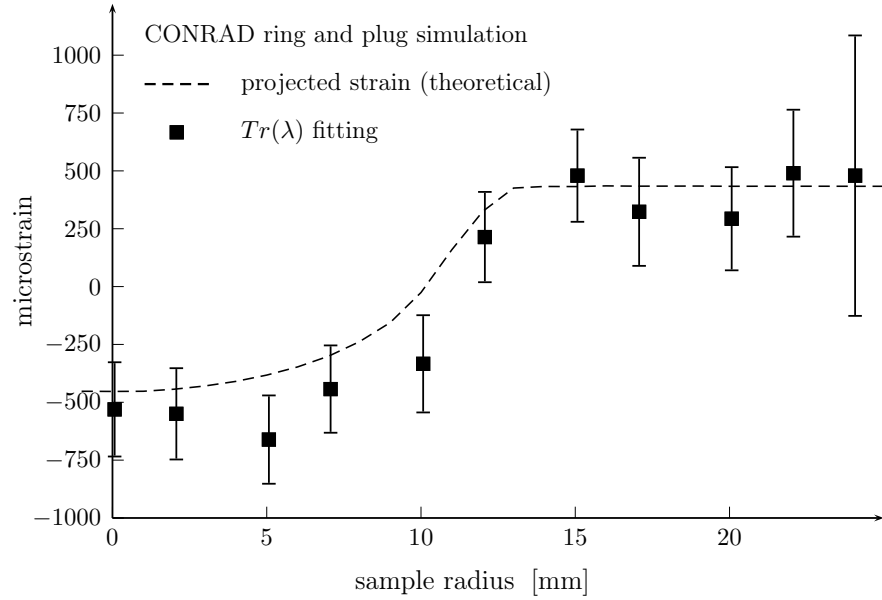
$$\varepsilon = \frac{t - t_0}{t_0} = \frac{\lambda - \lambda_0}{\lambda_0} \quad (7.8)$$

$t_0$  is the reference Bragg edge positions. For the CONRAD results, the fit function was modified. Instead of the time-of-flight, the neutron wavelength  $\lambda$  is accounted for the Bragg edge position. Furthermore, the parameter  $\tau$  describing the asymmetric Bragg edge broadening was not required in the application of a fit on CONRAD. The double monochromator device provides symmetric peaks around the selected wavelength. Hence, the general model of a Gaussian to be used within the fitting routine is reasonable. As described by Vogel [2000], the convolution of the Gaussian profile and the step function modelling the Bragg edge leads to the application of the complementary error function (erfc), which has also been used before. In contrast to ENGIN-X, the fit function for CONRAD simplifies to:

$$Tr(\lambda) = \exp(-nw\sigma_0) \left\{ \exp(-nw\sigma_{hkl}) + (1 - \exp(-nw\sigma_{hkl})) \frac{1}{2} \operatorname{erfc} \left( -\frac{\lambda - \lambda_{hkl}}{\sqrt{2}\sigma} \right) \right\} \quad (7.9)$$



(a)



(b)

**Figure 7.6.:** Comparison of ENGIN-X (a) and CONRAD (b) simulation with the theoretical projected strains along the neutron transmission path through the sample.

where  $\sigma$  is the only parameter accounting for the instrumental influence on the Bragg edge. In the following, the projected strain, obtained in section 7.2.2, is considered as a “theoretical” strain curve for a comparison with the fitting results of the simulations as it was calculated by means of the theoretical hoop and radial strain components.

The resulting strain curves along the sample diameter are shown in figure 7.6. Both simulations are compared with the theoretical projected strain (dashed curve). The ENGIN-X simulation shows a very good agreement to the theoretical assumptions made before. The absolute strain values fit to the projected strain curve. Here, the error bars have been considered as well. Although, the relative fitting error of the Bragg edge position for each sample position is below 0.05 %, the resulting error bars are around  $\pm 150$  microstrains. This follows from the error propagation when evaluating equation 7.8. The error at 24 mm is even higher, which is due to the low statistical information at a very thin sample position. The results of the CONRAD simulation are shown in diagram 7.6b. Here, the symmetric Gaussian profile used in the fitting routine exhibits varying deviations from the theoretical projected strain. However, the same strain gradient along the sample diameter is visible. Again, the instrumental setup at CONRAD including the monochromator settings causes larger difference than those determined with the ENGIN-X simulation. It turned out that the application of a Gaussian function is not reliable enough, especially for the study of strains. The uncertainty during the fit maybe the result of the higher-order wavelengths also provided by the monochromator system. They also contribute to the detected transmission signal and therefore also to the Bragg edge. Hence, a possible solution for the deviations observed on CONRAD is to consider the second and third order wavelengths in the fit. However, the error bars for both tests are comparable and should be decreased by longer measurements, i.e. more neutrons to be simulated.

## 7.4. Validation with Experiments

### 7.4.1. ENGIN-X

In addition to the theoretical assumptions and the neutron simulations discussed above, the ring and plug sample has been measured experimentally. The specimen was investigated on ENGIN-X in transmission mode<sup>3</sup>. Similarly to the simulation presented above the sample was orientated such, that the cylinder axis  $y$  was pointing to the top. Thus, as previously,

---

<sup>3</sup>The experiments presented here have been proposed and evaluated in collaboration with the ENGIN-X group (Ed Oliver, Shu Yan Zhang, Anna Paradowska) and the Solid Mechanics & Materials Engineering group from University of Oxford (Prof. Alexander Korsunsky, Brian Abbey).

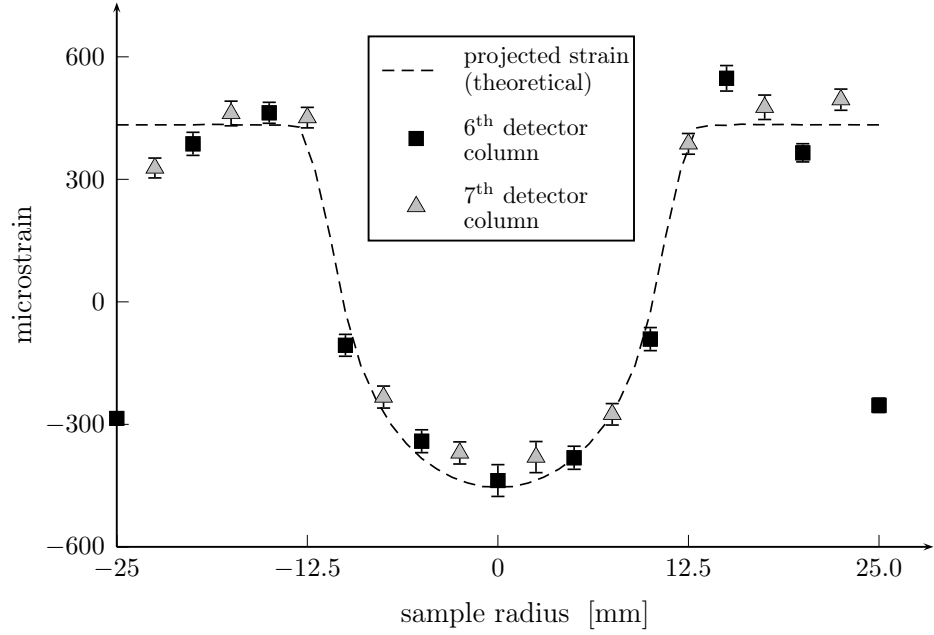


**Figure 7.7.:** Evaluation of the measured ring and plug specimen. The ideal curve is obtained from averaging over the simulated  $d$ -values from figure 7.3b in transmission direction. The dots visualise the evaluated strain after fitting the Bragg edge position measured on ENGIN-X (squares = 6<sup>th</sup> detector column, triangles = 7<sup>th</sup> detector column).

the average strain in the horizontal plane was measured with the transmission detector. The neutron beam size was selected to be 9.5 mm horizontally and 20 mm vertically. The sample centre (radius position  $r = 0$  mm) was aligned to the 6<sup>th</sup> column of the  $10 \times 10$  pixelated transmission detector. In order to face different local positions, the sample was shifted in  $x$  direction along the whole diameter from  $-25$  mm to  $25$  mm in  $5$  mm steps. Moreover, the reference plug sample was measured to determine the stress-free lattice spacing  $d_0$ . The Bragg edge positions for each position have been localised by fitting the resulting time-of-flight spectra with the function from equation 7.7. Therefore, the detector elements from the 6<sup>th</sup> detector column have been summed up to provide better statistics. The fitted Bragg edge positions have been translated to strains (equation 7.8) using the reference value obtained from the plug measurement. The resulting strain is plotted against the sample radius in figure 7.7. For a comparison, the ideal projected strain curve is shown as well. The squared blue dots visualise the evaluated strains for each sample position. Referring to the ideal computation, the measured strain values show a good agreement. The only mismatch occurs at the two sample edge positions at  $\pm 25$  mm. The reason for that is the position and size of

the detector elements. The  $2 \times 2 \text{ mm}^2$  pixel elements cover only half of the sample area at  $\pm 25 \text{ mm}$ . The rest already faces neutrons outside the sample volume. Thus, the Bragg edge signal is affected by the passed neutrons as kind of a systematic error. Due to the selected beamsize, the results from the neighbouring detector columns have been analysed as well. Hence, the diagram also shows the results from the evaluation of the 7<sup>th</sup> detector column. Since the centre of the 7<sup>th</sup> column is placed 2.5 mm away from the 6<sup>th</sup> column, the resulting strains (red triangle dots) are plotted in between. Using this correction, the results also agree to the theory. It is shown that the experimentally determined strains follow the same trend as the calculated one. The only deviation at  $\pm 25 \text{ mm}$  is because of systematic errors.

#### 7.4.2. CONRAD

On CONRAD, radiographic images were taken using the monochromatic instrument option. A wavelength scan from  $3 \text{ \AA}$  to  $5.5 \text{ \AA}$  in steps of  $0.01 \text{ \AA}$  was performed with and without the samples, i.e. a flatfield correction has been included here. Additionally, darkfield images have been captured to consider the uncertainty of the dark current of the CCD camera. Both the ring and plug and the reference plug sample have been measured at the same time. The samples were aligned using the same orientation as presented above. After dark- and flatfield corrections, the radiographic images have been evaluated towards variations of the Bragg edge position. In figure 7.8, a radiographic image taken at  $4.5 \text{ \AA}$  shows the ring and plug sample as well as the reference plug. The picture demonstrates, that both specimens are covered by one shot. Hence, an additional shifting to measure the individual local sample positions as conducted on ENGIN-X was not needed here. The potential of the radiography application is the analysis of all sample regions inside one picture with respect to the spatial resolution of the instrument. Ideally, the evaluation of the transmission spectrum could be performed pixel by pixel. Here, multiple regions of interest (ROI) have been selected to cover different sample areas being analysed. In principle, a separate evaluation for each image pixel would have been possible. But due to the weak yield of neutrons in a single pixel, the analysis would not make sense relating to the results. One individual ROI was selected to be  $20 \times 40$  pixels, which is equivalent to a sample area of  $(4.5 \times 9) \text{ mm}^2$ . Altogether, eleven regions in a row were chosen to mark the local sample positions to be analysed. Further,



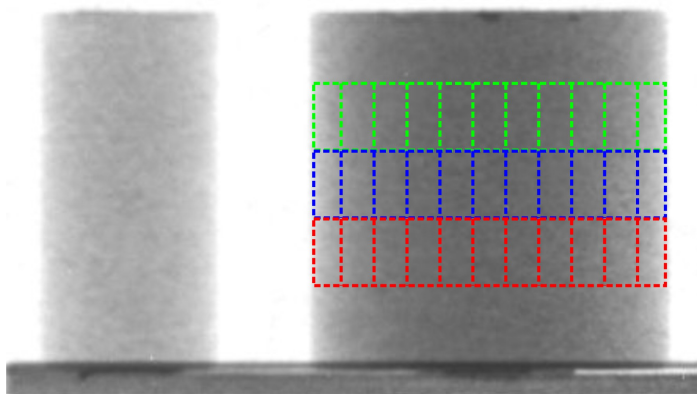


**Figure 7.8.:** Radiographic image of the ring and plug sample (right) and the reference plug (left) taken on CONRAD with monochromatic neutrons at  $4.5 \text{ \AA}$ .

multiple rows have been evaluated. The radiographic image (figure 7.8) shows some of these areas indicated by the coloured frames as an example. The Bragg edge variations along the horizontal axis have been considered as well as vertically. The mean grey values of each ROI have been collected together with every single wavelength step to summarise a transmission spectrum for each selected area. Thus, the statistical information has been increased — and noise was reduced. The collected Bragg edge spectra have been evaluated by fitting the transmission signal with the  $Tr(\lambda)$  function (equation 7.9). Thus, the position of the Bragg edge has been determined. The same procedure has been applied to the selected regions of the reference sample as well. For each row of the reference plug ROI the results have been averaged to a single edge position. This is possible as there is no lattice spacing variation expected according to the local position inside the sample. However, the individual rows have been considered due to the wavelength distribution along the detector height (section 5.4.1). The results of the Bragg positions for both sample pieces were used to calculate the strain against the sample position. In figure 7.9, the strain gradient along the sample diameter is shown in comparison with the theoretical projected strain (dashed line). The three individual diagrams represent the results evaluated from the different heights framed in figure 7.8.

For all three selected cases, it is apparent that the resulting strain signal deviates from the ideal strain curve. Although, the gradient along the sample diameter is comparable, the differences between the curves range up to 3000 microstrains. Moreover, the results seem to be

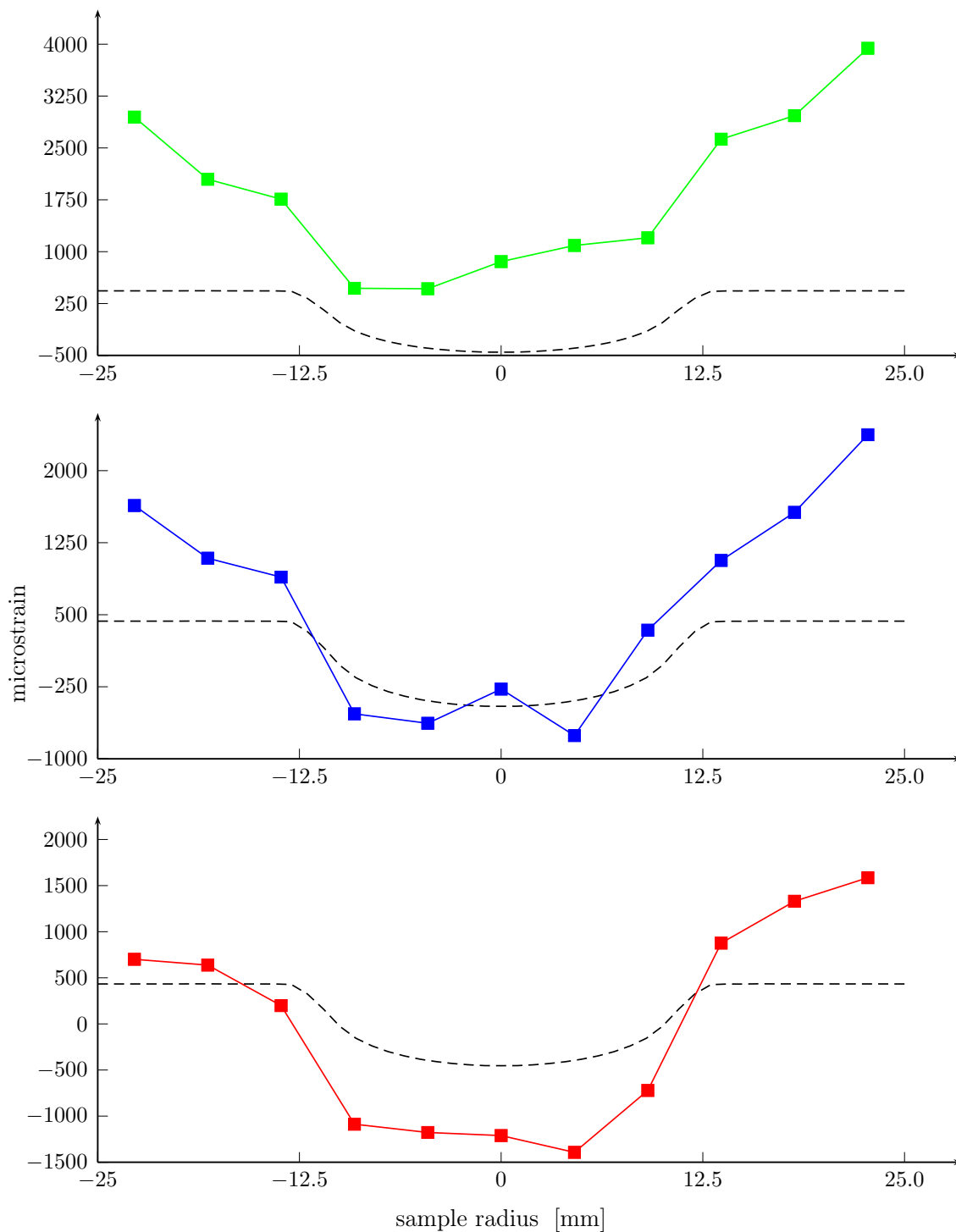


**Figure 7.9.:** Ring and plug strain results evaluated from the CONRAD transmission measurements at three different detector positions. The dashed line represents the ideal projected strain.

shifted along the y-axis relative to the position on the detector height. In principle, this effect follows from the wavelength distribution on the detector plane due to the monochromator

setup. Because the mean selected wavelength increases with the detector height the fitted Bragg edge positions will be represented by smaller wavelength. Thus, the denominator of the strain equation (7.8), i.e. the reference lattice spacing, is decreasing with the detector height. However, a correction with the findings from chapter 5 (especially section 5.4.1) would only lead to a scaling of the strain results. Then, a shifting of the absolute strain value (along the y-axis), including possible changes of the algebraic sign, is not feasible. Last but not least, there is a huge relative error, that is not indicated here. The error bars vary from  $\pm 3700$  microstrains to  $\pm 6100$  microstrains. For reasons of clarity, they have not been presented in the diagrams.

## 7.5. Discussion on Strain Reconstruction

The projected strain derived, simulated and measured above, is only an intermediate step towards realising the full potential of Bragg edge strain experiments. The intention is to be able to resolve the principle strain directions from the projected signal. The reconstruction of the strain profile belongs to the family of inverse problems. In order to reconstruct higher-order information from a lower-order signal, in tomography applications, the projected signal is detected from multiple sample orientations. The collected projections will then be used to calculate the reconstruction by means of appropriate methods. Here, the radial strain symmetry of the ring and plug sample simplifies the collection of projections. Ideally, the projected strain is the same from all sample orientations in the horizontal plane. The axial strain direction is neglected here as it has no influence to the projections in case of a perfect parallel neutron beam. However, the development of a suitable reconstruction method is the key towards the determination of the strain components with Bragg edge transmission. Therefore, Abbey et al. [2009] developed a model to reconstruct the radial and hoop strain. The authors demonstrated their reconstruction by means of steel cylinder that is also radially symmetric. An exponential fit function was used to describe the individual strain components in terms of the sample radius. The complete model is attended with a forward calculation of the projected signal from the reconstructed strains. This calculation follows the same principle as described above (section 7.2.2). The differences between the measured and calculated projected strain will be used to terminate the iteration when a small error has been

reached. Thus, a suitable fit has been found for the presented steel sample. The authors have stated that the exponential function does not adequately describe the strain components at every sample radius. For the case of the ring and plug aluminium sample investigated in this chapter, the strain components cannot be described by continuous fit functions. Hence, other functions must be applied and implemented to reconstruct more general cases. Furthermore, the symmetry of the ring and plug specimen simplifies the problem, but other geometries must be considered as well. Nevertheless, the feasibility of a reconstruction of individual strain components has been demonstrated. Improvements and extensions to the model have been mentioned. The work is concerned to establish that a neutron strain tomography is under way [Abbey et al., 2009].

The McStas simulations developed in this thesis provide results ranging from ideal transmission signals up to Bragg edge pattern influenced by the emulated instrument environment. The simulation tools are therefore also available to reproduce projected strains to be evaluated with reconstruction algorithms as presented above. In Abbey et al. [2009], the measured (by neutron diffraction) and reconstructed strain components have been compared with a finite element calculation. Hence, the McStas experiments may help towards the development of tomography algorithms concerned with the presented problems. Thus, time-consuming and cost-intensive investigations with neutron instruments can be saved.

## 7.6. Concluding Remarks

In the sections above, the strain signal in the transmission direction has been explained and the term projected strain was introduced. A standard residual stress sample has been investigated with Bragg edge neutron transmission. The three principal strain directions measured in conventional diffraction experiments have been applied to calculate the effective strain in neutron transmission geometry. This computation has been implemented into the McStas Bragg edge simulation to emulate experimental conditions on CONRAD and ENGIN-X. The detected signal has been compared with both the theoretical and experimental results obtained from these machines. Thus, a statement suggesting the feasibility of such measurements has been made. The results on ENGIN-X match well with the predicted

projected strains: suggesting the reliability of further evaluations. Although, the neutron time-of-flight cannot be determined exactly because of the moderator uncertainty, the Bragg edge broadening is not crucial towards the strain result. The appropriate fit function was successfully applied. The CONRAD results reveal larger differences, however a tendency to at least follow the strain gradient was visible. Hence, the CONRAD instrument can also be used to investigate local lattice spacing variations and strain, at least in a qualitative manner. Proposals towards improvements have already been mentioned. In summary, it was shown, that projected strain can be resolved by means of Bragg edge spectroscopy and visualised by radiography respectively. Moreover, it was demonstrated that the transmission detector system on ENGIN-X can be used to evaluate more than one local sample position in parallel. Although the spatial resolution is low, it can be applied to measure multiple sample locations by one measurement.



## Multiple scattering

In this chapter, another possible influence on the neutron transmission signal is discussed in order to find explanations for deviations between theory and practice obtained in Bragg edge experiments. Based on theoretical considerations of multiple scattering events inside a specimen, extinction effects of the total neutron cross section will be described. A Monte Carlo simulation will be applied in order to investigate the effect of multiple scattering in Bragg edge transmission mode. Experimental measurements will be presented for a comparison with the results obtained from the simulation.

### 8.1. Motivation

Since Bragg transmission edges occur due to coherent scattering events along the transmission path through the sample, the possibility of multiple scattering is given as well. Hence, an investigation of this effect with regard to its contribution to the detected neutron intensity is reasonable. With reference to figure 8.1, taken from Santisteban et al. [2001], a further deviation to the calculated theoretical neutron cross section exists. Although the experiment was conducted with an iron powder, i.e. strain and texture effects are excluded, the Bragg edge spectrum measured on ENGIN, the predecessor of ENGIN-X, shows significant differences from the theoretical prediction (especially in the region of the (110) iron Bragg edge). The former ENGIN instrument had a shorter flight path of 15 m. However, the difference from the new ENGIN-X makes no impact on the conclusions about the phenomenon investigated here. The instrumental settings do not account for the observed extinction in the measured neutron cross section. Hence, for example Steuwer [2008] stated that the difference

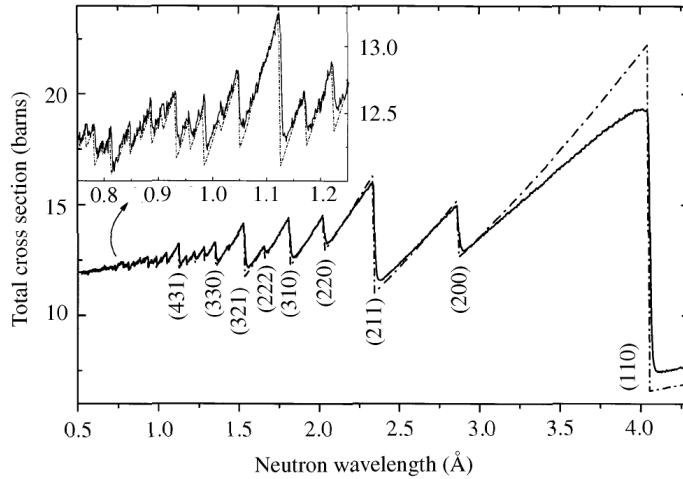


**Figure 8.1.:** Total neutron cross section (solid line) of iron powder after Santisteban et al. [2001, figure 1] determined by Bragg edge transmission measurements on ENGIN in comparison with the theoretical calculation (dashed line) from Kropff & Granada [1977].

between theoretical calculations and measurements on ENGIN may occur due to multiple neutron interactions inside the specimen. In particular, the deviation between theory and practice near where the first (110) Bragg edge is growing up to the Bragg cut-off position. The assumption that multiple scattering in the powder sample is responsible for that is the motivation for the investigation presented in the following. If this is the case, then, not only structural sample properties but the sample geometry and position within the instrument will affect the experimental results.

### 8.1.1. Background

In chapter 5 the instrument influence on the neutron transmission signal was investigated. By means of a double monochromator setup on the CONRAD tomography machine, a wavelength selection was realised in order to perform Bragg edge radiographic measurements. However, it turned out that the wavelength selection itself causes deformations of the Bragg edge shape. On the one hand, the Bragg edge position is affected by the mosaicities of the monochromator crystals, plus it was shown that the selected wavelength varies with the detector height due to the instrumental setup and the wavelength spread. Hence, the evaluation of the Bragg edge position must take the local sample position into account. On the other hand, the influence of higher order monochromator reflections affects the Bragg edge



magnitude. Therefore, the contribution of second and third order reflections will impact on the amplitude of a Bragg edge measured on CONRAD.

On ENGIN-X (section 4.2) a different approach to detect the Bragg edge is used. There, a pulsed polychromatic neutron beam travels to a specimen. The beam attenuation is captured by a pixelated time-of-flight detector. Thus, the polychromatic neutron beam is evaluated by the detector elements, i.e. the wavelength mapping is handled by the detector electronics taking the neutron time-of-flight into account. Hence, there is no additional wavelength selection before the detector. Compared to the CONRAD setup, this provides a very precise Bragg edge position determination. The only broadening of a Bragg edge is caused by the finite resolution of the instrument. Then, the influence of the moderator is considered. The uncertainty in time and position at which a neutron leaves the moderator cannot be resolved by the time-of-flight detectors afterwards. Hence, the shape of the time-of-flight transmission signal behind a specimen is also affected. According to that, the beam profile has already been analysed in [e.g. Santisteban et al., 2001; Steuwer et al., 2001]. A fit function, that has been used in chapter 7, was derived to determine the accurate Bragg edge position with respect to the instrumental uncertainties. Thus, many influences describing typical instrument characteristics have been investigated.

### 8.1.2. Theory

Although many instrumental parameters have been included in the analysis of Bragg edge transmission spectra, the possibility of multiple scattering has been neglected so far. Here, the multiple scattering term that characterises a sequence of single scattering events inside a sample is considered. The investigation of multiple scattering processes is important whenever the detected signal is affected by that and leads to uncertainties in the interpretation of the measured results. Referring to neutron diffraction measurements, many studies have been performed already. In Mildner & Carpenter [1977] for example, a computer simulation has been created to calculate the score into the detector from each scattering point inside the sample. Thus, the individual contribution to the measured intensity could be estimated. Moreover, multiple scattering correction factors have been derived, which are useful for the

analysis of the structure factor for instance.

In the work of [Farhi et al., 2009] a new sample component for neutron scattering experiment simulations with McStas was presented. The authors stated, that there is no experimental method available to measure the multiple scattering contribution precisely. Due to the fact that multiple scattering may become significant, the Monte Carlo simulation is a valuable tool to solve this issue. As a result of that work, the new McStas component also treats the effects of multiple scattering. The contribution of multiple scattered neutrons to the detector signal showed good agreement to former calculations made by Copley [1974]. Thus, the multiple scattering part can also be subtracted from the total signal to achieve consistent results.

## 8.2. Multiple scattering McStas component

The assumption that multiple scattering is influencing the detected transmission signal has been tested with McStas. Therefore, the BraggEdge\_Powder component has been extended to enable multiple events for a single simulated neutron.

### 8.2.1. Simulation principle

Referring to the theory of the coherent elastic scattering cross section, the probability of a neutron being scattered by a particular lattice plane increases with the neutron wavelength up to the position where no scattering by this lattice plane is possible — the Bragg edge. Taking the transmission geometry into account, the neutrons with wavelengths close to an edge position can be scattered by a Bragg angle close to  $\theta = 90^\circ$ . Then, the neutron will be sent in backwards direction up to  $2\theta = 180^\circ$ . Regarding the current probability of a neutron to be scattered, it is further possible that another scattering event will occur. Thus, multiple scattering is activated. The basic principle of these possible neutron-matter events is visualised in figure 8.2. Taking advantage of the neutron cross section code implemented in the nxs library, the effect of neutron absorption and transmission can be extended to enable multiple neutron scattering to be simulated with McStas. Again, the Monte Carlo principle of McStas has proved to be useful as there are several neutron events to be considered

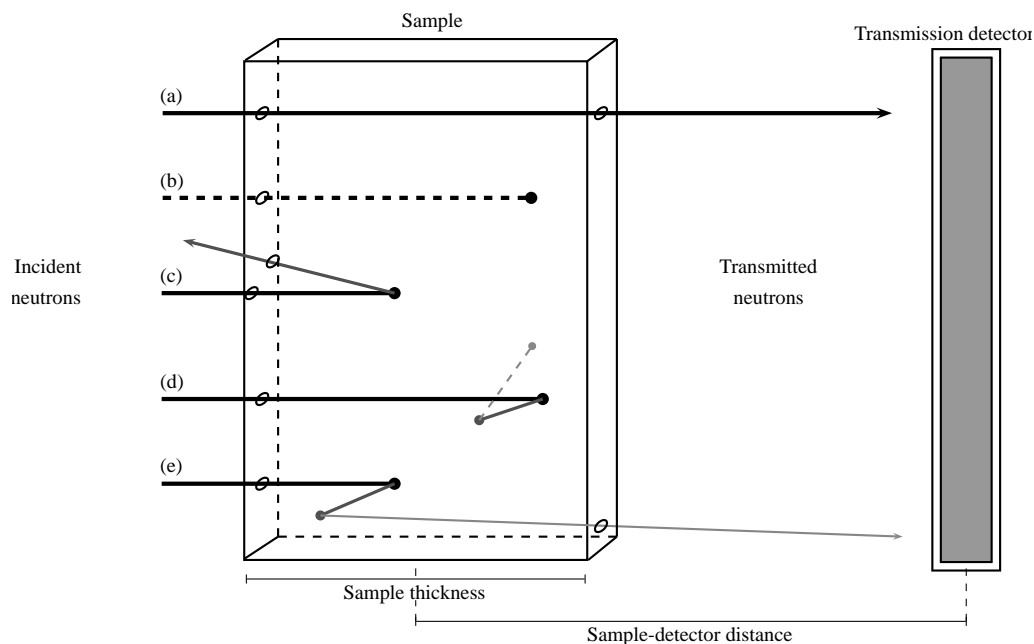


**Figure 8.2.:** Schematic drawing of possible neutron transmission (a), absorption (b) and scattering events (c) inside a sample. The Bragg edge simulation module has been extended to realise multiple scattering events. Thus, further scattering events are possible until the neutron is absorbed (d) or leaves the sample (e).

for a theoretical calculation of multiple scattering. Moreover, this includes the neutron scattering range in space over  $4\pi$ , although only neutrons in the transmission direction will be detected. The additional neutron events outlined in figure 8.2 (c-e) have been realised here by a modification of the Bragg edge sample component. As a result, the effect on the number of neutrons in transmission direction could be simulated.

### 8.2.2. Algorithm & Implementation

In McStas, syntax extensions, such as `JUMP` and `COPY` statements and `WHEN` conditions, exist to handle component loops, duplication of component instances and non-sequential neutron propagation. Thus, it is possible to simulate neutron scattering by multiple instances of identical monochromator blades [Willendrup et al., 2008] for example. However, there is no general possibility to allow multiple scattering events to be activated for the complete simulation. Hence, multiple scattering events with respect to a Bragg edge transmission simulation must have been handled within the sample component. Therefore, the Bragg edge module created in section 5.2 was extended to investigate the multiple scattering dependence

of the detected transmission signal. The basic principle to realise the simulation is described as follows.

1. The neutron wavelength is calculated by means of the neutron velocity vector and the neutron cross sections are determined with the help of the `nxs` library routines, such as implemented before in section 5.2.2.
2. An event point on the neutron transmission path through the sample is determined randomly taking advantage of the neutron-sample intersection times  $t_1$  and  $t_2$  calculated before. The current neutron is propagated to that point using the McStas macro function `PROP_DT`.

```
PROP_DT( rand01() * (t2-t1) + t1 );
```

3. The transmission probability  $p_{tr}$  for that neutron is calculated by equation 3.2 and 3.3. If a random number between 0 and 1 is smaller than this probability the actual neutron is transmitted and leaves the sample component. Otherwise, the algorithm differs between an absorption and a coherent elastic scattering event. Other scattering cross sections are neglected here.
4. In order to divide randomly between absorption and scattering, the neutron cross sections are considered.

```
random_number = rand01() * ( nxsAbsorption(lambda,&uc) +  
nxsCoherentElastic(lambda,&uc) );
```

The neutron is absorbed if the random number is smaller than or equal to the absorption cross section. The McStas macro `ABSORB` is applied. Otherwise, coherent elastic scattering will be handled.

5. For the scattering case, the Bragg angle  $\theta$  is determined by means of Bragg's law (equation 2.3). Therefore, the current neutron wavelength and a possible  $hkl$  lattice spacing is considered. With  $\theta$ , a random point on the Debye-Scherrer cone is selected. In order to change the neutron flight direction, the velocity vector is modified using the rotation functions predefined in the McStas library. Finally, new intersection times

$t_1$  and  $t_2$  are calculated by the McStas library function taking the new neutron velocity vector into account.

6. The steps 2 - 5 will be repeated until the actual neutron is absorbed (using the **ABSORB** macro) or leaves the sample. Depending on the scattering angle, the latter could be in the original transmission direction, but any other direction is also allowed (see figure 8.2c), although the neutron will not be detected afterwards. Thus, multiple scattering events are realised and additional neutrons scattered in forward transmission direction can be captured by a detector.

According to the coherent elastic scattering by a selected lattice plane applied in step 5, all lattice spacings  $d_{\vec{h}}$  with  $2d_{\vec{h}} \geq \lambda$  and  $\vec{h} = (hkl)$  have been considered. Thus, one neutron with wavelength  $\lambda$  may scatter by  $\vec{h}_a$  while another neutron with the same wavelength is scattered by  $\vec{h}_b$  if the previous condition is fulfilled. Likewise, it is possible that one and the same neutron scatters first by  $\vec{h}_a$  and then by  $\vec{h}_b$ . The  $hkl$  lattice plane selection is selected randomly taking the weight of their individual contribution to the coherent elastic scattering cross section into account. The calculation follows the principle of a roulette wheel. A random number is generated between 0 and the value of the neutron cross section  $\sigma_{coh}^{el}$ , which is the sum of the individual  $hkl$  structure factor and lattice spacing contributions. In equation 8.1, which follows from equation 3.9,  $\sigma_{coh}^{el}$  is normalised by the unit cell volume  $V_0$  and the neutron wavelength  $\lambda$  to speed up the calculation. Then, the random value indicates the selected  $hkl$  lattice plane similar to the ball that stops at a slot position of the roulette wheel. Here, the slot position is equivalent to one of the summands in equation 8.1:

$$\sigma_{coh}^{el}(\lambda) \frac{2V_0}{\lambda^2} = |F_{\vec{h}_1}|^2 d_{\vec{h}_1} + |F_{\vec{h}_2}|^2 d_{\vec{h}_2} + \dots + |F_{\vec{h}_n}|^2 d_{\vec{h}_n} \quad (8.1)$$

Finally, the selected lattice plane was used to determine the Bragg angle and continue with neutron scattering as denoted in step 5. The presented algorithm has been implemented to the McStas Bragg edge sample component in order to make it available within instrument simulations.

### 8.3. Simulation Testing using ENGIN-X

The above extended sample component has been applied within McStas instrument simulations. In order to demonstrate the multiple scattering effect on the evaluated total neutron cross section, the ENGIN-X model, introduced in section 5.5, was utilised to simulate experiments with a number of varying parameters. Later on, the simulation will be used to compare the effect with the results presented in figure 8.1. In the following, the time-of-flight detector was set to the same size of the sample. Thus, only transmitted neutrons have been mapped by this monitor, which is comparable with the analysis of imaging experiments with pixelated detectors (e.g. CCD camera) where only selected pixels mark the region of interest. Usually, the area outside the sample region is not considered. Finally, the modified Bragg edge sample module was added to the ENGIN-X instrument definition, placed in front of the time-of-flight transmission monitor. In order to study the influence of different sample thicknesses and sample-detector distances, the simulation was executed with varying input parameters. However, for all cases the sample width and height was set to 2 cm. For all following diagrams in this section, the neutron transmission intensities, resulting from the individual simulations, have been converted to the total cross sections  $\sigma_{total}$  in order to compare them with the calculations from the nxs library routines, denoted as theoretical neutron cross section. This means, the latter has no instrumental influence, is calculated and used within the sample module during the simulation and will be plotted as a dashed line throughout the following diagrams.

#### 8.3.1. Sample Thickness

Using the instrument description of the ENGIN-X machine, Bragg edge transmission simulations with varying sample thicknesses have been performed. The time-of-flight detector was placed on a fixed position behind the sample. The resulting time-of-flight transmission spectrum was converted to a wavelength spectrum using the de Broglie relation (equation 6.4). Additionally, the simulation has been tested with different unit cell settings representing different materials. Figure 8.3 presents the simulation results of iron (bcc) and aluminium (fcc), using a secondary flight path of  $L_2 = 4$  cm and  $L_2 = 8$  cm respectively. The tests were performed using a neutron spectrum of 2 Å to 5 Å to be captured by the monitor component.

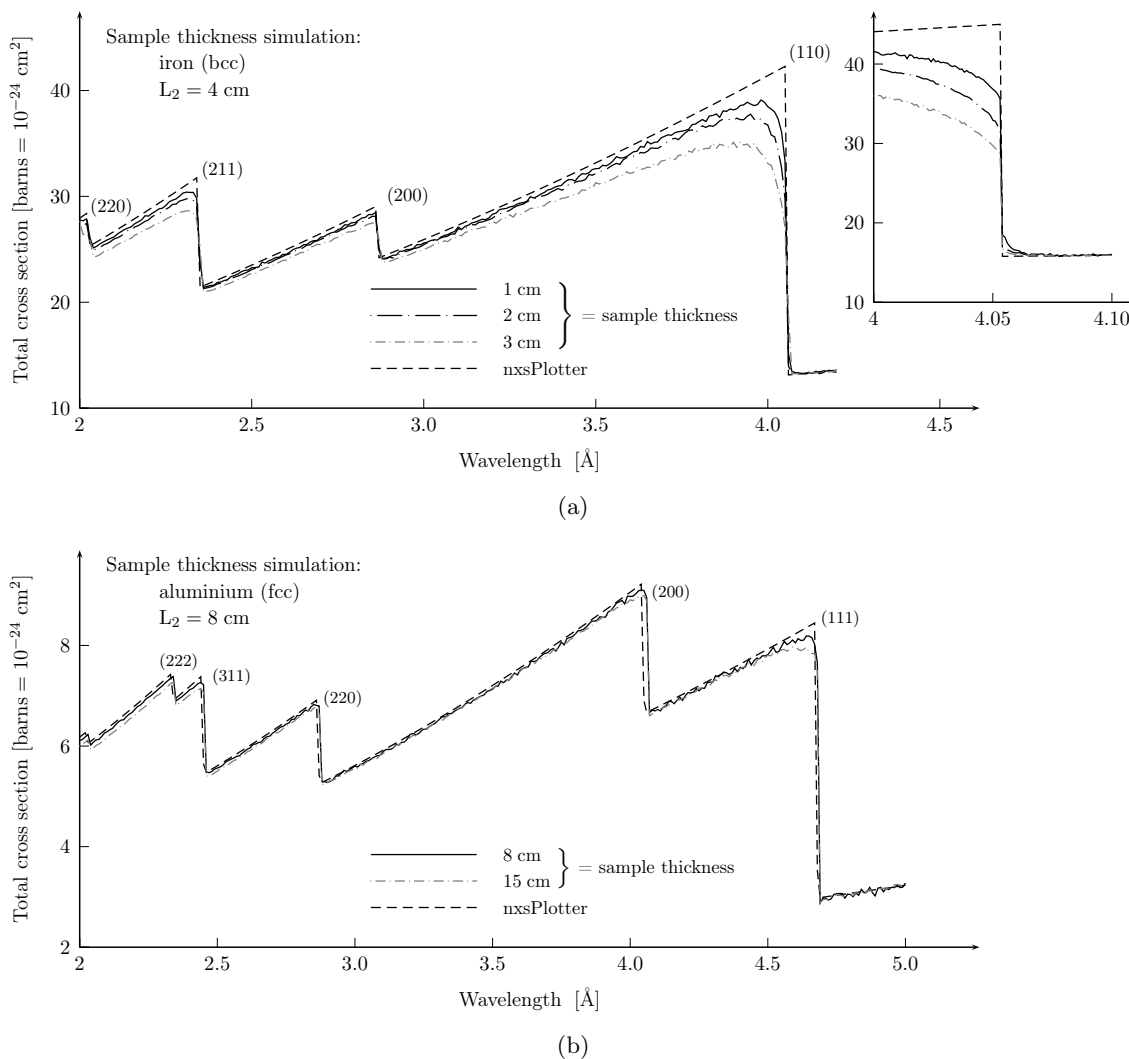


**Figure 8.3.:** Multiple scattering simulations: (a) with iron and (b) with aluminium samples of different thicknesses.

The detected neutron intensity was transformed to neutron cross section values with respect to the actual sample thickness. This normalisation enables the comparison with the initial cross section. In the diagrams 8.3, the evaluated total neutron cross section for multiple sample thicknesses is shown relative to the intrinsic theoretical cross section curve (dashed line), calculated with the nxs routines. The Bragg edge spectra demonstrate the influence of the different sample thicknesses. Compared to the theoretical nxs values, the magnitude of the simulation results is reduced systematically with respect to the sample thickness. In figure 8.3a, the (110) iron Bragg edge exhibits the most significant extinction. This means, more neutrons in the transmission direction will be detected due to multiple scattering. As described in figure 8.2, some neutrons will be scattered multiple times. Thus, in the area

before the Bragg edge (on the short wavelength side), the slope of the total cross section decreases. An explanation for this phenomenon can be found by the high scattering probability near the Bragg edge as introduced above. As indicated by the calculation of the coherent elastic neutron cross section (equation 3.9), the longer the neutron wavelength, the higher is the probability for a neutron to be scattered by a selected lattice plane. For the case of the region left of the (110) Bragg edge, there is only one chance for coherent elastic scattering — the (110) lattice plane. Hence, the probability for multiple scattering increases with the wavelength, i.e. with the Bragg angle, up to the position of pure backscattering at  $2\theta = 180^\circ$  and  $\lambda = 2d_{hkl}$  — the Bragg edge. Thus, the Bragg edge position itself is not affected by that, because for neutrons with  $\lambda > 2d_{hkl}$  no scattering by this lattice plane can occur, i.e. the transmitted neutron intensity still changes suddenly at  $\lambda = 2d_{hkl}$ . The inset in 8.3a clarifies this. The total neutron cross section, evaluated from the simulated intensity, decreases with the sample thickness. Due to the bigger sample volume, more scattering events can occur and thus, more neutrons have been detected in the forward transmission direction.

Moreover, the same effect is visible for all other Bragg edges, even though the strength differs with the magnitude of the total cross section. Additionally, the chance for backscattering around  $2\theta = 180^\circ$  is smaller as there are more lattice planes present for coherent elastic scattering. For example, the probability to scatter by (200), and still multiple times to reach the forward transmission direction, is smaller as there is the (110) lattice plane that causes to scatter away from the forward direction at the same wavelength. In diagram 8.3b, the same results are pointed out for the case of an aluminium (fcc) sample. However, the unit cell exhibits smaller cross sections (especially  $\sigma_{coh}^{el}$ ) and therefore smaller probabilities for neutron scattering events. Hence, the extinction due to multiple scattering is weaker, and becomes clear only for larger sample thicknesses.

### 8.3.2. Sample-Detector Distance

According to the tests shown above, a second simulation sequence was started to visualise the multiple scattering influence. Therefore, the sample thickness was set constant. Here the distance  $L_2$  between sample and detector was varied. In particular, a 3-cm thick iron sample



was tested with a detector distance from 4 cm to 10 cm. The rest of the virtual instrument setup was the same. Again, the time-of-flight signal and the transmitted intensity have been converted to neutron wavelengths and total neutron cross sections respectively. The results are presented in figure 8.4. All plots are compared with the initial cross section values that were used in the simulation. Thus, the difference between input and evaluated output neutron cross sections is visible. The diagram shows the same extinction behaviour as above. The closer the detector is placed to the specimen the stronger is the influence of multiple scattering events. With the growing detector distance the simulation results converge with the theoretical curve (dashed line). The reason for this behaviour follows from the principle of secondary beam collimation. The direction of coherent elastically scattered neutrons with a Bragg angle  $\theta < 90^\circ$ , but in the near of a Bragg edge, is not perfectly parallel to the incident beam direction. For a large portion of scattered neutrons it is not even close to that. Thus, the probability to detect them in transmission direction decreases with the size and distances of the detector. Similar to an incident beam divergence the neutron beam after multiple scattering will be spread according the lattice planes available for diffraction. Hence, more neutrons will be detected the closer the monitor is installed. As a result, the evaluated total neutron cross section values will be decreased. Concluding, the extension of the secondary beam path is equivalent to a beam collimation behind the sample. Consequently, a chance to avoid the multiple scattering influence on the transmission signal is to use collimator elements between sample and detector. According to this, the secondary beam collimation will further enhance the definition of the gauge volume. An example for this is applied by Muhrer et al. [2007].

### 8.3.3. ToF vs. Wavelength Monitor

The experiment simulation enables the opportunity to analyse individual instrument components. In McStas, it is further possible to divide between the time-of-flight and the wavelength of every single neutron. In the following, the original simulated neutron wavelength is compared with the one detected with the ToF monitor component, which is recalculated by means of the total neutron flight path  $L$ . For this analysis, a wavelength monitor `L_monitor` (available from the McStas library) was added to the instrument simulation. The detector

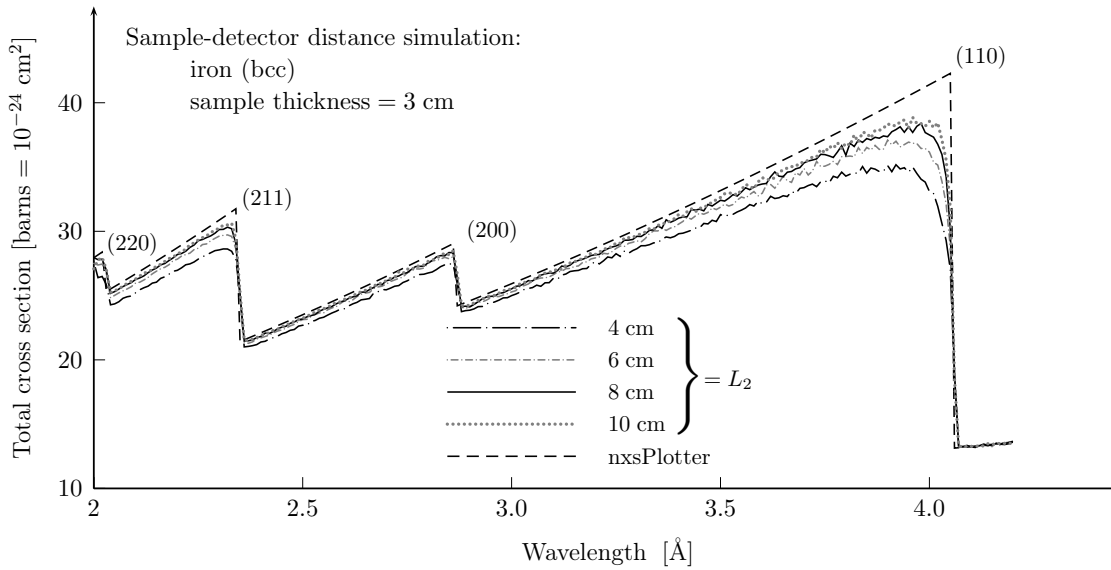


**Figure 8.4.:** Multiple scattering simulations of a 3 cm thick iron sample. The influence of different sample-detector distances is compared with the neutron cross sections (dashed line) calculated with *nxsPlotter*.

was placed directly behind the time-of-flight monitor component. Thus, a simulated neutron can be detected twice – once by capturing the neutron time-of-flight, which is affected by scattering events within the sample and a second time by monitoring its wavelength, which is determined by the actual neutron velocity vector  $\vec{v}$ , but not by its time-of-flight. In the example of figure 8.5 the Bragg edge spectrum of a 3 cm iron sample with a sample-detector distance  $L_2 = 4$  cm was simulated. The result shows the same extinction discussed above. In general, the effect of the increasing deviation is apparent for both detectors, especially in the wavelength region near the first (110) transmission edge. However, the diagram clarifies a difference between the “measured” (converted from the neutron time-of-flight) and the actual neutron wavelength (detected by the  $L$ -monitor component). While  $L$ -monitor already delivers neutron wavelength values, the  $TOF$ -monitor values must be converted taking the length  $L$  of the neutron flight path into account. This corresponds to measurements on the real instrument. In the example diagram, the amplitude of the total neutron cross section left of the (211) Bragg edge, i.e.  $\lambda < 2.3 \text{ \AA}$ , shows differences between both types of monitoring component. This effect can be explained by the individual probabilities for scattering events within the sample. In the region of  $2.1 \text{ \AA} < \lambda < 2.3 \text{ \AA}$ , multiple chances exist to scatter coherent elastically, i.e. neutron scattering by the (211), (200) or (110) lattice

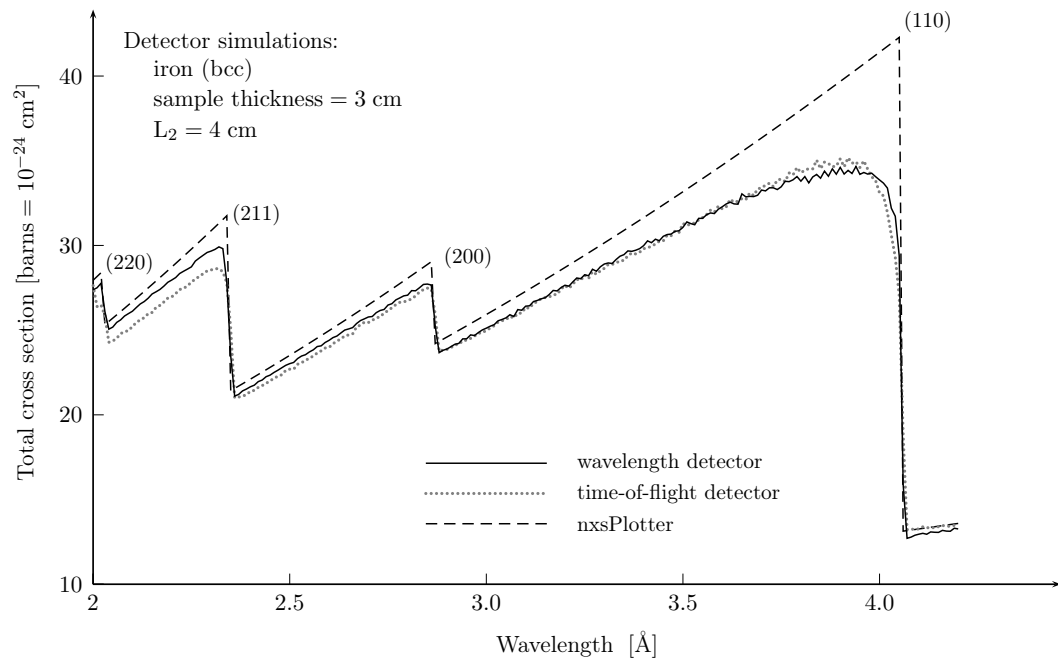


**Figure 8.5.:** Comparison of virtual time-of-flight and wavelength detectors by means of a multiple scattering simulation with a 3 cm thick iron sample.

plane is possible. The total time-of-flight of a multiple scattered neutron increases, but its actual wavelength remains constant. Hence, multiple scattered neutrons detected by the ToF monitor exhibit a larger deviations from the theoretical values compared to them which are detected by a wavelength monitor. Although, this effect decreases from one Bragg edge to the next — the individual scattering contributions disappear with each transmission edge — a small change between both signals is also visible close to the (110) edge. An additional uncertainty in position and time exists when a neutron leaves the sample, such as the uncertainty from the moderator. For example, if the neutron transmission path inside a 3-cm thick sample, for neutrons with a wavelength of 4 Å, is two times longer due to multiple scattering, then the detected time-of-flight uncertainty is  $\Delta t \approx 30 \mu\text{s}$ . With a total beam path of  $L = L_1 + L_2 = 50$  m, this is equivalent to a wavelength uncertainty  $\Delta\lambda = 2.4 \times 10^{-3}$  Å. The detection of the time-of-flight signal therefore prevents a very precise analysis of the neutron wavelength [Santisteban et al., 2001]. In order to overcome this problem, a secondary beam collimation can be realised as stated above. Additionally, a wavelength detector taking advantage of the neutron energy could bridge this gap. However, the latter is only useful if the

same precise wavelength resolution can be achieved.

### 8.3.4. Powder Simulation

The simulation tests presented above already provided a possible explanation for the rounding effects in the area of a Bragg edge. The implementation of multiple scattering events inside a virtual specimen shows a similar behaviour as presented in figure 8.1. However, a small deviation between the results from the developed simulations and from the presented experiment still exists in the region after the Bragg cut-off position ( $\lambda > 4.1 \text{ \AA}$ ). The original experiment, described in Santisteban et al. [2001], was conducted with an iron powder instead of a solid polycrystalline sample. Hence, preferred crystal orientation effects were excluded. The powder was placed inside a boxed vanadium can. The total sample thickness was  $2.54 \text{ cm} = 1 \text{ inch}$ . The iron powder has a smaller density than a solid sample, hence, the macroscopic density affecting the neutron beam attenuation is not defined by the unit cell composition (see equation 3.22). For the comparison between the measured and the theoretical neutron cross sections, the estimation of the powder density is difficult. All in all, a fitting of the density  $\rho$  is equivalent to a normalisation of the cross section result  $\sigma$ . Since  $\rho$  is only a factor in the relation of  $\sigma$  and the attenuation coefficient  $\mu$  (see equation 3.3), the measured total neutron cross section will be scaled by the sample density.

In the following simulation, half the density of the iron (bcc) unit cell was used to emulate a powder specimen ( $\rho = 3.94 \text{ g/cm}^3$ ). The rest of the neutron cross section calculation was the same. Again, the ENGIN-X instrument simulation was applied although the powder specimen was measured on the former ENGIN. This can be justified with the similar apparatus. The most important difference between both instruments is the primary beam path, i.e. the moderator-sample distance which is  $L_1 = 15 \text{ m}$  and  $L_1 = 50 \text{ m}$  for ENGIN and ENGIN-X respectively. However, for the investigated subject presented in this chapter, the difference of  $L_1$  does not impact on the results of the multiple scattering simulation. In addition to the iron, a second and third Bragg edge simulation module has been inserted to the instrument definition. Both were characterised by a vanadium description. Therefore, the input file mechanism (section 5.2.3) was used. Consequently, the wavelength-dependent neutron

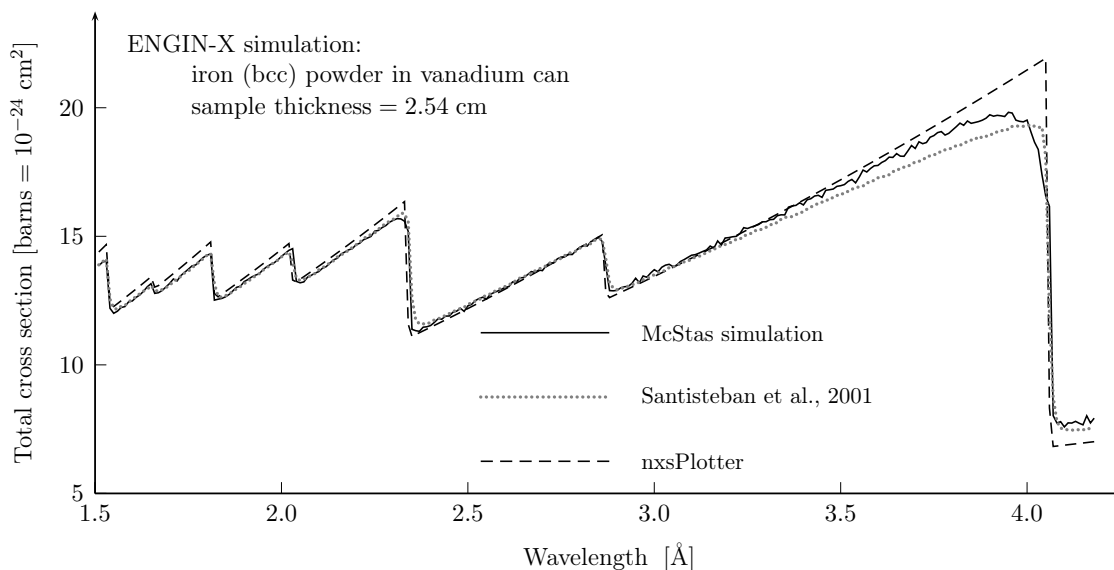


**Figure 8.6.:** *Iron powder simulation: The influence of the thin vanadium can walls is shown as an increase of the total neutron cross section after the Bragg cut-off position.*

cross section calculation was enabled for vanadium also. The two vanadium components were placed before and after the iron powder sample and their thicknesses (important for transmission) were set to 0.5 mm each. Thus, a simulation of the iron powder inside the vanadium sample can was realised as utilised by Santisteban et al. [2001]. In figure 8.6, the result of the experiment simulation is shown. The neutron transmission signal was converted to the total neutron cross section with respect to 2.54 cm sample thickness. Furthermore, the theoretical Bragg edge curve (dashed line) takes the modified sample density into account. Hence, the overall amplitude is scaled compared to the iron simulations presented before. The multiple scattering influence is quite evident. The influence of the vanadium components inside the neutron beam is weak. Vanadium is an incoherent scatterer, i.e. there are no Bragg edges in the transmission spectrum — the . The total cross section is therefore dominated by the strong incoherent and absorption contribution. Consequently, the iron Bragg edges (position, shape, magnitude) are not affected by that. However, the vanadium contribution becomes visible in the region outside the Bragg edges. For wavelengths longer than the Bragg cut-off, the total neutron cross section obtained from the experiment and the simulation is higher than the theoretical one (dashed line). The vanadium influence appears like a shift along the y-axis. Thus, the differences in figure 8.1 can be explained. The evaluation of the simulation

has shown that the vanadium can causes a small but systematic error during the analysis of the experiment if its influence on the detected signal is neglected. Although the can walls are very thin their influence to the transmission signal is significant.

## 8.4. Step Wedge Investigations on CONRAD

With respect to the multiple scattering contribution to the transmission signal, a further set of experiments has been performed on the CONRAD tomography instrument. The influence of different sample thicknesses was tested by means of the analysis of an iron step wedge. Furthermore, the experimental setup was replicated with a McStas simulation. A comparison of both results was used to discuss the multiple scattering influence.

### 8.4.1. CONRAD Radiography Experiments

An iron step wedge sample with four steps was measured<sup>1</sup> in radiographic mode on CONRAD. Each of the steps is 1 cm high and 1 cm wide. The depth of a step is 5 mm. Thus, the sample thickness in transmission geometry varies with each step. A sketch of the sample is shown in figure 8.7a. The transmission paths of 5 mm, 10 mm, 15 mm and 20 mm will be evaluated in the following. The experiment shown here was performed with a different monochromator setting than presented in section 5.4.1. Therefore, another set of single crystals with approx. 3° mosaic spread was used. However, the monochromator mosaicity was not validated by neutron measurements. Hence, it was expected that a different value may match with the simulations presented afterwards. The measurement was conducted in radiographic mode, i.e. radiographic and flatfield images have been taken to analyse the transmission signal. An example radiography is shown in figure 8.7b. Altogether, a wavelength scan from 2 Å to 6 Å in steps of 0.1 Å has been performed.

After flatfield correction, the detector images were analysed by averaging the grey values at each step. Due to the different sample thickness, the area of a single step is clearly visible in the radiography (see figure 8.7b). A region of interest of about 1600 pixels covering an area of almost (10 × 10) mm<sup>2</sup> was selected for each step. Thus, a single mean transmission value

---

<sup>1</sup>The radiographic measurements shown here have been performed by Michael Schulz from FRM-II, Munich.

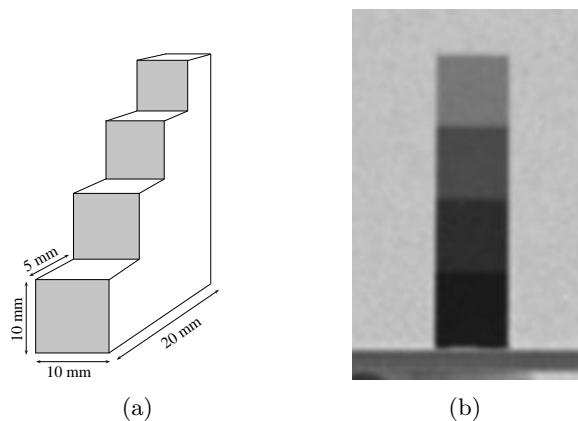


**Figure 8.7.:** Schematic drawing of a step wedge (a) and a radiogram (b) of an iron step wedge sample measured on CONRAD.

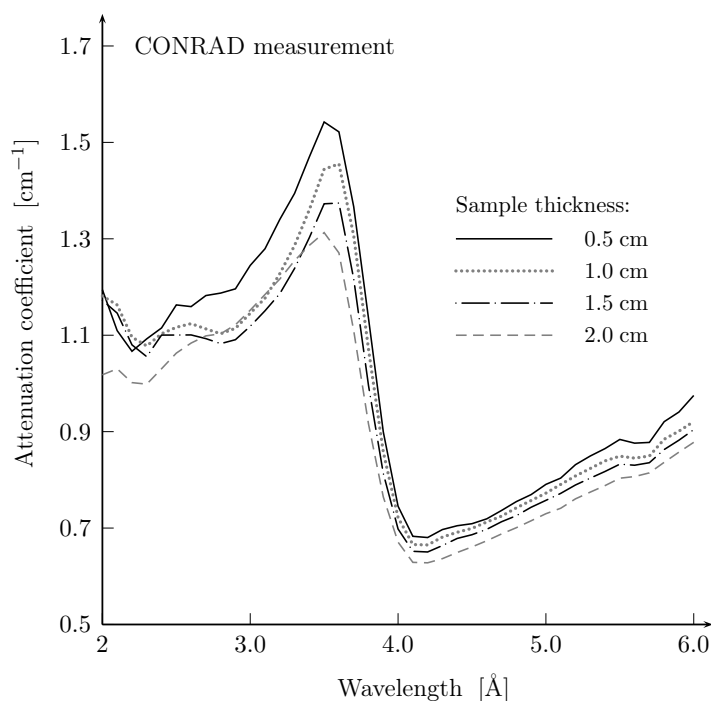


**Figure 8.8.:** Bragg edge scan of an iron step wedge with different transmission paths.

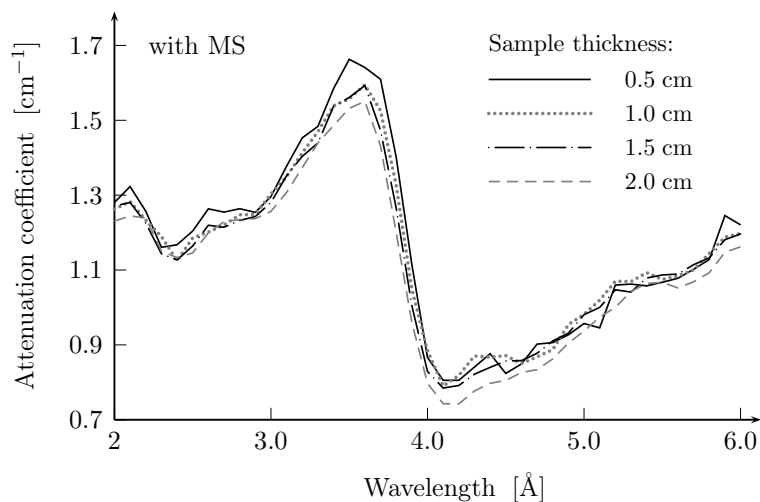
was obtained for every single wavelength step. The wavelength scan was further evaluated in terms of the attenuation coefficient  $\mu$ . According to this,  $\mu$  was normalised by the appropriate sample thickness. As a result, figure 8.8 displays the gradient of the attenuation coefficient for each sample step. The diagram shows a very broad (111) iron Bragg edge. The broadening is related to the higher degree of monochromator mosaicity. Hence, the Bragg edges before (at  $2 - 3 \text{ \AA}$ ) have been blurred and almost disappeared. However, the comparison of the different

transmission paths shows a significant variation of the measured attenuation coefficient and therefore of the total neutron cross section also. As presented before, the effect of the cross section decrease in relation to the sample thickness can be explained by multiple neutron scattering events inside the sample. In order to confirm this assumption for the current measurement, a simulation of the experiment has been performed.

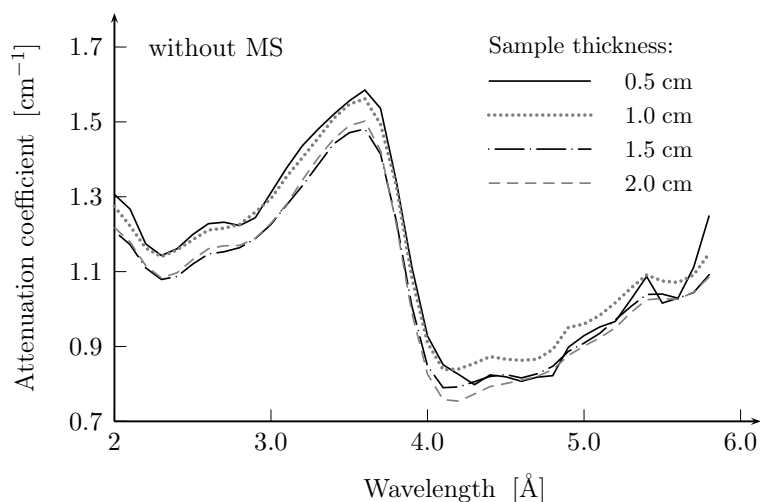
#### 8.4.2. Evaluation with Experiment Simulations

In order to find explanations of the differences observed in the Bragg edge spectra, the above presented experiment was emulated with the McStas simulation. Therefore, the CONRAD instrument definition, demonstrated in section 5.4, was used in combination with the multiple scattering modification to the BraggEdge\_Powder sample component. Because the standard McStas algorithms are limited to the case of cubic or cylindrical sample geometries, the step wedge was constructed from individual sample pieces. Four individual steps with the appropriate depth (0.5 – 2.0 cm) have been arranged next to each other to emulate the step wedge shape. Supplementarily, the sample arrangement has been surrounded by a component loop. The JUMP statement was applied behind the sample to realise non-sequential neutron propagations [Willendrup et al., 2008]. Thus, multiple scattering events inside a sample piece as well as within the complete step wedge have been enabled. As a further test case, the four individual step pieces have been applied within another simulation. A second simulation was performed with the iron step wedge, but without the multiple scattering modification. Thus, the same instrument and sample conditions have been tested in order to compare the multiple scattering effect to the CONRAD machine. Additionally, the neutron intensity monitor behind the sample has been modified. In order to simplify the evaluation, four monitors have been added to the instrument definitions. The replacement of the original monitor component was done to map the transmitted neutron intensity at each of the selected sample positions — the four steps. The monochromator mosaicity was set to  $5^\circ$ . Thus, a good agreement towards the smoothing of the Bragg edge was achieved. Similar to the real experiment, a wavelength scan from 2 Å to 6 Å in steps of 0.1 Å including flatfield simulations have been conducted for both cases.





(a)



(b)

**Figure 8.9.:** CONRAD Bragg edge simulations of a step wedge sample with (a) and without (b) the multiple scattering modification.

After flatfield correction, the attenuation coefficient has been determined by normalisation with the individual sample thicknesses. The resulting plots for all experiment simulations are shown in figure 8.9. Compared to the real CONRAD experiment, the same blurring of the Bragg edges between 2 Å and 3 Å due to the selected monochromator mosaicity has been simulated. Moreover, the resulting slope of the (110) iron edge is comparable to that obtained from the experiment. This effect is visible for both tests. However, a fundamental difference between both simulations is not identifiable in general. Both graphs agree with the experiment. In particular, the decrease of the attenuation coefficient and the Bragg edge

shift related to the sample thickness are comparable, although the emulation was tested with (figure 8.9a) and without (8.9b) the multiple scattering modification. Hence, the multiple scattering influence to the Bragg edge signal is very weak. Likewise, this also means that the observed effects cannot be explained by multiple scattering events inside the specimen.

Although there is no variation of the lattice constant, neither in the step wedge sample, nor in the simulation components, the Bragg edge position decreases with an increasing sample thickness. Due to the sample alignment in the experiment and the simulations (thin step on top), the wavelength shift relative to the detector height, discussed in section 5.4.2, is not responsible here. In contrast, this would cause the opposite effect, since the mean wavelength increases with the height at the detector. From top to bottom, the Bragg edges would then be shift towards longer wavelengths due to the monochromator setup. Nevertheless, the monochromator influence is accounted for the differences before and after the Bragg edge. The decrease of the attenuation coefficient relating to the sample thickness, could also be seen as a shift of the signal towards longer neutron wavelengths. Beyond that, an influence called “beam hardening”, that produces image artefacts in tomography applications [e.g Hsieh, 2003], intensifies this effect. The principle problem is described as follows. The incident polychromatic neutron beam will be trimmed during the transmission through the sample, since low energetic neutrons (long wavelengths) will be absorbed rather than higher energetic neutrons (short wavelengths). As a result, the total beam attenuation is falsified. Here, the problem corresponds to the Bragg edge spectrum. Although the monochromatic option was used, a multitude of different neutron wavelengths will be measured appearing as a Gaussian function with varying peak width depending on the monochromator mosaicity. Consequently, the mean selected wavelength on CONRAD decreases with the sample thickness, which shifts the signal even stronger. The explanation for the Bragg edge shift in contrary direction is also rooted in the phenomena of beam hardening, although longer wavelengths dominate here. The reason for that is the Bragg edge itself. Due to the extreme intensity difference before and after the edge, the mean wavelength value will increase. The Gaussian signal, selected by the double monochromator, is convoluted with the Bragg edge. Hence, when transmitting through the sample, the fraction of shorter wavelengths is much more decreased than the

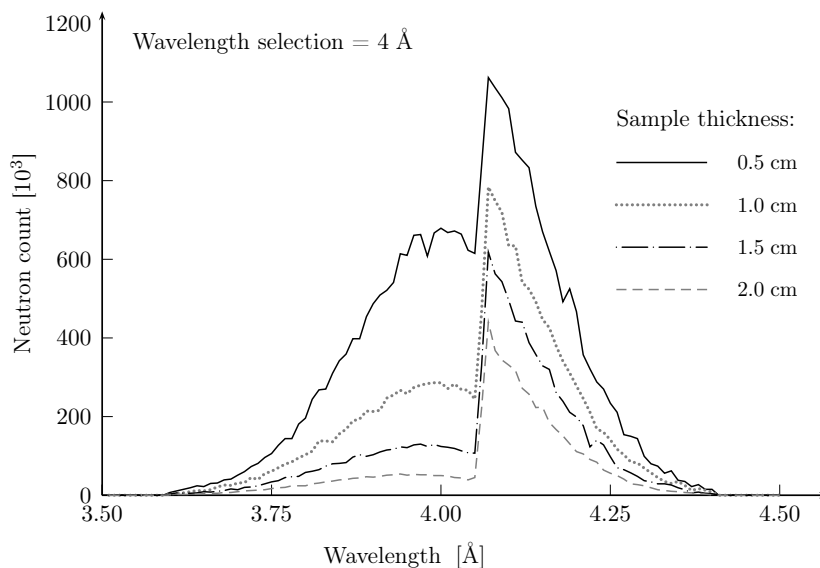


**Figure 8.10.:** Beam hardening at the Bragg edge position.

longer wavelengths after the edge. In order to visualise this effect the simulation has been extended with further components monitoring the neutron wavelength. Figure 8.10 shows the wavelength band captured behind the individual sample positions. The diagram represents the transmitted neutrons for a single instrument setting at 4 Å. For all sample positions, the initial neutron signal has been affected by the Bragg edge transmission. The mean wavelength is no longer the centre of the Gaussian distribution, but leans to the long wavelengths. The longer the path through the sample the more neutrons on the short wavelength side of the edge disappear. Accordingly, the actual selected wavelength increases with the sample thickness. As a consequence, the resulting Bragg edge position in the wavelength scan (figure 8.9) decreases.

## 8.5. Discussion

As stated above, the evaluation of multiple scattering contributions to the detector signal with Monte Carlo algorithms is a reliable tool since there is no experimental procedure available to solve this accurately. Hence, an implementation of multiple scattering events into a Bragg edge transmission simulation was realised with the McStas neutron ray-tracing software. The simulation of the ENGIN-X instrument has shown that the theoretical assumption of a growing scattering probability in the near of a Bragg edge leads to multiple scattering.

Moreover, the detection in transmission geometry demonstrated that more neutrons will be captured because of multiple scattering. Hence, an extinction of the evaluated total neutron cross section is visible. Furthermore, an increase of the multiple scattering influence was illustrated by simulation test of different sample thicknesses and detector distances. As a result of this computation, the extinction increases with the sample volume that is captured by the detector. In addition, it was shown that multiple scattering becomes unimportant for wavelength longer than the Bragg cut-off. The powder simulation of section 8.3.4 further revealed the significant influence of the sample environment. Although the vanadium sample can was very thin and vanadium has no influence on the Bragg reflections of iron, a difference between evaluated and expected theoretical neutron cross section has been detected after the Bragg cut-off position. Due to the vanadium can walls a small but systematic error is included in the measurement. However, the experimental results in figure 8.1, originally motivating the work presented in this chapter, have been emulated by a simulation of the experiment setup. The influence of multiple scattering as well as of the vanadium can has been demonstrated. A validation of the simulation principle was shown by the evaluation of the time-of-flight signal and the “real” neutron wavelength, that obtained small but significant differences. Furthermore, the modification of the Bragg edge simulation module was tested in order to investigate the effects occurring in the transmission spectrum of an iron step wedge. The results of the CONRAD experiment have been emulated with the McStas simulation. The variations inside the Bragg edge spectrum have been explained by beam hardening effects. In parallel, it was demonstrated that a multiple scattering contribution to the transmission signal on CONRAD is not apparent due to the large monochromator mosaicity and the size of selected wavelength band.

It is noted that small discrepancies still exist between the simulated and experimental results. For example, a small discrepancy is apparent in the shape of the cross section decrease. In figure 8.6, the rounding of the first Bragg edge still differs from the experiment shown in figure 8.1. Hence, the multiple scattering effect may be only one additional contribution to the Bragg edge transmission amongst others. Weiss [1952a] for example, investigated extinction effects in neutron transmission mode. The classification into primary and secondary

extinction, originally considered in diffraction experiments, was used to analyse their influence to the total cross section measurements in polycrystalline media. The first one is related to the grain size of the specimen and is of higher importance towards diffraction intensity changes. Whereas the secondary extinction describes an increment of the absorption depending on the mosaic spread. Related to that, changes of the Bragg edge amplitude as well as of its sharpness have been demonstrated. Furthermore, the discrepancy of measured and theoretical total cross section curves has been investigated by Petriw et al. [2010]. An increase in the total cross section was observed and associated to small angle neutron scattering. A dependency on the sample porosity and density was derived. According to this, a theoretical model was proposed and fitted with experiments of different graphite samples. An agreement was found to describe the total cross section at neutron wavelength longer than the first Bragg edge. This correction principle is equivalent to an adjustment of the attenuation coefficient in order to correct secondary extinction effects. For both types, it is assumed that multiple scattering takes place. On the one hand, large grains are concerned. On the other hand, secondary extinction occurs in small, slightly misaligned crystallites. However, the difference for the application presented in this chapter is the deviation between kinematical and dynamical theory of diffraction. The latter includes the extinction effects due to the consideration of refraction and interference. Unfortunately, this is not implemented in McStas as there is only one neutron present at any time. Each neutron trajectory is computed individually, one after the other. Moreover, an implementation of grain properties, such as size and orientation, into a sample module has not been realised up to now. However, it should be mentioned, that the step wedge sample is expected to have a homogeneous distribution of grains (including size and orientation). But extinctions effects have been detected anyhow. Nevertheless, multiple scattering was tested based on coherent elastic scattering cross section calculations. Therefore, the kinematic approach is adequate. As a result, the total neutron cross section is decreased according to the sample geometry and the instrument setup. The multiple scattering simulation was validated by the presented experiments. With the use of a secondary beam collimation, a way to decrease and avoid this influence was shown.



## Summary

### 9.1. Results & Conclusion

A simulation of Bragg edge neutron transmission experiments was presented in this thesis. To do this, a model to describe the transmission for cold and thermal neutrons was implemented into the nxs C library. The library routines developed have been applied to the graphical plotting program nxsPlotter as well as to the McStas Monte Carlo neutron ray-tracing software. In this way, McStas was extended to make simulations of wavelength-dispersive neutron transmission experiments. Subsequently, McStas was used to investigate instrument parameters and sample properties influencing the Bragg edge transmission pattern. By means of a new sample module, the neutron-matter interactions, based on neutron cross section calculations, were added to the McStas neutron ray-tracing computation. For the first time in McStas, the decision to perform neutron scattering, absorption or transmission takes into account the crystallographic description of a sample, i.e. its unit cell composition. The implementation of the Bragg edge prediction was validated with existing programs. Together with the graphical representation in nxsPlotter, the nxs routines are able to assist the preparation of an experiment, through, for example the prediction of interesting Bragg edge positions and magnitudes. The new sample module may therefore be seen as indicating the feasibility of an experiment. In particular, the analysis of instrumental influences in combination with specific sample properties is made available by this simulation module. The emulation of the CONRAD and ENGIN-X machines has been demonstrated and results compared against experiment.

The new McStas Bragg edge sample component has been applied to multiple experiment configurations. In a first attempt, the wavelength-selective option on CONRAD has been implemented in terms of a virtual double crystal monochromator. Thus, the simulation of the complete CONRAD beamline has been realised. The effect of the monochromator device on the Bragg edge spectrum has been investigated and systematic uncertainties arising from this setup have been evaluated. Specifically, the fact that the contribution of the higher order wavelengths reflected from the monochromator affects the Bragg edge result at the detector was investigated as well as the correlation of the monochromator mosaicity with the broadening of the Bragg edge. Furthermore, it was verified that the instrumental setup causes a spatial distribution of selected neutron wavelength on the detector. As a result, the height of the detector image can be used to provide additional information about the resolution of the selected wavelength. However, the analysis of such experiment must take this effect into account. The instrument simulation has been tested and validated by applied examples. The results of the simulations and the experiments coincide.

Since it is a declared objective of transmission spectroscopy to provide information comparable to that of elastic coherent neutron diffraction, the Bragg edge method has been studied in relation to the analysis of preferred crystallographic orientations. Therefore, the texture of an aluminium sample has been determined by conventional neutron diffraction measurements. These reference datasets were compared with the results from the Bragg edge transmission experiments. Taking the different initial conditions of the applied instruments into account, a good agreement was found for the determination of the crystallographic preferred orientation. The simulations of the CONRAD and ENGIN-X instruments using a constant sample texture description have been shown to coincide with the experimental results. The implementation of the March-Dollase model for the correction of the coherent elastic neutron cross section was confirmed experimentally. Thus, a quantitative comparison of textured Bragg edges measured on two different instruments has been enabled. By the application of the March-Dollase factor within the simulation, the measurement method was validated to be self-consistent. The results of the experiments on the two instruments agreed with the simulation using one and the same sample and texture description. As a further



result, a first model to describe texture effects was realised and validated to be used with the McStas framework.

Extending the evaluation of Bragg edge transmission spectra, local lattice spacing variations have been investigated. By means of a standard residual stress sample the projected strain in neutron transmission direction has been examined. A simulation module was created to emulate the strain components obtained from neutron diffraction measurements. Here, their influence to the transmitted signal was computed and tested on virtual instruments. Thus, an ideal projected strain result could be compared with the simulations and measurements on CONRAD and ENGIN-X. For the first time, such local sample properties have been implemented in a McStas sample module. Based on the input file principle further local sample characteristics are possible to be tested within McStas. Measurements on ENGIN-X and CONRAD demonstrated the feasibility of such Bragg edge studies. It is hoped and expected that the results will contribute to the further development of a neutron strain tomography proposed elsewhere.

The simulation of the CONRAD and ENGIN-X instruments has further been used to test the effect of multiple scattering to the Bragg edges. Therefore, the new Bragg edge module was further extended to enable repetitive scattering of neutrons inside the sample. The influence of the sample geometry as well as the effect of the secondary beam path on the Bragg edge spectrum has been demonstrated. For both instruments, different experiment results have been explored via simulations. While on ENGIN-X the multiple scattering contribution appears to exhibit a significant influence on the Bragg edge spectrum, the effect is not apparent on CONRAD. We suggest that this is due to the effect of wavelength selection with the double monochromator. However, the discussion around the multiple scattering results also suggested that effects assigned to primary and secondary extinction should be considered.

Summarising, the implementation of the Bragg edge transmission simulation enabled a large variety of test cases to be validated. Thus, multiple problems have been evaluated by the comparison of virtual and real experiments including two very different instruments.

Altogether, the Bragg edge transmission simulation was shown to be helpful towards the ongoing development of this type of measurement method. Thus, the outcome of this work is useful towards the upgrade of existing and the installation of new instruments applying Bragg edge neutron transmission. As an example, the new McStas sample component has already been applied towards the development of a new beamline, which will be described in the following.

## 9.2. Case Study: IMAT beamline

In 2009, a second target station (TS-II) was completed at ISIS and seven neutron instruments dedicated to phase one of this project are operational. The science case for the TS-II project (see ISIS website<sup>1</sup>) demonstrated that providing neutrons over a broad wavelength spectrum and with high resolution will enable a significant step forward to solve problems in three key areas of science (Soft matter, Bio-science, Advanced materials). In total, TS-II has the capacity for 18 instruments in the future to cover these fields. Both target stations (TS-I and TS-II) will be fired by high-energy protons initially created and accelerated inside a linear and a circular accelerator, a linac and a synchrotron respectively. After thousands of revolutions of the synchrotron the protons are separated into a pair of bunches that pass beamlines to each of the target stations. There, the protons hit the target material which releases the neutrons. This whole cycle repeats 50 times every second (50 Hz). Four pairs of bunches go to the first and one pair goes to second target station, i.e. TS-II runs at 10 Hz.

In phase two (timeline from 2011 to 2015), four new instruments will be built. One of them will be the IMAT beamline for imaging and material science & engineering, which provides separate modes for imaging and diffraction experiments. At ISIS, no imaging capabilities are available, i.e. that IMAT would serve a multidisciplinary community beyond the traditional scattering areas [Kockelmann et al., 2007b]. Besides conventional radiography and tomography, this includes energy-resolved imaging, taking advantage of Bragg edges for contrast variations and applying the strain tomography method as discussed in this thesis. Furthermore, the diffraction mode will provide complementarity to the ENGIN-X instrument, e.g.

---

<sup>1</sup>ISIS second target station: <http://www.isis.stfc.ac.uk/about-isis/target-station-2/>

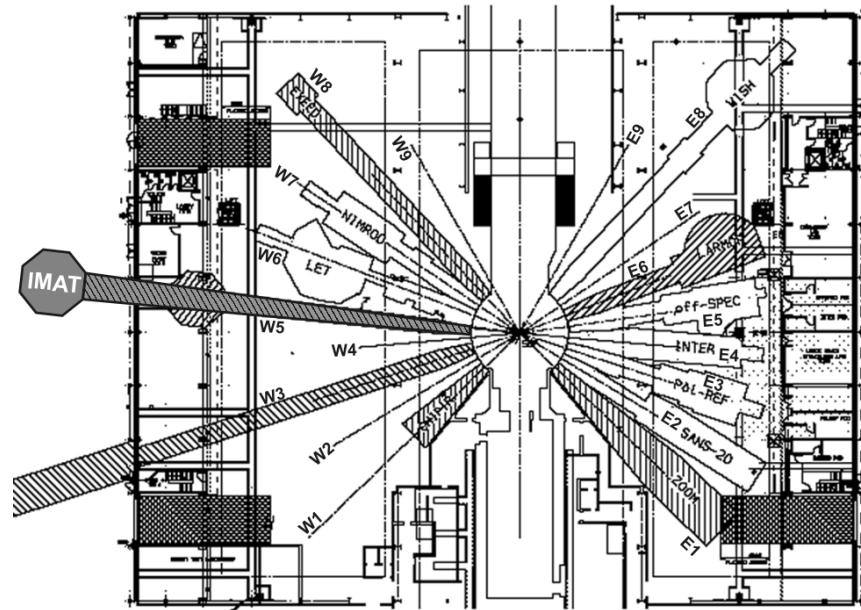


**Figure 9.1.:** Drawing of the TS-II main building, which is divided into east and west sides, each provided with 9 beam ports (W1 - W9 and E1 - E9). The phase one instruments are shown in white while the upcoming instruments are dashed. IMAT (shown in gray) will be placed on W5 and extended to be outside the TS-II hall to achieve a longer flight path.

fast texture determination and in-situ process monitoring.

The McStas Bragg edge module developed in this thesis was used in the design phase of IMAT. Two of the simulation applications will be described here.

### 9.2.1. Moderator choice

One of the key issues in the design phase of an instrument is the decision of the position of an instrument to be built and, in the case of the ISIS second target station, the choice for the appropriate moderator. Figure 9.1 shows a drawing of the TS-II main building with the target in the centre, providing 18 different beam ports, E1 - E9 (east) and W1 - W9 (west), for the neutron instruments. An overview of the available moderator faces, that the beam ports view, was presented in the report of Oliver & Kockelmann [2008] for example. In principle, the TS-II moderators release neutrons with different pulse shapes depending on whether the available moderator materials are coupled or de-coupled. On the east side, the E7 and E9 beam ports were considered for the IMAT position. Both ports view a de-

coupled solid methane moderator, which provides sharp pulses and hence, is advantageous for the diffraction and strain analysis. However, a long flight path would be obstructed on E9. On the west side, W2 (solid methane moderator), W5 and W8 (both: coupled moderator, liquid hydrogen / solid methane) have been discussed. In order to evaluate the performance of the different moderator options, a simple virtual time-of-flight instrument has been created to simulate openbeam measurements. The instrument definition consists of a moderator component a pinhole with 3 mm diameter and  $(20 \times 20)$  cm<sup>2</sup> monitor to capture the simulated neutrons. For all simulations, the moderator-detector distance was set to 40 m, which is the maximum length to be realised inside the TS-II main building. Neutron guide systems could help to transport the maximum flux to different sample/detector positions, but for the moderator evaluation the simulation was conducted without these components to compare the results under the same conditions. Furthermore, the simulations have been benchmarked against the performance of the TS-I liquid methane moderator (CH<sub>4</sub>). Here, a 10 Hz and 40 Hz setting has been used to represent a worst case and best case scenario respectively for TS-I [Oliver & Kockelmann, 2008], because TS-I will operate at four times the repetition rate of TS-II. The discussed beam ports have been used as input parameters for the `ISIS_moderator` component within the simulation definition. The resulting flux profiles for the simulated pinhole instrument are shown in figure 9.2a. The plots demonstrate how the intensities vary for the different moderators. A high intensity is beneficial for imaging. The high neutron flux, especially in the region from 2 – 6 Å is apparent for the W5 and W8 beam ports. In order to evaluate the performance for the Bragg edge imaging application, the McStas simulation was extended with the Bragg edge sample module developed in this thesis. The same moderator options have been chosen. The results of the transmission simulations through a 15 mm thick bcc iron sample are shown in figure 9.2b. Again, W5 and W8 deliver the greatest contrast for the first Bragg edges with descending wavelength.

To justify the decision for one of the considered beamline positions, ratings have been established based on the results of the simulations. Therefore, the flux profiles (figure 9.2a) have been integrated over the wavelength range of 0.5 – 8 Å and transformed to relative integrated fluxes, for which the value of W8 is 100 % for example. For the analysis of the Bragg

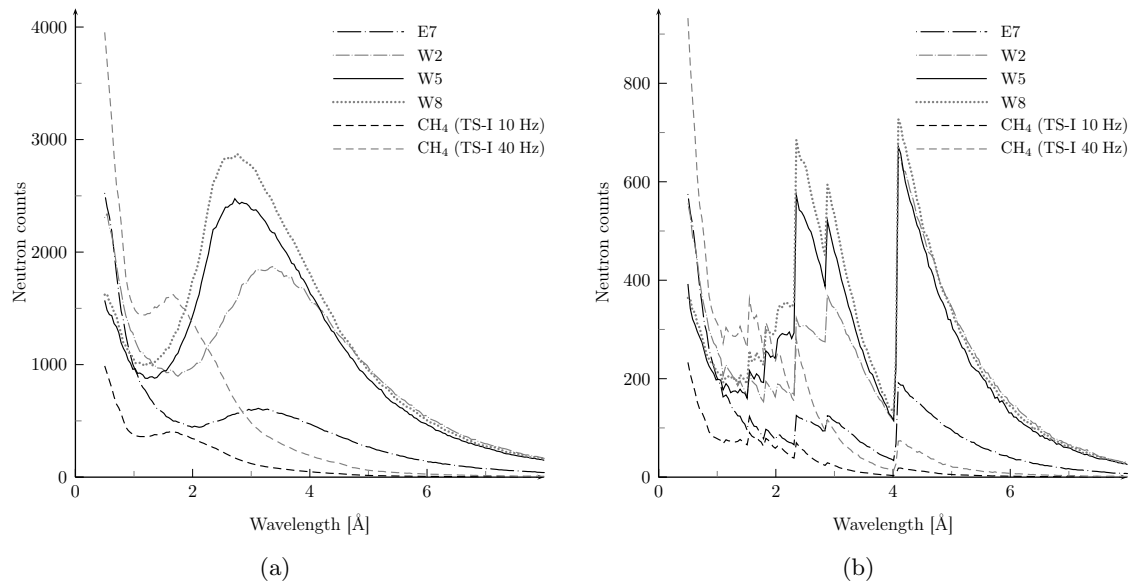


**Figure 9.2.:** Simulated flux profiles (a) for the possible positions of the new IMAT beamline. For benchmarking against the TS-I, the 10 Hz and 40 Hz settings for CH<sub>4</sub> moderator setting are shown with dashed lines. In (b), the new McStas sample module was included to simulate the Bragg edge effect on the beam profiles. Here, a 15-mm thick iron (bcc) sample was simulated.

edges, the intensity difference across the strongest Bragg edge has been used to quantify the available contrast provided at the different beam ports. In the report on the moderator choice of Oliver & Kockelmann [2008], this evaluation has been continued with the analysis of the diffraction mode of the instrument, which includes the integrated diffraction peak intensity and the moderator-dependent peak width. Based on the results of the simulations, the final position of the IMAT instrument was demonstrated in the presentation of Kockelmann [2010]. W8 has the highest neutron flux, but IMAT would have to compete with other instruments for this beam port. Almost the same flux can be achieved on W5 and furthermore, a longer flight path ( $> 40$  m) could be accommodated. Since the beamline can be pulled out of the experimental hall, there is more space for the sample position. One is not constrained by neighbouring instruments and can include large detector arrays for the diffraction mode. Moreover, this provides more space for sample preparation areas and laboratory. Therefore, IMAT will be built at W5 56 m away from the moderator and outside the TS-II main building [Kockelmann, 2010], such as shown in figure 9.1.

### 9.2.2. Aluminium windows

The second application of the Bragg edge simulation belongs to the discussion of the necessary neutron guide windows in the primary beam. The total primary flight path will be evacuated as far as possible. To define the pulsed beam IMAT will have three choppers, each of them having two windows, because to run them in vacuum needs further development. Further windows will be necessary at the target wall, at the end of the last beamtube, in the shutter section and for a beamtube between moderator and shutter. In total, 12 Al windows each with a standard thickness of 0.5 mm could be possible. For IMAT thinned-down windows (e.g. 0.25 mm thickness) have also been considered but safety issues might preclude this option. In order to test the effect of different numbers of windows on the incident neutron beam, the above presented simulation has been continued with IMAT placed at 56 m including an aluminium fcc Bragg edge sample component to emulate different window thicknesses  $l$ . An openbeam simulation ( $l = 0$  mm) was compared with different values for  $l$  representing various situations:

- 0.5 mm ( $2 \times 0.25$  mm: Best case — thin windows only at the two ends of a beamtube)
- 1.0 mm ( $2 \times 0.5$  mm or  $4 \times 0.25$  mm: Shutter included)
- 2.0 mm ( $4 \times 0.5$  mm: If vacuum choppers are available)
- 6.0 mm ( $12 \times 0.5$  mm: Worst case — 12 thick windows)

The listed situations have been applied to the simulation using the Bragg edge sample component to emulate different window thicknesses. No neutron guides have been included here to focus on the amount of aluminium material in the incident neutron beam, i.e. the number and thickness of the windows is represented by a single sample component with a varying input parameter  $l$ . The resulting spectra are plotted in figure 9.3a. The diagram shows a zoomed view of the region from 2.5 Å to 5 Å in order to visualise the very small differences between the curves. The Bragg edges are very small and almost invisible for the very thin Al windows. However, the complete simulated spectra have been integrated over the total region from 1 Å to 8 Å. The integrated intensities relative to the openbeam measurement are shown in figure 9.3b. In order to determine an overall loss of intensity per millimeter

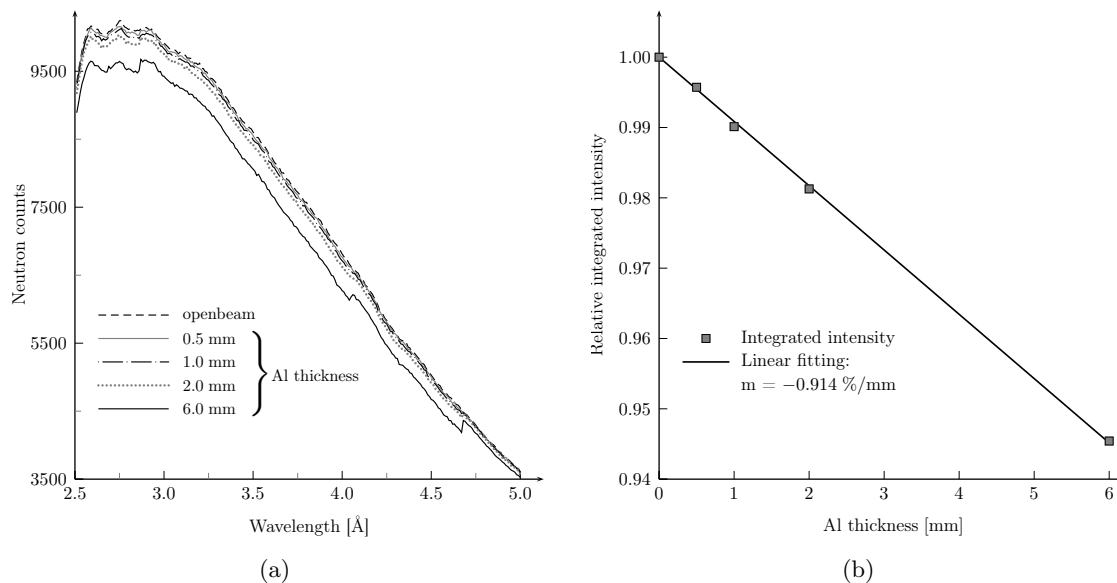


**Figure 9.3.:** Simulated openbeam measurement and transmission spectra (a) of an aluminium sample of different thicknesses. The integrated intensities (b) of these spectra have been fitted to a linear function to determine the intensity loss per mm aluminium thickness.

aluminium thickness, the calculated values have been fitted to a linear function  $y = mx + n$ , with  $n = 1 = 100\%$  representing the openbeam measurement ( $l = 0$  mm). The resulting loss of the overall intensity is  $m = -0.914 \text{ \%/mm}$ , i.e. for the worst case scenario still 94.6 % of the original intensity will be available. Although, this seems acceptable and the shape of the incident beam profile including Bragg edges could be corrected by openbeam/flatfield measurements for every transmission measurement, problems might occur when the moderator profile changes over time (minutes or hours). When the moderator cools down or warms up the incident spectrum will change which could also affect the shape of the Bragg edges. Then, the normalisation with openbeam measurements could compromise the analysis of the actual experiment, especially when the aluminium Bragg edges overlap with those of the investigate specimen. Hence, the responsible campaign for thin guide windows and vacuum choppers to minimize this effect.

### 9.3. Further Work

The simulation of Bragg transmission edges and the effect thereon of the different conditions and parameters of existing neutron instruments suggest considerable potential for this kind of

measurement method. It was shown, that experiment simulations can be applied to evaluate and support neutron transmission measurements. Possible improvements and further work with this technique, as well as extensions to the software site will be mentioned below.

The nxs library routines take advantage of input files providing the necessary parameters for the sample description. However, the library could also be extended to be able to read additional (existing) file formats. One example that is already used within the analysis of diffraction patterns is the support of the crystallographic information files (cif) published by the International Union of Crystallography [Hall et al., 1991]. These files also contain a description of the crystallographic sample structure to be refined with measured results. An implementation would therefore be helpful in order to easily exchange initial structure files between different programs that already provide this format and between neutron diffraction and Bragg edge transmission experiments. Thus, one and the same file could be used multiple times and in parallel. Therefrom, a cif file support would be enabled for McStas as well, which has not been realised so far. A more general idea would be to apply the nxs library globally to the McStas framework. Hence, the calculation of the individual neutron cross sections and the crystallographic description of the sample would be available for other instrument components as well. Then, the decision for the scattering type and absorption or transmission would be based on the individual material composition. Thus, the simulated incident beam spectrum could be affected by further instrument elements and would therefore conform even more to the real beam.

According to the experimental simulation, further improvements could be tested. The CONRAD instrument simulation, for example, could be optimised by the investigation of the monochromator crystals. As reported in chapter 5, a wavelength-dependent reflectivity as well as the influence of the neutron penetration depth has been neglected. The simulation has been abstracted to the application of a mosaicity value. In order to achieve better agreements between simulation and measurement for the CONRAD instrument, the single crystal component available in McStas (`Single_crystal.comp`) could be implemented in the instrument definition to replace the monochromator component and tested. Referring to the fitting of textured Bragg edges, a possible implementation of more complex correction



models could improve the analysis of preferred crystallographic orientations. Thus, more general texture types would be enabled in McStas. Algorithms to be considered for this purpose have already been mentioned in section 6.6. Moreover, the simulation of varying lattice parameters, due to stress and strain, should be extended to cover hexagonal and also more general crystal structures. Thus, more sample materials would be included in the application of Bragg edge strain measurements and simulations. Finally, grain size effects have not been recognised in this work. Weiss [1952a], for example, showed that the grain size in polycrystalline media influences the evaluated neutron cross sections obtained with neutron transmission. Furthermore, he developed a general expression to calculate the neutron cross section, including factors for the grain size, mosaic block size and the angular spread of the mosaic blocks, such that a comparison with experimental data could be made. Figure 9.4 shows examples of Bragg edge amplitude changes by means of varying grain sizes for the 111 Al edge (a) and the 110 Fe edge (b). It is shown that the Bragg edge height decreases with increasing grain sizes. The simulation developed within this thesis could be extended to take this effect into account. An appropriate implementation with regard to primary and secondary extinction effects in Bragg edge transmission as discussed by Weiss [1952a] could contribute to the discussion of possible shape changes of Bragg edges.

The visualisation of preferred crystallographic orientations using Bragg edge radiography provides the potential to analyse local changes. Hence, local texture variations may also be visualised and evaluated on instruments like CONRAD. According to this, first test measurements have already been made using an extruded Mg AZ31 sample and presented in [Boin et al., 2009]. The sample was investigated with Bragg edge transmission on CONRAD. A comparison with reference diffraction measurements could validate the observed local texture data.

The reconstruction of principle strain directions from the projected strain is one of the main aspects in Bragg edge neutron transmission. The work of Abbey et al. [2009] presented a model that successfully reconstructed the strains and therefore demonstrated the feasibility of a neutron strain tomography. However, further fit functions are needed to reconstruct other than the presented strain profiles. In combination with the McStas simu-

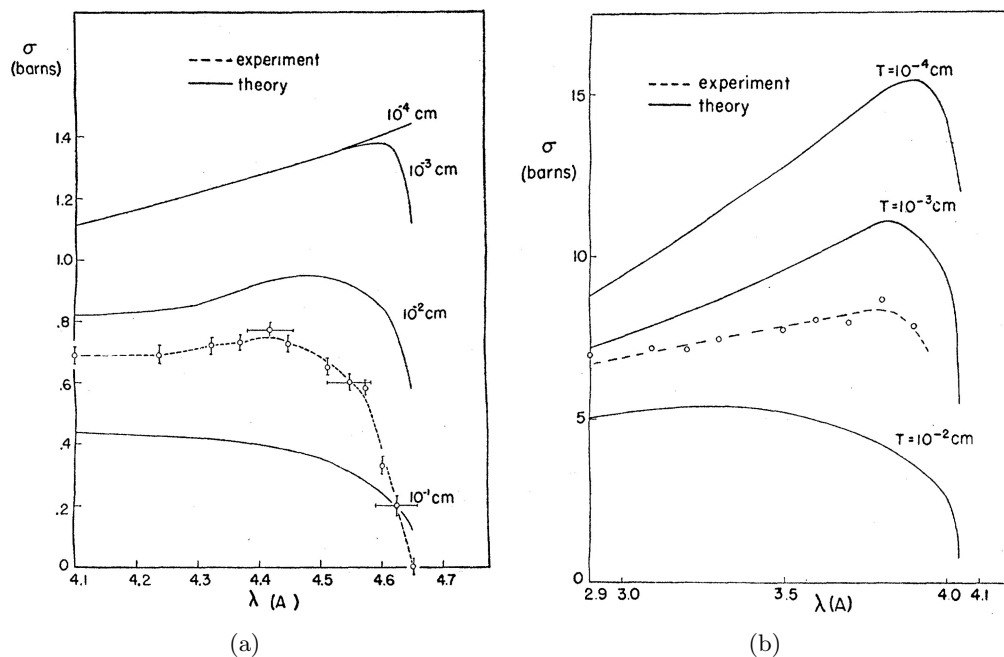


**Figure 9.4.:** The grain size effect on the Bragg edge amplitude, after Weiss [1952a, figure 3 & 4], for the 111 Al edge (a) and the 110 Fe edge (b).

lation the model development could be continued even without neutron experiments. With regard to the CONRAD experiments, further fitting algorithms towards the determination of the Bragg edge position could be developed to improve the results, which is crucial when studying strain effects. Therefore, the higher order reflections from the CONRAD double monochromator device could be considered in the fitting of a Bragg edge as they are included in the transmission signal at a selected wavelength.

In order to quantify the multiple scattering effect, it is useful to investigate a series of common materials with different thicknesses. Thus, the strength of the multiple scattering influence on the Bragg edge could be estimated for subsequent transmission measurements. These findings could further improve the evaluation of the exact Bragg edge position by incorporating them into the fitting routine.

As many of the proposed applications and their implementation are challenging and time-consuming tasks, for example the implementation of the proposed texture correction models with respect to the Bragg edge transmission geometry, one has to weigh up the cost benefit ratio. However, as introduced in the beginning, many advances in tomography [Strobl et al.,

2009] have been achieved motivating for the development of the Bragg edge approach to be continued. Especially for local texture and strain variations, i.e. resolving the preferred orientation distribution in 3D, the Bragg edge technique could be the method of the future.



## References

- B. Abbey; S. Y. Zhang; W. Vorster & A. M. Korsunsky.** *Feasibility study of neutron strain tomography.* *Procedia Engineering* **1**(1) (2009) pp. 185–188.
- I. S. Anderson; R. L. McGreevy & H. Z. Bilheux** (eds.). *Neutron Imaging and Applications.* Neutron Scattering Applications and Techniques. Springer US, Boston, MA (2009).
- G. Arnold & A. Weber.** *Crystal Orientation in Al by Slow Neutron Diffraction.* *Phys. Rev.* **73**(11) (1948) pp. 1385–1389.
- M. F. Ashby & D. R. H. Jones.** *Engineering Materials 2: An Introduction to Microstructures, Processing and Design.* Butterworth-Heinemann, 2nd edn. (1998).
- N. W. Ashcroft & N. D. Mermin.** *Solid State Physics.* Saunders College, Philadelphia (1976).
- F. Bachmann; R. Hielscher & H. Schaeben.** *Texture Analysis with MTEX - Free and Open Source Software Toolbox.* *Solid State Phenomena* **160** (2010) pp. 63–68.
- G. E. Bacon.** *Neutron diffraction.* Clarendon Press, Oxford (1967).
- S. Baechler; N. Kardjilov; M. Diericke; J. Jolie; G. Kühne; E. H. Lehmann & T. Materna.** *New features in cold neutron radiography and tomography Part I: thinner scintillators and a neutron velocity selector to improve the spatial resolution.* *Nucl. Instrum. Methods Phys. Res., Sect. A* **491**(3) (2002) pp. 481–491.

- 
- J. Banhart.** *Advanced Tomographic Methods in Materials Research and Engineering.* Oxford University Press (2008).
- S. Beucher & C. Lantuejoul.** *Use of watersheds in contour detection.* In: Workshop on Image Process., Real-time Edge Motion Detection/Estimation. Rennes, France (1979) pp. 17–21.
- K. Binder.** *Total Coherent Cross Sections for the Scattering of Neutrons from Crystals.* Phys. Status Solidi B **41**(2) (1970) pp. 767–779.
- J. Blanchette & M. Summerfield.** *C++ GUI Programming with Qt 4.* Prentice Hall Open Source Software Development Series, 2nd edn. (2008).
- M. Boin.** *Kompensation von Artefakten bei der Rekonstruktion tomographischer Datensätze.* Diploma thesis, Berufsakademie, FHW Berlin (2005).
- M. Boin & A. Haibel.** *Compensation of ring artefacts in synchrotron tomographic images.* Opt. Express **14** (2006) pp. 12071–12075.
- M. Boin; N. Kardjilov; W. Kockelmann & R. Schneider.** *Fundamentals of Bragg edge transmission.* In: NEUWAVE2. ISIS, Abingdon, UK (2009) .
- C. Bowman; P. Egelstaff & H. Priesmeyer.** *Experiments Using Single Neutron Pulses.* In: M. Misawa; M. Furusaka & H. Ikeda (eds.), Proc. ICANS XI (1991) .
- W. H. Bragg & W. L. Bragg.** *The Reflection of X-rays by Crystals.* Proc. R. Soc. London, Ser. A **88**(605) (1913) pp. 428–438.
- W. L. Bragg.** *The Diffraction of Short Electromagnetic Waves by a Crystal.* Proc. Cambridge Philos. Soc. **17** (1913) pp. 43–57.
- H.-G. Brokmeier.** *General Introduction in Crystallographic Textures.* Clausthal-Zellerfeld, IWW, TEXMAT workshop (2006).
- M. J. Buerger.** *Crystal-Structure Analysis.* Wiley & Sons, New York (1960).
- H.-J. Bunge.** *Texture Analysis in Materials Science: Mathematical Methods.* Göttingen (1993).

- H.-J. Bunge & H. Klein.** *Determination of quantitative, high-resolution pole figures with the area detector.* *Z. Metallkd.* **87**(6) (1996) pp. 465–475.
- H.-J. Bunge & R. A. Schwarzer.** *Orientation Stereology - A New Branch in Texture Research.* *Adv. Eng. Mater.* **3**(1-2) (2001) pp. 25–39.
- T. M. Buzug.** *Einführung in die Computertomographie: Mathematisch-physikalische Grundlagen der Bildrekonstruktion.* Springer, Berlin (2005).
- W. D. Callister.** *Materials Science and Engineering: An Introduction.* Wiley & Sons, 7th edn. (2007).
- J. M. Carpenter.** *Pulsed spallation neutron sources for slow neutron scattering.* *Nucl. Instrum. Methods* **145**(1) (1977) pp. 91–113.
- J. Chadwick.** *The Existence of a Neutron.* *Proc. R. Soc. London, Ser. A* **136**(830) (1932) pp. 692–708.
- S. Chandrasekhar.** *A first-order correction for extinction in crystals.* *Acta Cryst.* **9**(11) (1956) pp. 954–956.
- S. Chandrasekhar.** *Extinction in x-ray crystallography.* *Adv. Phys.* **9**(36) (1960) pp. 363–386.
- C. T. Chantler.** *Theoretical Form Factor, Attenuation and Scattering Tabulation for  $Z=1-92$  from  $E=1-10$  eV to  $E=0.4-1.0$  MeV.* *NIST, J. Phys. Chem. Ref. Data* **24**(1) (1995) pp. 71–643.
- T. Collins.** *ImageJ for microscopy.* *BioTechniques* **43**(S1) (2007) pp. S25–S30.
- J. R. D. Copley.** *Monte Carlo calculation of multiple scattering effects in thermal neutron scattering experiments.* *Comput. Phys. Commun.* **7**(6) (1974) pp. 289–317.
- B. D. Cullity & S. R. Stock.** *Elements of X-ray diffraction.* Prentice-Hall, Elements of X-ray diffraction, 3rd edn. (2001).

- 
- J. A. Dann; M. R. Daymond; L. Edwards; J. A. James & J. R. Santisteban.** *A comparison between Engin and Engin-X, a new diffractometer optimized for stress measurement.* Physica B **350**(1-3) (2004) pp. E511–E514.
- J. A. Dann; M. R. Daymond; J. A. James; J. R. Santisteban & L. Edwards.** *ENGIN-X: A New Diffractometer Optimised for Stress Measurement.* In: **G. Mank & H. Conrad** (eds.), Proc. ICANS XVI. Forschungszentrum Jülich, Düsseldorf-Neuss, Germany (2003) pp. 231–238.
- C. G. Darwin.** *The reflexion of X-rays from imperfect crystals.* Phil. Mag. **43**(257) (1922) pp. 800–829.
- M. R. Daymond; M. A. M. Bourke & R. B. Von Dreele.** *Use of Rietveld refinement to fit a hexagonal crystal structure in the presence of elastic and plastic anisotropy.* J. Appl. Phys. **85**(2) (1999) pp. 739–747.
- P. Debye.** *Interferenz von Röntgenstrahlen und Wärmebewegung.* Ann. Phys. **348**(1) (1913) pp. 49–92.
- P. D. Debye & P. Scherrer.** *Interferenz an regellos orientierten Teilchen im Röntgenlicht.* Phys. Z. **17** (1916) pp. 277–283.
- D. Deniz; J. M. E. Harper; J. W. Hoehn & F. Chen.** *Tilted fiber texture in aluminum nitride thin films.* J. Vac. Sci. Technol., A **25**(4) (2007) pp. 1214–1218.
- R. E. Dinnebier & S. J. L. Billinge.** *Powder diffraction: theory and practice.* RSC Publishing, Cambridge, UK (2008).
- W. A. Dollase.** *Correction of intensities for preferred orientation in powder diffraction: application of the March model.* J. Appl. Cryst. **19**(4) (1986) pp. 267–272.
- P. Egelstaff** (ed.). *Thermal neutron scattering.* Academic Press, London (1965).
- O. Engler & V. Randle.** *Introduction to Texture Analysis: Macrotexture, Microtexture, and Orientation Mapping.* CRC Press, Taylor & Francis, Boca Raton, USA, 2nd edn. (2009).



- E. Farhi; T. Hansen; A. Wildes; R. Ghosh & K. Lefmann.** *Designing new guides and instruments using McStas.* Appl. Phys. A **74** (2002) pp. s1471–s1473.
- E. Farhi; V. Hugouvieux; M. R. Johnson & W. Kob.** *Virtual experiments: Combining realistic neutron scattering instrument and sample simulations.* J. Comput. Phys. **228**(14) (2009) pp. 5251–5261.
- V. Favre-Nicolin & R. Černý.** *FOX, 'free objects for crystallography': a modular approach to ab initio structure determination from powder diffraction.* J. Appl. Cryst. **35**(6) (2002) pp. 734–743.
- E. Fermi; W. J. Sturm & R. G. Sachs.** *The Transmission of Slow Neutrons through Microcrystalline Materials.* Phys. Rev. **71**(9) (1947) pp. 589–594.
- M. E. Fitzpatrick & A. Lodini** (eds.). *Analysis of Residual Stress by Diffraction using Neutron and Synchrotron Radiation.* Taylor & Francis, London (2003).
- W. Friedrich; P. Knipping & M. V. Laue.** *Interferenzerscheinungen bei Röntgenstrahlen.* Ann. Phys. **346**(10) (1913) pp. 971–988.
- U. Garbe.** *New pole figure calculation software: 2DiffCalc.* J. Appl. Cryst. **42**(4) (2009) pp. 730–733.
- A. Giannakidis; L. Kotoulas & M. Petrou.** *Virtual sensors for 2D vector field tomography.* Journal of the Optical Society of America A **27**(6) (2010) pp. 1331–1341.
- J. R. Granada.** *Total Scattering Cross Section of Solids for Cold and Epithermal Neutrons.* Z. Naturforsch. A **39** (1984) pp. 1160–1167.
- W. Gropp.** *MPICH2: A New Start for MPI Implementations.* In: **D. Kranzlmüller; J. Volkert; P. Kacsuk & J. Dongarra** (eds.), Recent Advances in Parallel Virtual Machine and Message Passing Interface, vol. 2474 of *Lecture Notes in Computer Science*, pp. 37–42. Springer Berlin / Heidelberg (2002).
- R. W. Grosse-Kunstleve.** *SgInfo, a Comprehensive Collection of ANSI C Routines for the Handling of Space Groups.* <http://cci.lbl.gov/sginfo/> (1998).

- 
- R. W. Grosse-Kunstleve; N. K. Sauter; N. W. Moriarty & P. D. Adams.** *The Computational Crystallography Toolbox: crystallographic algorithms in a reusable software framework.* J. Appl. Cryst. **35**(1) (2002) pp. 126–136.
- S. J. Gurman.** *Maximizing structural information: neutron diffraction, X-ray diffraction and EXAFS.* In: **M. C. Fairbanks; A. N. North & R. J. Newport** (eds.), Conference on Neutron and X-ray scattering: Complementary techniques. Institute of Physics, London (1990) pp. 25–40.
- A. Haase; C. Genzel; D. Dantz; M. Löhmann; B. Wallis; C. Stock & W. Reimers.** *A New X-Ray Diffractometer 'ETA' for Surface Gradient Investigations in Phase, Texture and Stress Analysis.* In: **H. Morawiec & D. Stróz** (eds.), Proc. of the XVIII Conf. on Appl. Crystallography. World Scientific, 4.–7.9.2000, Katowice, Poland (2001) pp. 97–100.
- T. Hahn** (ed.). *International Tables for Crystallography. Vol. A, Space-group symmetry.* International Union of Crystallography, Chester, England, online edn. (2006).
- M. Haimerl.** *Modalitätsspezifische Anpassung medizinischer Bilddaten.* Ph.D. thesis, University of Karlsruhe (2003).
- S. R. Hall; F. H. Allen & I. D. Brown.** *The crystallographic information file (CIF): a new standard archive file for crystallography.* Acta Crystallogr., Sect. A: Found. Crystallogr. **47**(6) (1991) pp. 655–685.
- V. Hauk & H.-J. Nikolin.** *The Evaluation of the Distribution of Residual Stresses of the I. Kind (RS I) and of the II. Kind (RS II) in Textured Materials.* Textures and Microstructures **8 & 9** (1988) pp. 693–716.
- M. P. Hentschel; A. Lange & J. Schors.** *Direct iterative reconstruction of computed tomography trajectories (DIRECTT).* In: Proc. of SPIE, vol. 5766. San Diego, USA (2005) pp. 25–31.
- G. T. Herman.** *Image Reconstruction from Projections: Fundamentals of Computed Tomography (Computer Science & Applied Mathematics)* (1980).

- C. H. Hermann.** *Zur systematischen Strukturtheorie I. Eine neue Raumgruppensymbolik.* Z. Kristallogr. **68** (1928) pp. 257–287.
- R. Hielscher & H. Schaeben.** *A novel pole figure inversion method: specification of the MTEX algorithm.* J. Appl. Cryst. **41**(6) (2008) pp. 1024–1037.
- A. Hilger.** *Charakterisierung magnetischer Strukturen durch bildgebende Verfahren mit kalten Neutronen.* Ph.D. thesis, TU Berlin (2009).
- A. Hilger; N. Kardjilov; M. Strobl; W. Treimer & J. Banhart.** *The new cold neutron radiography and tomography instrument CONRAD at HMI Berlin.* Physica B **385** (2006) pp. 1213–1215.
- M. Hochhold; H. Leeb & G. Badurek.** *Tensorial neutron tomography: A first approach.* J. Magn. Magn. Mater. **157-158** (1996) pp. 575–576.
- J.-U. Hoffmann; D. Hohlwein & R. Schneider.** *TVtueb - Visualization and analysis of two and three dimensional diffraction data.* In: BENSU Users Meeting. Hahn-Meitner-Institut, Berlin (2003) .
- M. Hofmann; J. Rebelo-Kornmeier; U. Garbe; R. C. Wimpory; J. Repper; G. A. Seidl; H.-G. Brokmeier & R. Schneider.** *Scientific Review: Stress Spec: Advanced Materials Science at the FRM II.* Neutron News **18**(4) (2007) pp. 27–30.
- J. Hsieh.** *Computed Tomography: Principles, Design, Artifacts, and Recent Advances.* SPIE Press, Washington (2003).
- J. H. Hubbell & S. M. Seltzer.** *Tables of X-Ray Mass Attenuation Coefficients and Mass Energy-Absorption Coefficients (version 1.4).* online available at <http://physics.nist.gov/xaamdi>, National Institute of Standards and Technology, Gaithersburg, MD .
- M. Hutchings; P. Withers; T. Holden & T. Lorentzen.** *Introduction to the Characterization of Residual Stress by Neutron Diffraction.* CRC Press, Taylor & Francis, Boca Raton, USA (2005).
- B. Jähne.** *Digital Image Processing: Concepts, Algorithms, and Scientific Applications.* Springer, Berlin, 6th edn. (2005).

- 
- F. James.** *Monte Carlo theory and practice.* Rep. Prog. Phys. **43** (1980) pp. 1145–1189.
- J. A. James; E. C. Oliver; J. R. Santisteban; M. R. Daymond & J. A. Dann.** *Engin-X User Manual.* ISIS & The Open University, UK (2004).
- E. Jericha; R. Szeywerth; H. Leeb & G. Badurek.** *Reconstruction techniques for tensorial neutron tomography.* Physica B **397**(1-2) (2007) pp. 159–161.
- T. Jevremovic.** *Nuclear Principles in Engineering.* Springer US, Boston, MA, 2nd edn. (2008).
- W. Jones & N. H. March.** *Theoretical Solid State Physics, Vol.1: Perfect Lattices in Equilibrium.* John Wiley & Sons Ltd, New York (1973).
- A. C. Kak & M. Slaney.** *Principles of Computerized Tomographic Imaging (Classics in Applied Mathematics).* IEEE Press, University of Michigan (1988).
- W. A. Kalender.** *Computed Tomography: Fundamentals, System Technology, Image Quality, Applications.* Wiley-VCH, 2nd edn. (2000).
- N. Kardjilov; A. Hilger; I. Manke; M. Strobl; M. Dawson & J. Banhart.** *Neutron-Imaging Instrument CONRAD.* Neutron News **20**(2) (2009a) pp. 20–23.
- N. Kardjilov; A. Hilger; I. Manke; M. Strobl; M. Dawson & J. Banhart.** *New trends in neutron imaging.* Nucl. Instrum. Methods Phys. Res., Sect. A **605**(1-2) (2009b) pp. 13–15.
- N. Kardjilov; A. Hilger; I. Manke; M. Strobl; W. Treimer & J. Banhart.** *Industrial applications at the new cold neutron radiography and tomography facility of the HMI.* Nucl. Instrum. Methods Phys. Res., Sect. A **542**(1-3) (2005) pp. 16–21.
- N. Kardjilov; I. Manke; M. Strobl; A. Hilger; W. Treimer; M. Meissner; T. Krist & J. Banhart.** *Three-dimensional imaging of magnetic fields with polarized neutrons.* Nat. Phys. **4**(5) (2008) pp. 399–403.
- S. Kikuchi.** *Diffraction of Cathode Rays by Mica.* Jap. J. Phys. **5** (1928) pp. 83–96.

- S. Kirste.** *Entwicklung einer 64 bit-Software zur Separation morphologischer Strukturen in dreidimensionalen Bildern.* Diploma thesis, Berufsakademie, FHW Berlin (2005).
- C. Kittel.** *Introduction to solid state physics.* Wiley & Sons, 7th edn. (1995).
- K. H. Kloos.** *Eigenspannungen, Definition und Entstehungsursachen.* Materialwiss. Werkstofftech. **10**(9) (1979) pp. 293–302.
- W. Kockelmann.** *Status of the IMAT Facility at ISIS.* In: NEUWAVE3. Sapporo, Japan (2010) .
- W. Kockelmann; G. Frei; E. H. Lehmann; P. Vontobel & J. R. Santisteban.** *Energy-selective neutron transmission imaging at a pulsed source.* Nucl. Instrum. Methods Phys. Res., Sect. A **578**(2) (2007a) pp. 421–434.
- W. Kockelmann & A. Kirfel.** *Neutron diffraction imaging of cultural heritage objects.* Archeometriai Műhely / Archaeometry Workshop pp. 1–15.
- W. Kockelmann; E. C. Oliver & P. G. Radaelli.** *IMAT - An imaging and materials science & engineering facility for TS-II.* IMAT - draft proposal for discussion, ISIS, Didcot, UK (2007b).
- U. F. Kocks; C. N. Tomé & H.-R. Wenk.** *Texture and Anisotropy: preferred orientations in polycrystals and their effect on materials properties.* Cambridge University Press (2000).
- S. Koerner; E. H. Lehmann & P. Vontobel.** *Design and optimization of a CCD-neutron radiography detector.* Nucl. Instrum. Methods Phys. Res., Sect. A **454**(1) (2000) pp. 158–164.
- F. Kropff & J. R. Granada.** *CRIPO: A fast computer code for the evaluation of  $\sigma_{total}$  polycrystalline materials.* unpublished report CAB .
- F. Kropff; J. R. Granada & R. E. Mayer.** *The bragg lineshapes in time-of-flight neutron powder spectroscopy.* Nucl. Instrum. Methods **198**(2-3) (1982) pp. 515–521.
- J. Kulda; P. Mikula; P. Lukáš & M. Kocsis.** *Utilisation of bent Si crystals for elastic strain measurements.* Physica B **180-181** (1992) pp. 1041–1043.

- 
- M. F. L'Annunziata & W. Burkart.** *Radioactivity: introduction and history.* Elsevier, Amsterdam (2007).
- A. C. Larson & R. B. Von Dreele.** *General structure analysis system (GSAS).* Los Alamos National Laboratory Report LAUR **86-748**(86-748).
- K. Lefmann & K. Nielsen.** *McStas, a general software package for neutron ray-tracing simulations.* Neutron News **10**(3) (1999) pp. 20–23.
- L. Li.** *A general exact method for synthesizing parallel-beam projections from cone-beam projections via filtered backprojection.* Phys. Med. Biol. pp. 5643–5654.
- K. Lieutenant; T. Gutberlet; A. Wiedenmann & F. Mezei.** *Monte-Carlo simulations of small angle neutron scattering instruments at European spallation source.* Nucl. Instrum. Methods Phys. Res., Sect. A **553**(3) (2005) pp. 592–603.
- K. Lieutenant; G. Zsigmond; S. Manoshin; M. Fromme; H. N. Bordallo; D. Champion; J. Peters & F. Mezei.** *Neutron instrument simulation and optimization using the software package VITESS.* In: **M. S. del R o** (ed.), *Advances in Computational Methods for X-Ray and Neutron Optics*, vol. 5536. SPIE (2004) pp. 134–145.
- S. W. Lovesey.** *Theory of Neutron Scattering from Condensed Matter: Nuclear Scattering Vol 1 (International Series of Monographs on Physics)* (1986).
- J. Lu.** *Handbook of Measurement of Residual Stresses.* Fairmont Press, Lilburn, GA (1996).
- L. Lutterotti.** *Maud: a Rietveld analysis program designed for the internet and experiment integration.* In: 19th European Crystallographic Meeting (ECM). Nancy, France (2000) .
- E. Macherauch; H. Wohlfahrt & U. Wolfstieg.** *Zur zweckm aigen Definition von Eigenspannungen.* Harterei-Tech. Mitt. **28** (1973) pp. 201–211.
- E. Maire; P. Merle; G. Peix; J. Baruchel & J.-Y. Buffiere.** *X-Ray Tomography in Material Science.* Hermes Science Publications, Paris (2000).
- A. March.** *Mathematische Theorie der Regelung nach der Korngestalt bei affiner Deformation.* Z. Kristallogr. **81** (1932) pp. 285–297.

- S. Matthies & G. W. Vinel.** *On the Reproduction of the Orientation Distribution Function of Texturized Samples from Reduced Pole Figures Using the Conception of a Conditional Ghost Correction.* Phys. Status Solidi B **112**(2) (1982) pp. K111–K114.
- C.-V. Mauguin.** *Sur le symbolisme des groupes de répétition ou de symétrie des assemblages cristallins.* Z. Kristallogr. **76** (1931) pp. 542–558.
- N. Metropolis & S. Ulam.** *The Monte Carlo Method.* Journal of the American Statistical Association **44**(247) (1949) p. 335.
- P. Mikula; V. Wagner; P. Lukáš & R. Scherm.** *Real and momentum space focusing of neutrons by a cylindrically bent silicon crystal.* Physica B **180-181** (1992) pp. 981–983.
- D. F. R. Mildner & J. M. Carpenter.** *Multiple scattering correction to neutron diffraction data of isotropic systems using optimized Monte Carlo techniques.* Acta Crystallogr., Sect. A: Found. Crystallogr. **33**(6) (1977) pp. 954–961.
- G. Muhrer; T. Hill; F. Tovesson & E. Pitcher.** *Comparison of the measured and the calculated total thermal neutron cross-section of Pb.* Nucl. Instrum. Methods Phys. Res., Sect. A **572**(2) (2007) pp. 866–873.
- T. Mura.** *Micromechanics of Defects in Solids.* Kluwer Academic, New York, 2nd edn. (1987).
- K. Nielsen.** *McStas - Monte Carlo Simulation of Triple Axis Spectrometre.* Mcstas prototype report (1998).
- S. J. Norton.** *Tomographic Reconstruction of 2-D Vector Fields: Application to Flow Imaging.* Geophysical Journal International **97**(1) (1989) pp. 161–168.
- M. Nöthe; K. Pischang; P. Ponizil; B. Kieback & J. Ohser.** *Investigation of sintering processes by microfocus computer tomography ( $\mu$ -CT).* In: **J. Goebbels & U. Zscherpl** (eds.), International Symposium on Computed Tomography and Image Processing for Industrial Radiology (2003) pp. 273–280.
- I. C. Noyan & J. B. Cohen.** *Residual Stress. Measurement by Diffraction and Interpretation.* Springer, New York (1987).

- 
- I. C. Noyan; T. C. Huang & B. R. York.** *Residual stress/strain analysis in thin films by X-ray diffraction.* Crit. Rev. Sol. State and Mat. Sci. **20**(2) (1995) pp. 125–177.
- E. C. Oliver & W. Kockelmann.** *Report on moderator choice for IMAT* (2008).
- J. D. Patterson.** *Introduction to the theory of solid state physics.* Addison-Wesley, London (1971).
- S. Petriw; J. Dawidowski & J. R. Santisteban.** *Porosity effects on the neutron total cross section of graphite.* J. Nucl. Mater. **396**(2-3) (2010) pp. 181–188.
- M. Petrou & A. Giannakidis.** *Complete tomographic reconstruction of 2-D vector fields using a system of linear equations.* In: Proc. of the 12th Annual Medical Image Understanding and Analysis Conference (MIUA 2008). July 2-3, Dundee, Scotland, UK (2008) pp. 132–136.
- G. Placzek.** *Incoherent Neutron Scattering by Polycrystals.* Phys. Rev. **93**(4) (1954) pp. 895–896.
- T. Poeste; R. C. Wimpory & R. Schneider.** *The New and Upgraded Neutron Instruments for Materials Science at HMI - Current Activities in Cooperation with Industry.* Mater. Sci. Forum **524-525** (2006) pp. 223–228.
- W. H. Press; S. A. Teukolsky; W. T. Vetterling & B. P. Flannery.** *Numerical Recipes 3rd Edition: The Art of Scientific Computing.* Cambridge University Press, 3rd edn. (2007).
- H. G. Priesmeyer.** *Transmission Bragg-edge measurements.* In: **M. T. Hutchings & A. D. Krawitz** (eds.), *Measurement of residual and applied stress using neutron diffraction.* NATO ARW, Oxford (1992) .
- H. G. Priesmeyer; M. Stalder; S. Vogel; K. Meggers; R. Bless & W. Trela.** *Bragg-Edge Transmission as an Additional Tool for Strain Measurements.* Textures and Microstructures **33**(1-4) (1999) pp. 173–185.



- E. Prince** (ed.). *International Tables for Crystallography. Vol. C, Mathematical, physical and chemical tables*. International Union of Crystallography, Chester, England, online edn. (2006).
- A. R. Pyzalla**. *Analyse stark plastisch verformter Werkstoffe mit Beugungsverfahren*. Hahn-Meitner-Institut, BENSCH, Berlin (2001).
- A. Rack**. *Charakterisierung komplexer Materialsysteme mittels Synchrotron-Tomographie und 3D-Bildanalyse*. Ph.D. thesis, TU Berlin (2006).
- J. Radon**. *Über die Bestimmung von Funktionen durch ihre Integralwerte längs gewisser Mannigfaltigkeiten*. Berichte Sächsische Akademie der Wissenschaften, Leipzig, Mathematisch-Physikalische Klasse **69** (1917) pp. 262–277.
- C. Randau & H.-G. Brokmeier**. *Influence of the pole figure window on the quantitative texture of an Al7020 sheet*. In: 3rd International Conference on Texture and Anisotropy of Polycrystals (ITAP-3). Trans Tech Publications Ltd, GeoScience Center (GZG), Georg-August University of Göttingen, Germany (2009) .
- C. Randau; U. Garbe & H.-G. Brokmeier**. *StressTextureCalculator : a software tool to extract texture, strain and microstructure information from area-detector measurements*. J. Appl. Cryst. **44**(3) (2011) pp. 641–646.
- V. Randle & O. Engler**. *Introduction to Texture Analysis: Macrotecture, Microtexture and Orientation Mapping*. CRC Press, London (2000).
- W. Reimers; A. R. Pyzalla; A. K. Schreyer & H. Clemens** (eds.). *Neutrons and Synchrotron Radiation in Engineering Materials Science: From Fundamentals to Material and Component Characterization*. Wiley-VCH, Weinheim (2008).
- H. M. Rietveld**. *A profile refinement method for nuclear and magnetic structures*. J. Appl. Cryst. **2**(2) (1969) pp. 65–71.
- M. S. del Río & D. R. J.** *XOP: a multiplatform graphical user interface for synchrotron radiation spectral and optics calculations*. In: **P. Z. Takacs & T. W. Tonnessen** (eds.),

---

Materials, Manufacturing, and Measurement for Synchrotron Radiation Mirrors, vol. 3152. Proc. of SPIE (1997) pp. 148–157.

**J. Rodríguez-Carvajal.** *Recent Developments of the Program FULLPROF.* Commission on Powder Diffraction, IUCr Newsletter **26** (2001) pp. 12–19.

**J. Santisteban; L. Edwards; M. Fitzpatrick; A. Steuwer & P. Withers.** *Engineering applications of Bragg-edge neutron transmission.* Appl. Phys. A **74** (2002a) pp. s1433–s1436.

**J. R. Santisteban; M. R. Daymond; J. A. James & L. Edwards.** *ENGIN-X: a third-generation neutron strain scanner.* J. Appl. Cryst. **39**(6) (2006a) pp. 812–825.

**J. R. Santisteban; L. Edwards; M. E. Fitzpatrick; A. Steuwer; P. J. Withers; M. R. Daymond; M. W. Johnson; N. Rhodes & E. M. Schooneveld.** *Strain imaging by Bragg edge neutron transmission.* Nucl. Instrum. Methods Phys. Res., Sect. A **481**(1-3) (2002b) pp. 765–768.

**J. R. Santisteban; L. Edwards; H. G. Priesmeyer & S. C. Vogel.** *Comparison of Bragg-Edge neutron-transmission spectroscopy at ISIS and LANSCE.* Appl. Phys. A **74** (2002c) pp. S1616–S1618.

**J. R. Santisteban; L. Edwards & V. Stelmukh.** *Characterization of textured materials by TOF transmission.* Physica B **385-386** (2006b) pp. 636–638.

**J. R. Santisteban; L. Edwards; A. Steuwer & P. J. Withers.** *Time-of-flight neutron transmission diffraction.* J. Appl. Cryst. **34**(3) (2001) pp. 289–297.

**J. R. Santisteban; A. Steuwer; L. Edwards; P. J. Withers & M. R. Daymond.** *Phase analysis and imaging by TOF neutron transmission.* In: **G. Mank & H. Conrad** (eds.), Proc. ICANS XVI. Forschungszentrum Jülich, Düsseldorf-Neuss, Germany (2003) pp. 239–246.

**H. Schaeben & K. G. V. D. Boogaart.** *Spherical harmonics in texture analysis.* Tectonophysics **370**(1-4) (2003) pp. 253–268.

**A. M. Schönflies.** *Krystallsysteme und Krystalstruktur.* Teubner Verlag, Leipzig (1891).

- P. A. Seeger & L. L. Daemen.** *The neutron instrument simulation package, NISP.* In: Proc. of SPIE, vol. 5536 (2004) pp. 109–123.
- J. F. Shackelford.** *Introduction to Materials Science for Engineers.* Prentice Hall, 6th edn. (2004).
- V. A. Sharafutdinov.** *Tomographic problem of photoelasticity.* In: Proc. of the SPIE, vol. 1843 (1992) pp. 234–243.
- S. W. Smith.** *The scientist and engineer's guide to digital signal processing.* California Technical Pub., 2nd edn. (1999).
- W. F. Smith.** *Principles of Materials Science and Engineering.* Mcgraw-Hill College (1995).
- R. V. Southwell.** *An introduction to the theory of elasticity for engineers and physicists.* Oxford University Press, 2nd edn. (1941).
- L. Spieß; G. Teichert; R. Schwarzer; H. Behnken & C. Genzel.** *Moderne Röntgenbeugung: Röntgendiffraktometrie für Materialwissenschaftler, Physiker und Chemiker.* Vieweg+Teubner, Wiesbaden, 2nd edn. (2009).
- A. Steuwer.** *The essence of Bragg edges or Pulsed Neutron Transmission.* In: NEUWAVE. TU Munich, FRM2, Garching (2008) .
- A. Steuwer.** *Bragg edges, from theoretical concepts to practical experiments.* In: NEUWAVE2. ISIS, Abingdon, UK (2009) .
- A. Steuwer; J. R. Santisteban; P. J. Withers; L. Edwards & M. E. Fitzpatrick.** *In situ determination of stresses from time-of-flight neutron transmission spectra.* J. Appl. Cryst. **36**(5) (2003) pp. 1159–1168.
- A. Steuwer; J. R. Santisteban; P. J. Withers; L. Edwards & M. E. Fitzpatrick.** *Pattern decomposition and quantitative-phase analysis in pulsed neutron transmission.* Physica B **350**(1-3) (2004) pp. 159–161.
- A. Steuwer; P. J. Withers; J. R. Santisteban; L. Edwards; G. Bruno; M. E. Fitzpatrick; M. R. Daymond; M. W. Johnson & D. Q. Wang.** *Bragg Edge Deter-*

- 
- mination for Accurate Lattice Parameter and Elastic Strain Measurement.* Phys. Status Solidi A **185**(2) (2001) pp. 221–230.
- M. Strobl.** *Time-of-flight imaging at continuous (and pulsed) neutron sources.* In: NEUWAVE2. ISIS, Abingdon, UK (2009) .
- M. Strobl; I. Manke; N. Kardjilov; A. Hilger; M. Dawson & J. Banhart.** *Advances in neutron radiography and tomography.* J. Phys. D: Appl. Phys. **42**(24) (2009) p. 243001.
- P. Strunz; P. Lukáš; P. Mikula; V. Wagner; Z. Kouřil & M. Vrána.** *Data Evaluation Procedure for Energy-Dispersive Neutron-Transmission-Diffraction Geometry.* In: **T. Ericsson; M. Odén & A. Andersson** (eds.), The Fifth International Conference on Residual Stresses ICRS-5, vol. 2. University Press, Linköping, Sweden (1997) pp. 688–693.
- M. Tamaki.** *Conceptual monochromatic digital neutron radiography using continuous cold neutron beam.* Nucl. Instrum. Methods Phys. Res., Sect. A **542**(1-3) (2005) pp. 32–37.
- W. Treimer; M. Strobl; N. Kardjilov; A. Hilger & I. Manke.** *Wavelength tunable device for neutron radiography and tomography.* Appl. Phys. Lett. **89** (2006) p. 203504.
- S. C. Vogel.** *A Rietveld-Approach for the Analysis of Neutron Time-Of-Flight Transmission Data.* Ph.D. thesis, Christian-Albrecht-Univ. Kiel (2000).
- J. Šaroun & J. Kulda.** *RESTRAX — a program for TAS resolution calculation and scan profile simulation.* Physica B **234-236** (1997) pp. 1102–1104.
- J. Šaroun; T. Pirling & R. Rogge.** *Optimization of a focusing monochromator for neutron strain-scanning diffractometer.* Appl. Phys. A **74** (2002) pp. s1489–s1491.
- I. Waller.** *Zur Frage der Einwirkung der Wärmebewegung auf die Interferenz von Röntgenstrahlen.* Phys. Z. **17**(1) (1923) pp. 398–408.
- D. Q. Wang & L. Edwards.** *Pulsed neutron strain scanning.* Technical Report FRG/97/3/1, Faculty of Technology, Open University, Milton Keynes, UK (1997).
- G. A. Webster.** *Neutron Diffraction Measurements of Residual Stress in a Shrink-fit Ring and Plug.* VAMAS Report No. 38 .

- R. J. Weiss.** *Extinction Effects in Neutron Transmission of Polycrystalline Media.* Phys. Rev. **86**(3) (1952a) pp. 271–275.
- R. J. Weiss.** *Extinction Effects in Powders.* Proc. Phys. Soc. **B 65** (1952b) pp. 553–555.
- H.-R. Wenk & P. V. Houtte.** *Texture and anisotropy.* Rep. Prog. Phys. **67**(8) (2004) pp. 1367–1428.
- H. Wiedemann.** *Synchrotron Radiation.* Springer, Berlin (2002).
- P. K. Willendrup.** *McStas 1.7 - a new version of the flexible Monte Carlo neutron scattering package.* Physica B **350**(1-3) (2004) pp. E735–E737.
- P. K. Willendrup; E. Knudsen; E. Farhi & K. Lefmann.** *Users and Programmers Guide to the Neutron Ray-Tracing Package McStas.* Risø DTU, Roskilde, Denmark (2008).
- R. C. Wimpory; P. Mikula; J. Šaroun; T. Poeste; J. Li; M. Hofmann & R. Schneider.** *Efficiency Boost of the Materials Science Diffractometer E3 at BENSC: One Order of Magnitude Due to a Horizontally and Vertically Focusing Monochromator.* Neutron News **19**(1) (2008) pp. 16–19.
- C. G. Windsor.** *Pulsed Neutron Scattering.* Taylor & Francis, London (1981).
- L. Winsberg; D. Meneghetti & S. Sidhu.** *Total Neutron Cross Sections of Compounds with Different Crystalline Structures.* Phys. Rev. **75**(6) (1949) pp. 975–979.
- P. J. Withers & P. J. Webster.** *Neutron and Synchrotron X-ray Strain Scanning.* Strain **37**(1) (2001) pp. 19–33.
- W. Witt.** *Absolute Präzisionsbestimmung von Gitterkonstanten an Germanium- und Aluminium-Einkristallen mit Elektroneninterferenzen.* Z. Naturforsch. A **22** (1967) p. 92.
- U. Wolfstieg & E. Macherauch.** *Zur Definition von Eigenspannungen.* Härtereitech. Mitt. **31** (1976) pp. 2–3.
- S. I. Wright & B. L. Adams.** *Automatic analysis of electron backscatter diffraction patterns.* Metall. Mater. Trans. A **23**(3) (1992) pp. 759–767.

- 
- R. W. G. Wyckoff.** *The Analytical Expression of the Results of the Theory of Space-groups.* Carnegie Institution of Washington (1922).
- R. A. Young** (ed.). *The Rietveld Method.* Oxford University Press (1995).
- W. H. Zachariasen.** *The secondary extinction correction.* Acta Cryst. **16**(11) (1963) pp. 1139–1144.
- E. Zolotoyabko.** *Determination of the degree of preferred orientation within the March-Dollase approach.* J. Appl. Cryst. **42**(3) (2009) pp. 513–518.

## Calculation of $\varphi_1$ and $\varphi_3$

After [Granada, 1984], the function  $\varphi_1$  and  $\varphi_3$  introduced in section 3.2.1 can be evaluated by:

$$\varphi_m(\theta) = \int_{-1}^1 \frac{\varepsilon^m}{\exp(-\varepsilon/\theta) - 1} d\varepsilon = \frac{(-1)^{m+1}}{m+1} + I_m \left( (-1)^{m+1} + 1 \right) \quad (\text{A.1})$$

Towards an implementation, the function is further evaluated with the calculation of the term  $I_m$  and the consideration of the Riemann zeta function. Both is derived in [Granada, 1984] and [Vogel, 2000]. With  $m = 1$  the expression of  $\varphi_m$  becomes:

$$\varphi_1(\theta) = \frac{1}{2} + 2 \left[ \theta \log \left( 1 - \exp(-1/\theta) \right) + \theta^2 \left( \frac{\pi^2}{6} - \sum_{n=1}^{\infty} \frac{1}{\exp(n/\theta)n^2} \right) \right] \quad (\text{A.2})$$

Applying the same derivation for  $m = 3$ , the function  $\varphi_m$  included in the determination of the total incoherent neutron cross section becomes:

$$\varphi_3(\theta) = \frac{1}{4} + 2 \left[ \theta \log \left( 1 - \exp(-1/\theta) \right) + 6\theta^2 \left( \frac{\pi^4}{90} \theta^2 - \sum_{n=1}^{\infty} \frac{1}{\exp(n/\theta)n^2} \left( \frac{1}{2} + \frac{\theta}{n} + \left( \frac{\theta}{n} \right)^2 \right) \right) \right] \quad (\text{A.3})$$

Both equations are implemented to the nxs library according the Bragg edge calculation. As proposed by [Vogel, 2000], it is enough to execute the summation until the difference between two iterations is smaller than  $10^{-6}$ . Thus, the computation is usually limited to approximately 10 steps.





## Unit Cell Calculations

The equation shown here are used in the **nxs** library to calculate the lattice spacings  $d_{\vec{h}}$  of a given reflection  $\vec{h} = (h, k, l)$  and the unit cell volume  $V_0$  of a crystal system by means of the lattice parameters. A differentiation between the possible crystal structures is done in order to speed up the computation.

**Cubic**  $a = b = c; \alpha = \beta = \gamma = 90^\circ$

$$d_{\vec{h}} = \frac{a}{\sqrt{h^2 + k^2 + l^2}} \quad (\text{B.1})$$

$$V_0 = a^3$$

**Hexagonal**  $a = b; \alpha = \beta = 90^\circ; \gamma = 120^\circ$

$$d_{\vec{h}} = \frac{a}{\sqrt{\frac{4}{3}(h^2 + hk + k^2) + \frac{a^2}{c^2}l^2}} \quad (\text{B.2})$$

$$V_0 = a^2 c \sin\left(\frac{\pi}{3}\right)$$

**Trigonal**  $a = b; \alpha = \beta = \gamma \neq 90^\circ$

$$d_{\vec{h}} = \frac{\sqrt{3}ac}{\sqrt{4c^2(h^2 + k^2 + hk) + 3l^2a^2}} \quad (\text{B.3})$$

$$V_0 = a^2 c \sin\left(\frac{\pi}{3}\right)$$

---

**Tetragonal**  $a = b; \alpha = \beta = \gamma = 90^\circ$

$$d_{\vec{h}} = \frac{a}{\sqrt{h^2 + k^2 + \frac{a^2}{c^2}l^2}} \quad (\text{B.4})$$

$$V_0 = a^2c$$

**Orthorhombic**  $\alpha = \beta = \gamma = 90^\circ$

$$d_{\vec{h}} = \frac{1}{\sqrt{\frac{h^2}{a^2} + \frac{k^2}{b^2} + \frac{l^2}{c^2}}} \quad (\text{B.5})$$

$$V_0 = abc$$

**Monoclinic**  $\alpha = \beta = 90^\circ; \gamma \neq 90^\circ$

$$d_{\vec{h}} = \frac{abc\sqrt{1 - \cos^2\beta}}{\sqrt{b^2c^2h^2 + a^2c^2k^2\sin^2\beta + a^2b^2l^2 - 2ab^2chl\cos\beta}} \quad (\text{B.6})$$

$$V_0 = abc\sin\gamma$$

**Triclinic**

$$A = h^2b^2c^2\sin^2\alpha + a^2k^2c^2\sin^2\beta + a^2b^2l^2\sin^2\gamma$$

$$B = 2abc\left(hkc(\cos\alpha\cos\beta - \cos\gamma) + hbl(\cos\alpha\cos\gamma - \cos\beta) + akl(\cos\beta\cos\gamma - \cos\alpha)\right)$$

$$d_{\vec{h}} = \frac{abc\sqrt{1 - \cos^2\alpha - \cos^2\beta - \cos^2\gamma + 2\cos\alpha\cos\beta\cos\gamma}}{\sqrt{A + B}}$$

$$V_0 = abc\sqrt{1 - \cos^2\alpha - \cos^2\beta - \cos^2\gamma + 2\cos\alpha\cos\beta\cos\gamma}$$

(B.7)

## McStas Listings

The Bragg edge sample component implemented for the McStas neutron simulation is listed below. To keep up appearances, the input file reading routine `readParameterFile()` is listed within a separate section C.3.

### C.1. The Bragg Edge Sample Component

```
DEFINE COMPONENT BraggEdge_Powder
DEFINITION PARAMETERS ( string space_group="229" )
SETTING PARAMETERS ( double xwidth=0.05, double yheight=0.05, double
    zthick=0.05, double radius=0.0, string filename="", int max_hkl=8 )
OUTPUT PARAMETERS ( isrect )
STATE PARAMETERS ( x,y,z,vx,vy,vz,t,s1,s2,p )

SHARE
%{
    %include "nxs.h"
    %include "read_table-lib"

    int readParameterFile( char *fileName, UnitCell *uc )
    {
        ...
    }
%}

DECLARE
%{
    int isrect;
    int intersect;
    double p_transmit;
    double xsect_total;

    double lambda;
    double velocity;
    double fullpath;
```

```

double t1;
double t2;
double temperature;
UnitCell uc;
double A;
double mu_factor;
int V2L;
int i;
%}

INITIALIZE
%{
isrect = 0;
if ( !radius || !yheight )
{
if ( !xwidth || !yheight || !zthick )
exit( fprintf(stderr, "Error: %s has no volume (zero dimension)",
NAME_CURRENT_COMP) );
else
isrect = 1;
}

uc.maxHKL_index = max_hkl;
readParameterFile( filename, &uc );
mu_factor = 1.0 / uc.volume;
V2L = 2.0 * PI / V2K;
%}

TRACE
%{
intersect = 0;
if ( isrect )
intersect = box_intersect(&t1,&t2,x,y,z,vx,vy,vz,xwidth, yheight,
zthick);
else
intersect = cylinder_intersect(&t1,&t2,x,y,z,vx,vy,vz,radius, yheight
);

if( intersect && (t2>0) )
{
PROP_DT( rand01() * (t2-t1) + t1 );
velocity = sqrt( vx*vx + vy*vy + vz*vz );
lambda = V2L / velocity;
fullpath = velocity * (t2-t1);

xsect_total = 0.0;
xsect_total += nxsCoherentElastic(lambda, &uc );
xsect_total += nxsIncoherentElastic(lambda, &uc );
xsect_total += nxsTotalInelastic(lambda, &uc );
xsect_total += nxsAbsorption(lambda, &uc );

p_transmit = exp( -xsect_total * mu_factor * fullpath*1E2 );
p *= p_transmit;
}

```

```

%}

MCDISPLAY
%{
  double h;
  h=yheight;
  magnify("xyz");
  if (!isrect) {
    circle("xz", 0, h/2.0, 0, radius);
    circle("xz", 0, -h/2.0, 0, radius);
    line(-radius, -h/2.0, 0, -radius, +h/2.0, 0);
    line(+radius, -h/2.0, 0, +radius, +h/2.0, 0);
    line(0, -h/2.0, -radius, 0, +h/2.0, -radius);
    line(0, -h/2.0, +radius, 0, +h/2.0, +radius);
  } else {
    double xmin = -0.5*xwidth;
    double xmax = 0.5*xwidth;
    double ymin = -0.5*yheight;
    double ymax = 0.5*yheight;
    double zmin = -0.5*zthick;
    double zmax = 0.5*zthick;
    multiline(5, xmin, ymin, zmin, xmax, ymin, zmin, xmax, ymax, zmin,
              xmin, ymax, zmin, xmin, ymin, zmin);
    multiline(5, xmin, ymin, zmax, xmax, ymin, zmax, xmax, ymax, zmax,
              xmin, ymax, zmax, xmin, ymin, zmax);
    line(xmin, ymin, zmin, xmin, ymin, zmax);
    line(xmax, ymin, zmin, xmax, ymin, zmax);
    line(xmin, ymax, zmin, xmin, ymax, zmax);
    line(xmax, ymax, zmin, xmax, ymax, zmax);
  }
%}

END

```

## C.2. Sample Input File “Fe.txt”

```

# sample definition file for Bragg edge McStas simulation
#
# alpha_Fe
# space_group      229
# lattice_a        2.866
# lattice_b        2.866
# lattice_c        2.866
# lattice_alpha    90
# lattice_beta     90
# lattice_gamma    90
#
# column_label     1
# column_b_coherent 2
# column_sigma_inc 3
# column_sigma_abs 4
# column_molar_mass 5
# column_debye_temp 6

```

```
# column_x      7
# column_y      8
# column_z      9
#
26  9.45  0.4  2.56  55.85  464.0  0  0  0
```

### C.3. Parameter File Reading Routine

```
int readParameterFile( char *fileName, UnitCell *uc )
{
    uc->spaceGroup = "229";
    uc->a = 2.866;

    t_Table dataTable;
    Table_Read(&dataTable, fileName, 1);

    int i;
    char **parsing;

    int column_label = 10;
    int column_b_coherent = 2;
    int column_sigma_inc = 3;
    int column_sigma_abs = 4;
    int column_molar_mass = 5;
    int column_debye_temp = 6;
    int column_x = 7;
    int column_y = 8;
    int column_z = 9;

    parsing = Table_ParseHeader(dataTable.header,
        "space_group", "lattice_a", "lattice_b", "lattice_c", "lattice_alpha",
        "lattice_beta", "lattice_gamma", NULL);

    if (parsing)
    {
        if (parsing[0]) uc->spaceGroup = &parsing[0][strspn(parsing[0], " ")]
        ];
        else {
            fprintf(stderr, "%s: Error: No value for 'space_group' found in
                file %s\n", NAME_CURRENT_COMP, fileName);
            return -1;
        }
        if (parsing[1]) uc->a = atof(parsing[1]);
        else {
            fprintf(stderr, "%s: Error: No value for 'lattice_a' found in
                file %s\n", NAME_CURRENT_COMP, fileName);
            return -1;
        }
        if (parsing[2]) uc->b = atof(parsing[2]);
        else {
```

```
        fprintf(stderr, "%s: Error: No value for 'lattice_b' found in
            file %s\n", NAME_CURRENT_COMP, fileName);
    }
    if (parsing[3]) uc->c = atof(parsing[3]);
    else {
        fprintf(stderr, "%s: Error: No value for 'lattice_c' found in
            file %s\n", NAME_CURRENT_COMP, fileName);
    }
    if (parsing[4]) uc->alpha = atof(parsing[4]);
    else {
        fprintf(stderr, "%s: Error: No value for 'lattice_alpha' found in
            file %s\n", NAME_CURRENT_COMP, fileName);
    }
    if (parsing[5]) uc->beta = atof(parsing[5]);
    else {
        fprintf(stderr, "%s: Error: No value for 'lattice_beta' found in
            file %s\n", NAME_CURRENT_COMP, fileName);
    }
    if (parsing[6]) uc->gamma = atof(parsing[6]);
    else {
        fprintf(stderr, "%s: Error: No value for 'lattice_gamma' found in
            file %s\n", NAME_CURRENT_COMP, fileName);
    }
} else {
    fprintf(stderr, "%s: Error: parsing file %s - using default values\n"
        , NAME_CURRENT_COMP, fileName);
}
initUnitCell( uc );

if (dataTable.columns < 9)
{
    fprintf(stderr, "%s: Error: The number of columns in %s should be at
        least %d for [label,b_coherent,sigma_inc,sigma_abs,molar_mass,
        debye_temp,x,y,z] - using default values\n", NAME_CURRENT_COMP,
        fileName, 9);

    AtomInfo ai;
    ai.label = "Fe";
    ai.b_coherent = 9.45;
    ai.sigmaIncoherent = 0.4;
    ai.sigmaAbsorption = 2.56;
    ai.molarMass = 55.85;
    ai.debyeTemp = 464.0;
    ai.x[0] = 0.0;
    ai.y[0] = 0.0;
    ai.z[0] = 0.0;
    addAtomInfo( uc, ai );
}
else
{
    parsing = Table_ParseHeader(dataTable.header, "column_label", "
        column_b_coherent", "column_sigma_inc", "column_sigma_abs", "
        column_molar_mass", "column_debye_temp", "column_x", "column_y",
        "column_z", NULL);
}
```

```

if (parsing)
{
    if (parsing[0]) column_label = atoi( parsing[0] );
    if (parsing[1]) column_b_coherent = atoi( parsing[1] );
    if (parsing[2]) column_sigma_inc = atoi( parsing[2] );
    if (parsing[3]) column_sigma_abs = atoi( parsing[3] );
    if (parsing[4]) column_molar_mass = atoi( parsing[4] );
    if (parsing[5]) column_debye_temp = atoi( parsing[5] );
    if (parsing[6]) column_x = atoi( parsing[6] );
    if (parsing[7]) column_y = atoi( parsing[7] );
    if (parsing[8]) column_z = atoi( parsing[8] );
    for (i=0; i<9; i++)
        if (parsing[i])
            free(parsing[i]);
    free(parsing);
}

AtomInfo ai;
for( i=0; i<dataTable.rows; i++ )
{
    ai.label = "unknown";
    ai.b_coherent = Table_Index( dataTable,i,column_b_coherent-1 );
    ai.sigmaIncoherent = Table_Index( dataTable,i,column_sigma_inc-1 );
    ai.sigmaAbsorption = Table_Index( dataTable,i,column_sigma_abs-1 );
    ai.molarMass = Table_Index( dataTable,i,column_molar_mass-1 );
    ai.debyeTemp = Table_Index( dataTable,i,column_debye_temp-1 );
    ai.x[0] = Table_Index( dataTable,i,column_x-1 );
    ai.y[0] = Table_Index( dataTable,i,column_y-1 );
    ai.z[0] = Table_Index( dataTable,i,column_z-1 );
    addAtomInfo( uc, ai );
}
}
initHKL( uc );
return 0;
}

```

## C.4. LambdaYPSD\_monitor.comp

```

DEFINE COMPONENT LambdaYPSD_monitor
DEFINITION PARAMETERS (string filename, ny=150, nLambda=200,
    restore_neutron=0)
SETTING PARAMETERS (xmin=0, xmax=0, ymin=0, ymax=0, xwidth=0, yheight=0,
    Lambdamin, Lambdamax)
OUTPUT PARAMETERS (PSD_N, PSD_p, PSD_p2)
STATE PARAMETERS (x,y,z,vx,vy,vz,t,s1,s2,p)
POLARISATION PARAMETERS (sx,sy,sz)
DECLARE
%{
    double PSD_N[ny][nLambda];
    double PSD_p[ny][nLambda];
    double PSD_p2[ny][nLambda];
%}
INITIALIZE
%{
    int i,j;

```



```

if (xwidth > 0) { xmax = xwidth/2; xmin = -xmax; }
if (yheight > 0) { ymax = yheight/2; ymin = -ymax; }

if ((xmin >= xmax) || (ymin >= ymax)) {
    printf("LambdaYPSD_monitor: %s: Null detection area !\n"
           "ERROR (xwidth,yheight,xmin,xmax,ymin,ymax). Exiting",
           NAME_CURRENT_COMP);
    exit(0);
}

for (i=0; i<ny; i++)
    for (j=0; j<nLambda; j++)
    {
        PSD_N[i][j] = 0;
        PSD_p[i][j] = 0;
        PSD_p2[i][j] = 0;
    }
%}

TRACE
%{
    int i,j;
    double lambda,v;

    PROP_Z0;
    v = sqrt( vx*vx + vy*vy + vz*vz );
    lambda = K2V*(2.0*PI/v);

    if (x>xmin && x<xmax && y>ymin && y<ymax && lambda>Lambdamin && lambda<
        Lambdamax)
    {
        i = floor((y - ymin)*ny/(ymax - ymin));
        j = floor((lambda - Lambdamin)*nLambda/(Lambdamax - Lambdamin));
        PSD_N[i][j]++;
        PSD_p[i][j] += p;
        PSD_p2[i][j] += p*p;
    }
    if (restore_neutron)
        RESTORE_NEUTRON(INDEX_CURRENT_COMP, x, y, z, vx, vy, vz, t, sx, sy,
            sz, p);
%}

SAVE
%{
    DETECTOR_OUT_2D("LambdaYPSD monitor", "Y Position [m]",
        "Wavelength [A]", ymin, ymax, Lambdamin, Lambdamax, ny,
        nLambda, &PSD_N[0][0], &PSD_p[0][0], &PSD_p2[0][0],
        filename);
%}

END

```



## Ring and Plug Simulation

### D.1. Ring and Plug Sample Modification

#### TRACE

```
%{
...
/* get lattice spacings from current neutron position [i] */
/* use linear sampling between two listed positions */
d_axial = (sd.axial_list[i] - sd.axial_list[i-1]) / (sd.position_list[i] -
sd.position_list[i-1]) * (pos - sd.position_list[i-1]) + sd.
axial_list[i-1];

d_hoop = (sd.hoop_list[i] - sd.hoop_list[i-1]) / (sd.position_list[i] -
sd.position_list[i-1]) * (pos - sd.position_list[i-1]) + sd.
hoop_list[i-1];

d_radial = (sd.radial_list[i] - sd.radial_list[i-1]) / (sd.
position_list[i] - sd.position_list[i-1]) * (pos - sd.position_list
[i-1]) + sd.radial_list[i-1];

/* use sin2psi method to determine current dvalue */
sin2psi = sin(acos( (x*vx + z*vz) / sqrt(x*x + z*z) / sqrt(vx*vx + vz*
vz) ));
sin2psi = sin2psi * sin2psi;
dvalue = (d_hoop-d_radial) * sin2psi + d_radial;

/* include axial direction */
sin2psi = sin(acos( vy / sqrt(vx*vx + vy*vy + vz*vz) ));
sin2psi = sin2psi * sin2psi;
dvalue = (dvalue-d_axial) * sin2psi + d_axial;

/* recalculate lattice spacings for all hkl */
for( i=0; i<uc.nHKL; i++ )
{
uc.a = dvalue;
HKL *hkl = &(amp;uc.hklList[i]);
hkl->dhkl = calcDhkl( hkl->h, hkl->k, hkl->l, &uc );
hkl->FSquare = calcFSquare( hkl, &uc );
}
}
```

```
...  
%}
```

## D.2. Ring and Plug Input File

```
# VAMAS Ring and Plug Al lattice spacings  
#  
# space_group      225  
# lattice_a       4.0495  
# lattice_b       4.0495  
# lattice_c       4.0495  
# lattice_alpha   90  
# lattice_beta    90  
# lattice_gamma   90  
#  
# numAtoms        1  
# atom1_label     Al  
# atom1_b_coherent 3.449  
# atom1_sigma_inc 0.008  
# atom1_sigma_abs 0.23  
# atom1_molar_mass 26.98  
# atom1_debye_temp 429  
# atom1_x         0.0  
# atom1_y         0.0  
# atom1_z         0.0  
#  
#  
# d_hoop 4.04997   reference values for lattice spacing  
# d_radial 4.05151  
# d_axial 4.05037  
#  
# column_position 1  
# column_hoop 2  
# column_radial 3  
# column_axial 4  
#  
# position[m] hoop      radial      axial  
0.000  4.04782613  4.04782613  4.050293794  
0.002  4.04782613  4.04782613  4.050293794  
0.005  4.04782613  4.04782613  4.050293794  
0.008  4.04782613  4.04782613  4.050293794  
0.010  4.04782613  4.04782613  4.050293794  
0.013  4.05448267   4.04563324   4.049235402  
0.014  4.05387314   4.04624276   4.049235402  
0.015  4.05338141   4.04673450   4.049235402  
0.016  4.05297896   4.04713695   4.049235402
```

0.017	4.05264542	4.04747049	4.049235402
0.018	4.05236591	4.04775000	4.049235402
0.019	4.05212936	4.04798655	4.049235402
0.020	4.05192739	4.04818851	4.049235402
0.021	4.05175359	4.04836231	4.049235402
0.022	4.05160295	4.04851296	4.049235402
0.023	4.05147152	4.04864439	4.049235402
0.024	4.05135618	4.04875973	4.049235402
0.025	4.0512544	4.04886151	4.049235402